National & Kapodistrian University of Athens
Physics Department
Sector of Astrophysics, Astronomy and Mechanics

A study of broadband variability in the context of hybrid leptohadronic models for TeV blazars

Margaritis Chatzis
Supervisor: Assistant Professor Dr. Maria Petropoulou
Advisory Committee: Professor Dr. Apostolos Mastichiadis, Assistant Professor Dr. Kalliopi Dasyra

July 2024

Contents

Acknowledgments

Special Thanks to my supervisor Assistant Professor Dr. Maria Petropoulou for her continuous assistance during the duration of this project. I would also like to thank Dr. George Vasilopoulos for his help with questions related to observational data and data analysis, as well as Ph.D. candidate Stamatios Ilias Stathopoulos for his assistance in the implementation of the numerical code LeHaMoC. Without the guidance of these individuals, this thesis would not have been possible.

Margaritis Chatzis acknowledges support from the Hellenic Foundation for Research and Innovation (H.F.R.I.) under the "2nd call for H.F.R.I. Research Projects to support Faculty members and Researchers" through the project UNTRAPHOB (Project ID 3013).

Abstract

Blazars – a subclass of active galaxies – are intrinsically time-variable broadband sources of electromagnetic radiation. While modeling their time-average spectral energy distribution (SED) can be informative about the average physical conditions in the blazar radiation zone, the time domain of blazar models has not been adequately explored. The association of high-energy neutrinos from active galaxies has sparked the interest in models invoking the presence of relativistic protons in these sources. In this contribution, we explore relativistic proton (hadronic) signatures in the time domain blazar emission and search for those parameter combinations that unveil their presence during flaring epochs.

We investigate the time domain of a broad blazar sample. Utilizing the Gaussian process modeling method of the `celerite2` code, we model the parameters of stochastically-driven damped simple harmonic oscillators. These parameters enable us to create synthetic light curves describing the high-energy band of each source, thereby motivating the generation of time series for key model parameters. In particular, we investigate time variations of the particle energy injection rate, the magnetic field strength, and power law index variations of the lepto(-hadronic) particle population.

To conduct this SED model exploration we choose the TeV blazar Mrk 501 as our test case, as it has been the study ground for extensive investigations during individual flaring events. Using the code `LeHaMoC` we compute the electromagnetic radiation for a period of several years that contains several flares of interest. We search for energy windows where the hadronic emission may dominate, while discussing time lags and flux-flux correlations between different energy bands. Finally, we provide light curve predictions of Mrk 501 for the upcoming CTAO with `Gammapy`.

Blazars - υποκατηγορία ενεργών γαλαξιακών πυρήνων - είναι χρονομεταβαλλόμενες πηγές που εκπέμπουν σε όλο το μήκος του φάσματος. Αν και η μοντελοποίηση της μέσης φασματικής ενεργειακής κατανομής (SED) τους είναι χρήσιμη στην εξαγωγή των μέσων φυσικών συνθηκών εντός της περιοχής εκπομπής, η χρονική εξέλιξη των πηγών αυτών δεν έχει επαρκώς διερευνηθεί. Η συσχέτιση υψηλοενεργειακών νετρίνων από ενεργούς γαλαξιακούς πυρήνες δημιούργησε το ενδιαφέρον για μοντέλα που περιλαμβάνουν σχετικιστικά πρωτόνια στην θεώρηση τους. Σε αυτή την μεταπτυχιακή διπλωματική εργασία, διερευνούμε την ύπαρξη σχετικιστικών πρωτονικών (αδρονικών) σημάτων στην χρονομεταβλητότητα της εκπομπής των blazar και διερευνούμε συνδιασμούς παραμέτρων που αποκαλύπτουν την ύπαρξη τους σε περιόδους υψηλής ενεργότητας (Flares). Διερευνούμε τον παραμετρικό χώρο του χρόνου ενός ευρύ δείγματος από blazar. Αξιοποιώντας την "Gaussian process" μεθόδο του κώδικα `celerite2` μοντελοποιούμε τις παραμέτρους ενός στοχαστικά διεγερμένου αποσβήμενου απλού αρμονικού ταλαντωτή. Αυτές οι παράμετροι είναι ικανοί να δημιουργήσουν προσομοιώσεις καμπυλών φωτός που περιγράφουν το υψηλοενεργειακό κομμάτι του φάσματος κάθε πηγής. Αυτές οι καμπύλες ύστερα θα αξιοποιηθούν ως κίνητρο για την δημιουργία χρονοσειρών για σημαντικές φυσικές παραμέτρους της πηγής. Συγκεκριμένα, θα μελετήσουμε χρονομεταβολές στον ρυθμό έγχυσης ενέργειας των σωματιδίων, στην ισχύ του μαγνητικού πεδίου και στις μεταβολές του δείκτη του νόμου δύναμης του πληθυσμού των λεπτο(-αδρονικών) σωματιδίων. Για την διεξαγωγή αυτής της SED έρευνας επιλέγουμε τον TeV blazar Mrk 501 ως ενδεικτική πηγή καθώς έχει αποτελέσει πεδίο μελέτης για λεπτομερές έρευνες αναλύοντας μεμονωμένα flares. Χρησιμοποιώντας τον κώδικα `LeHaMoC` υπολογίζουμε την ηλεκτρομαγνητική ακτινοβολία για περίοδο μερικών ετών που εμπεριέχουν flares ενδαφέροντος. Διερευνούμε την ύπαρξη περιόδων όπου η αδρονική συνεισφορά είναι η κυρίαρχη και συζητάμε χρονικές υστερήσεις καθώς και συσχετίσεις σε διαγράμματα ροής-ροής μεταξύ διαφορετικών ενεργειακών μπαντών. Τέλος, υπολογίζουμε προσομειώσεις καμπυλών φωτός για τον Mrk 501 για το CTAO με το λογισμικο του Gammapy.

Chapter 1

Introduction

In this Chapter, we will briefly introduce the reader to active galaxy classifications highlighting blazars, mentioning their general observational characteristics (Section 1.1) and provide the motivation of this study (Section.1.2).

1.1 Blazars: A subclass of active galaxies

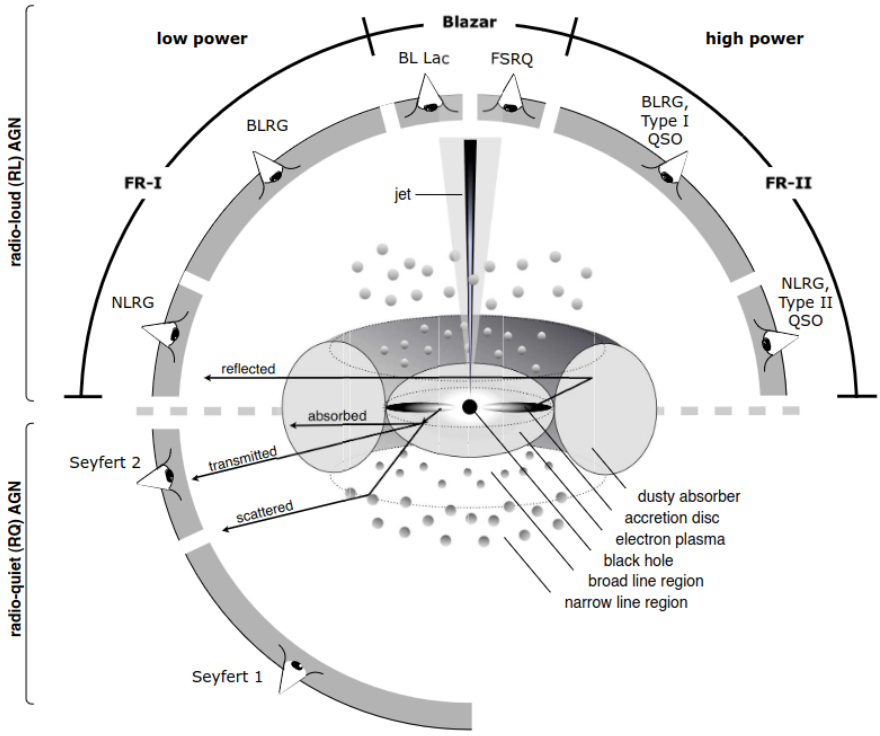

Figure 1.1: Unification schematic for Active Galactic Nuclei (AGN)[1].

Blazars are a subcategory of Active Galactic Nuclei (AGN). This section will briefly present the classifications and unified scheme of AGN.

AGN are galaxies that host a central supermassive black hole that is actively accreting

matter. They feature a hot accretion disk and a corona. They are multi-wavelength emitters radiating from optical through X-ray. Furthermore, narrow- and broad-line regions are defined by low- and high-velocity gas regions, respectively. A torus can obscure these regions depending on the viewing angle. Lastly, they are divided into radio-loud and radio-weak based on the power of their radio emission. AGN that launch relativistic jets of plasma usually belong to the radio-loud category According to the paradigm for AGN unification [2], the phenomenology of AGN can be explained as a result of viewing angles. Various AGN "types" are depicted in Fig. 1.1. The upper part of the schematic is dedicated to the radio-loud AGN while the lower part represents the radio quiet case. We note that for radio-loud systems, the AGN has 2 symmetric jets.

We provide a brief overview of the above classifications:

- **Blazars**: Blazars are the most extreme of the AGN "family" and the subject of this study. Their highly collimated outflows are directly pointed toward Earth and their emission results in the majority of the extra-galactic gamma-ray emission. They are divided into Bl Lacs and Flat-Spectrum Radio Quasars (FSRQs). The former have weak optical emission lines (equivalent width < 5 Å[3]) while the latter feature broad emission lines. Furthermore, we can classify them as Low-, Intermediate, or High-Synchrotron Peaked (LSP, ISP, HSP) depending on the peak range of the synchrotron emission as seen in Fig. 1.2 [4].

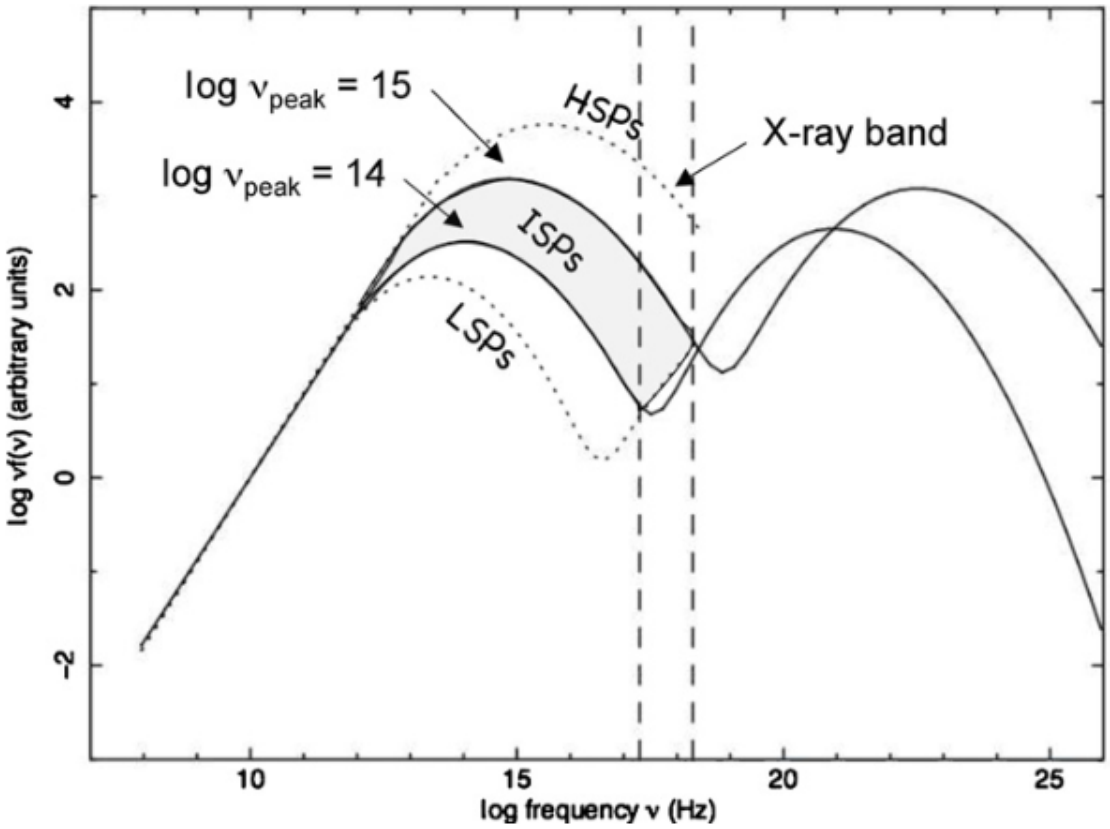

Figure 1.2: Differentiation between LSP sources ($\nu_{pk}^{syn} < 10^{14}$Hz), ISP sources ($10^{14}Hz < \nu_{pk}^{syn} < 10^{15}Hz$), and HSP sources ($\nu_{pk}^{syn} > 10^{15}Hz$) [4].

- **Seyferts**: Seyferts are radio-quiet AGN with total luminosities between $10^{44} - 10^{46}$ erg/s. They are mostly found within spiral galaxies and can be divided into two types. Seyfert 1 galaxies have broad and narrow absorption lines while Seyfert 2 galaxies only exhibit narrow line features as illustrated in Fig. 1.3. Furthermore, Seyfert 1 galaxies are more luminous in the 2-10 keV range than their type 2 counterparts [5],[6].

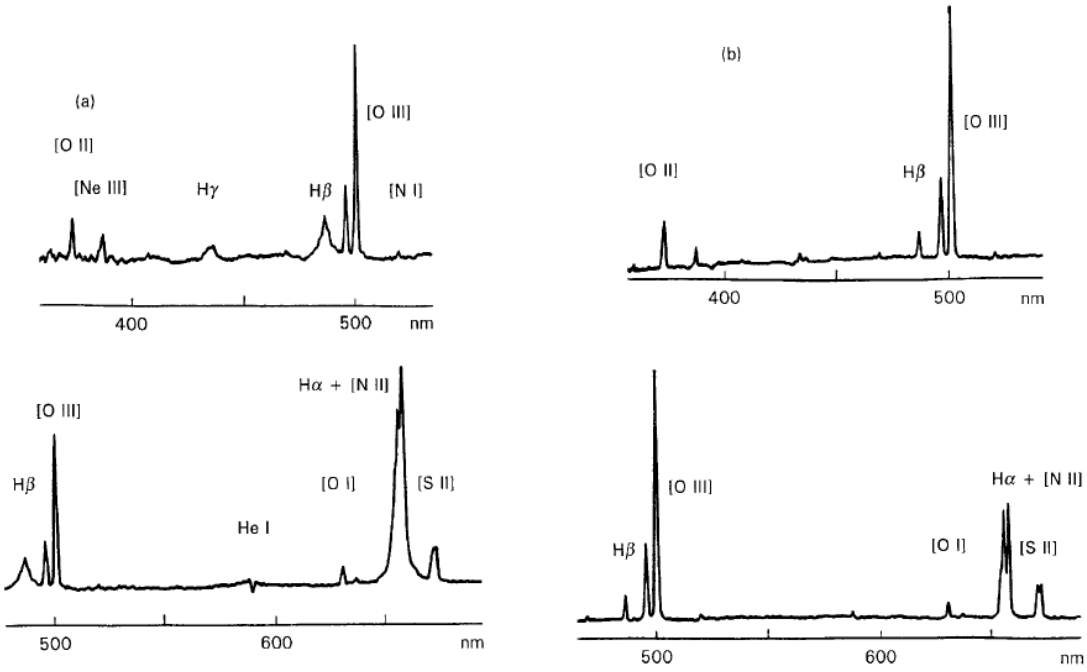

Figure 1.3: Optical spectrum of (a) Seyfert 1 galaxy NGC3227 and (b) Seyfert 2 Mkn 1157. The narrow [OIII] emission lines are comparable between the two types but the broad emission of [Hα] and [Hβ] is missing in the Seyfert 2 case [5].

- **Fanaroff and Riley types**: Fanaroff and Riley (FR) AGN are radio-loud galaxies divided into two types depending on their total power output. FR-I are less luminous than FR-II. Furthermore, FR-I have their bright spots close to the center while FR-II are most luminous at the outermost parts of the lobes as depicted in Fig. 1.4 for RF-I IC4296 on the left and RF-II 3C175 on the right [7]. Depending on the viewing angle both types are further classified as Broad- or Narrow-Line Regions (BLRG & NLRG) similar to Seyferts. However, unlike Seyferts, they are mostly found in elliptical galaxies.

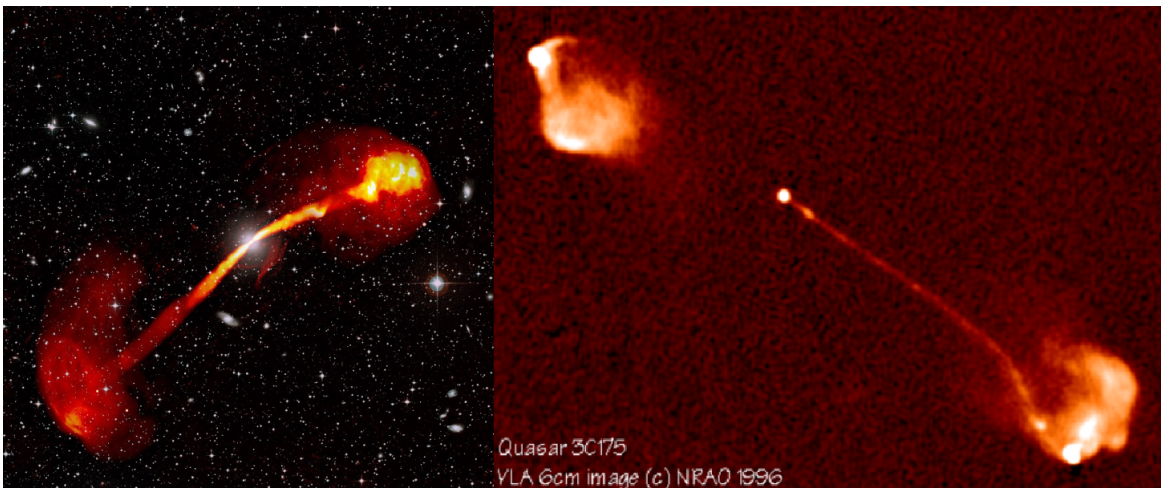

Figure 1.4: Comparison between RF-I and II radio images. Left: The RF-I IC4296 galaxy is most luminous close to the center. Right: The RF-II 3C175 is most luminous at the lobe edges [7].

Lastly, we will summarize the observational tools and properties used in blazar investigations [8]:

1. **Multi-wavelength observations.** Blazars and their variability are observed across the entirety of the multi-wavelength spectrum. These observations will be the foundations of this study and are:
   - Spectral energy distributions (SEDs). Extensive work has been conducted to observe sources across different energy bands simultaneously. This is supplemented by theoretical investigations, aiming to model the physical source parameters leading to the observed SEDs. In this study, we will model the time evolution of these SEDs.
   - Intra-day light curves. Blazars exhibit extreme variability reaching timescales on the order of minutes. This imposes constraints on the emitting region's size and its Doppler factor.
   - Long-term light curves. Blazars have been observed throughout the multi-wavelength spectrum over time scales on the order of magnitude of years. These observations reveal their long-term behavior (e.g. periodic) and uncover correlations between different energy bands. We will use several long-term light curves throughout this study.
2. **Very-long-baseline interferometry.** Blazars can be spatially resolved only at radio and millimeter waves through interferometry. In interferometry, several radio telescopes at varying locations on Earth observe the same source forming an interferometer. The angular resolution depends on the observing frequency and the distance between telescopes.
3. **Multi-messenger observations.** The recent high-energy neutrino detection from blazar TXS 0506+056 has sparked an interest in hadronic components of blazar SED models. This constitutes the basis of our motivation and is outlined in the following section.

1.2 Motivation

The extragalactic gamma-ray sky is dominated by blazars, a subclass of active galaxies with jets extending to millions of light years in distance that are closely aligned to our line of sight. Blazar jets are magnetized outflows of plasma, traveling almost at the speed of light and "shining" across the electromagnetic spectrum. Their spectral energy distribution (SED) exhibits variability on different timescales, ranging from minutes to months. Recent studies of blazar TXS 0506+056, the first astrophysical source to be associated with high-energy neutrinos, have shown that the emission of accelerated electrons in the jet produces most of the observed photon flux. Meanwhile, the photon emission arising from the relativistic proton population in the jet, which is needed to explain the neutrino emission, is sub-dominant. A dedicated study of blazar variability in the context of this new SED model, known as hybrid leptohadronic, is still missing, and the goal of this study is to fill this gap.

Using a sample of TeV-detected blazars with dense spectral coverage across the spectrum we first determine their behavior at gamma-ray energies. We will answer questions such as "How do we create synthetic time series describing their gamma-ray properties? What kind of processes do we use? Can the sample be described by the same "family" of models or do we need models of varying complexity to capture each source's characteristic behavior? What are the limitations of our chosen models and how do they impact our subsequent analysis?".

Having answered the above our aim is to choose one source out of this sample and using the numerical code, LeHaMoC, first derive baseline parameters by modeling the time-average source SED. We will investigate which dataset to use to describe the time-average state and argue for a best-practice scenario in modeling the leptonic and hadronic components.

Utilizing the above results, we turn our attention to specific time variations in singular key parameters or combinations thereof. We will investigate methods of connecting the aforementioned synthetic light curves through physical arguments to variations of source parameters. We will conduct experiments to answer open questions such as "Which parameters should we vary and in what way? What is the qualitative behavior of a hybrid leptohadronic SED time variation while varying those parameters? Are hadronic signatures present in those variations and if so what is their impact?". And most importantly "What is the proposed benefit of each time variable model in explaining long-term behavior or short periods of high activity? Are our models able to capture the behavior of the source?". To answer the latter, we will choose specific energy bands and compare flux variability between models and observations. Furthermore, we will investigate time lags and flux-flux correlations between the proposed energy bands to determine any hidden or periodic features. Lastly, we plan to use our results to generate simulated TeV light curves for the next-generation Cherenkov Telescope Array, which is expected to start operations within the next decade. This serves as another predictive tool to compare our models to future observations.

Therefore, through this contribution, we will analyze and describe the temporal domain of a sample of TeV-detected blazars. After selecting and modeling the time-average SED of a specific source of this sample, we answer some contemporary open questions of the field. We

will investigate the behavior of hybrid leptohadronic models in a time-variable scheme and search for parameters leading to "hadronic flares", i.e. time periods where the emission from the hadronic population may dominate in some part of the electromagnetic spectrum. Lastly, we will provide a series of statistical tools to compare our models' behavior to the source's observational behavior.

Chapter 2

Theoretical Background

In this chapter, we will introduce several ideas and concepts alongside some mathematical approximations to describe them. In particular, we will split the chapter into 3 parts. First, we will shortly describe the effect of bulk relativistic motion on the emission of an astrophysical source differentiating between our observer's frame and the source's rest frame (Section 2.1). Then, we will focus on a leptonic description of an astrophysical system. In other words, we will describe the main physical processes that are needed to explain the observed spectra: the electron synchrotron radiation, synchrotron-self Compton radiation, and the $\gamma\gamma$ pair absorption of the resulting spectra (Section 2.2). Lastly, we will describe the processes that have a hadronic origin. These include the direct contribution to the spectrum via proton synchrotron emission, photo-pion interactions, and Bethe-Heitler pair productions (Section 2.3). To provide the theoretical background necessary for this thesis we follow a multitude of textbooks ([9],[10],[11],[12]) and scientific articles ([13],[14],[15]), as well as references therein. Appropriate references have been made throughout the text to highlight specific results and methods.

2.1 Doppler Boosting

As our region of interest travels towards us with velocities comparable to the speed of light, the emitted light is subject to relativistic kinematics and Doppler boosting. What follows is a brief overview of the transformations of relevant source parameters we will encounter in our analysis. We adopt the convention that primed parameters are measured in the source's rest frame. We define the Doppler factor as [10]:

$$\delta = \Gamma^{-1}(1 - \beta\cos\theta)^{-1}, \tag{2.1}$$

where Γ is the Lorentz factor of the bulk plasma motion, $\beta = v/c$ is the bulk velocity over the speed of light, and θ is the angle between the velocity and our line of sight. Thus, for a general parameter A we define the Doppler boost as:

$$A = \delta^n A'$$

For the energy and frequency, we have a Doppler boost of $d\varepsilon' = \delta^{-1} d\varepsilon$ and $d\nu' = \delta^{-1} d\nu$,

respectively. For the time and length variable, a Lorentz transformation yields $dt' = \Gamma^{-1}dt$ and $ds' = \Gamma ds$ respectively. The latter implies a volume and number density transformation of $dV' = \Gamma dV$ and $dn' = \Gamma^{-1}dn$.

Utilizing the emission coefficient

$$j_\nu = n\frac{dW}{dtd\Omega d\nu}$$

and the relation for the solid angle $d\Omega' = \delta^2 d\Omega$ we conclude

$$j'_{\nu'} = \delta^{-2} j_\nu.$$

Defining the differential luminosity of a source at distance D as:

$$L_\nu = 4\pi D^2 S_\nu \;\; ; \;\; S_\nu = \int j_\nu dV/D^2 \tag{2.2}$$

we infer $L_\nu = \delta^3 L'_{\nu'}$ and by extension integrating over frequencies the expression for the total luminosity reads:

$$L = \delta^4 L' \tag{2.3}$$

For the remainder of this chapter, we will use the above transformations between the observed and intrinsic frames of reference without explicitly stating them.

2.2 Leptonic Interactions

2.2.1 Synchrotron Radiation - Total Power of Single Particle

Synchrotron radiation is the emission resulting from the relativistic motion of a particle moving in a magnetic field of strength B. Given the relativistic expression of Newton's second law, we have an equation for the particle's momentum and energy. Assuming a particle charge of q, a mass of m, and a Lorentz factor of γ, for a Lorentz force of $F_L = \frac{q}{c}\mathbf{v} \times \mathbf{B}$ we have [9]:

$$\frac{d}{dt}(\gamma m\mathbf{v}) = \frac{q}{c}\mathbf{v} \times \mathbf{B}$$

$$\frac{d}{dt}(\gamma mc^2) = q\mathbf{v} \cdot \mathbf{E} = 0,$$

where c is the speed of light and $\mathbf{v}$ is the particle's velocity. The second equation results in a constant Lorentz factor γ and thus implies a constant velocity magnitude $|\mathbf{v}|$. Decomposing the velocity into two orthogonal vectors, we obtain from the first equation:

$$\frac{d\mathbf{v}_\parallel}{dt} = 0, \quad \frac{d\mathbf{v}_\perp}{dt} = \frac{q}{\gamma mc}\mathbf{v}_\perp \times \mathbf{B}.$$

From the first equation, we conclude that $|\mathbf{v}_\perp|$ remains constant. The second equation on the other hand describes uniform circular motion perpendicular to the magnetic field, and by omitting vector notations, it can be rewritten as:

$$\frac{dv_\perp}{dt} = \omega_B v_\perp, \tag{2.4}$$

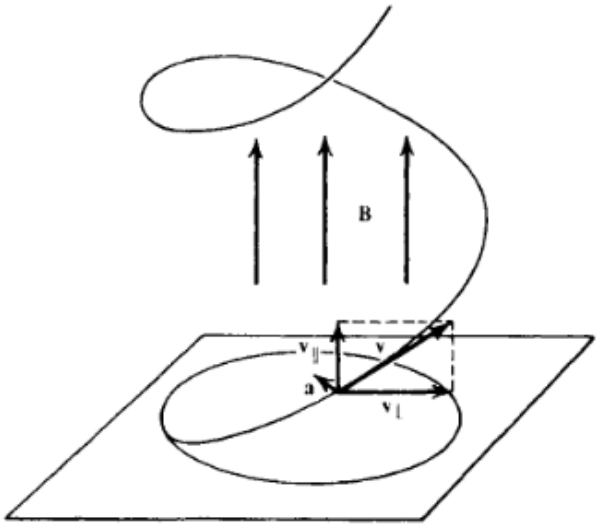

Figure 2.1: Helical motion of a particle moving in a magnetic field B [9].

where $\omega_B = \frac{qB}{\gamma mc}$ is called the frequency of gyration. Therefore, we have proven that a particle emitting synchrotron radiation moves with a constant velocity on the axis of the magnetic field. In contrast, it performs a uniform circular motion on the perpendicular one. The combination of these two results in a helical motion for the particle as seen in Fig. 2.1. To derive the total power emitted by a particle, we refer to the relativistic expression of the Larmor formula:

$$P = \frac{2q^2}{3c^3}(a_\perp^2 + \gamma^2 a_\parallel^2),$$

where, as discussed above, we only have $a_\perp$ given by $a_\perp = \omega_B v_\perp$. Expressing the perpendicular velocity as $v_\perp = c\beta_\perp/c$, and defining the classical electron radius, $r_0 = \frac{e^2}{m_e c^2}$ the synchrotron electron power is

$$P = \frac{2}{3} r_0^2 c \beta_\perp^2 \gamma^2 B^2.$$

Introducing the pitch angle α, the angle between the velocity and the magnetic field, we average $\beta_\perp$ over all angles:

$$< \beta_\perp^2 >= \frac{\beta^2}{4\pi} \int \sin^2\alpha d\Omega = \frac{2\beta^2}{3}.$$

Finally, the total electron synchrotron power is:

$$P = \frac{4}{3} \sigma_T c \beta^2 \gamma^2 U_B, \tag{2.5}$$

where we also utilized the relation between the classical electron radius r_0 and the Thomson cross section $\sigma_T = 8\pi r_0^2/3$, and the relation between the magnetic field and field density $U_B = B^2/8\pi$. From the above, we estimate the synchrotron cooling timescale as:

$$t_{cool} = \frac{E}{-\frac{dE}{dt}} = \frac{E}{P} = \frac{6\pi m_e c^2}{\sigma_T c \beta^2} B^{-2} \gamma^{-1}. \tag{2.6}$$

2.2.2 Synchrotron Radiation - Power Spectrum

Although the exact derivation of the power spectrum for a single particle is beyond the scope of the current discussion, we will provide here a qualitative overview of the results to enhance

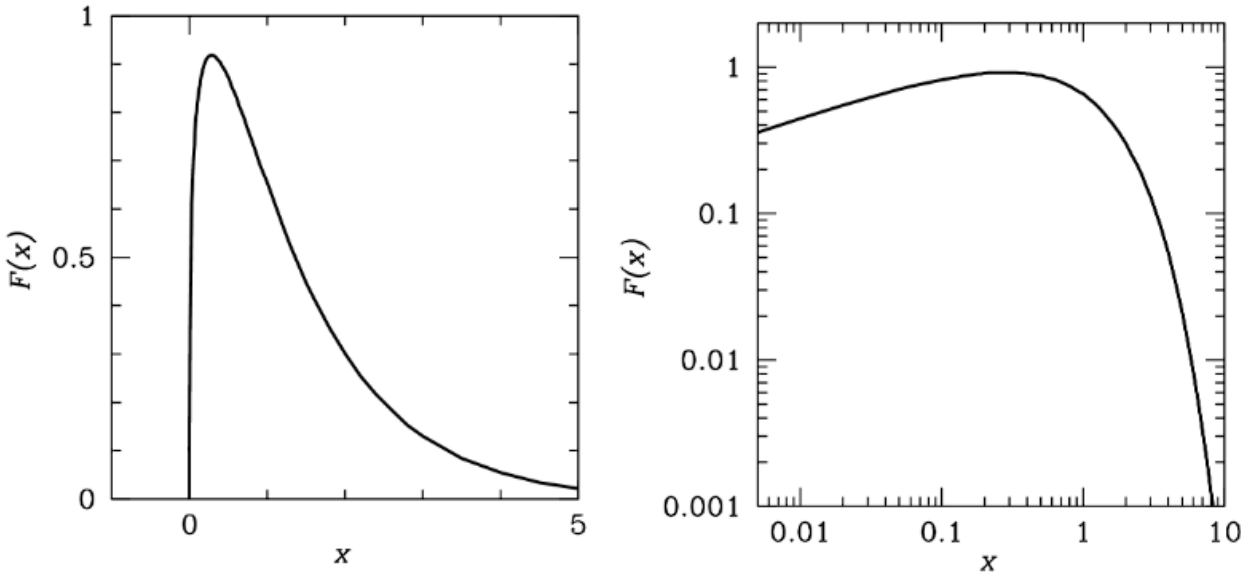

Figure 2.2: Synchrotron radiation spectrum of a single electron shown (Left) with linear axes; (Right) with logarithmic axes. The function is in terms of $x = \omega/\omega_c$. Analytic expressions for ω_c and F(x) are given within the text [11].

our comprehension of the observed spectra. The power distribution for a single particle is given by:

$$j(x) = \frac{\sqrt{3}q^3 B \sin\alpha}{2\pi m c^2} F(x) \ ,$$

$$F(x) = x \int_x^\infty K_{5/3}(\xi) d\xi \ ,$$

$$x = \omega/\omega_c \ ,$$

$$\omega_c = \frac{3\gamma^2 q B \sin\alpha}{2mc} \ .$$

We define a critical frequency ω_c depending on the properties of our particle and the magnetic field strength. $F(x)$, as seen in Fig. 2.2 has a peak at $x = 0.29$ with a value of almost 1. As such, ω_c is a good approximation for an order of magnitude estimation of the frequency at which the particle radiates the most. Furthermore, $F(x)$ has two interesting limits for the asymptotic behavior of x. Namely, a well-defined tail with a slope of 1/3 and a sharp cut-off:

$$F(x) \sim x^{1/3} \ , \ x << 1$$

$$F(x) \sim e^{-x} x^2 \ , \ x >> 1$$

From the definition of ω_c we deduce an approximate relation between emitted photon and electron energy. Namely, $\varepsilon_c = \frac{ehB}{2\pi m_e c} \gamma_c^2$ or normalizing at the rest mass electron energy:

$$\epsilon = b\gamma^2 \ \ ; \ \ b = B/B_{cr}, \ B_{cr} = \frac{m_e^2 c^3}{e\hbar}. \tag{2.7}$$

The above can be generalized for a distribution of particles. The derivation following [11] is presented below.

Assuming a power law distribution of particles given by:

$$N(E)dE = KE^{-p}dE \ , \ E_{min} < E < E_{max},$$

the total power distribution is:

$$J_{Pl}(\omega) = \int_0^\infty j(\omega/\omega_c)N(E)dE.$$

If

$$x = \frac{\omega}{\omega_c} = \frac{\omega}{(3/2)(qB/m)\gamma^2 \sin\alpha} = \frac{2\omega m^3 c^4}{3E^2 qB\sin\alpha} = \frac{A}{E^2},$$

it follows

$$E = (A/x)^{1/2} \ ; \ dE = -A^{1/2}x^{-3/2}dx$$

and

$$J_{Pl}(\omega) = \frac{K}{2A^{(p-1)/2}} \int_0^\infty j(x)x^{(p-1)/2}dx.$$

Finally:

$$J_{Pl}(\omega) = \frac{\sqrt{3}q^3 KB\sin\alpha}{2\pi mc^2(p+1)}\Gamma\left(\frac{p}{4}+\frac{19}{12}\right)\Gamma\left(\frac{p}{4}-\frac{1}{12}\right)\left(\frac{mc\omega}{3qB\sin\alpha}\right)^{-(p-1)/2}, \tag{2.8}$$

where we used

$$\int_0^\infty x^\mu F(x)dx = \frac{2^{\mu+1}}{\mu+2}\Gamma\left(\frac{\mu}{2}+\frac{7}{3}\right)\Gamma\left(\frac{\mu}{2}+\frac{2}{3}\right)$$

with $\mu = (p-3)/2$. If we assume that the escape timescale is $t_{esc} = R/c$ we can calculate a characteristic cooling frequency from Eq. (2.6) by equating $t_{esc} = t_{cool}$:

$$\nu_c = \delta b \gamma_c^2 \frac{m_e c^2}{h} \ ; \ \gamma_c = \frac{3m_{el}c^2}{4\sigma_T R_0 U_B}. \tag{2.9}$$

Assuming a continuous particle injection in the source, our cooled power law distribution steepens by 1 above this frequency, and thus our emission becomes $J_{Pl}(\nu) \sim \nu^{-p/2}$.

Throughout the above discussion we assumed an optically thin source, we assumed the optical depth τ to be smaller than 1. In other words, the radiation passes throughout the source without significant attenuation. On the other hand, in an optically thick source, $\tau > 1$, the radiation cannot pass through the source without significant attenuation[1]. When the synchrotron emission is optically thick to the particle population producing the emission we are in the synchrotron self-absorption (ssa) regime. We note, without proof, the slope of the ssa component as $J_{Pl}(\nu) \sim \nu^{5/2}$.

[1]For a detailed analysis of optical depths the interested reader is redirected to [9].

2.2.3 The δ Function Approximation of the Single-Particle Synchrotron Spectrum

Defining a delta approximation for the synchrotron radiation of a particle distribution is useful for estimating source parameters motivated by observed features. Following [10] we define a general photon emissivity (ph cm^{-3} s$^{-1}\epsilon^{-1}$) of:

$$\dot{n}_{syn}(\epsilon) = An_{el},$$

where $\epsilon = \varepsilon/m_e c^2$ and n_{el} an arbitrary electron distribution. If we assume the density of 1 electron cm^{-3}, $\frac{dN}{d\gamma dV} = n_{el}(\gamma) = \delta(\gamma - \bar{\gamma})$ we must recover the energy loss rate of electrons for a distribution of isotropic pitch angles.

$$\begin{aligned} -\dot{\gamma}_{syn} &= \int d\epsilon \epsilon \dot{n}_{syn}(\epsilon) \\ &= \int A\epsilon\delta(\gamma - \bar{\gamma})d\epsilon \\ &= \int_0^\infty A\epsilon\delta\left(\sqrt{\frac{\epsilon}{b}} - \bar{\gamma}\right)d\epsilon \\ &= \frac{4}{3}\sigma_T c \frac{U_B}{m_e c^2}\bar{\gamma}^2. \end{aligned} \tag{2.10}$$

But if

$$x = \frac{\epsilon}{b} \rightarrow \epsilon = \sqrt{x}^2 b,$$

then

$$\begin{aligned} &\sqrt{x} = b^{-1/2}\epsilon^{1/2} \\ &\Rightarrow d(\sqrt{x}) = \frac{1}{2}b^{-1/2}\epsilon^{-1/2}d\epsilon \\ &\Rightarrow d\epsilon = 2b\sqrt{x}d(\sqrt{x}). \end{aligned}$$

Thus,

$$\int_0^\infty A2b^2\sqrt{x}^3\delta(\sqrt{x} - \bar{\gamma}) = \frac{4}{3}\sigma_T c\frac{U_B}{m_e c^2}\bar{\gamma}^2 \Rightarrow A = \frac{2}{3}\sigma_T c U_B b^{-2}\bar{\gamma}^{-1}.$$

And finally

$$\dot{n}_{syn}(\epsilon) = \frac{2}{3}\sigma_T c U_B b^{-2}\epsilon^{-1/2}b^{-3/2}n_e(\gamma). \tag{2.11}$$

To transform (ph $cm^{-3}s^{-1}\epsilon^{-1}$) to (erg s^{-1}):

$$\epsilon L_\epsilon^{syn} = m_e c^2 V_b \epsilon^2 \dot{n}_{syn}(\epsilon) = \frac{2}{3}c\sigma_T U_B \gamma^3 N_e(\gamma).$$

And lastly to generalize for observed flux from a source at at a luminosity distance d_L and redshift z [14]:

$$f_\epsilon^{syn} = \frac{\delta^4}{4\pi d_L^2}\epsilon L_\epsilon^{syn} \Rightarrow f_\epsilon^{syn} = \frac{\delta^4}{6\pi d_L^2}c\sigma_T U_B \gamma'^3 N_e'(\gamma') \ ; \ \gamma' = \sqrt{\frac{\epsilon(1+z)}{\delta b}} \tag{2.12}$$

2.2.4 Energy Minimization

Having derived an expression for the delta approximation for the synchrotron flux we can derive a value for the magnetic field strength and the injected electron luminosity from an observational SED. Throughout this analysis, redshift effects will be disregarded. From the SED:

$$f_{\epsilon}^{syn} \sim \epsilon F_{\epsilon}^{syn} \sim \epsilon^{-\alpha+1} \; ; \; \alpha = (p-1)/2.$$

Assuming $N_{el}(\gamma)d\gamma = K\gamma^{-p}d\gamma$ for $\gamma_{min} < \gamma < \gamma_{max}$ and $p > 2$ we have for the total electron energy:

$$W_{el} = Km_e c^2 (2-p)^{-1} \left(\frac{\varepsilon_{max}}{\delta b m_e c^2}\right)^{1-p/2} \left[1 - \left(\frac{\varepsilon_{min}}{\varepsilon_{max}}\right)^{1-p/2}\right]. \tag{2.13}$$

Noting that $f_{\epsilon}^{syn} = F_{pk}\left(\frac{\epsilon}{\epsilon_{max}}\right)^{-(p-3)/2}$, we combine this with Eq. (2.12) and Eq. (2.13) to get:

$$W_{el} = \frac{6\pi d_L^2 m_p c^2 F_{pk}}{\sigma_T c U_{cr}(p-2)} \left[\left(\frac{\varepsilon_{max}}{\varepsilon_{min}}\right)^{p/2-1} - 1\right] \delta^{-7/2} \left(\frac{m_e c^2}{\varepsilon}\right)^{1/2} b^{-3/2} = A_{el} b^{-3/2}. \tag{2.14}$$

For a source of radius R the total energy of the magnetic field is:

$$W_B = U_B V = \frac{4\pi}{3} R^3 U_{cr} b^2 = A_B b^2. \tag{2.15}$$

The total energy is therefore written as:

$$W_{Tot} = A_{el} b^{-3/2} + A_B b^2. \tag{2.16}$$

And minimizing it for b we have:

$$\frac{\partial W_{Tot}}{\partial b}|_{b=b_{EM}} \Rightarrow b_{EM} = \left(\frac{3}{4}\frac{A_{el}}{A_B}\right)^{2/7}. \tag{2.17}$$

Thus:

$$W_B|_{b=b_{EM}} = A_B^{11/7} A_{el}^{-3/7}. \tag{2.18}$$

We also have:

$$u_{el} = \frac{W_{el}}{\frac{4\pi}{3}R^3} = \frac{A_{el}}{\frac{4\pi}{3}R^3} b^{-3/2} \Rightarrow u_{el}|_{b=b_{EM}} = \frac{1}{\frac{4\pi}{3}R^3}\left(\frac{3}{4}\right)^{-3/7} A_{el}^{4/7} A_B^{3/7}.$$

And therefore:

$$L_{el}^{inj} = \frac{4\pi}{3} R^2 c u_{el} = R^{-1} A_{el} b^{-3/2} \Rightarrow L_{el}^{inj}|_{b=b_{EM}} = R^{-1}\left(\frac{3}{4}\right)^{-3/7} A_{el}^{4/7} A_B^{3/7}. \tag{2.19}$$

2.2.5 Inverse Compton Radiation

Compton radiation is the scattering of photons by electrons. The "Inverse" in the name suggests an upscattering of low-energy photons on high-energy electrons. If the target photon population is produced from synchrotron radiation this phenomenon is referred to as Synchrotron-Self Compton. Although we will not provide a rigorous analysis of the Inverse Compton process, we will focus on a qualitative understanding of select characteristics of the phenomenon and discuss useful approximations. Throughout this analysis, we assume a pre- and post-scattering photon energy of ε and ε_1 respectively.

Before discussing particular examples it is noteworthy to emphasize two distinct limits:

- The Thompson limit. This limit occurs when the photon energy in the rest frame of the electron is much smaller than the rest mass energy of the electron, $\varepsilon' \ll mc^2$. Here, the cross-section is a constant given by $\sigma_T = 6.65 \cdot 10^{-25}\text{cm}^2$. After a scattering event, the maximum photon energy (in the observer's frame) is given by $\varepsilon_1^{max} = 4\gamma^2\varepsilon$ while the average energy is $< \varepsilon_1 >= 4/3\gamma^2\varepsilon$ [13].

- The Klein-Nishina limit. When the contrary condition holds, we enter the realm of the Klein-Nishina limit. This occurs when the energy of the photon in the rest frame of the electron exceeds the rest mass energy of the electron, $\varepsilon' \geq mc^2$. The cross-section takes on a complex form that in the extreme relativistic limit is approximated by $\sigma = \frac{3}{8}\sigma_T\epsilon^{-1}\left(ln(2)\epsilon + \frac{1}{2}\right)$ with $\epsilon = \varepsilon/mc^2$ [9]. The cross-section, and thus the number of events, rapidly falls off for increasing energies. In this limit, all the energy of the relativistic electron is transferred to the photon in a single scattering. Thus the photon energy after the scattering event is $\varepsilon_1 = \gamma mc^2$. We will not discuss this regime further.

To derive an expression for the energy-loss rate, we approximate:

$$\frac{dE}{dt} \approx \frac{dN}{dt} \cdot (\text{average energy}) = c\sigma_T n_{ph} \cdot \frac{4}{3}\gamma^2\varepsilon = \frac{4}{3}\sigma_T c\gamma^2 U_{ph},$$

$$P = \frac{4}{3}\sigma_T c\gamma^2 U_{ph}$$

where we estimated the scattering rate as $dN/dt = cn\sigma_T$ and $U_{ph} = n_{ph} \cdot \varepsilon$. The scattering rate is the cross-section of the event times the density of the targets times the speed of light. It can be shown that, despite being derived through estimations and approximations in this context, the resulting energy-loss rate can be reproduced by exact calculation in the Thomson limit.

From an SED of a Synchrotron+SSC scenario, we can compare the two peaks to derive the ratio between the energy density of the magnetic field, U_B, and the energy density of the photon field produced by the synchrotron emission, U_{ph}:

$$\frac{P_{syn}}{P_{IC}} = \frac{U_B}{U_{ph}}$$

For instance, if the peak of the SSC component is one order of magnitude lower than the peak of the synchrotron component, we infer that the energy density of the photon field must also be lower by an order of magnitude compared to the energy density of the magnetic field.

Similar to the synchrotron emission, for the SSC flux we have [14]:

$$f_{\epsilon}^{SSC,T} = \frac{\delta^4}{6\pi d_L^2} c\sigma_T U'_{syn} \gamma_T'^3 N'_e(\gamma'_T) \ ; \ \gamma'_T = \sqrt{\frac{\epsilon(1+z)}{\delta b}}. \tag{2.20}$$

We can improve this approximation by combining it with equations for the synchrotron radiation. Therefore, solving Eq. (2.12) for $N_e^{'}(\gamma^{'})$ we have:

$$N'_e(\gamma') = \frac{6\pi d_L^2 f_{\epsilon}^{syn}}{c\delta^4 \sigma_T U_B \gamma'^3}. \tag{2.21}$$

From Eq. (2.11) we get:

$$n'_{syn} = \frac{R'_b}{c} \dot{n}'_{syn}.$$

Inserting $n'_e(\gamma') = \frac{N'_e(\gamma')}{V'_b}$ into the above:

$$n'_{syn}(\epsilon') = \frac{3 d_L^2 f_{\epsilon}^{syn}}{m_e c^3 R_b'^2 \delta b^2 \gamma'^4}. \tag{2.22}$$

And thus:

$$u'_{syn}(\epsilon') = \epsilon' m_e c^2 n'_{syn}(\epsilon') = \frac{3 d_L^2 f_{\epsilon}^{syn}}{c R_b'^2 \delta b^2 \gamma'^4 \epsilon'} \tag{2.23}$$

We estimate that the variability timescale t_{var} must be at least of the order of R_b/c or if considering the relativistic scenario at redshift z:

$$t_{var} = \frac{(1+z) R'_b}{\delta c}.$$

Therefore, inserting Eq. (2.21) and Eq. (2.23) into Eq. (2.20) we have the result of [14]:

$$f_{\epsilon_s}^{SSC,T} = \frac{24\pi}{c^3} \frac{(1+z)^2 d_L^2 f_{\epsilon}^{syn}(\epsilon_{syn}^{pk}) f_{\epsilon}^{syn}(\epsilon_{syn})}{(t_{var} B \delta^3)^2} \ ; \ \epsilon_{syn} \frac{\delta b \epsilon_s}{\epsilon_{syn}^{pk}(1+z)}, \tag{2.24}$$

where ϵ_{syn} can be understood as the energy of the target photons.

2.2.6 Photon-Photon Absorption

A scattering event of 2 photons can result in their annihilation and the creation of an electron-positron pair, which is called pair production. As positrons radiate the same as electrons we consider them the same population. To create such a pair, an energy threshold must be met [12]:

$$\varepsilon \varepsilon_1 (1 - cos\theta) \geq 2(m_e c^2)^2, \tag{2.25}$$

where ε and ε_1 are the energies of the colliding photons, and theta is the angle between them. Therefore, if we are interested in photons of energy ε_1, we can calculate the minimum energy of the target photons for pair production as:

$$\varepsilon = 2(m_e c^2)^2 / \varepsilon_1.$$

Combined with a cross-section $\sigma_{\gamma\gamma}$ sharply peaked around the threshold energy (Figure. 2.3), we can estimate that most of the events will happen around this threshold energy.

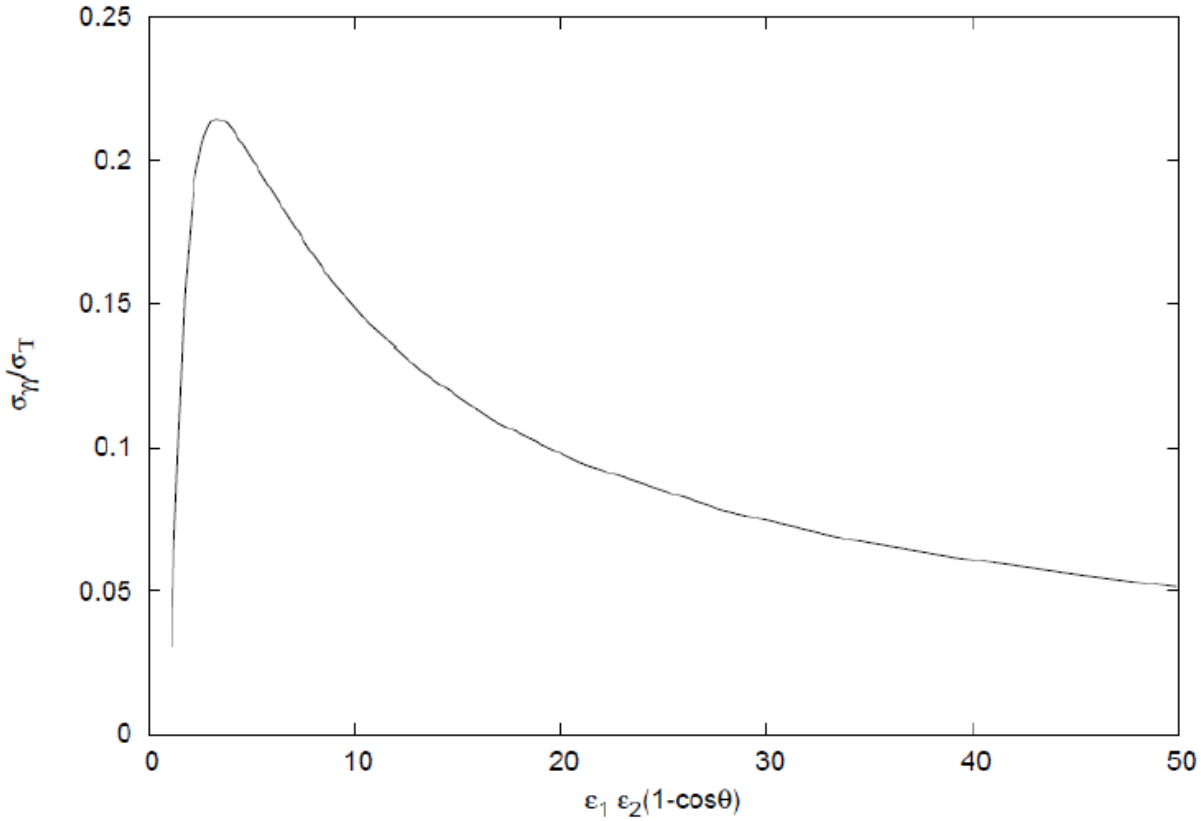

Figure 2.3: Cross section of $\gamma\gamma$ absorption. Function normalized at σ_T and in terms of colliding photon energies and their collision angle [12].

We define the optical depth for photons of energy $\epsilon = \varepsilon_1/m_e c^2$ in a source of radius R as [14],[16],[17]:

$$\tau_{\gamma\gamma} = R' \int_{-1}^{1} d\mu'(1-\mu') \int_{2/\epsilon'(1-\mu)}^{\infty} d\epsilon' \sigma_{\gamma\gamma}[\epsilon', \epsilon_1'(1-\mu')] n'(\epsilon', \mu'), \tag{2.26}$$

where $\mu = cos\theta$ and $n'(\epsilon', \mu')$ is the number density of the target photon field. If this field is isotropic (in the comoving frame) we can simplify it as $n'_{iso}(\epsilon') = n'(\epsilon', \mu')/2$ and thus:

$$\tau_{\gamma\gamma} = R' \int_{0}^{\infty} d\epsilon' \sigma_{\gamma\gamma}(\epsilon', \epsilon_1') n'_{iso}(\epsilon') \tag{2.27}$$

Since in our analysis, we are interested in modeling the internal $\gamma\gamma$ absorption on a photon field produced by the δ approximation of synchrotron radiation, we can use Eq. (2.22) and a cross-section of [18]:

$$\sigma_{\gamma\gamma}(\epsilon', \epsilon_1') \approx \frac{1}{3}\sigma_T \epsilon' \delta(\epsilon' - \frac{2}{\epsilon_1'}).$$

The resulting optical depth for photons of energy ϵ_1 is thus given by

$$\tau_{\gamma\gamma}(\epsilon_1) \approx \frac{(1+z)^2 \sigma_T d_L^2}{2 m_e c^4 t_{var} \delta^6} \epsilon_1 f_{\bar{\epsilon}}^{syn} \quad ; \quad \bar{\epsilon} = \frac{2\delta^2}{(1+z)^2 \epsilon_1} \tag{2.28}$$

Requiring the observed source to be optically thin ($\tau_{\gamma\gamma} < 1$) to gamma rays of energy ϵ_1, we define a lower limit for the Doppler factor [14],[19]:

$$\delta > \left[\frac{2^{a-1}(1+z)^{2-2a}\sigma_T d_L^2}{m_e c^4 t_{var}}\epsilon_1 f_{\epsilon_1^{-1}}^{syn}\right]^{1/(6-2a)}, \tag{2.29}$$

where we assumed a power law of $f_\epsilon \sim \epsilon^a$ for the synchrotron flux.

2.3 Hadronic Interactions

2.3.1 Proton Synchrotron

Protons are charged particles that radiate due to the synchrotron process outlined in the previous section. They have the same (but opposite) charge to electrons and a different mass. The difference in the sign of the charge does not change our result, it only reverses the circular component of the helical motion compared to the electrons. However, the different masses will lead to the following correction:

$$P_p^{syn} = (\frac{m_e}{m_p})^2 P_e^{syn} = \mu^2 P_e^{syn}.$$

Considering how $\mu = m_e/m_p = 1/1836$, it is significantly harder to observe synchrotron radiation due to a proton component. As an extension of the above, we also have:

$$t_p^{cool} = \mu t_e^{cool}.$$

Generally, the difference to our electron synchrotron results will be the substitutions: $m_e \rightarrow m_e/\mu$.

2.3.2 Photohadronic interactions

Photohadronic interactions of astrophysical interest can be classified into 2 categories.

1) Photopion production ($p\pi$)

Photopion production can manifest in one of two versions. We can either produce a neutral pion which then will decay into 2 gamma ray photons:

$$p + \gamma \rightarrow \pi^0 + p$$

$$\pi^0 \rightarrow \gamma + \gamma$$

or we can have a charged pion which will lead to the production of 1 electron and 3 neutrinos:

$$p + \gamma \rightarrow \pi^{\pm} + n(\Delta^{++})$$

$$\pi^{\pm} \rightarrow \mu^{\pm} + \nu_\mu(\bar{\nu}_\mu)$$

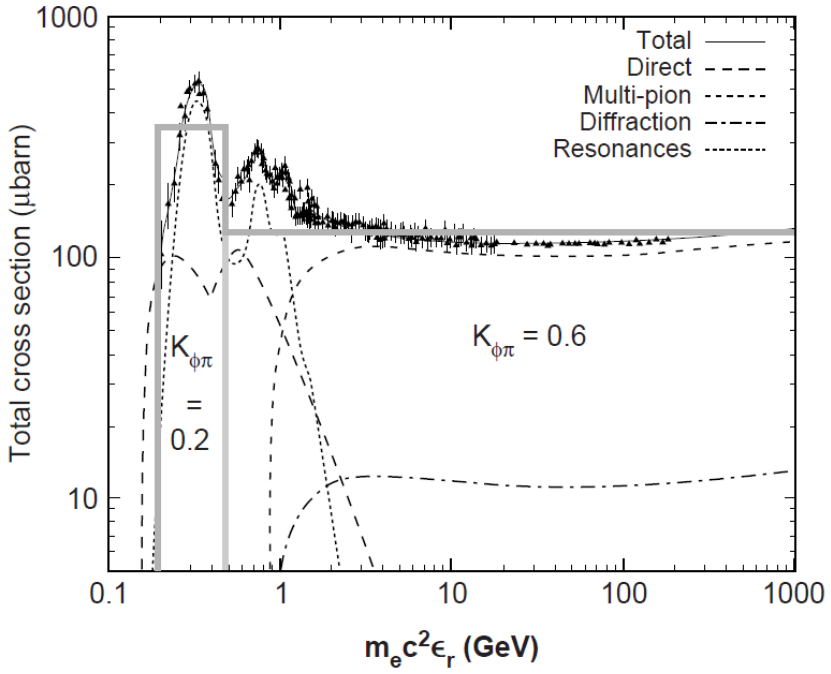

Figure 2.4: Photo-pion cross-section. Individual components and two-step-function approximation are noted. Inelasticities are mentioned in each region [10].

$$\mu^{\pm} \rightarrow e^{\pm} + \bar{\nu}_{\mu}(\nu_{\mu}) + \nu_{e}(\bar{\nu}_{e}).$$

The cross-section of this event can be found in Fig. 2.4 but a complete treatment of the different components is beyond the scope of this analysis. We refer the interested reader to [10] for a more thorough investigation. We, on the other hand, will assume the two-step-function approximations also depicted in Fig. 2.4. The transition from the former to the latter occurs at a photon energy, in the rest frame of the photon, of 500 MeV. Similarly, we assume a two-region approximation to the inelasticity of the process, the energy transfer ratio from the proton to the pion. As depicted in the figure, in the first region, named single-pion channel, we have a mean inelasticity of $K_{p\gamma} = 0.2$, while in the second, named multi-pion channel, we have $K_{p\gamma} = 0.6$ which becomes 0.2 for each pion population $(\pi^{\pm}, \pi^{0})$.

To approximate the energies at which the electrons are injected we first define the proton energy threshold of this process [15]:

$$\gamma_{p}^{th} = x_{th}/x_{syn}.$$

Here, x_{syn} is the dimensionless threshold energy $x_{th} = m_{\pi}c^2/m_{e}c^2$ with $m_{\pi}c^2 = 145MeV$. x_{syn} is the dimensionless energy of the target synchrotron photons given by:

$$x_{syn} = \frac{h\nu_{syn}(1+z)}{\delta} \quad ; \quad \nu_{syn} = 3 \cdot 10^{6}\delta B\gamma^{2}. \tag{2.30}$$

Therefore, for a typical synchrotron peak frequency of $\nu_{syn}^{pk} = 10^{18}Hz$:

$$\gamma_{p,p\gamma}^{th} = 3.5 \cdot 10^{4}(1+z)^{-1}\delta\nu_{18}^{-1} \tag{2.31}$$

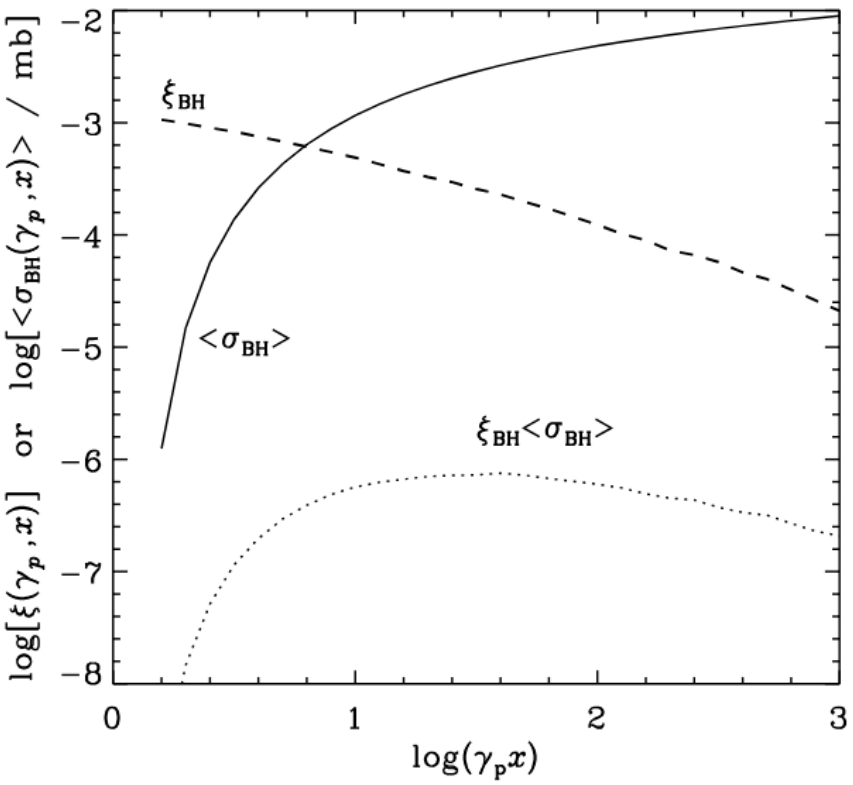

Figure 2.5: Mean cross-section, inelasticity, and their product for the Bethe-Heitler process. Functions are in terms of the proton Lorentz factor and the dimensionless photon energy $x = \epsilon_{ph}/m_e c^2$ [20].

and to translate this into secondary electrons [15]:

$$\gamma_{e,pg}^{th} = K_{p\gamma}\gamma_{p,p\gamma}^{th} m_p/(4m_e). \tag{2.32}$$

Thus, we have a proxy for the energies of the secondaries and their resulting synchrotron emission.

2) Bethe-Heitler pair production (pe)

In the Bethe-Heitler process, a relativistic moving proton can scatter a photon producing an electron-positron pair. This results in secondary electron injection at energies different from the primary population. To describe the proton energy loss rate of such an event, it is beneficial to consider the cross-section of the event, as well as the cross-section multiplied by the mean inelasticity. This can be seen in terms of the proton Lorentz factor γ and the dimensionless photon energy $x = \epsilon_{ph}/m_e c^2$ in Figure 2.5.

To approximate the energy at which the electrons are injected the proton threshold energy reads [15]:

$$\gamma_{p,BH}^{th} = 1.2 \cdot 10^2 (1+z)^{-1} \delta \nu_{18}^{-1} \tag{2.33}$$

Noting how the Bethe-Heitler process yields $\gamma_p \sim \gamma_e$, we have a proxy for the energies of the secondaries and their resulting synchrotron emission.

Chapter 3

Celerite - Generation of Time Series

Our goal is to study the time variability of blazars. To that end, we need 3 key components, the average state of the source, a time series after which to vary our parameters, and the relation between time series and parameters. Here, we will conduct a time series analysis for a broad sample of blazars before selecting and modeling a specific source throughout the next chapters. We will be using Gaussian process modeling via the software `celerite2`[1] ([21],[22]) (Introduced in Section 3.1) to derive the statistical properties of the long-term Fermi-LAT Light Curves[2] (LCs) ([23]) of each source (Section 3.2) while illustrating the limitations of the method (Section. 3.3).

3.1 Gaussian Processes and Celerite

3.1.1 Introduction

To understand the modeling process we first examine the characteristics of a Gaussian distribution. Therefore, for a single variable x, we can define the univariate Gaussian (or normal) distribution as the function:

$$p(x;\mu,\sigma^2) = \frac{1}{\sqrt{2}\pi\sigma} exp\left(-\frac{1}{2\sigma^2}(x-\mu)^2\right),$$

where μ is the mean and σ the standard distribution, while the normalization term of $\frac{1}{\sqrt{2}\pi\sigma}$ ensures $\int_{-\infty}^{\infty} p(x;\mu,\sigma^2)dx = 1$.

Generalizing for a vector of coordinates $X = (x_1 \dots x_n)^T$ of dimension N we write the multivariate Gaussian distribution as

$$p(x;\mu,K_\alpha) = \frac{1}{(2\pi)^{N/2}|K_\alpha|^{1/2}} exp\left(-\frac{1}{2}{r_\theta}^T K_\alpha^{-1} r_\theta\right),$$

with

$$r_\theta = (x_1 - \mu_\theta \dots x_n - \mu_\theta).$$

[1] https://celerite2.readthedocs.io/en/latest/

[2] https://fermi.gsfc.nasa.gov/ssc/data/access/lat/LightCurveRepository/

Here, μ_θ is the mean function parametrized by the parameter θ. K_α is the covariance matrix parametrized by α, with elements the covariance or "kernel" functions k_α, such that $[K_\alpha]_{nm} = k_\alpha(x_n, x_m)$. The covariance of 2 variables is defined through the expectation $E[X] = \sum_{x_n}^{N} x_i p(x_n; \mu, \sigma^2)$ of a discrete random variable as follows:

$$Cov[X, Y] = E[(X - E[X])(Y - E[Y])] = E[XY] - E[X]E[Y].$$

To estimate the best choices for θ and α given a data set of $Y = (y_1 \dots y_n)^T$ we calculate the log-likelihood of the previous equation which gives the conditional probability that Y is realized given X, θ, and α:

$$\ln \mathcal{L}(\theta, \alpha) = \ln p(y|X, \theta, \alpha) = -\frac{1}{2} r_\theta^T K_\alpha^{-1} r_\theta - \frac{1}{2} \ln(\det K_\alpha) - \frac{N}{2} ln(2\pi). \tag{3.1}$$

The celerite process reduces the computational cost of the above log-likelihood maximization by considering only a specific set of acceptable kernel functions. Namely, the input parameters x_n need to be a one-dimensional data set, in our case time, while the kernel themselves need to be stationary, i.e. $k_\alpha(t_n, t_m)$ is only a function of $\tau = |t_n - t_m|$. The simplest form a celerite kernel can take is[3]:

$$k_\alpha(\tau_{nm}) = \sigma_n^2 \delta_{nm} + a e^{-c\tau_{nm}},$$

where σ_n^2 are the measurement uncertainties and α is a function of a, c. The generalization of the above is:

$$k_\alpha(\tau_{nm}) = \sigma_n^2 \delta_{nm} + \sum_{j=1}^{J} \left[\frac{1}{2}(a_j + i b_j) e^{-(c_j + i d_j)\tau_{nm}} + \frac{1}{2}(a_j - i b_j) e^{-(c_j - i d_j)\tau_{nm}} \right],$$

with a Power Spectral Density (PSD) of

$$S(\omega) = \sum_{j=1}^{J} \sqrt{\frac{2}{\pi}} \frac{(a_j c_j + b_j d_j)(c_j^2 + d_j^2) + (a_j c_j - b_j d_j)\omega^2}{\omega^4 + 2(c_j^2 - d_j^2)\omega^2 + (c_j^2 + d_j^2)^2}.$$

This general mathematical formulation is given astrophysical meaning through the correct choice of coefficients. The choice made by the `celerite2` authors is presented in the next section.

3.1.2 Stochastically-Driven Damped Simple Harmonic Oscillator (SHO)

`Celerite2` provides the model of a stochastically-driven damped simple harmonic oscillator (SHO) as a fundamental framework for the analysis. Any time series analysis will use a combination or singular SHO described by the differential equation:

$$\left[\frac{d^2}{dt^2} + \frac{\omega_0^2}{Q} \frac{d}{dt} + \omega_0^2 \right] y(t) = \epsilon(t), \tag{3.2}$$

[3]Expression similar to a Damped Random Walk (DRW) model, but not all values of a and c are permitted. `Celerite2` discourages the use of these kernels and redirects the user to the SHOs of Section 3.1.2.

where ω_0 is the undamped oscillator frequency and Q is a dampening factor regulating the strength of the oscillation. If $\epsilon(t)$ is a white noise term the PSD simplifies to:

$$S(\omega) = \sqrt{\frac{2}{\pi}} \frac{S_0 \omega_0^4}{(\omega^2 - \omega_0^2)2 + \omega^2 \omega_0^2 / Q^2}, \tag{3.3}$$

with S_0 a proportionality constant at ω_0, $S(\omega_0) = \sqrt{2/\pi} S_0 Q^2$.

Although `celerite2` has been developed having in mind asteroseismic oscillations, the SHO framework can be applied to describe stochastic time series with hidden quasi-periodicities. Extensive work has been done to model blazars and more generally AGNs with SHOs through `celerite2` or other Gaussian fitting methods ([24],[25],[26],[27],[28]). This is achieved by the SHO's ability to describe the stochastic nature of a source and determine any hidden periodic variation based on its dampening factor, Q. For values of $Q > 1/2$ the system is described by a damped oscillation, while for $Q < 1/2$ it is described by a random walk. Both cases are described by Eq. (3.3), while $Q = 1/2$ is a limiting case that cannot be directly evaluated by celerite and corresponds to a critically damped oscillator. As such, it won't be further discussed. The kernel for the 2 regimes of interest are:

$$k_{SHO}(\tau;, S_0, Q, \omega_0) = S_0 \omega_0 Q e^{-\frac{\omega_0 \tau}{2Q}} \begin{cases} \cosh(\eta \omega_0 \tau) + \frac{1}{2\eta Q} \sinh(\eta \omega \tau) & 0 < Q < 1/2 \\ \cos(\eta \omega_0 \tau) + \frac{1}{2\eta Q} \sin(\eta \omega \tau) & 1/2 < Q \end{cases}, \tag{3.4}$$

where

$$\eta = \left| 1 - (4Q^2)^{-1} \right|^{1/2}.$$

To better illustrate the impact of each of the 3 parameters (S_0, Q, ω_0) on the power spectrum, a short investigation of the parameter space for both cases follows. As we are interested in qualitative changes, the base parameter values of each scenario have been chosen without any theoretical motivation for any specific problem but rather are those that best illustrate their impact. Moreover, in the qualitative examples, the parameter and Power unit values are unimportant and therefore disregarded.

In Fig 3.1 we present the case of $Q > 1/2$, i.e. an oscillation with base parameters of $Q = 10$, $S_0 = 1$, and $\omega_0 = 1$ rad/day. In the left panel, we can see how greater damping factor Q values lead to higher-quality oscillations. In the limit of $Q \gg 1$ an undamped oscillation can approximate the SHO. This can be mathematically understood through Eq. (3.4) taking the limit of $Q \to \infty$ and thus $\eta \to 1$. In the middle panel, the linear impact of the normalization factor S_0 is depicted as predicted by Eq. (3.3). Lastly, the right panel illustrates how a change in the undamped oscillator frequency shifts the PSD on the horizontal axis. Colored vertical guides are noted at frequencies of $\omega_0/2\pi$ which corresponds to the sharp peaks.

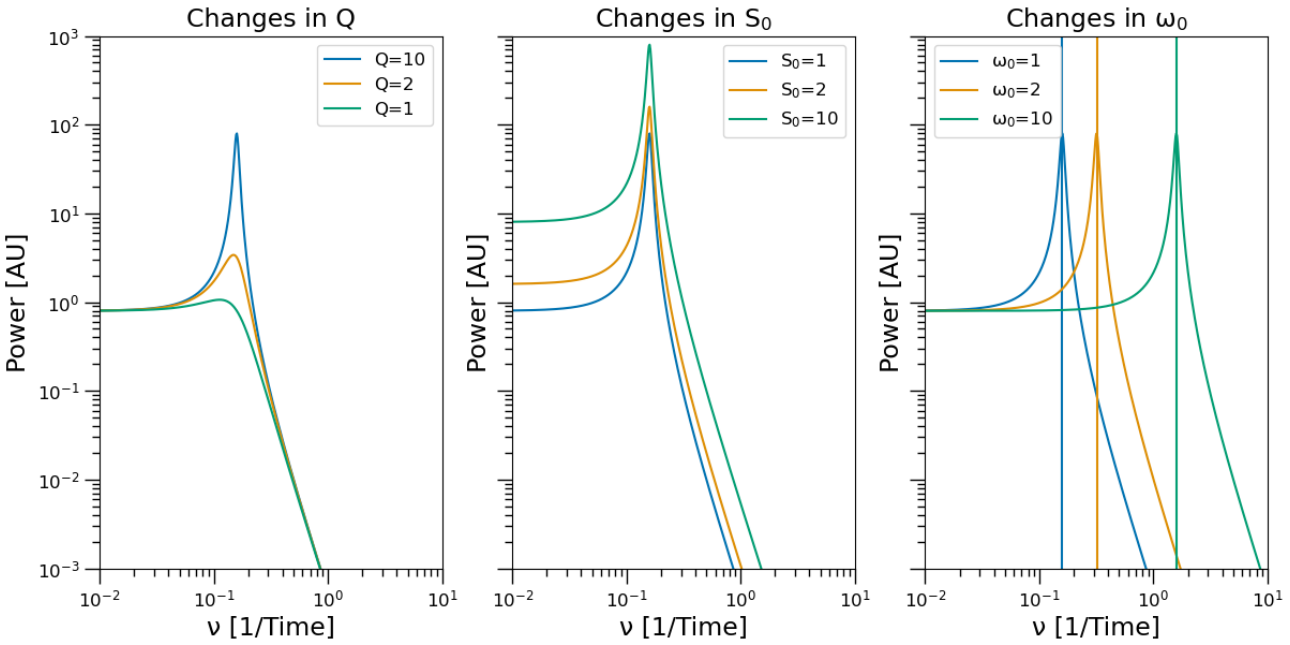

Figure 3.1: Impact of parameter changes in the oscillation scenario. Vertical lines at $\omega_0/2\pi$.

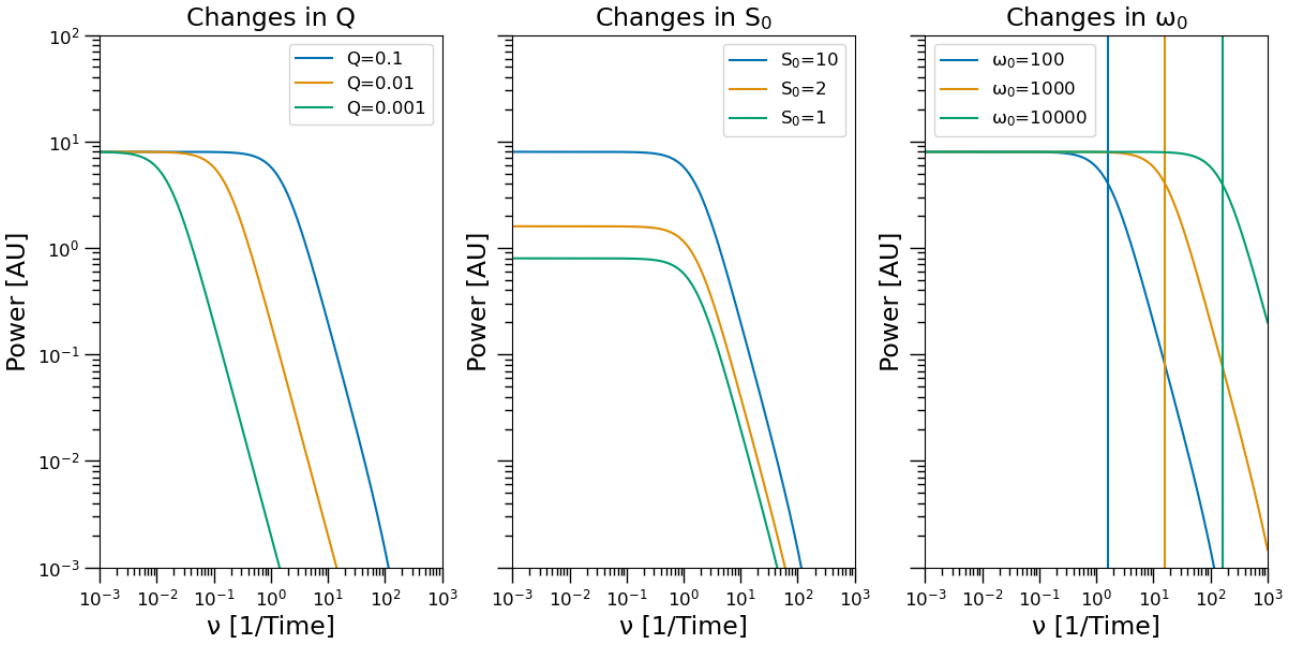

Figure 3.2: Impact of parameter changes in the random walk scenario. Vertical lines at ν_{br}.

In contrast to the above, Fig 3.2 explores the scenario of $Q < 1/2$, where randomness is the driving force behind the PSD. The immediate difference, the absence of a sharp rise, and the slope's meaning will be explained shortly after this parameter investigation. Here, the baseline parameters need to change due to the inherent difference in the physical interpretation of the PSD. Now we have $Q = 0.1$, $S_0 = 10$, $\omega_0 = 100$ rad/day. Again, the middle panel shows how S_0 plays the role of the normalization factor while the impact of Q, and ω_0, as seen in the left and right panels, is limited to shifting the break frequency on the horizontal axis. Because η has now become important, the break frequency, noted again by colored vertical guides for each case on the right panel, is not the same as the peak frequency of $\omega_0/2\pi$ as it was in the

oscillation case. Without proof, we note that in this scenario, the break frequency is given by $\nu_{br} = \frac{\omega_0/2\pi}{2Q}[1 - \sqrt{1-4Q^2}]$.

In other words, S_0, always plays the role of the normalization, Q either dampens an oscillation or shifts the break frequency of noise, and ω_0 is the undamped oscillator frequency which can be seen either directly in the PSD via a sharp peak, or shifted by a factor of $\frac{1}{2Q}[1-\sqrt{1-4Q^2}]$ and displayed by a break in the power spectrum.

The slopes of random processes are of particular interest as they carry physical meaning. In particular, in our above example for $Q < 1/2$, we can see a slope of $S(\nu) \sim \nu^0$ for low frequencies and a slope of about $S(\nu) \sim \nu^{-2}$ for higher ones. These are known as white and red noise respectively which we will discuss now alongside a third scenario, pink noise, as it is of astrophysical interest [29],[30]:

- "White" noise or $S(\nu) \sim \nu^0$. White noise is named after the fact that it carries equal parts power in each frequency similar to white light which has approximately equal power at all photon frequencies, has a constant value along the PSD. Examples of white noise are found in photon noise, quantization noise, and events that stem from discrete quantized instantaneous events. In our case, the presence of a white noise component in the PSD is anticipated, as we assume our stochastic driving force to be white noise.

- "Red" noise or $S(\nu) \sim 1/\nu^2$, also known as "Random walk" or "Brownian motion". We have red noise when the process in question undergoes a random walk. Random walks are a subset of Markov processes, which are agnostic to past behavior. In a Markov process, each step is dependent only on its current state multiplied by its probability. If all step transitions are equally likely, a random walk occurs. An example is the study of diffusion as the macroscopic result of the microscopic Brownian motion of particles. In our case, we see red noise in the higher frequency part of the spectrum. This combination of white and red noise has been previously observed in the study of the time variability of blazars with an empirical break frequency of around 150 days for OJ 287 [31], 25 days for 3C 66A [32], and 43 days for PKS2155-304 [32]. However, to the best of the authors' knowledge, no complete theoretical model has been proposed to explain those findings.

- "Pink" noise or $S(\nu) \sim 1/\nu$, also known as "flicker" noise. It carries equal amounts of power in every octave of frequency. Flicker noise can be found in many electronic devices as well as in physical systems (the flow rates of rivers, sunspot numbers). Although not represented in the examples of the SHO parameters above, flicker noise is found in the long-term low-level VHE PSD of TeV blazar PKS 2155-304 on timescales of ≥ 1 d [33],[34]. As such, we include it alongside the other 2 previously mentioned colors.

3.2 Time Series Analysis of Source Sample

In Fig. 3.3 a sample of BL Lacs and FSRQs sources is presented. As discussed in Section 1.2, we will analyze all TeV BL Lacs, as well as the TeV FSRQ 3C 279 to contrast our results

Name	Class	z	RA	Dec	Name	Class	z	RA	Dec
Mrk 421	BLL*	0.030	166.114	38.2090	3C 454.3	FSRQ	0.859	343.491	16.1480
Mrk 501	BLL*	0.034	253.468	39.7600	3C 273	FSRQ	0.158	187.278	2.05200
PKS 2155-304	BLL*	0.116	329.717	-30.2260	3C 279	FSRQ*	0.536	194.047	-5.78900
BL Lacartae	BLL*	0.069	330.680	42.2780	4C+01.02	FSRQ	2.097	17.1620	1.58300
PG 1553+113	BLL*	0.360	238.929	11.1900	PKS 0208-512	FSRQ	0.999	32.6930	-51.0170
3C 66A	BLL*	0.444	35.6650	43.0350	PKS 0454-234	FSRQ	1.003	74.2630	-23.4140
PKS 0235+164	BLL	0.940	39.6620	16.6160	PKS 0502+049	FSRQ	0.954	76.3470	4.99500
PKS 0426-380	BLL	1.110	67.1680	-37.9390	PKS 0727-11	FSRQ	1.591	112.580	-11.6870
PKS 0537-441	BLL	0.894	84.7100	-44.0860	S5 0836+71	FSRQ	2.172	130.352	70.8950
S5 0716+714	BLL	0.300	110.430	71.3500	Ton 599	FSRQ*	0.725	179.883	29.2460
S4 0954+65	BLL*	0.368	149.697	65.5650	PKS B1222+216	FSRQ	0.432	186.227	21.3800
PKS 1502+106	FSRQ	1.838	226.104	10.4940	PKS 1830-211	FSRQ	2.507	278.416	-21.0610

Notes. Classification according to the *Fermi*-LAT 4FGL Catalog [53] (BLL: BL Lac object; FSRQ: Flat Spectrum Radio Quasar). Redshifts are from NASA/IPAC Extragalactic Database. TeV-detected sources from TeVCat are marked with *.

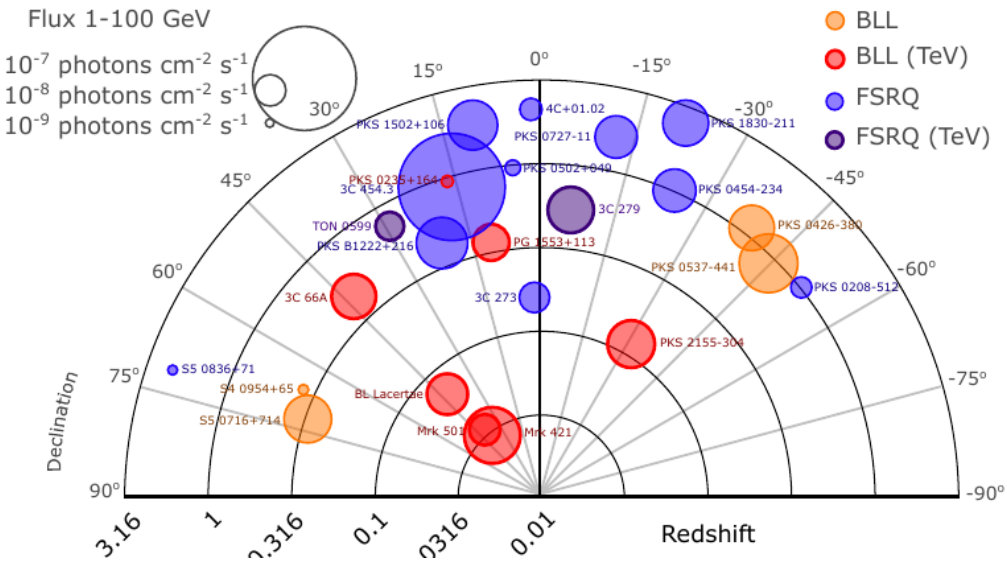

Figure 3.3: Redshift and γ-ray brightness distribution of blazars listed in the table.

between blazar classifications. This section will use the previously described celerite process and light curves in the Fermi energy band of 0.1-100 GeV taken from the Fermi LCR[4] [23] to model their statistical properties and study their PSDs.

We will use the 7-day-binning provided by the LCR, ignore upper limits, and use the log values of the energy flux. Our approach to the problem will utilize the simplest model with the lowest complexity: a single SHO. Generally, we will follow the method outlined in the `celerite2` documentation and the scientific literature [21],[24]. Namely, we run the L-BFGS-B optimization routine at random starting points to get initial parameter guesses for our model. Then, through a Markov Chain Monte Carlo (MCMC) fit via the module emcee [35], we derive our parameters for each data set. Utilizing 32 walkers, we deploy an initial 2000-step run that we consider a burn-in period and follow up with a 5000-step run to derive the final estimations. Our tests have concluded that this step and walker size is sufficient to converge on our final solutions. As we are considering the fixed model of a singular SHO we do not calculate the corrected Akaike information criterion (AICc).

To assess the accuracy of our resulting celerite parameters, we employ several statistical tests. We first calculate our fit's standardized residuals, which can be considered white noise. To do so, we connect the celerite process to moving averages by noting:

$$y^* = chol(K_\alpha)^T w.$$

Here, w are our standardized residuals, y^* are our zero-meaned data points, and $chol(K_\alpha)$ is the upper triangular Cholesky factorization of our best-fit covariance matrix K_α that has been introduced at the beginning of this chapter. Then we:

- Fit a normal distribution to the resulting histogram of the residuals via the χ^2 method. The desired result should yield a Gaussian with mean $\mu = 0$ and standard deviation $\sigma = 1$. The χ^2 value of a good fit is 1. Deviations towards higher values represent a poor fit while lower values indicate overfitting.

- Calculate the deviation of our results from a normal distribution via the Kolmogorov-Smirnov (KS) test. The null-hypothesis in this test is that the results do not originate from the same distribution. This is quantified by p-values, which describe the likelihood of an event. Values smaller than 0.05 imply that the null-hypothesis is true only 5% of the time. Therefore, p values greater than $p > 0.05$ confirm the hypothesis that our residuals stem from a normal distribution.

- Show how the residuals' Autocorrelation Function (ACF) lays mostly within the 95% confidence limits of white noise given by $\frac{1.96}{\sqrt{N}}$, where N = number of data points.

Furthermore, we compute the PSDs of the MCMC process alongside their respective slopes calculated for frequencies above the break frequency which we derived previously in this chapter. In Fig 3.4 through Fig 3.11 we present the above results for the TeV BL Lac of Fig 3.3 as well as

[4] https://fermi.gsfc.nasa.gov/ssc/data/access/lat/LightCurveRepository/

Table 3.1: Celerite parameters for select sample sources of Fig 3.3. μ is in units of log(Flux(0.1-100) GeV $cm^{-2}s^{-1}$) and ω_0 is in units of rad/day.

Source Name	μ [log(Flux)]	ln(S_0)	ln(Q)	ln(ω_0[rad days^{-1}])
Mrk 501	$-4.12^{+0.03}_{-0.03}$	$0.58^{+0.47}_{-0.39}$	$-3.20^{+0.83}_{-1.08}$	$-1.40^{+1.06}_{-0.83}$
Mrk 421	$-3.64^{+0.02}_{-0.02}$	$0.03^{+0.28}_{-0.24}$	$-3.16^{+0.70}_{-0.97}$	$-0.56^{+0.98}_{-0.69}$
PKS 2155-304	$-3.94^{+0.03}_{-0.03}$	$0.69^{+0.35}_{-0.30}$	$-3.21^{+0.74}_{-0.97}$	$-0.87^{+0.97}_{-0.72}$
S40954+65	$-4.49^{+0.04}_{-0.04}$	$1.29^{+0.27}_{-0.24}$	$-3.06^{+0.70}_{-0.96}$	$-0.34^{+0.94}_{-0.69}$
PG 1553+113	$-3.89^{+0.03}_{-0.03}$	$0.79^{+0.56}_{-0.44}$	$-3.09^{+0.91}_{-1.18}$	$-1.91^{+1.17}_{-0.91}$
BL Lacartae	$-3.82^{+0.05}_{-0.05}$	$2.01^{+0.31}_{-0.27}$	$-3.63^{+0.66}_{-0.89}$	$-0.39^{+0.88}_{-0.66}$
3C 66A	$-4.17^{+0.04}_{-0.04}$	$1.47^{+0.42}_{-0.36}$	$-3.67^{+0.72}_{-0.96}$	$-0.87^{+0.96}_{-0.71}$
3C 279	$-3.86^{+0.06}_{-0.06}$	$2.33^{+0.33}_{-0.28}$	$-3.47^{+0.69}_{-0.96}$	$-0.67^{+0.95}_{-0.67}$

Table 3.2: Statistical tests of goodness of fit and characteristic values of the PSD. The mean, standard deviation, and χ^2 value of the Gaussian fit on the standardized residuals, as well as the p-value of the KS test constitute the statistical test result. The slope of the PSD above the break frequency and the break frequency in days describe the blazar PSDs.

Source Name	μ (10^{-2})	σ	χ^2	KS p-value	PSD slope p	t_{br}[days]
Mrk501	2.95	0.98	0.96	0.2	$1.899^{+0.019}_{-0.029}$	$619.9^{+11.9}_{-9.4}$
Mrk421	1.32	1.06	1.13	0.28	$1.8429^{+0.0028}_{-0.0028}$	$258.4^{+5.1}_{-1.1}$
PKS 2155-304	1.55	1.05	1.1	0.22	$2.8672^{+0.0040}_{-0.0029}$	$371.55^{+8.1}_{-0.92}$
S40954+65	-2.29	0.99	0.99	0.15	$1.8208^{+0.0040}_{-0.0029}$	$188.1^{+4.0}_{-3.6}$
PG 1553+113	2.44	0.96	0.93	0.14	$1.932^{+0.021}_{-0.066}$	$935.4^{+8.7}_{-5.1}$
BL Lacartae	2.08	1.05	1.11	0.68	$1.8634^{+0.0083}_{-0.0096}$	$349.0^{+2.7}_{-4.2}$
3C 66A	1.38	0.98	0.96	0.15	$1.885448^{+0.000012}_{-0.00086}$	$584.0^{+5.3}_{-1.2}$
3C 279	0.0357	1.02	1.05	0.3	$1.867^{+0.011}_{-0.011}$	$391.0^{+8.3}_{-3.9}$

the TeV FSRQ 3C 279. In Table 3.1 we list the derived celerite parameters of each fit while in Table 3.2 we note the results of the statistical tests alongside the slopes of the PSDs. Although the remainder of this work will focus on the variability study of a specific source, the resulting SHO parameters can be utilized in future studies investigating the time domain of TeV blazars.

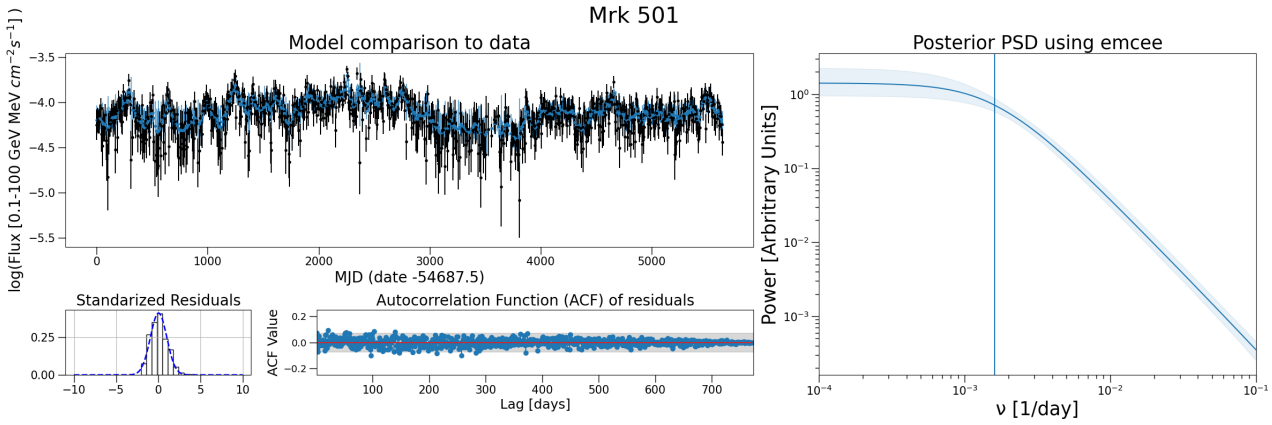

Figure 3.4: Summary of time series analysis for Mrk 501.

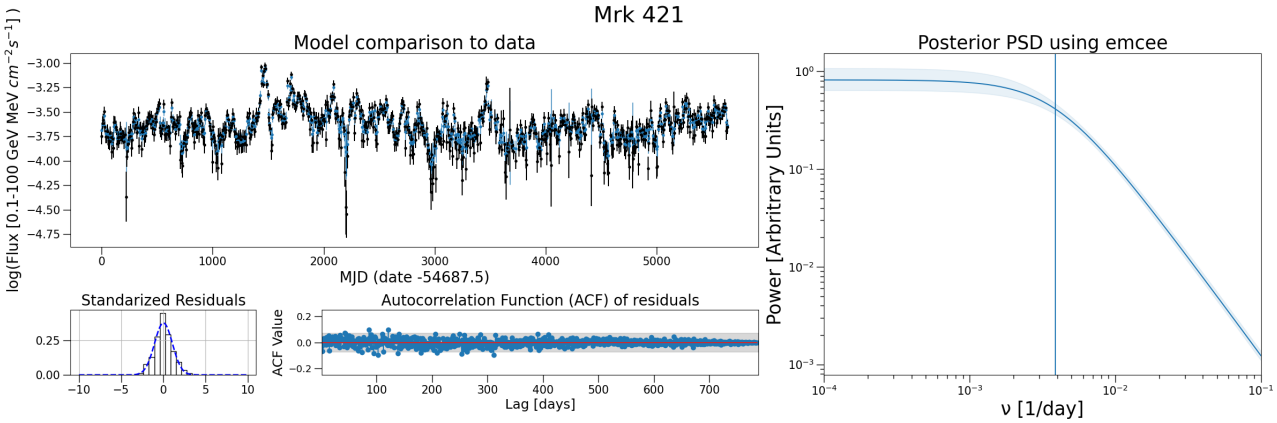

Figure 3.5: Summary of time series analysis for Mrk 421.

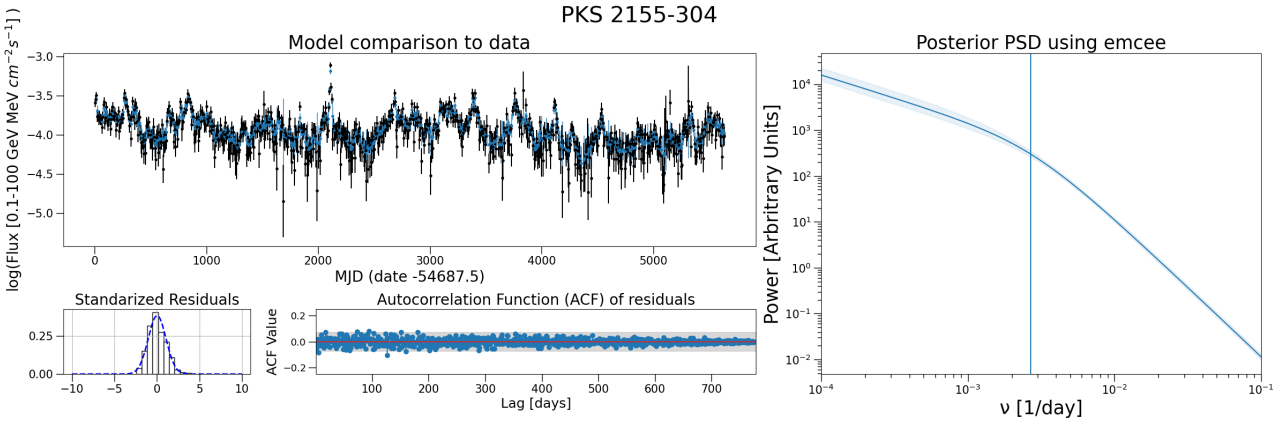

Figure 3.6: Summary of time series analysis for PKS 2155-304.

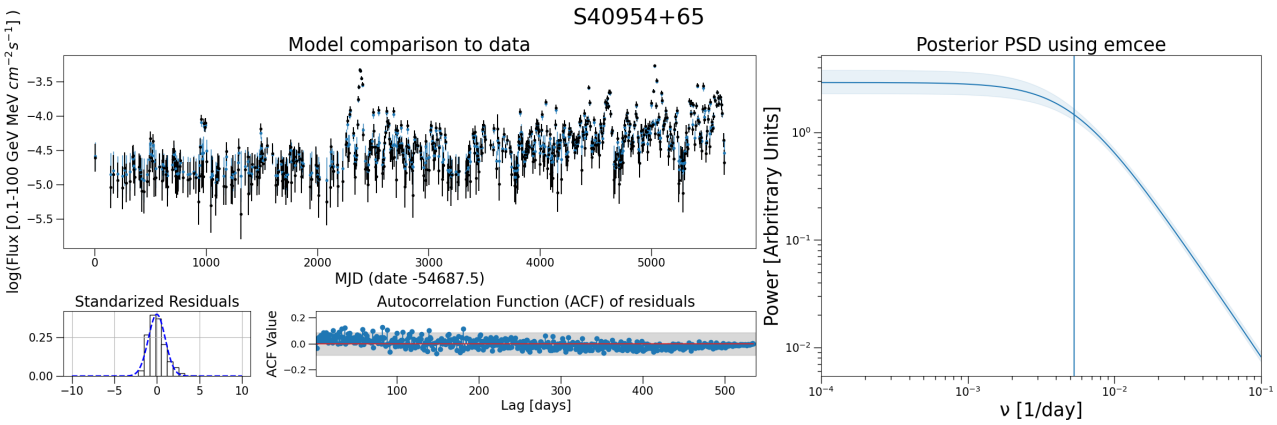

Figure 3.7: Summary of time series analysis for S40954+65.

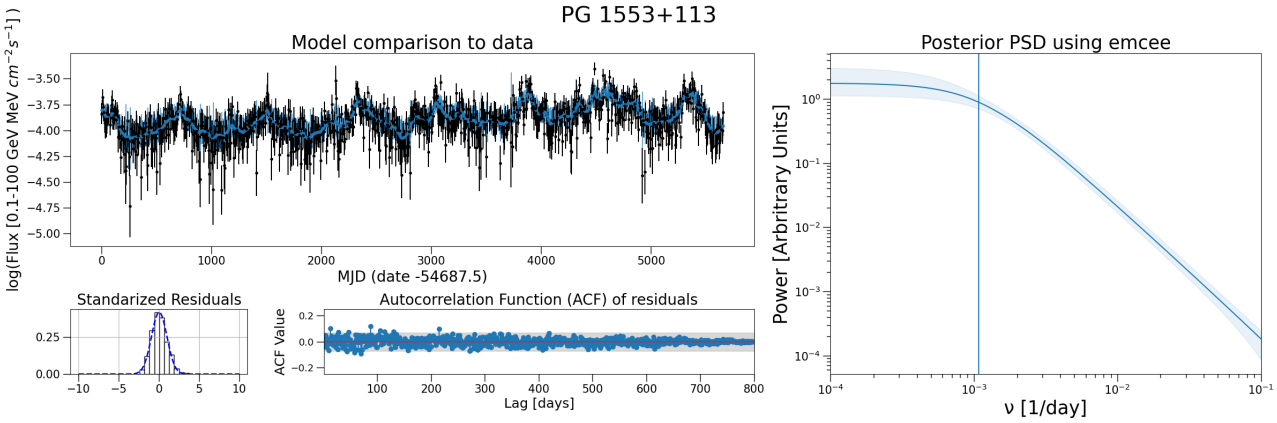

Figure 3.8: Summary of time series analysis for PG 1553+113.

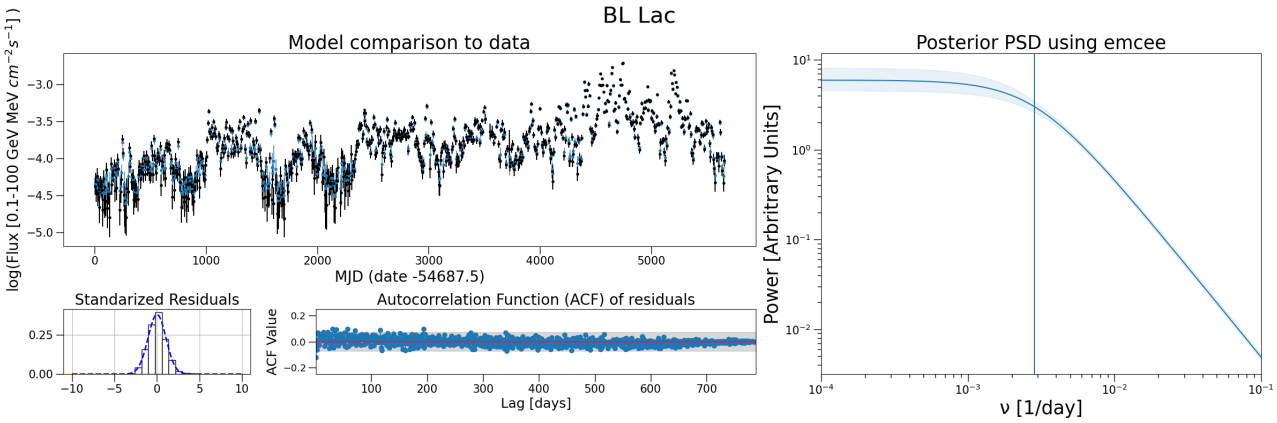

Figure 3.9: Summary of time series analysis for BL Lac.

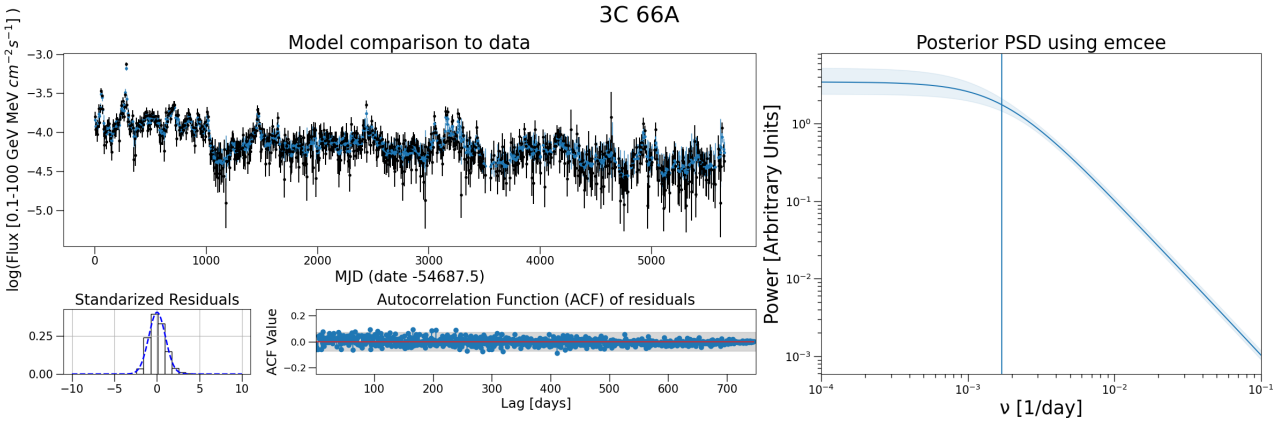

Figure 3.10: Summary of time series analysis for 3C 66A.

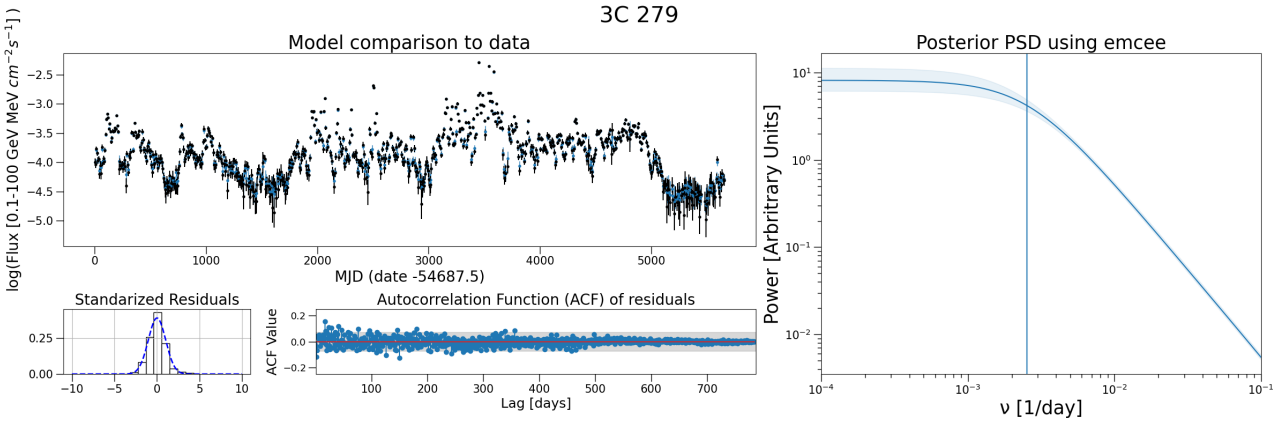

Figure 3.11: Summary of time series analysis for 3C 279.

3.3 Celerite Limitations

At this point, it is imperative to note 2 major limitations of our method that have to be considered while interpreting our results.

3.3.1 Extreme short-lived Flares

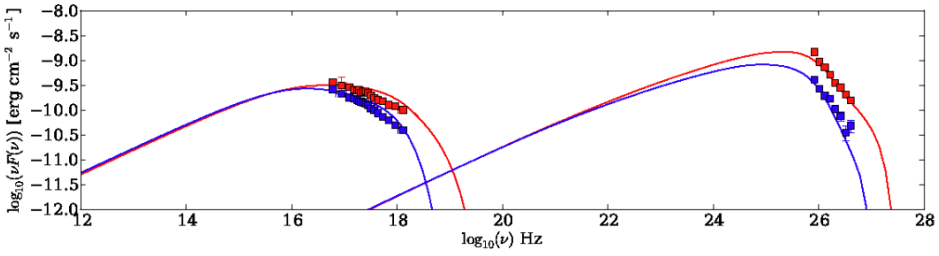

Figure 3.12: PKS2155-304 flare during the night of MJD 53946. The red and blue points are at the maximum and low-state flux levels for the CHANDRA and H.E.S.S. data. Solid lines represent modeled SEDs for each state [36].

The resulting fits as well as the simulated LCs derived from the fit parameters are unable to capture extreme flares on short timescales (i.e. comparable to the binning). To understand the importance of this we present the extreme flare of PKS 2155-304 in the VHE range during the night of MJD 53946 [36]. As seen in Fig. 3.12 the VHE flux increases for almost 1 order of magnitude within less than a day. Events like these cannot be captured nor predicted by our process. We emphasize that although we use the Fermi LAT and not the VHE or CHANDRA range for our analysis, the derived SHO parameters are unable to simulate extreme short-lived flares across the multiwavelength spectrum.

3.3.2 Hidden Periodicity

PG 1553+113 is a source with a detected periodicity of 2.18 years with an above 99% confidence level [37], or around 800 days with a local 95% confidence level [24]. Signs of periodicity can be inferred also by visual inspection of the Fermi LC of the source. However, in our analysis, we do not find any signs of periodic variability. To understand why this periodic behavior is not recovered by our analysis, we examine the impact of white noise on a signal. As such, we conduct the following experiment. We take the linear values of the observed LC and scale them by a factor of 10^5 so that our data range is approximately from 0 to 40. We construct a signal S, for the same time values as our data of PG 1553+113, given by

$$S = S_0\omega_0 Q \exp\left(-\frac{\omega_0 t}{2Q}\right) cos(\omega_0 t) + 12.$$

This is the expression of a high-quality oscillation given by Eq. (3.4) for $\eta = 1$ and $Q \gg 1$ with an added constant to scale our simulated signal to the observations. We add to the above signal white noise N, i.e. a random vector (with a random number seed of 42) of values between -1 and 1, multiplied by a constant a. Thus, our final simulated data set is $y = S + aN$, using the mean error of the PG 1553+113 flux for the error values. First, we investigate baseline parameters for $a = 0$ such that the amplitude and period approximate the flux deviations and period of the observations. Thus, the parameters used are $S_0 = 2$, $Q = 200$, and $\omega_0 = 2\pi/800$ rad/day. We slowly increase a until the celerite process does not produce a clear peak in the PSD. This we achieve starting at $a = 8.25$ as seen in the PSD shown in Fig 3.14. To illustrate the impact of a on the simulated LC we provide 3 examples for $a = 0, 4, 8.25$ in Fig. 3.13.

The PSD for $a = 8.25$, although not describing any physical process on its own, is the superposition between a stochastic and a periodic process. In other words, the walkers of the MCMC process are split between the two regimes. Similar to previous PSDs we show with a vertical line the characteristic frequency ω_0. Calculating the power of each component as $P = \frac{1}{N}\sum_i^N S_i^2$ and deriving the Signal-to-Noise Ratio (SNR) for $a = 8.25$ we get a value of $SNR = 6.37$, comparable to the $SNR = 5.96$, calculated as $SNR = \frac{\mu^2}{\sigma^2}$, of our blazar data.

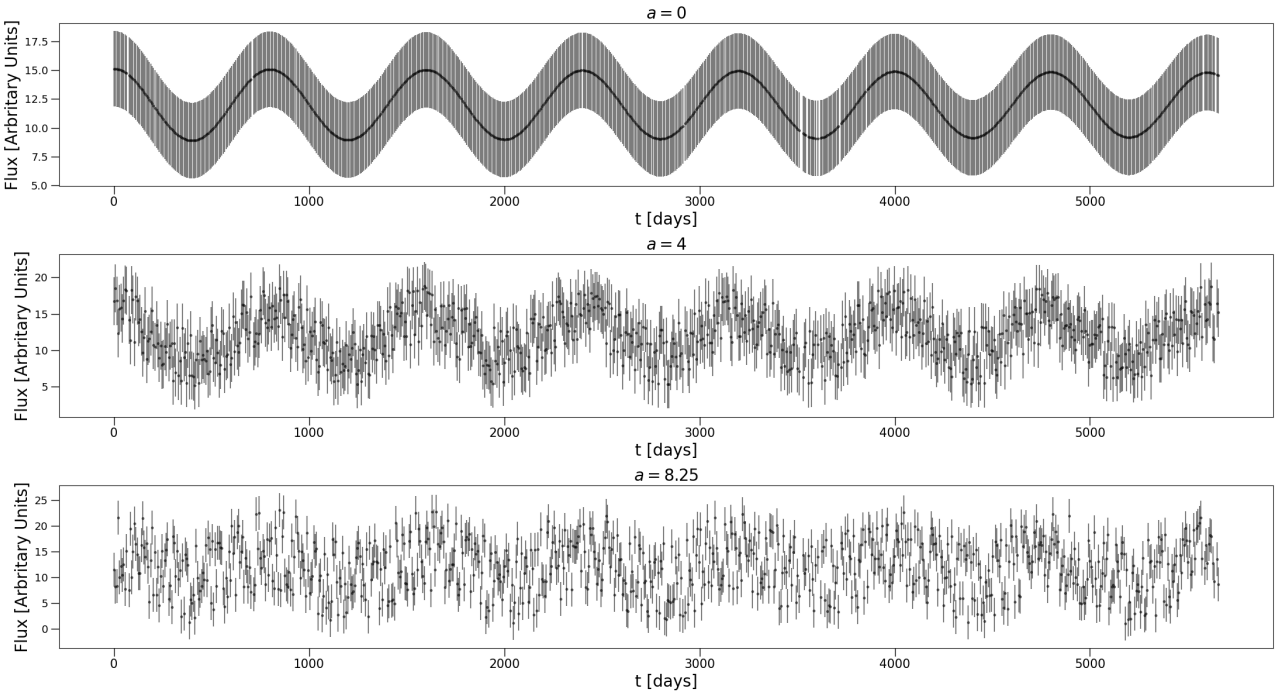

Figure 3.13: Impact of a on the linear scaling LC discussed in the text. Examples for $a = 0$ (upper panel), $a = 4$ (middle panel), and $a = 8.25$ (lower panel) are shown. The errors of the simulated flux points are the mean error of the observational flux of PG 1553+113.

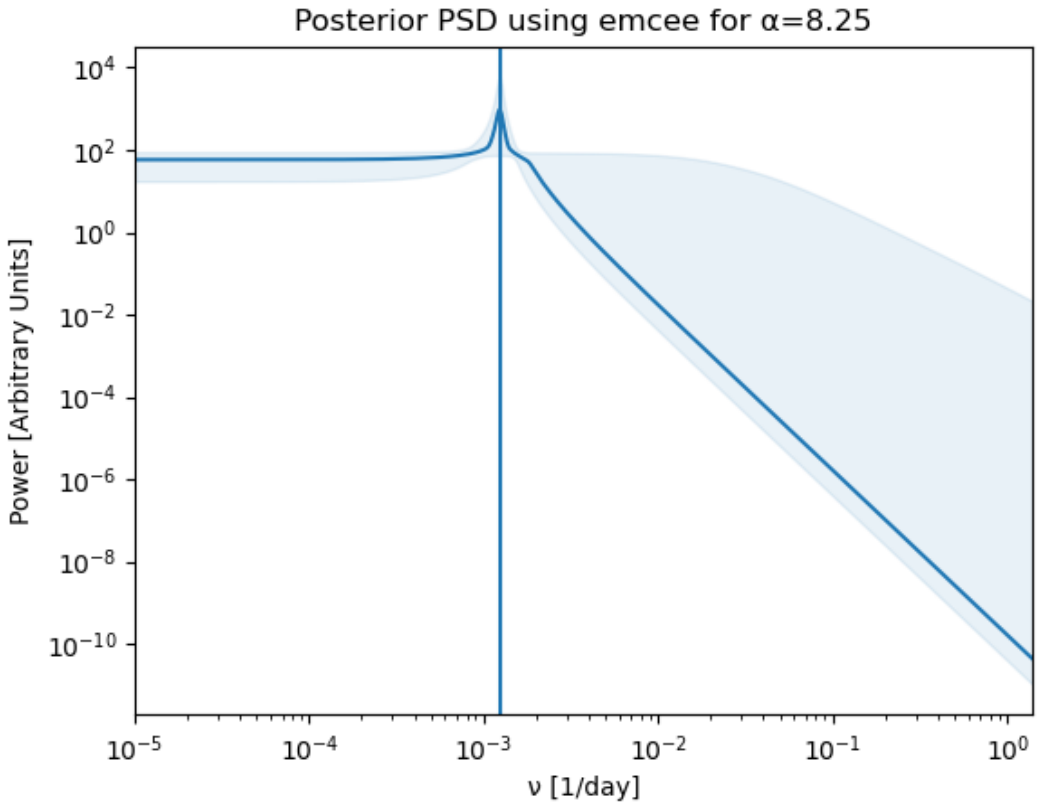

Figure 3.14: PSD for $y = S + 8.25N$ with linear scaling.

We repeat the above experiment taking the log values of our data with a scaling constant of -4:

$$S = S_0\omega_0 Q\exp\left(-\frac{\omega_0 t}{2Q}\right) cos(\omega_0 t) - 4.$$

This time, to approximate our data when $a = 0$ we need to take $S_0 = 0.2$, $Q = 200$, and $\omega_0 = 2\pi/800$ rad/day. As expected from our earlier parameter explanation a different scaling only changes the value of S_0. Now, the first deviation from a periodic process occurs at $a = 0.148$ as seen in the PSD in Fig. 3.15. Calculating again the SNR however does not result in comparable values. We have a value of $SNR = 2100$ for our simulated data while the observational data has a value of $SNR = 880$. Therefore, no direct correlation between the two SNR values can be established. To address this issue, one could investigate the feasibility of more complex celerite models. Combinations of SHOs could lead to descriptions of the dominant stochastic behavior without losing the underlying periodicity. Furthermore, for solely deriving periodic signals, specialized tools, such as the Lomb-Scargle periodogram [37] can be used. However, such an analysis exceeds the scope of our analysis and won't be further discussed. For a detailed discussion on alternative methods of "uncovering" periodicities, the interested reader is redirected to [37].

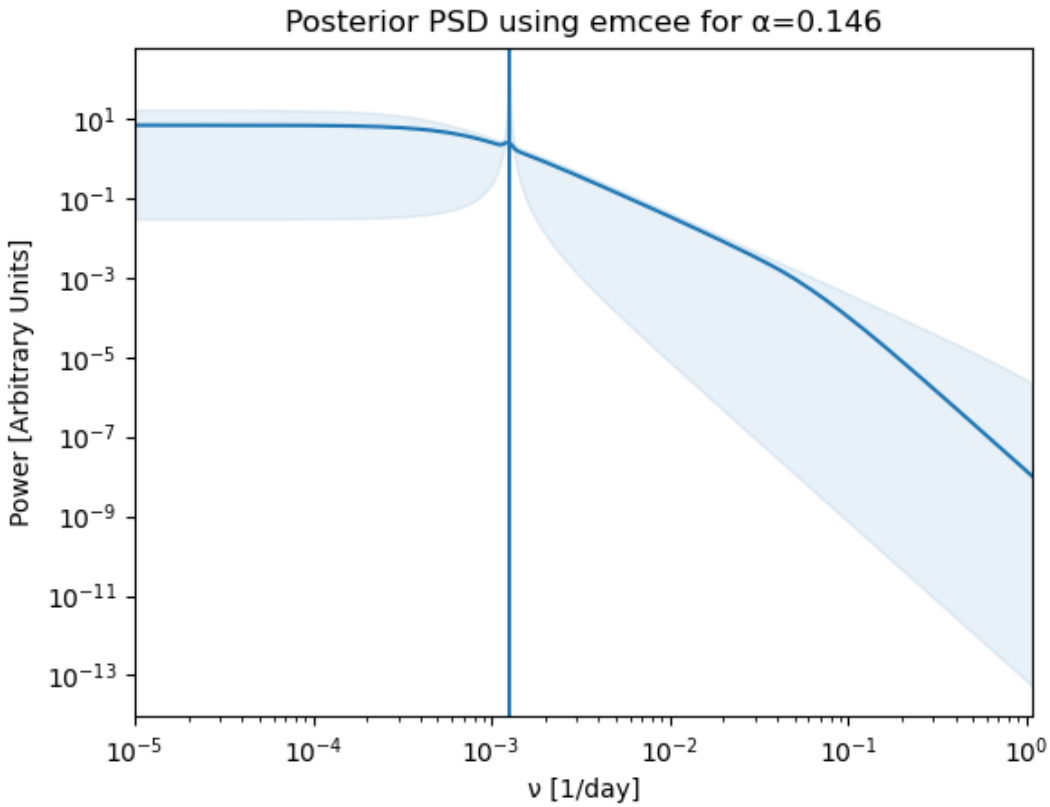

Figure 3.15: PSD for $y = S + 8.25N$ with logarithmic scaling.

Chapter 4

Computation of Time-Average SED

This chapter is dedicated to deriving the average-state parameters of Mrk 501 that will serve as a baseline for the variations discussed in Chapter 5. Mrk 501 is a high-synchrotron peaked (HSP) blazar at a luminosity distance of $d_L = 149.4$ Mpc that corresponds to a redshift of $z = 0.034$ [38],[39],[40]. Due to its proximity and time variability, it has been the focus of numerous observational campaigns. Its well-defined flaring events in the VHE energy range allow for precise distinctions in modeling its low- and high-activity. Furthermore, Mrk 501 features different flux variability across the multi-wavelength spectrum and exhibits spectral shape changes between quiescent and high-activity phases.

In Section 4.1 we present and prepare our data set. In Section 4.2.1 we will first discuss the used numerical code. In Section 4.2.2 a description of the derivation of the average leptonic source parameters follows. Lastly, we establish the parameters of the proton population.

4.1 Building the average observational SED

For our analysis, we use all the archival data available to us, accessed from the SED Builder website[1] presented in Fig. 4.1.

4.1.1 General

Our first step in constructing an SED that is representative of the time average state of the source consists in removing the outliers and the flaring states. The former consists of removing the cyan points at $log(\nu[\text{Hz}]) = 10$ and the points below $log(\nu F_\nu[\text{erg/s/cm}^2])= -13$ and above $log(\nu F_\nu[\text{erg/s/cm}^2])= -9$ in the $14 < log(\nu F_\nu[\text{erg/s/cm}^2])< 16$ range. To do the latter, in the VHE range we remove the flare that occurred during October 2011 and the flares of 1997, while in the X-ray range, we remove the extreme flare of 1997-04-16 [41],[42],[43],[44],[45]. Dividing the SED into regions of interest as well we have Fig. 4.2, where the black vertical lines separate the low-energy region (radio+IR), from the optical, X-ray, and (Very-)High-Energy [(V)HE]

[1] https://tools.ssdc.asi.it/SED/

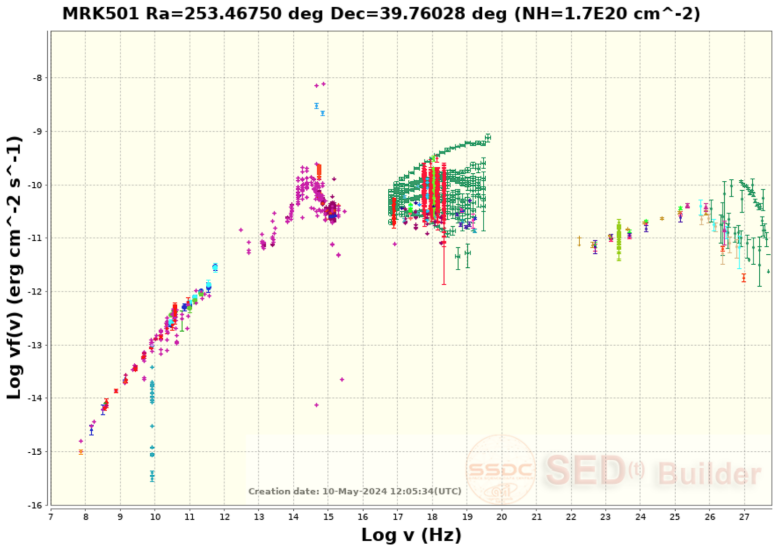

Figure 4.1: Archival data of blazar Mrk 501 accessed from SED Builder.

region.

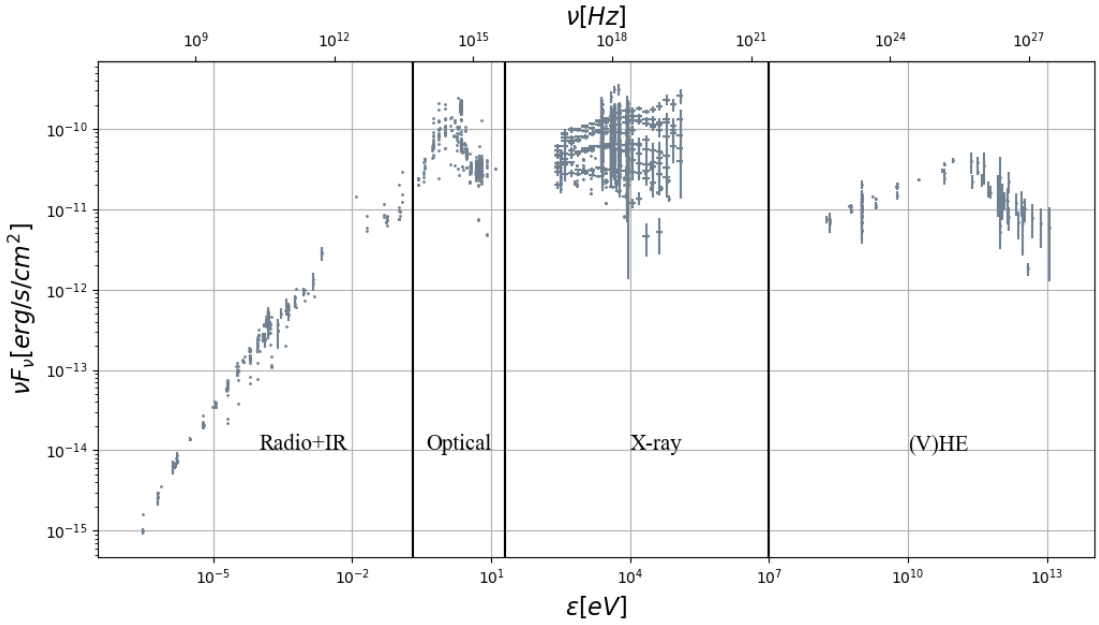

Figure 4.2: Segmented archival data without flares and outliers.

4.1.2 Radio/IR/Optical data

Our second step is to remove the optical bulge of the host galaxy. One way of removing the bulge is to use SED templates of elliptical galaxies that are fitted to the data and then removed. We opted for a model-independent way of removing the bulge. We isolated the the low-energy + optical region and fit a 3rd-degree polynomial to the data outside of the bounds of the bulge assuming a a continuous emission (e.g. arising from synchrotron emission along the jet):

$$poly(\varepsilon) = a\varepsilon^3 + b\varepsilon^2 + c\varepsilon + d \tag{4.1}$$

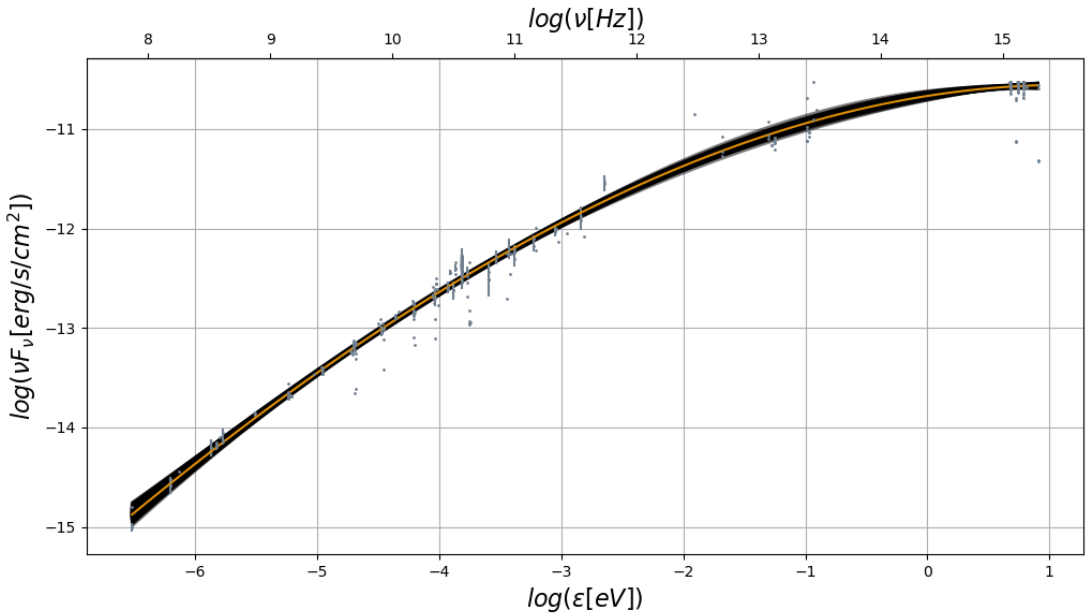

Figure 4.3: Low-energy data fit for the data region defined in the text.

Table 4.1: MCMC parameters for equation 4.1 alongside an uniform error added to the data, $\sigma^2 = \sigma_{data}^2 + f^2$

α[erg/s/cm^2/erg^3]	b[erg/s/cm^2/erg^2]	c[erg/s/cm^2/erg]	d [erg/s/cm^2]	$log(f)$
$-0.002^{+0.001}_{-0.001}$	$-0.084^{+0.008}_{-0.008}$	$0.195^{+0.014}_{-0.014}$	$-10.668^{+0.015}_{-0.015}$	$-4.558^{+0.034}_{-0.033}$

We exclude all data within $2 \cdot 10^{-1}$ eV$< \varepsilon <$ 4eV and any data with a flux above $\nu F_\nu = 3{\cdot}10^{-11}$ erg/s/cm^2. These bounds were manually chosen to approximate the region of the optical bulge. We have found this precision to be sufficient for our study. Utilizing the Levenberg-Marquardt algorithm for a non-linear least squares fit we derive the initial guesses for the Markov Chain Monte Carlo (MCMC) sampler `emcee` [35]. The sampler is running on 500 parallel walkers, a step size of 2000 with a burn-in phase of 300, and a Gaussian likelihood function. The parameters are summarized in Table 4.1 whereas the SED results are presented in Fig 4.3 alongside the initial parameter guess showcasing how the least-squares estimation is a robust approximation. For the final data selection outside the range used in the fit, we calculate the mean value of the squared residuals and compare it to the individual residual value. We only include the data point if its flux is smaller than the mean. The resulting low-energy+optical region is shown in Fig. 4.4.

4.1.3 X-ray data and above

We supplement our archival data from SED Builder with long-term observations from the X-ray Telescope (XRT, $0.2 - 10$ keV) and Burst Alert Telescope (BAT, $14 - 195$ keV) on board the Neil Gehrels Swift Observatory. In particular, we use the Swift-BAT 157-Month Hard X-ray

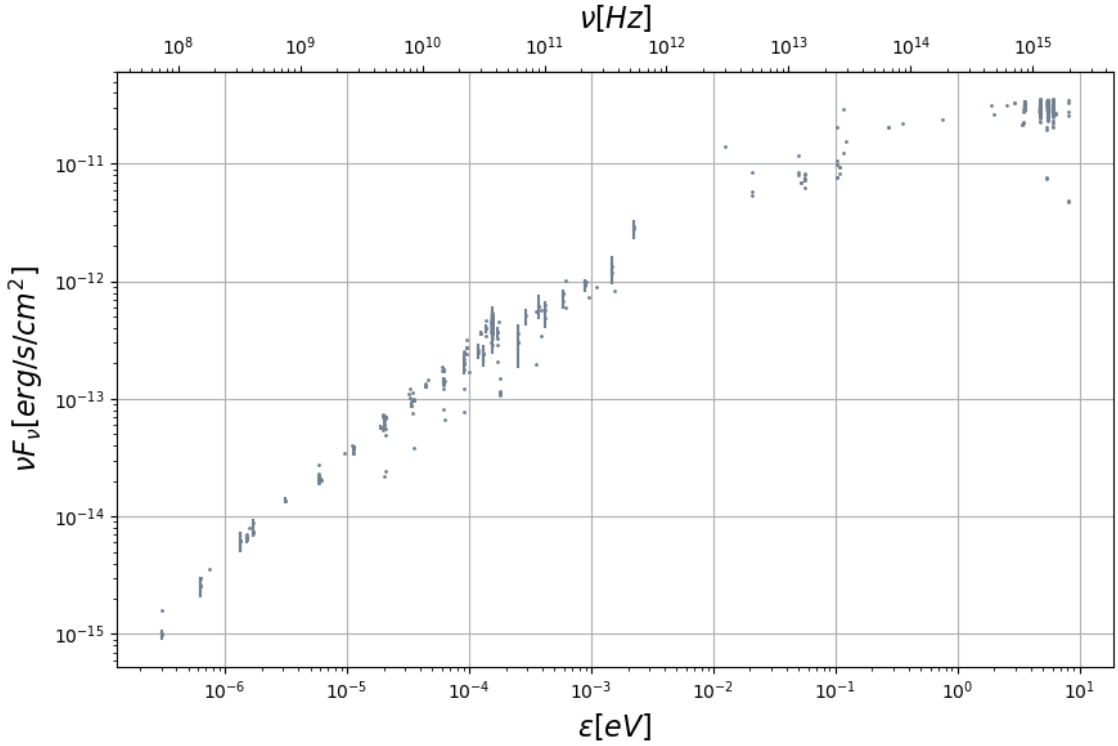

Figure 4.4: Final low-energy region data set.

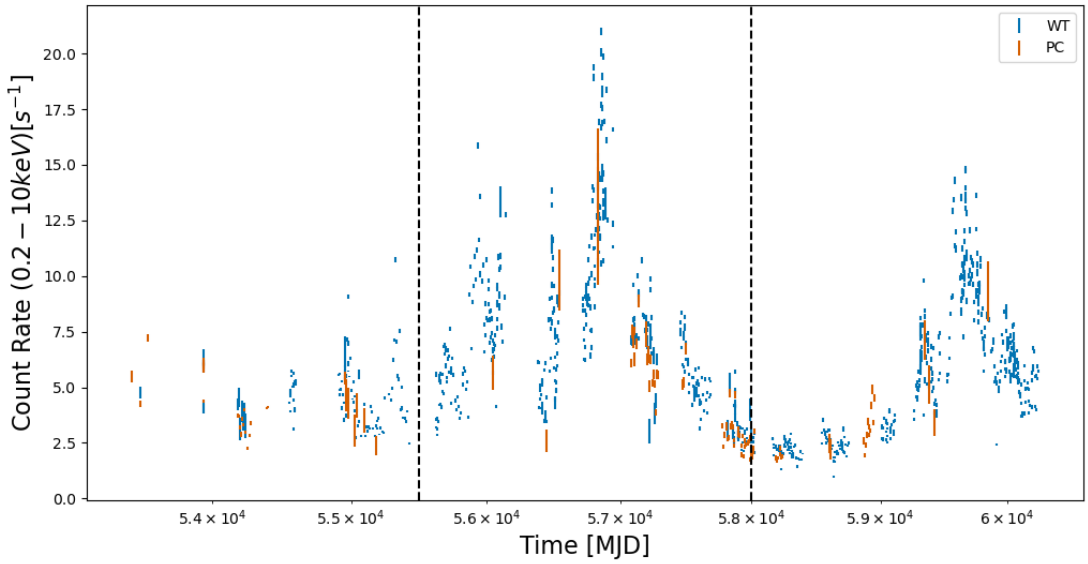

Figure 4.5: XRT light curve (0.3-10 keV). Blue and orange markers indicate Window Timing (WT) and Photon Count (PC) data. Dashed lines indicate the 3 epochs defined in the text.

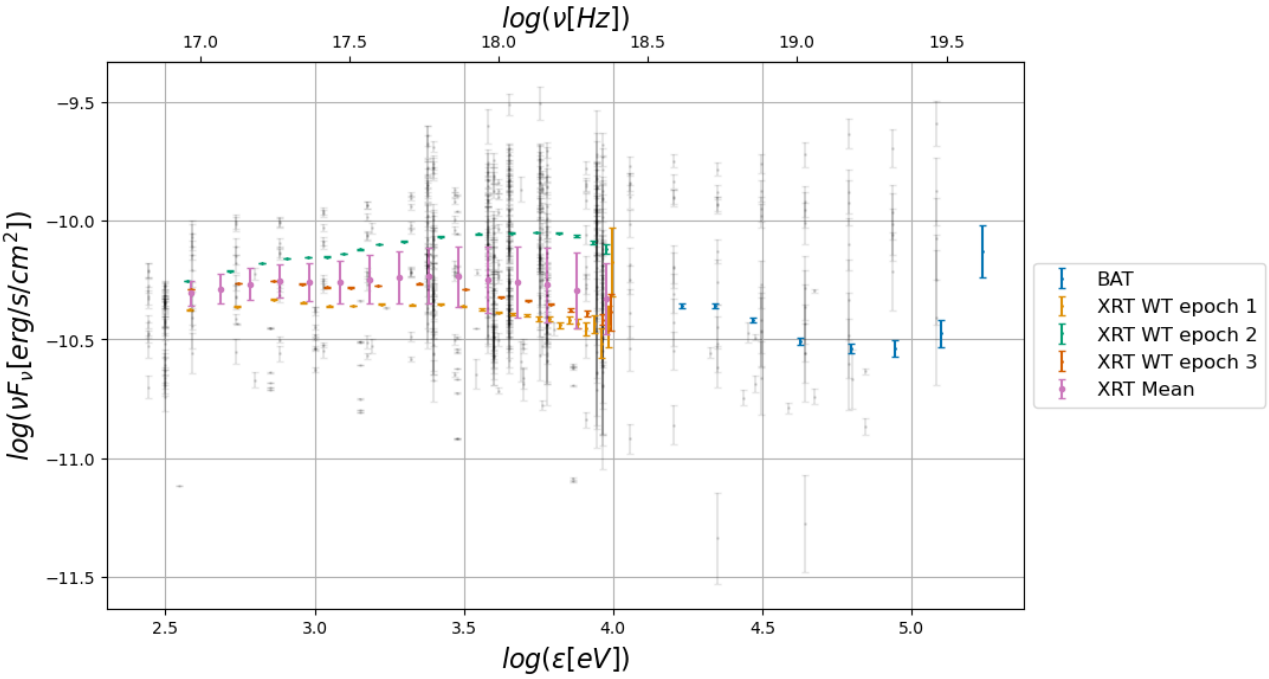

Figure 4.6: XRT and BAT energy flux spectra (colored markers) alongside archival X-ray data (grey markers). The 3 epochs of XRT between $T < 55500$ MJD, 55500 MJD$< T <$ 58000 MJD, and $T > 58000$ MJD are shown.

Survey Catalogue[2] and XRT data from The Neil Gehrels Swift Observatory[3]. Due to the large volume of the XRT data we are unable to request the entire dataset simultaneously from the XRT database. We divided the Light Curve (Fig. 4.5) into 3 segments, $T < 55500$ MJD, 55500 MJD$< T <$ 58000 MJD, and $T > 58000$ MJD. The first region exhibits low activity while the latter 2 capture the rise and decay of a high-activity period. We also use only the Windowed Timing mode (WT) data and not the Photon Counting mode (PC) as the former has a 1.8 milli-second time resolution. In contrast, the latter is saturated, as seen in Fig. 4.5, as it only has a resolution of 2.5 seconds. For each region, we build the spectrum using the online tools in https://www.swift.ac.uk/user_objects/ and fit an unabsorbed power law to the data resulting in 15 energy flux data points for each epoch. The mean and standard deviation of the epochs will be included in our data set as the representative XRT observations. We also fit an unabsorbed power law to the BAT spectrum provided by the BAT database. The BAT and the XRT (the final representative flux as well as each epoch separately) data are shown alongside the archival data (in faded black) in Fig. 4.6.

[2] https://swift.gsfc.nasa.gov/results/bs157mon/
[3] https://www.swift.ac.uk/user_objects/

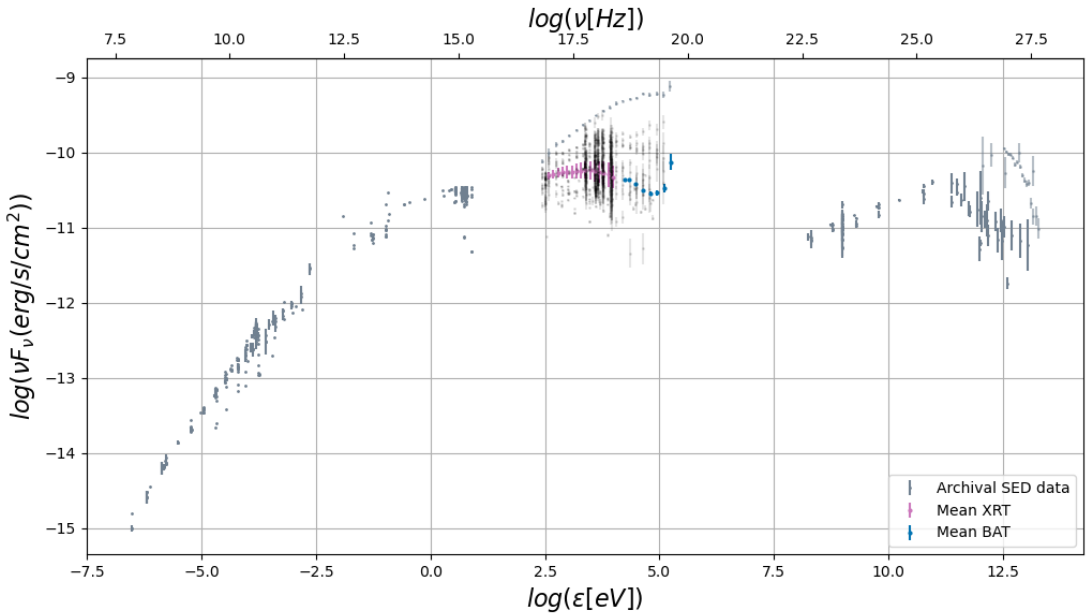

Figure 4.7: Mrk 501 dataset. With (faded) grey points the archival (flare) observations are shown. Faded black points represent the archival X-ray data not used in our modeling process. Highlighted are the BAT (Blue) and XRT (Magenta) observations.

The final data set is seen in Fig. 4.7 where the flares and the archival X-ray data are shown through faded colors (grey and black respectively) to signify that they have not been used in the following analysis. We highlight the BAT (Blue) and XRT (Magenta) observations to differentiate them from the archival data of the SED Builder website.

Lastly, in the (V)HE energy ranges we note that our used observations are time-averaged and not snapshots. In the HE range, we use data provided by the Fermi Large Area Telescope. The spectral data is either averaged over the entirety of the mission run at the time of the data release or represents monthly averaged observations. Similarly, the various observatories in the VHE range use long exposure times for their observations on an observation-to-observation basis and time-average the results in their analysis in producing spectral information. The exact time window for each spectral analysis varies between the provided data and the interested reader is directed to the observatories of HEGRA [43], ARGO [41], TACTIC [42], as well as MAGIC, and VERITAS [46].

4.2 SED Modelling

4.2.1 LeHaMoC Code Description

We model our emitting region as a spherical blob of size R within the jet of the AGN and assume a homogeneous magnetic field of strength B. For blazars, the motion of the blob will result in relativistic effects as the angle θ between the line of sight to the observer and the bulk plasma velocity is small. In particular, for a bulk plasma motion with Lorentz factor Γ

and bulk velocity $\beta = v/c$ we define the Doppler factor $\delta = \Gamma^{-1}(1 - \beta\cos\theta)^{-1}$. Throughout our discussion, all parameters are defined in the rest frame of the blob, unless explicitly stated otherwise. We assume the presence of an acceleration region from which particles escape upon their injection into the blob (radiation zone). The distribution of particles is described by a power law $N_j(\gamma_j) \sim \gamma_j^{-p}$ between energies $\gamma_{min,j}$ and $\gamma_{max,j}$, with a power law index p_j, where $j = e, p$ stands for electron-positrons and protons, respectively. The injected isotropically distributed luminosity of each population is also quantified via the compactness [47], a measure comparing the energy contents of a region to its spatial dimensions, $l = \frac{L\sigma_T}{4\pi R m_e c^2}$. We will use particle energy injection rate and compactness interchangeably throughout this chapter. The emitting particle populations produce photons γ as well as secondary particles, electron-positron pairs (e^-e^+) and neutrinos (ν). To quantify and accurately track the time evolution of a population j with time-dependent particle distribution N_j we use a set of integrodifferential equations, called kinetic equations parameterizing our problem as follows:

$$\frac{\partial N_j}{\partial t} + \frac{N_j}{\tau_{esc}} + \sum_i L_j^i(t) = \sum_i Q_j^i(t), \tag{4.2}$$

assuming a physical escape from the source with a timescale of $\tau_{esc} = R/c$. In the above, we consider the general form of a production and loss rate term of the process i and population j as Q_j^i and L_j^i respectively, and explicitly note their time dependence.

The complete equation set depends on the treated processes which in our case are:

- Injection (inj),
- Electron and positron synchrotron radiation (e, syn),
- Proton synchrotron radiation (p, syn),
- Electron and positron inverse Compton scattering (IC),
- Synchrotron self-absorption (ssa),
- Photon-photon pair creation ($\gamma\gamma$)
- Proton-photon pion production ($p\gamma, \pi$)
- Proton-photon (Bethe-Heitler) pair production (BH)

And thus reads:

- Electrons/Positrons,

$$\frac{\partial N_e}{\partial t} + \frac{N_e}{\tau_{e,esc}} + L_e^{syn} + L_e^{IC} = Q_e^{inj} + Q_e^{p\gamma,\pi} + Q_e^{BH} + Q_e^{\gamma\gamma}. \tag{4.3}$$

- Protons,

$$\frac{\partial N_p}{\partial t} + \frac{N_p}{\tau_{p,esc}} + L_p^{syn} + L_p^{BH} + L_p^{p\gamma,\pi} = Q_p^{inj}. \tag{4.4}$$

- Photons,

$$\frac{\partial N_\gamma}{\partial t} + \frac{N_\gamma}{\tau_{\gamma,esc}} + L_\gamma^{ssa} + L_\gamma^{\gamma\gamma} = Q_\gamma^{e,syn} + Q_\gamma^{p,syn} + Q_\gamma^{IC} + Q_\gamma^{p\gamma,\pi}. \tag{4.5}$$

- Neutrinos,

$$\frac{\partial N_\nu}{\partial t} + \frac{N_\nu}{\tau_{\nu,esc}} = Q_\nu^{p\gamma,\pi}. \tag{4.6}$$

In the above, we have ignored terms relating to pp collisions and adiabatic effects considering them insignificant for the problem we aim to solve. These 4 equations alongside the 7 parameter types, the source size R, the magnetic field B, the Doppler fact δ, the minimum/maximum Lorentz factor $\gamma_{min,max}$, the power law index p, and the injected luminosity/compactness, define the set of input parameters of the code `LeHaMoC` [48]. The interested reader is directed to [48] for a complete description of the operators.

`LeHaMoC` solves the equations Eq. (4.3) through Eq. (4.6) via an implicit difference scheme [49] discretizing the time into a grid with steps of light crossing times $t_{cr} = R/c$ and the energy through a logarithmic energy grid with user-defined endpoints. The selection of appropriate energy grid bounds and grid points is important to ensure the smoothness of the resulting SED and correctly include all secondary electrons produced via hadronic processes as these can extend beyond the primary injected electron distribution. The resulting discretized equations form tridiagonal matrices solvable through the Thomas algorithm[4].

An illustration of the above is presented through the electron kinetic equation for time steps of t_i and Lorentz factors of γ_j:

$$V_{1,j} N_{e,j-1}^{i+1} + V_{2,j} N_{e,j}^{i+1} + V_{3,j} N_{e,j+1}^{i+1} \;=\; N_{e,j}^{i} \tag{4.7}$$

with coefficients:

$$V_{1,j} = 0 \;\;;\;\; V_{2,j} = 1 + \frac{\Delta t}{\tau_{e,esc}} + \frac{\Delta t}{\Delta\gamma_j}\Sigma_p \left(\frac{d\gamma}{dt}\right)_{p,j}^{i,j} \;\;;\;\; V_{3,j} = -\frac{\Delta t}{\Delta\gamma_j}\Sigma_p \left(\frac{d\gamma}{dt}\right)_{p,j+1}^{i,j} \tag{4.8}$$

where $(d\gamma/dt)_p$ the electron energy losses of one electron due to the p process.

4.2.2 Average State Description

Fully describing our source in a leptohadronic hybrid synchrotron self-Compton (SSC) scenario requires therefore 11 parameters:

- 3 Global Parameters: R, B, δ
- 4 Electron Parameters,γ_e^{min}, γ_e^{max}, p_e, L_e^{inj}
- 4 Proton Parameters, γ_p^{min}, γ_p^{max}, p_p, L_p^{inj}

[4] http://www.industrial-maths.com/ms6021_thomas.pdf

We argue that the scientific literature supports an average state of a blazar to mostly be leptonic and not exhibit dominant hadronic signatures [50],[51],[52]. We thus first derive the parameters of a purely leptonic emission, namely synchrotron from IR to X-rays and SSC in gamma-rays (Section 4.2.2). The emission from relativistic protons, if present in the jet at all times, remains hidden below the leptonic spectral components. We will argue for the upper limit of the proton luminosity (Section 4.2.2) and later search for hadronic signatures on the SED during flaring activity (Chapter 5).

Leptonic Average State

To derive the leptonic average state we use the Markov Chain Monte Carlo (MCMC) sampler `emcee` [35] running on 32 parallel walkers. The step size and burn-in phase have been kept variable throughout our testing allowing for a flexible approach to computational time. The initial parameter guesses are important to capture the physical problem discussed. Therefore, we derive these initial parameter estimations by utilizing our observational SED and reverse engineering using our analytical expressions presented in Section 2.2.4:

- Assuming a power-law distribution of electrons with slope p at injection that produces the low-energy blazar emission via synchrotron, we can infer p as follows: From Chapter 2.2.2 we have the relation between spectral and power law index: $\alpha = (p-1)/2 \rightarrow p = 2\alpha + 1$. From the SED of Fig. 4.7 we estimate that between $\varepsilon_{min} = 1$eV and $\varepsilon_{max} = 10^{3.5}$eV we have $\nu F_\nu \sim \nu^{0.267} \rightarrow F_\nu \sim \nu^{-0.733} \sim \nu^{-\alpha}$ and therefore $p = 2.47$.

- The SSC component peaks at approximately 10^{13} eV. Assuming a fiducial value for the variability timescale of $t_{var} = 1$d we estimate from Eq. (2.29) the minimum value of the Doppler factor. Requiring the SSC region to be optically thin to $\gamma\gamma$ absorption we have $\delta = 4.63$.

- We estimate the radius from Eq. (2.2.5) as $R = 1.15 \cdot 10^{16}$ cm.

- To estimate the magnetic field and injected electron luminosity we minimize the energy in the system. Using $F_{pk} = 10^{10.2}$erg/s/cm^2, $\varepsilon_{min} = 1$ eV, and $\varepsilon_{max} = 10^{3.5}$eV we calculate from Eq.(2.18) and Eq.(2.19): $B = 0.49$G and $L_e^{inj} = 2.13 \cdot 10^{41}$ erg/s.

- Finally, $\gamma = \left(\frac{\varepsilon}{\delta b m_e c^2}\right)^{1/2}$ for $\varepsilon_{min} = 1$ eV and $\varepsilon_{max} = 10^{3.5}$eV. Or $\gamma_{min} = 10^{3.8}$ and $\gamma_{max} = 10^{5.54}$.

Inserting these values into `LeHaMoC`, our first SED estimation is depicted in Fig. 4.8. In the upper panel, we see the SED of our energy minimization model, which deviates significantly from the observations. We will offer some potential explanations for this discrepancy at the end of this section. To highlight this discrepancy, the middle panel compares observational to model data. Zero values indicate equality between the model and the observational data. Lastly, the bottom panel shows the spectral index throughout the model with indicative values noted throughout. To improve this initial guess we lower the magnetic field by one order of

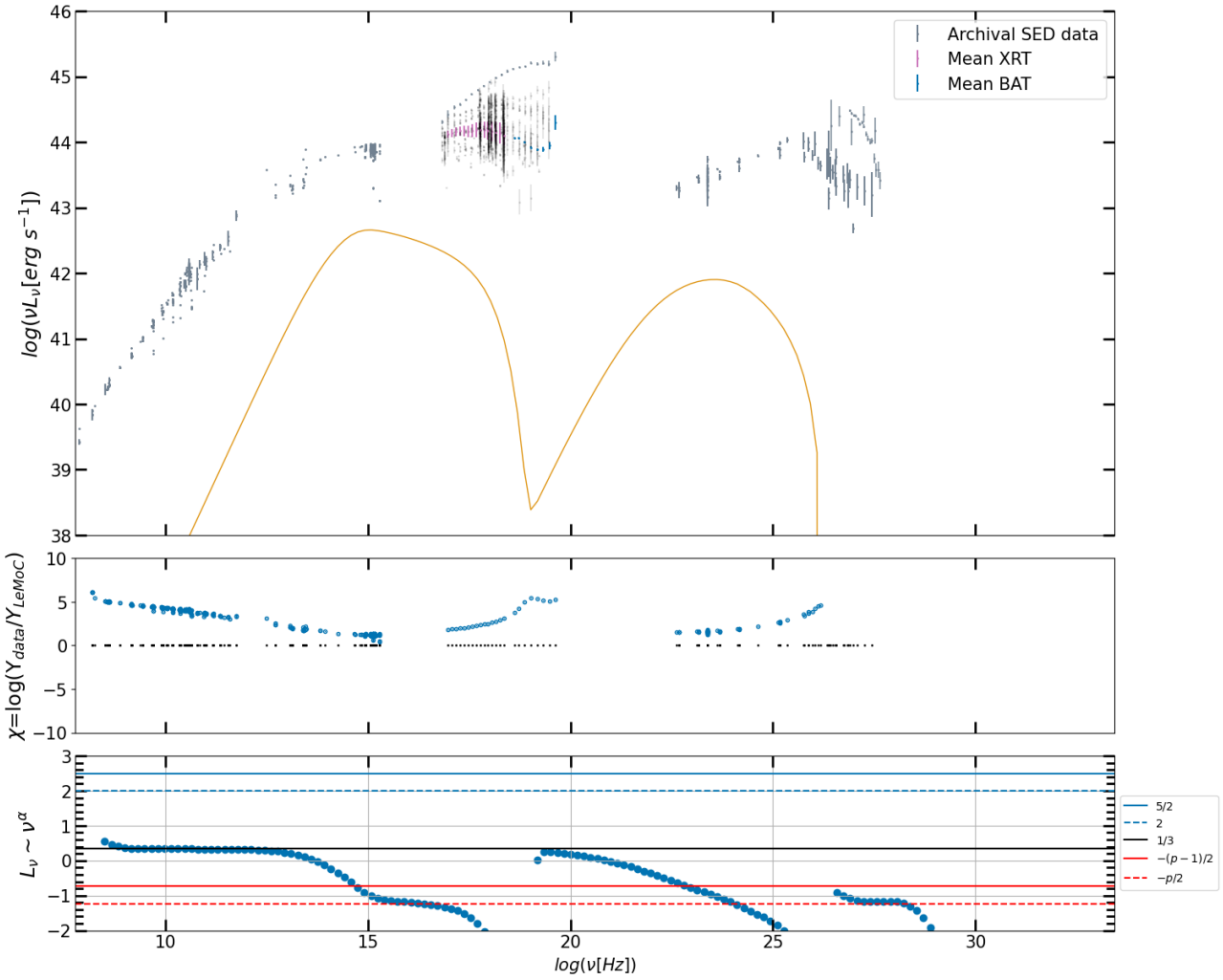

Figure 4.8: Parameter estimation using the energy minimization method outlined in Section 2.2.4. *Upper panel:* SED of the energy minimization model. *Middle panel:* Comparison between model and observations. *Lower panel:* The spectral index throughout the model. Indicative values are noted by vertical lines.

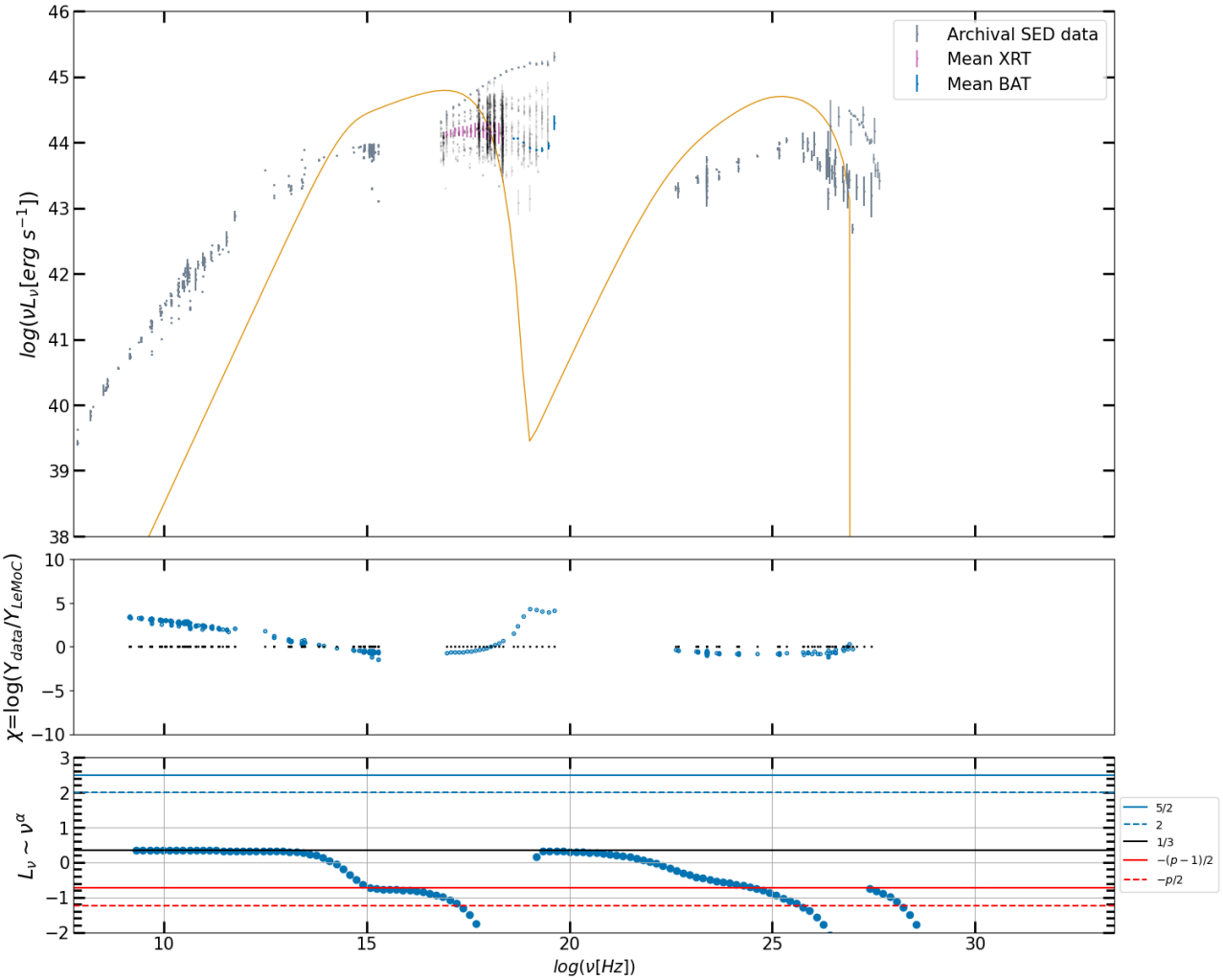

Figure 4.9: Same as Fig. 4.8 for a 10 times lower magnetic field and Doppler factor of $\delta = 30$.

magnitude to better agree with the available literature [41] and manually increase the Doppler factor to 30. The results, seen in Fig. 4.9 show a drastic improvement and will be the first step to the parameter derivation.

Throughout our testing, we have used a variety of permissible frequency ranges for the fit. We arrived at two important conclusions:

- We must exclude all the low-frequency data ($\nu < 300GHz$) in the fitting process as otherwise, our model does not return physical results. We assume this emission originates from a more extended region of the jet (and less opaque to ssa) and therefore disregard it. This treatment is consistent with previous studies where excluded observations have been used as upper limits [50].

- In testing a variety of permissible frequency ranges for the fit, we found in all cases the value of the Doppler factor δ to be approximately $\delta = 20$. Assuming a fiducial value of $t_{var} = 1d$ for the average time variability time scale we calculate an upper bound for the radius $R \lessapprox \frac{t_{var}c}{(1+z)\delta} = 10^{16.7}cm$. Therefore we set $R_{max} = 10^{16.5}cm$ to be within this bound.

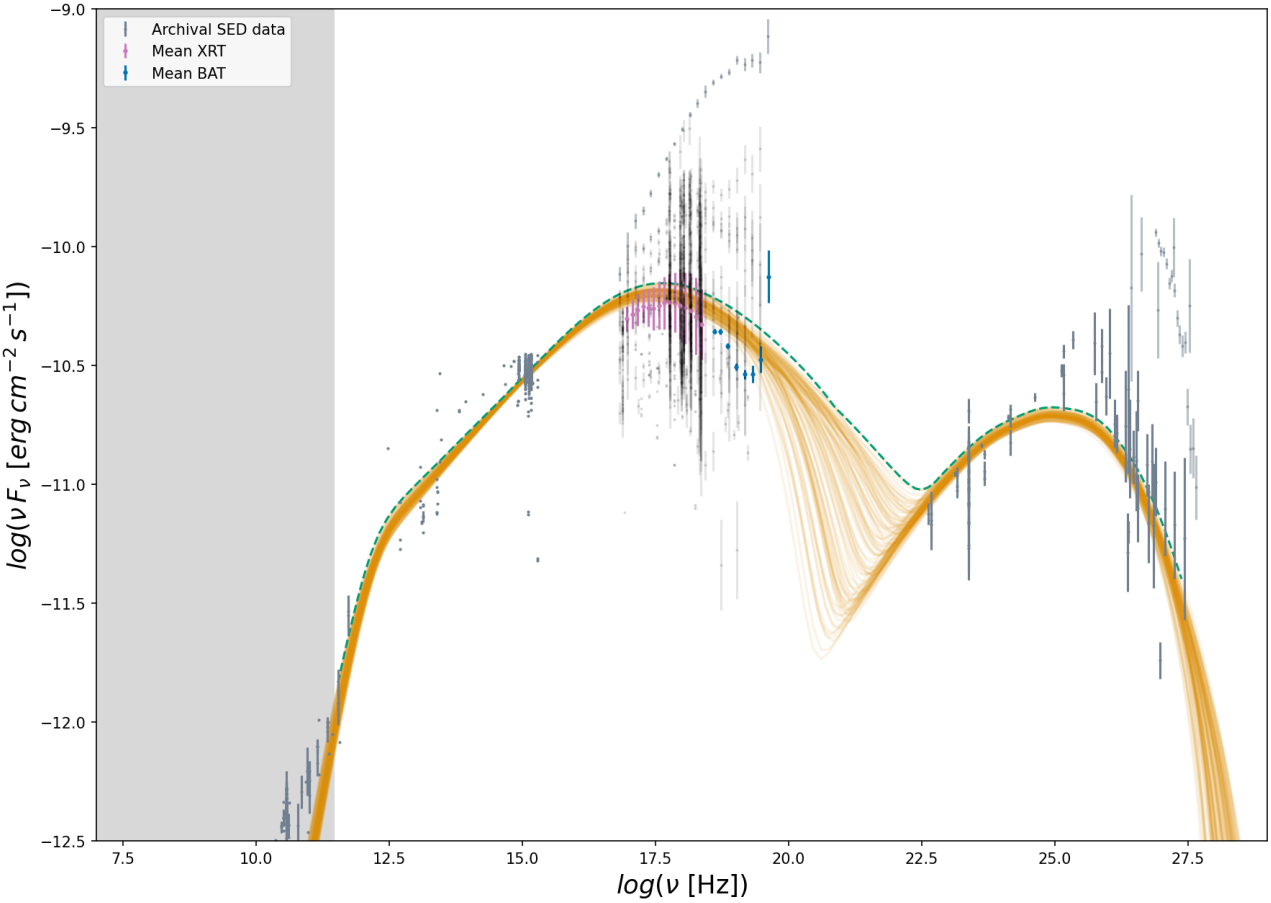

Figure 4.10: Sample from the posterior SED parameter space. The shaded band has been excluded from the fit as explained in the text. The green dashed line represents the 1% limit discussed in Chapter 4.2.2.

For our final result, we used a total step size of 10000 with a burn-in phase of 2000. In Fig. 4.10 the average-state SED, zoomed in to emphasize the synchrotron and SSC peaks, and a representative sample of model SEDs (Orange color) of the posterior are shown. A dashed line notes the upper limit we will use and discuss in the next section. The grey-shaded region on the left designates the previously discussed excluded low-frequency band. In Fig 4.11 we show the posterior distributions of the previously discussed parameters and an error value "$log(f)$" that we have added to the standard deviation of the Gaussian as [53],[54]:

$$\sigma^2 = \sigma_{data}^2 + f^2$$

All distributions are well-constrained except for the radius which we bound as described previously. We report that increasing the bound on the radius R and searching for parameter values that ensure all parameters are well-constrained results in a dynamic interplay between the radius and the magnetic field B where the former steadily increases while the latter steadily decreases until each one reaches its respective bound. To constrain both quantities simultaneously we need unnaturally high values for the radius and exceptionally small values for the magnetic field (see Appendix A). These values are unpreceded in the description of emission regions of blazar jets and should be disregarded as unphysical. Therefore, we conclude that

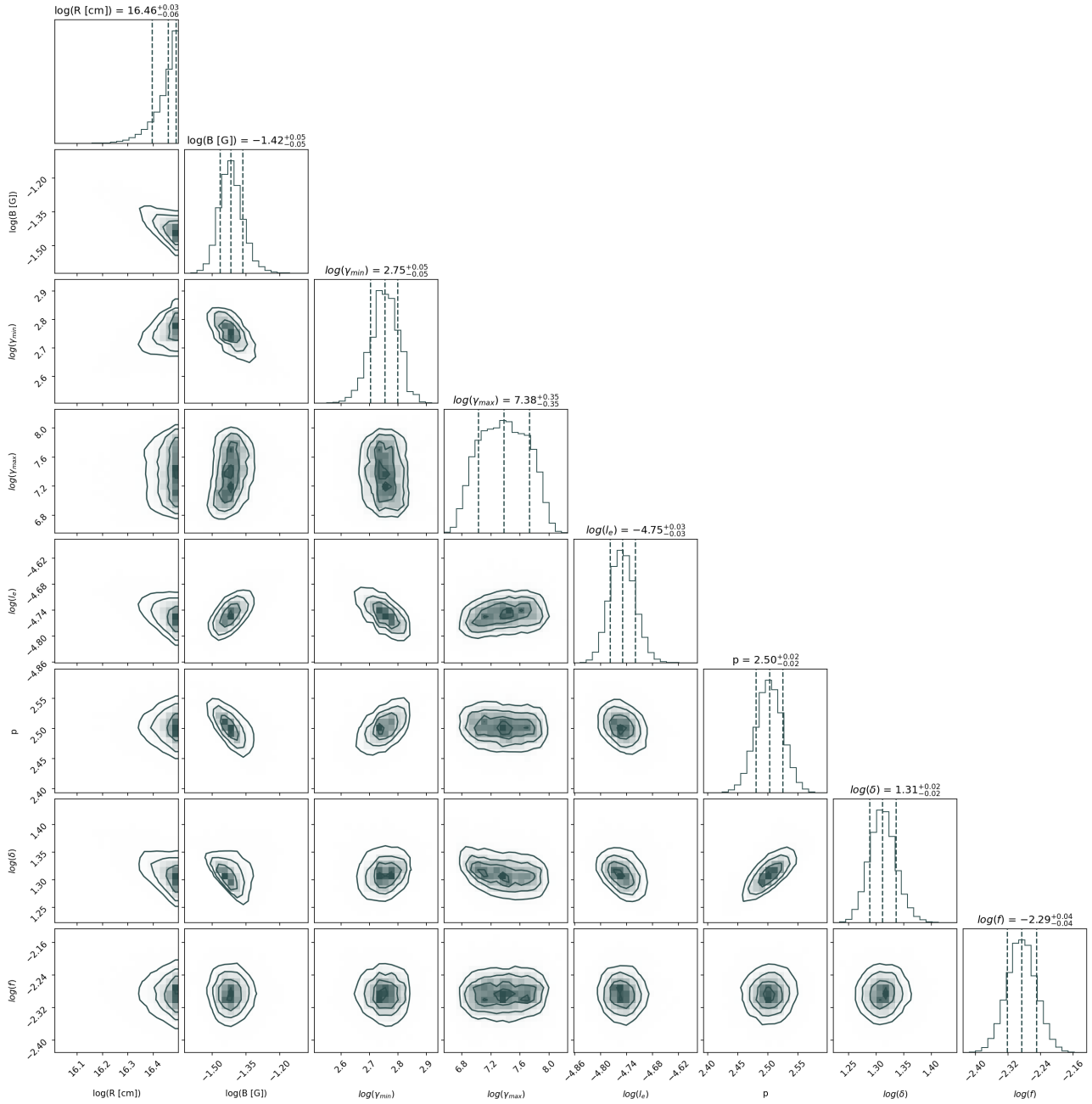

Figure 4.11: Posterior distributions for the fitting process with `emcee` and `LeHaMoC` for Mrk 501.

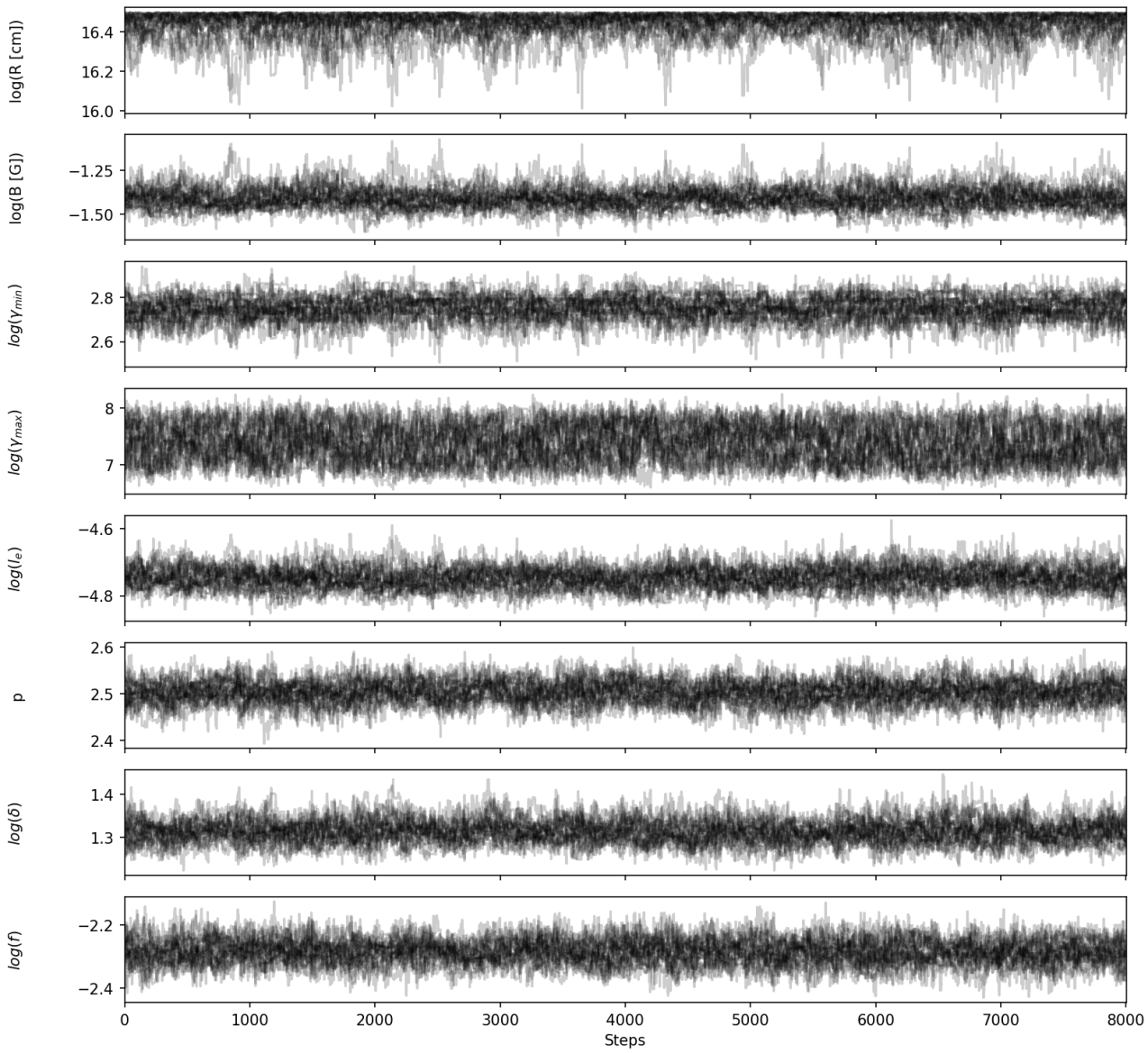

Figure 4.12: Chains of parameters obtained with `emcee` while fitting the average SED of Mrk 501.

even in the absence of the limit imposed on the radius by the Doppler factor we cannot find universally well-constrained parameters within our problem description. For completeness reasons, we show the posterior chains of the fit in Fig. 4.12.

As a result of our parameter investigation, we emphasize that the inclusion or not of the X-ray data does not heavily impact the resulting parameters nor their posterior distributions. The only exception is the value of γ_{max} and its distribution. Thus, we conclude that the fit is driven by the gamma-ray and optical/IR data and only slightly refined by the X-ray data. To illustrate this, we provide in Appendix B both posterior distributions of the fitting process with and without the inclusion of X-ray data.

To investigate the discrepancy between our initial SED parameter estimate and the best-fit `emcee` results we repeat the energy minimization calculations on the SED obtained by our best-fit solutions. We also make the following additional assumptions:

- We acknowledge the impact of synchrotron cooling. In Section 2.2.4 we assumed a steady state power law. Here, we inject a power law, which in the steady state may end up being a broken power law. We assume the synchrotron peak at ν_c and an electron distribution of $N(\gamma)d\gamma = K_e(\int_{\gamma_{min}}^{\gamma_c} \gamma^{-p}d\gamma + \int_{\gamma_c}^{\gamma_{max}} \gamma^{-p+1}d\gamma)$.

- Instead of estimating the minimum and maximum frequencies from the SED, we set $\nu_{min,max} = (\gamma_{min,max}^{Model})^2\delta^{Model}(B^{Model}/B_c r)m_e c^2/h$. Here, the subscript "Model" indicates the best-fit parameter values derived from the `emcee` run. This is the only point where we directly reference `LeHaMoC` parameter results.

Following the method of Section 2.2.4 we present our results in Fig. 4.13 contrasting the `LeHaMoC` SED to the energy minimization SED on the `LeHaMoC` results. We conclude that the energy minimization method fails if used on the observational SED. However, it also fails if we employ it on the derived best-fit parameter SED. Following the steps of Section 2.2.4 and the corrections of the above bullet points lead to inaccurate results even if we use the method on the best-fit parameter SED calculated via `LeHaMoC`. Contrasting the values of Fig. 4.11 to the ones used in the initial parameter guess, we see that we underestimated the range of the injected power law. This is an expected flaw while visually guessing bounds in an observational SED. Furthermore, the method overestimates the magnetic field and underestimates the Doppler factor. The energy minimization scenario is comparable to the equipartition scenario when $W_{el} = W_B$. Therefore, decreasing the energy minimization magnetic field by one order of magnitude implies an emission region where the electrons carry greater amounts of energy comparable to the magnetic field. Furthermore, lower estimations of the Doppler factor are expected as its derivation is composed only of a lower limit. Any value above this lower limit should be considered equally acceptable. Therefore we conclude that a scenario close to/of equipartition and lower limit estimations of the Doppler factor are not a valid approach to model the average emission of Mrk 501.

Leptohadronic Average State

Having derived the global and electron parameters, this chapter focuses on the final 4 proton parameters. We assume that both populations are accelerated before injection by the same mechanism and to the same Lorentz factors, $p_p = p_e$, $\gamma_p^{min/max} = \gamma_e^{min/max}$. Another equally acceptable choice would be $E_e^{min} = E_p^{min}$ and $E_e^{max} = E_p^{max}$. This, however, leads to non-physically meaningful choices for the injected proton luminosity as will be discussed shortly.

From our leptonic posterior analysis, we calculate the upper 1% limit (depicted in Fig. 4.10), meaning 99% of our solutions at each frequency are below it. We make the assumption that any leptohadronic model exceeding this limit by 10% cannot be approximated by a leptonic description. Thus, we investigate an injected proton luminosity of $L_p^{inj} = 10^{\alpha}L_e^{inj}$ searching for the maximum value of α satisfying the above condition. We found that for a value of $\alpha = 10^{5.62}$ this to be the case and showcase the first deviation point with a different color in Fig. 4.14. Thus, for our calculations, we assume $L_p^{inj} = 10^{5.61}L_e^{inj} \approx 10^{46.986} erg/s$.

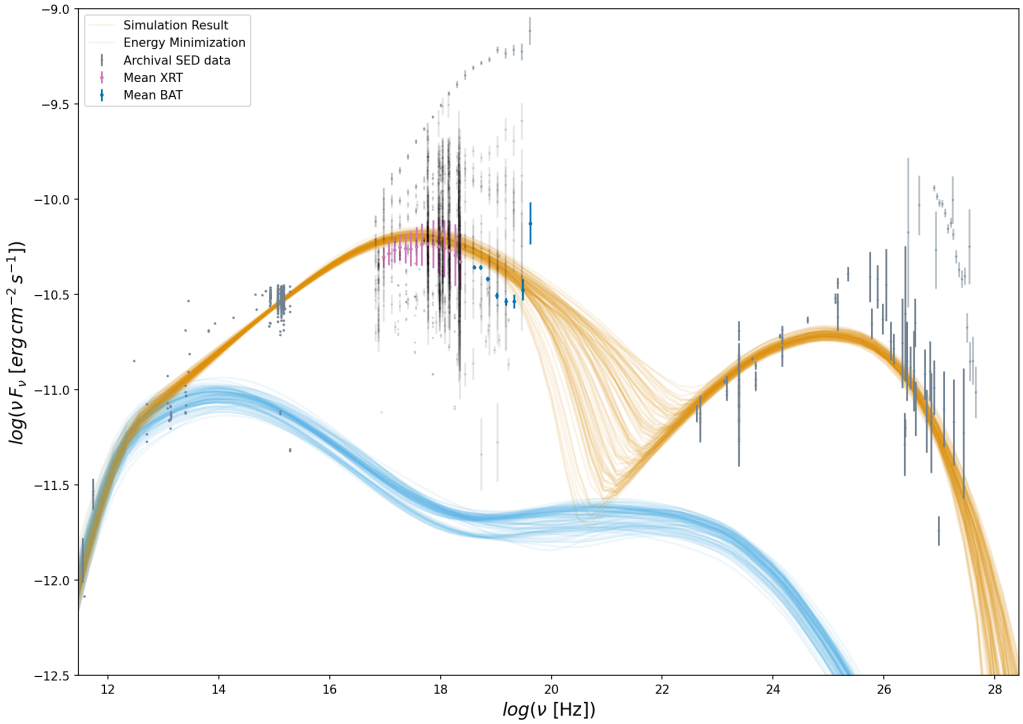

Figure 4.13: Testing the energy minimization scenario using the best-fit parameters of `LeHaMoC`.

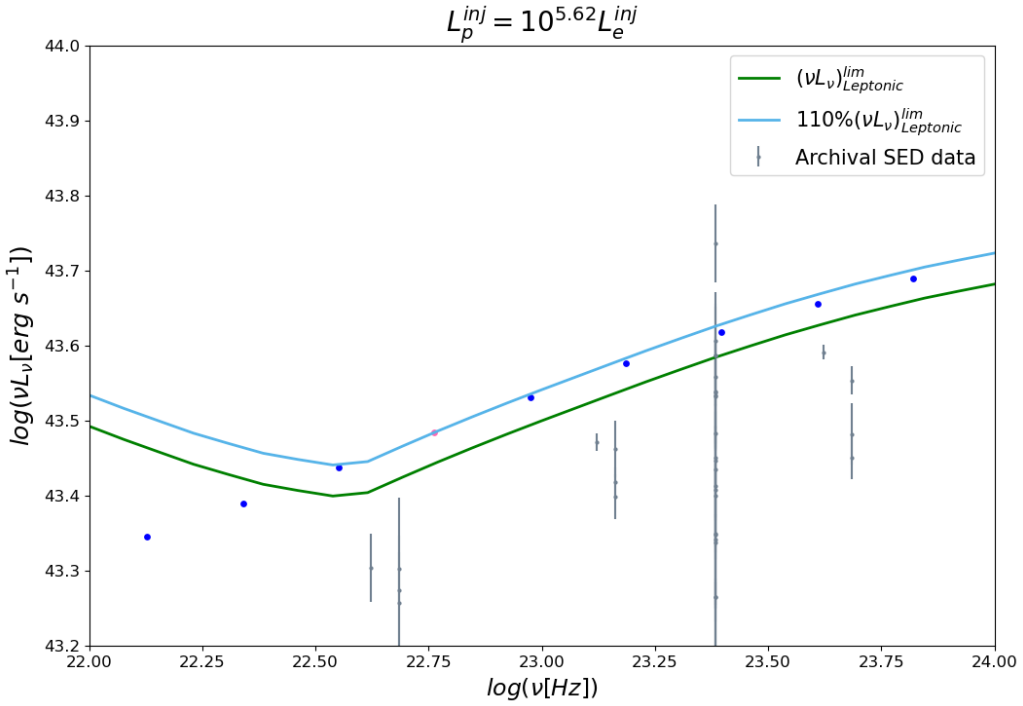

Figure 4.14: First deviation from the leptonic approximation. Shown are the upper leptonic limit discussed in the text (green line) and the 110% value of it (light blue line). The SED model data points not exceeding the imposed limit are shown as blue circles. The first deviation is highlighted by a magenta color.

We briefly note that equating the energies instead of the Lorentz factors of the two populations leads to α values unreasonably high (i.e. $\alpha > 10^9$). Thus, this scenario must be rejected and treated as nonphysical. To summarize, our complete set of parameters for Mrk 501 within `LeHaMoC` is presented in Table. 4.2.

Table 4.2: Parameters of the leptohadronic model describing the average SED of Mrk 501

Parameter	Value
$log(R[cm])$	$16.46^{+0.03}_{0.03}$
$log(B[G])$	$-1.42^{+0.05}_{-0.05}$
$log(\gamma_e^{min})$	$2.75^{+0.05}_{-0.05}$
$log(\gamma_e^{max})$	$7.38^{+0.35}_{-0.35}$
$log(l_e)$	$-4.75^{+0.03}_{-0.03}$
p_e	$2.50^{+0.02}_{-0.02}$
$log(\delta)$	$1.31^{+0.02}_{-0.02}$
p_e	2.50
$log(\gamma_p^{min})$	2.75
$log(\gamma_p^{max})$	7.38
$log(L_p^{inj}[erg/s])$	46.986

Chapter 5

Time Variability of Mrk 501

This Chapter is dedicated to exploring the time domain of Mrk 501. In particular, in Section 5.1 we will construct a synthetic Time Series (TS) of Mrk 501 using the celerite parameters of Chapter 3. Then, we will connect the simulated variations of the Fermi band to parameter variability within our source. We will investigate changes in the injection rate of the particle energy (Section 5.2) and changes in the magnetic field strength (Section 5.3). Lastly, we will argue for changes in the power-law slope of the particle distribution motivated by the magnetic field variability (Section 5.4).

5.1 Time Series of Mrk 501

The celerite parameters of Mrk 501, listed in Table 3.1, are: (α) $\mu[log(Flux)] = -4.12$, (b) $ln(S_0) = 0.58$, (c) $ln(Q) = -3.2$, and (d) $ln(\omega_0) = -1.4$. Using these, we create a synthetic Light Curve (LC) with statistical properties consistent with the observed LC in the Fermi energy band of 0.1-100 GeV. For the synthetic LC, we selected a number of points equal to that of the real LC and multiplied them by the mean cadence of 7 days, thus creating the TS. However, since we did not include upper limits in our analysis of the Fermi LC, the total number of points, and by extension the total time length of the derived LC, is slightly shorter than that of the observational one.

In Figure 5.1 we showcase the entirety of our used zero-meaned TS. As we are interested in the relative changes of the logarithmic flux, the flux units are disregarded. A horizontal line indicates the average state of the source. Additionally, we highlight two flares using a grey band in the upper panel and zoom into them in the lower panels. The first flaring event, labeled α, exhibits extreme variability exceeding the maximum observed flux of Mrk 501. The second flaring event, labeled β, is comparable to the observed flux variability.

We interpolate this TS at time steps of one light crossing time, $t_{cr} = 0.558$ days, to accurately capture changes in the parameter space of our source. Both the mean cadence and time step are in the observer's frame, as they are based on direct observational results. `LeHaMoC` performs calculations in the comoving frame of the blob in time-steps of 1 intrinsic light-crossing time.

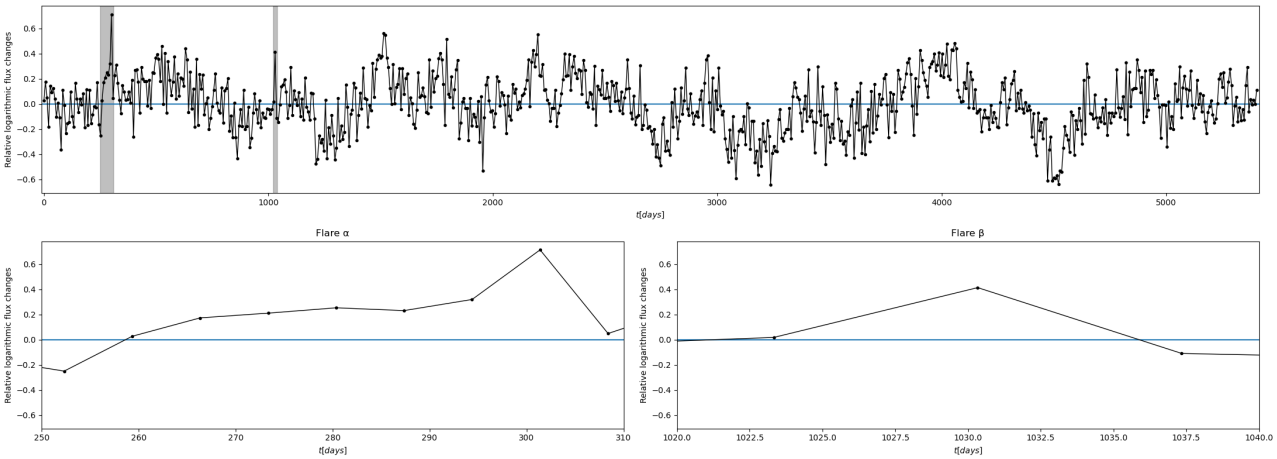

Figure 5.1: *Upper panel*: Simulated TS of Mrk 501. Grey bands designate analyzed flares. *Lower panel:* Left: Extreme flare labeled α. The total variation exceeds observations. Right: flare with variation similar to observed labeled β.

However, transformations between the comoving and the observer's frame, do not change the relative values of our generated TS. Therefore, we can use them despite the different reference frames.

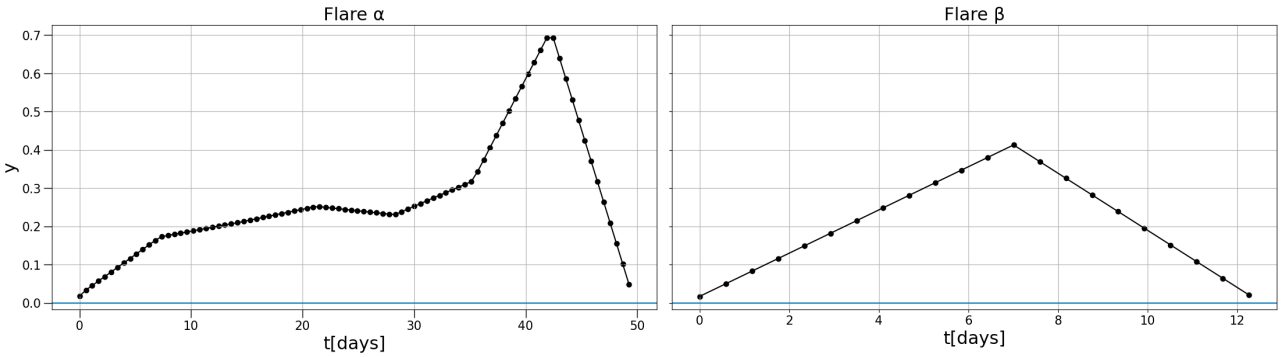

Figure 5.2: Interpolation of flare α (left) and flare β (right).

In Fig. 5.2 the interpolations for both flaring events are shown. Each TS starts close to zero to be able to model the evolution from the average state description. Furthermore, each TS has a 10-step "burn-in" phase where no changes occur in any parameter value. This allows the model to accurately converge to the average state description before any time variations occur.

5.2 Variability in the particle energy injection rate

The first time variation of this study is the energy injection rate for electrons, L_e^{inj}, and protons, L_p^{inj}. To relate the LC in the Fermi energy band to the above parameters, we note from Eq.(2.12):

$$f_\epsilon^{syn} \propto N'_e(\epsilon') \Rightarrow f_\epsilon^{syn} \propto L_e^{inj}, \tag{5.1}$$

and thus from Eq.(2.24):

$$f^{Fermi} \propto f^{SSC}_{\epsilon_s} \propto (f^{syn}_e)^2 \Rightarrow f^{Fermi} \propto (L^{inj}_e)^2 \tag{5.2}$$

or

$$log(f^{Fermi}) \propto 2log(L^{inj}_e). \tag{5.3}$$

Therefore, defining the relative flux values of the simulated TS as $y(t_i)$, where $t_i = i \cdot t_{cr}$ is the ith time step calculation in `LeHaMoC`, we derive the time evolution of L^{inj}_e:

$$log(L^{inj}_e(t_i)) = log(\langle L^{inj}_e \rangle) + \frac{1}{2} y(t_i). \tag{5.4}$$

In other words, to transform the TS of Fig. 5.1 into parameter variability for the electron energy injection rate, we divide it by 2. We adopt the same trend for L^{inj}_p assuming both populations are injected into the source via the same mechanism.

In Fig. 5.3 we present the SEDs throughout each time step in the leptohadronic and leptonic `LeHaMoC` run for the complete TS of Mrk 501. The initial average state SED is highlighted in mustard color. The resulting figure resembles a density plot differentiating between regions of frequent and rare occurrences. This is underlined by the sparse number of SEDs in the most luminous cases, contrasted by the predominantly monochrome region close to the average state description.

Furthermore, we investigate the effect of particle energy injection rate variability on smaller timescales emulating flaring events. Therefore, we repeat the numerical run for flares α/β discussed in 5.1. The time evolution SED plot for the flares is shown in Fig. 5.4.

We draw several conclusions from these runs:

- We accurately predict the synchrotron and SSC scaling. The high-energy portion of the SED produced by SSC exhibits twice as much flux variability as the synchrotron component. This is expected from Eq.(5.1) and Eq.(5.2). The relation is also illustrated in the flux-flux diagram of Fig. 5.5 comparing the peak fluxes of the synchrotron and the SSC component for the full leptohadronic run.

- No spectral changes occur. Following our discussion in Chapter 2.2 no spectral changes or spectral breaks are expected through changes in L^{inj}_e. We confirm this through our runs.

- We do not see a flux reduction in the pion bump around $\nu = 10^{30}$Hz. Although the optical depth for $\gamma\gamma$ interactions increases slightly caused by the increase of low-energy photon targets. This is counterbalanced by the increase of available protons and thus photomeson interactions. A detailed discussion on the impact of $\gamma\gamma$ absorption is found in Section 5.4.2 when a significant pion bump contribution is expected.

- The model cannot account for the observed range of fluxes. In particular, it fails to explain the highest fluxes observed in X-rays and VHE gamma-rays. The flux variations do not follow the observational trends in all energy bands. The similarities and discrepancies will be highlighted below through flux histograms, LCs, and coefficients of variation.

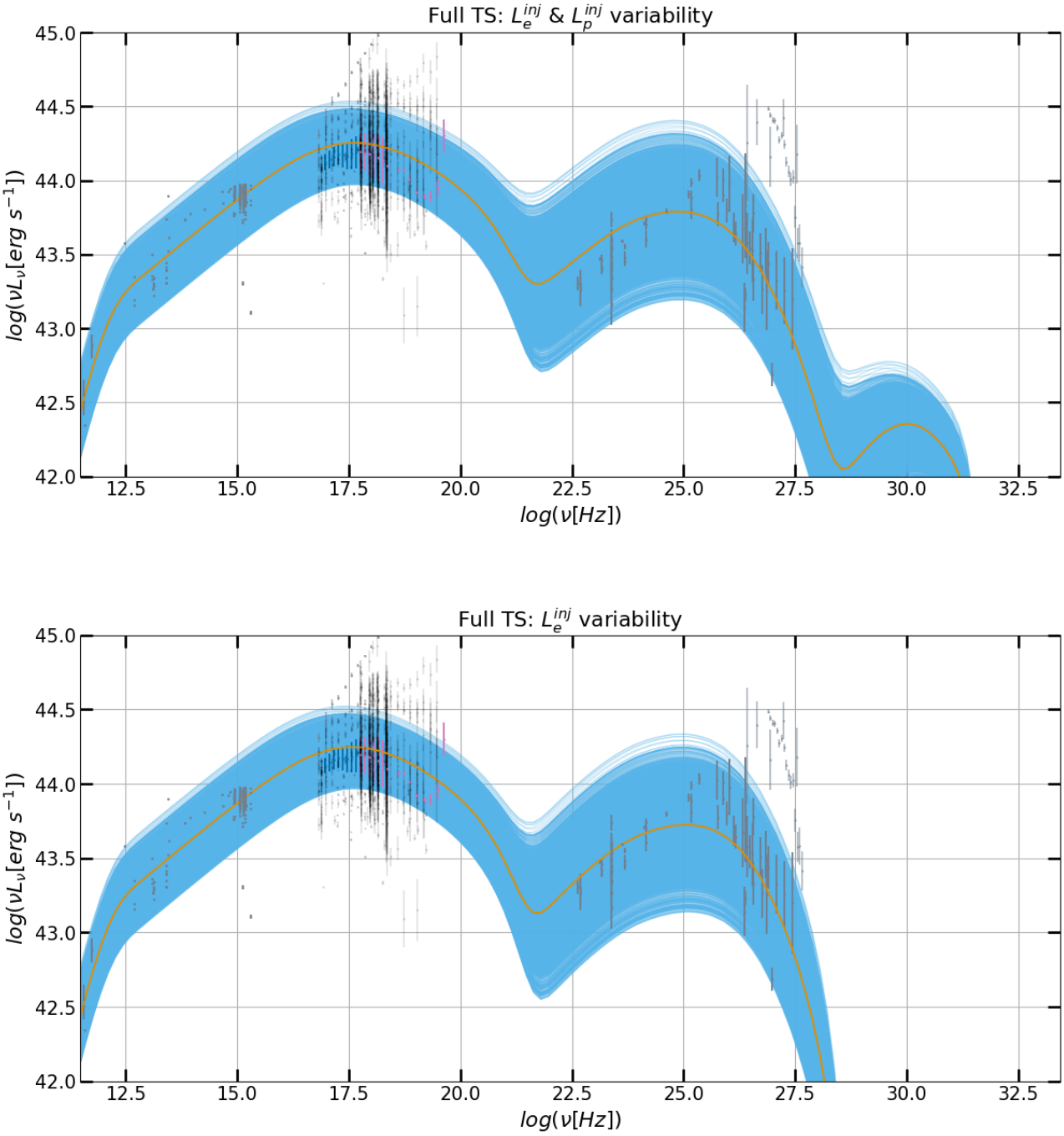

Figure 5.3: Time evolution SED plots for particle energy injection rate variability with the full TS. Leptohadronic (upper panel) and leptonic (lower panel) cases are shown, both with the average state of Mrk 501 indicated in mustard color. An animated version of the leptohadronic time evolution is found Here.

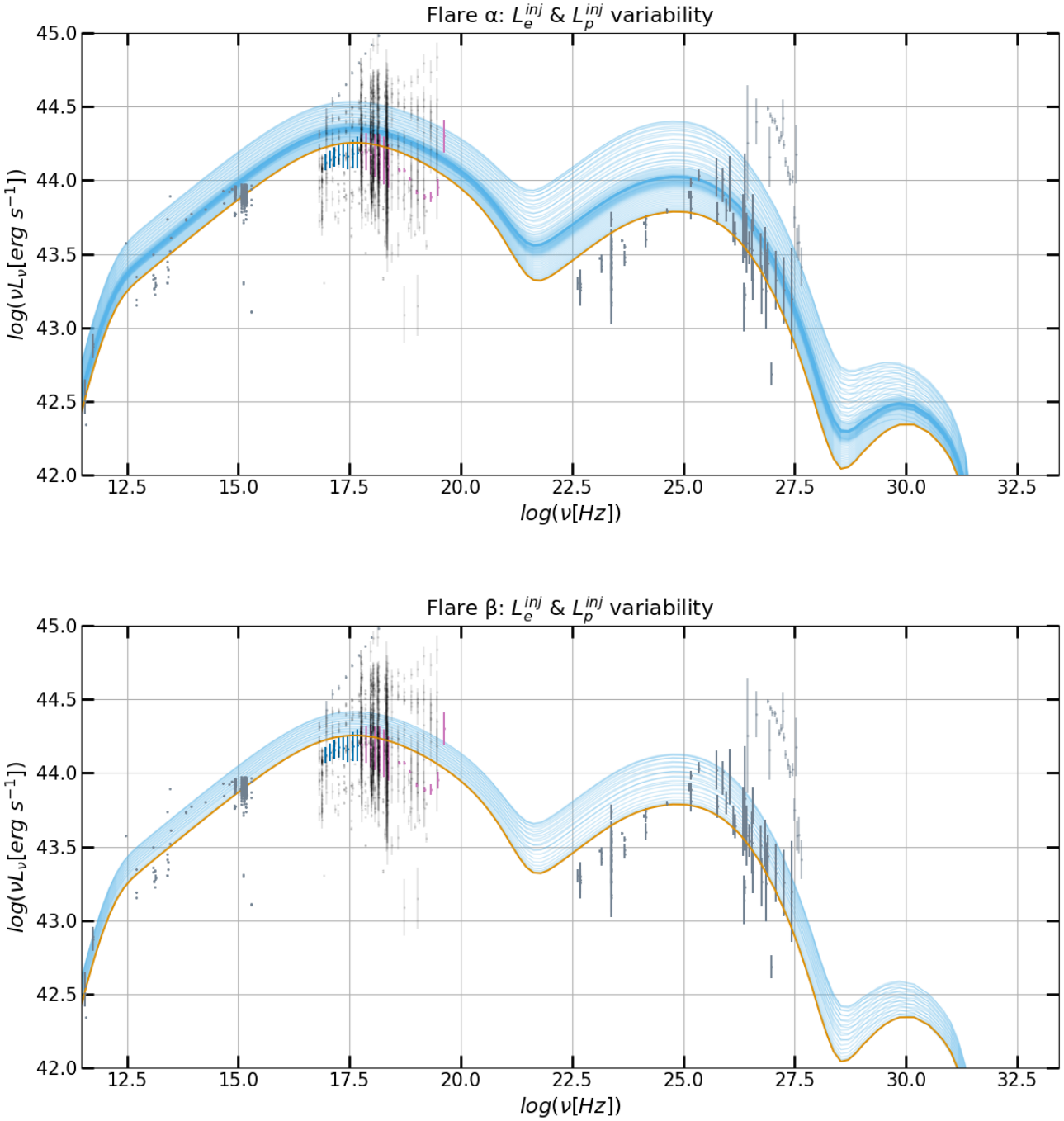

Figure 5.4: Time evolution SED plots for leptohadronic particle energy injection rate variability. Flare α (upper panel) and Flare β (lower panel) are shown, both with the average state of Mrk 501 indicated in mustard color.

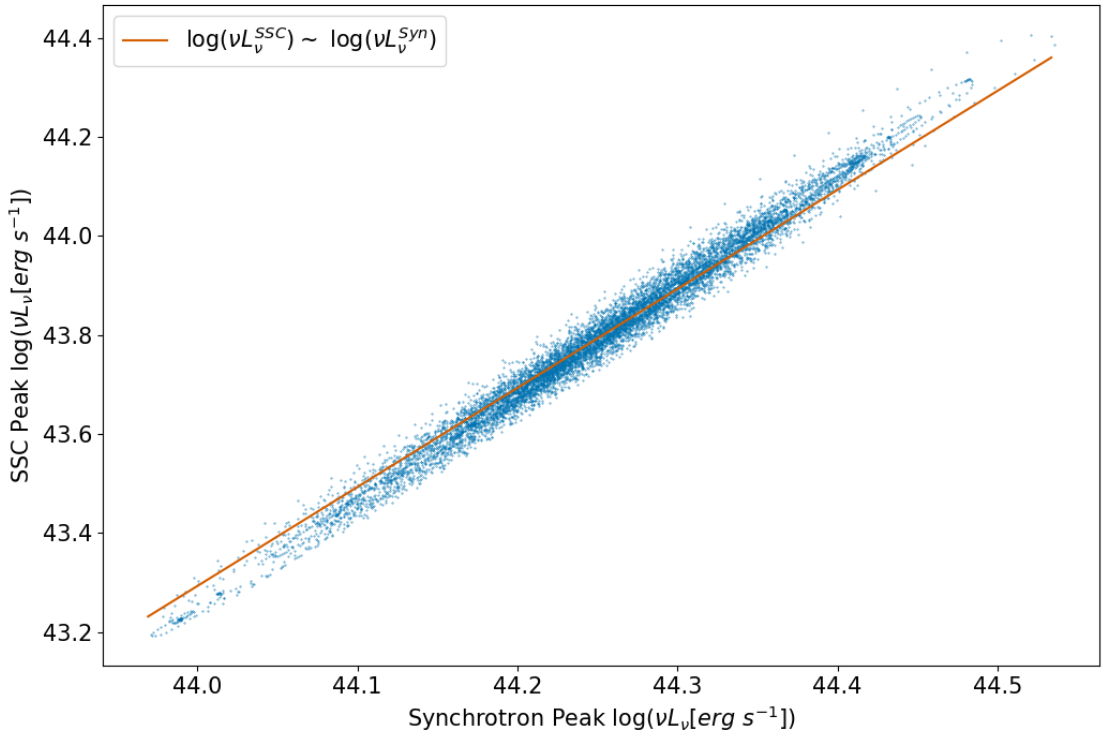

Figure 5.5: Flux-flux diagram of the synchrotron and SSC component peaks in the leptohadronic time-variable particle energy injection run. Noted with an orange line is the expected quadratic scaling between SSC and synchrotron peak luminosity.

- The inclusion of a hadronic population does not impact the above results. The inclusion of a proton (hadronic) component results in the production of secondary electrons through photohadronic interactions. Those electrons will contribute to the observed flux. From Section 2.3 we can estimate the proton threshold energies and the emission frequencies of the resulting secondary electrons. In particular assuming our average state values of $B = 0.038$G and $\delta = 20.41$, for photomeson interactions we have from Eq.(2.31):

$$\gamma^{th}_{p,p\gamma} \approx 3.5 \cdot 10^4 (1+z)^{-1} \delta \nu_{18}^{-1} \approx 10^{5.85}.$$

And from Eq.(2.32), Eq.(2.30):

$$\gamma^{th}_{e,p\gamma} \approx K_{p\gamma} \gamma^{th}_p m_p/(4m_e) \approx 10^{7.81} \Rightarrow \nu^{syn}_{e,p\gamma} \approx 3 \cdot 10^6 \delta B \left(\gamma^{th}_{e,p\gamma}\right)^2 \approx 10^{22}\text{Hz}.$$

Similarly, for Bethe-Heitler pair-production we have from Eq.(2.33):

$$\gamma^{th}_{p,pe} \approx 1.2 \cdot 10^2 (1+z)^{-1} \delta \nu_{18}^{-1} \approx 10^{3.38}.$$

And since $\gamma^{th}_{p,pe} \approx \gamma^{th}_{e,pe}$, from Eq.(2.30) it follows:

$$\nu^{syn}_{e,pe} \approx 3 \cdot 10^6 \delta B \gamma^2 \approx 10^{13.12}\text{Hz}.$$

We do not see any signatures of the above in our results. We will return to the effects of secondary particles in Section 5.4.2 when hadronic signatures become prominent.

- Focusing on small timescales of high variability does not change the above results. Isolated flaring states follow the above trends.

In what follows, we present different diagnostics for comparing our model against observations in different energy bands. We used the LC from the Fermi LCR for the time series analysis and thus chose the Fermi band of $0.1 - 100$ GeV for the high-energy region. Having utilized Swift XRT and BAT data in our average state analysis, we use their respective energy ranges of $0.2 - 10$ keV and $14 - 195$ keV to describe the soft and hard X-ray regions. For the very-high-energy (VHE) range, we use $0.3 - 3$ TeV to describe the region of high flux sensitivity of the upcoming Cherenkov Telescope Array Observatory (see Chapter 6)[55]. Lastly, we use the R-band ($138 - 658$ nm) to represent the low-energy region in the optical.

We present in Fig. 5.6 the flux histograms of the full leptohadronic `LeHaMoC` run for each energy band. We also included the histogram for the simulated LC used for the time variability. Furthermore, in each panel, an observational histogram is superimposed when available (Fermi, BAT, XRT, R-Band). As the available XRT data exceeds the duration of our variability run, we aligned the endpoints rather than the starting dates. This ensures a better visual comparison between model and observations as the data for the first years of the XRT lifecycle are sparse. For the R-Band we utilize observations from the GASP program of the Whole Earth Blazar Telescope (WEBT) and data from the Tuorla observatory using the KVA telescope. The resulting LC has a total length of 4 years, a binning time of 1 day, and has been adopted by Ref. [56]. The shorter duration of this observational LC is a caveat that needs to be taken into

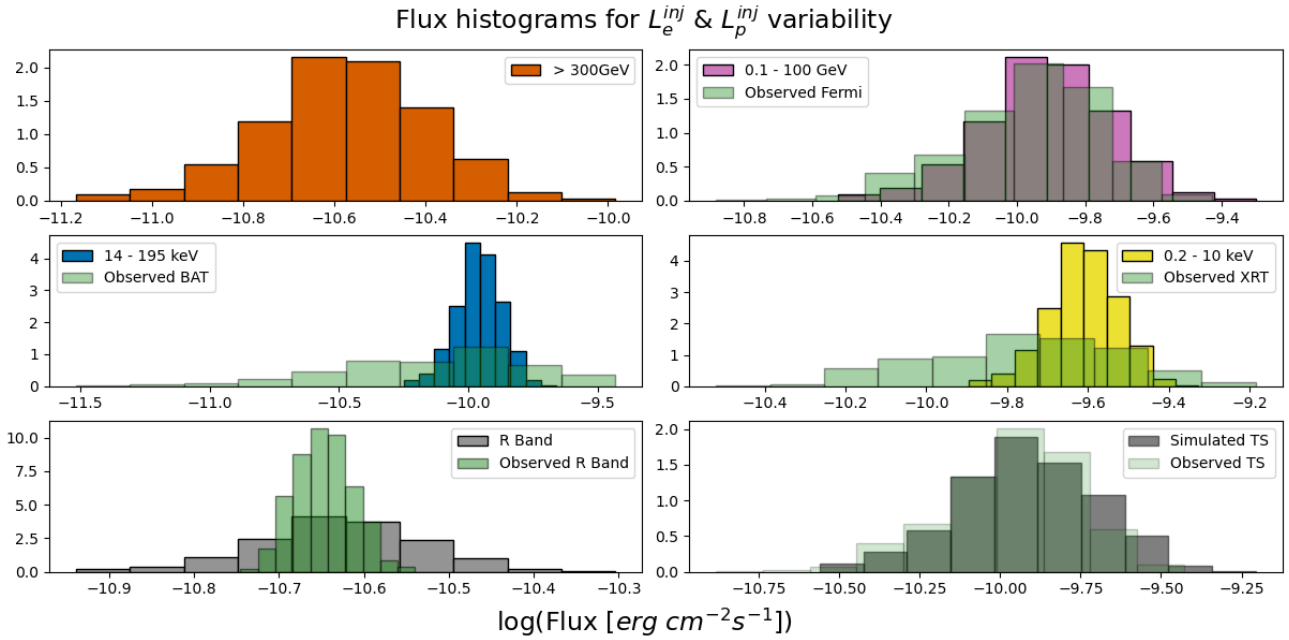

Figure 5.6: Flux histograms for the complete leptohadronic run for particle energy injection variability. The respective observational histograms outlined within the text have been superimposed. From left to right: *Upper panel:* Energy ranges of $0.3-3$ TeV and $0.1-100$ GeV. *Middle panel:* Energy ranges of $14-195$ keV and $0.2-10$ keV. *Lower panel:* Energy range of the R-band and the histogram for the simulated TS.

consideration when interpreting our results. In Fig. 5.7 we present the LCs of the discussed energy bands for the full leptohadronic run together with the observed LC superimposed. From these results, we conclude that particle energy rate variability alone cannot explain the observed variability. We have an agreement in the Fermi band between the model and observations (As expected. The time series were created in a way that reproduces the observed GeV variability). However, we do not recover the expected variability in the other energy bands. Observationally, we expect broader histograms in the X-ray range and more confined ones in the optical than predicted by our numerical experiment.

In Fig. 5.8 we present the LCs for the flares in the energy bands of $0.3-3$ TeV, $0.1-100$ GeV, and $14-195$ keV. To compare the differences between the model LCs and the injected TS we superimposed the TS of Fig. 5.2 in each panel. Since $y(t_i)$ is a function of the logarithmic flux variations with respect to the average flux value ($y(t_i = 0) = 0$ corresponding to the average state description), we added the initial average state value of the energy band LC to each case. On the horizontal axis, we see small shifts on daily timescales and skewness (see the decay part of the flare) compared to the peak of the flare TS. The shifts can be explained qualitatively as a delayed response to changes within the source and will shortly be investigated with Discrete Correlation Functions. On the vertical axis, we see an approximate agreement between the X-ray LC and the flare TS while the (V)HE LCs are at approximately double the values of the flare TS. This is expected from Eq.(5.1) and Eq.(5.2).

To further quantify the statistical properties of the time variability results we supplement the LCs and flux histograms with flux-flux diagrams, Coefficient of Variation (CV) calculations,

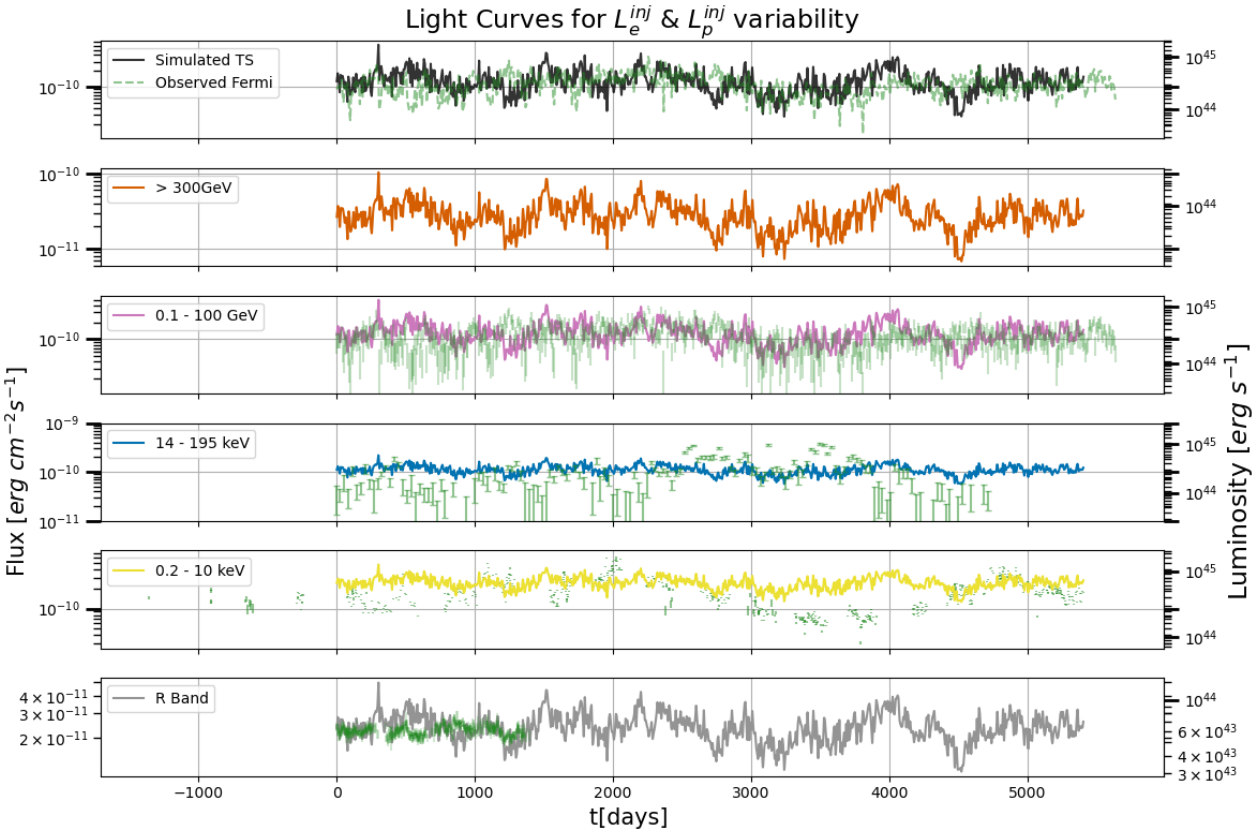

Figure 5.7: LCs for the complete leptohadronic run for particle energy injection variability. The respective observational histograms outlined within the text have been superimposed. From top to bottom: The histogram for the simulated TS. Energy ranges of $0.3-3$ TeV, $0.1-100$ GeV, $14-195$ keV, $0.2-10$ keV, and the R-band.

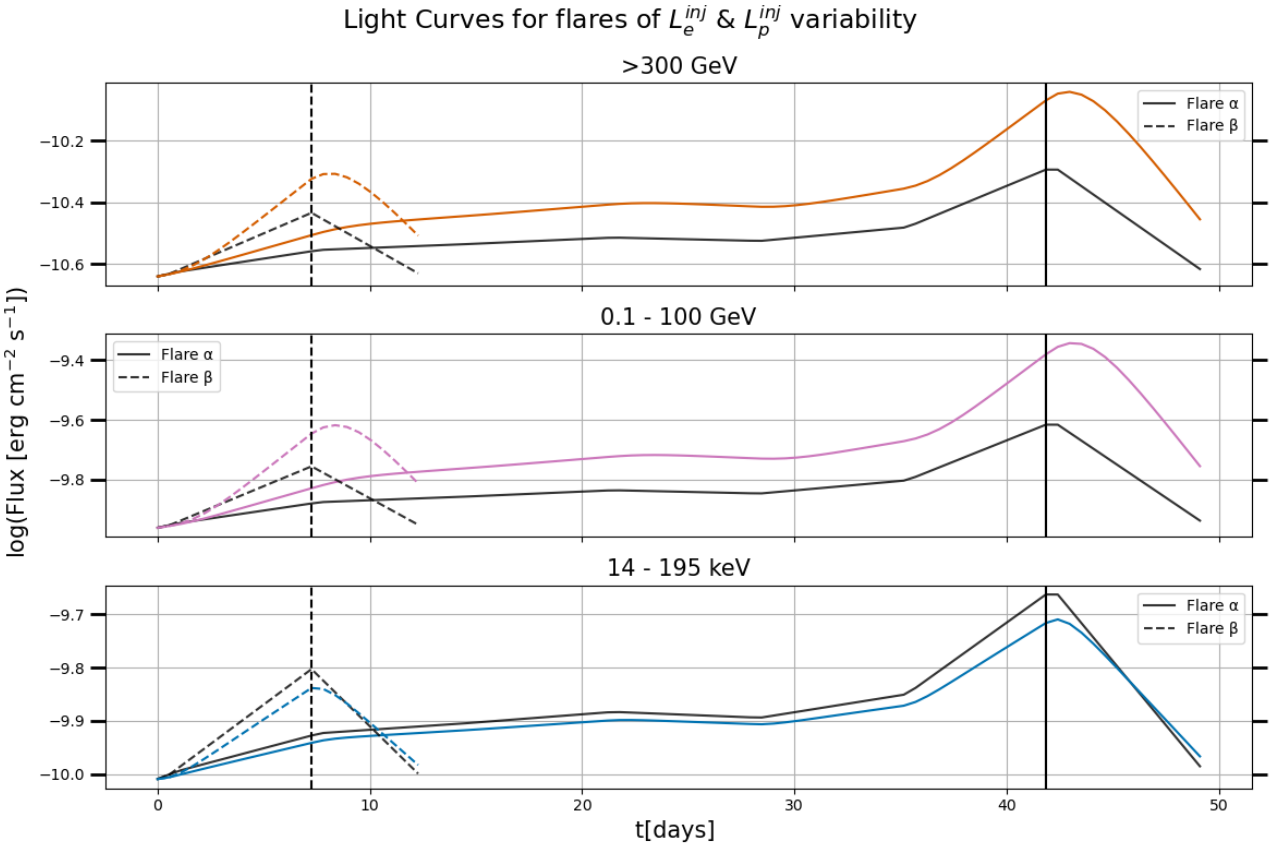

Figure 5.8: LCs for flares α (solid line) and β (dashed line) for particle energy injection variability. The renormalized TS used for each flare (see Fig.5.2) have been superimposed (with black lines) for comparison purposes. Results for the energy ranges of $0.3 - 3$ TeV (upper panel), $0.1 - 100$ GeV (middle panel), and $14 - 195$ keV (lower panel) are shown.

Energy bands	Slope value
VHE vs. Fermi	1.0310 ± 0.0003
BAT vs. Fermi	2.102 ± 0.003
XRT vs. Fermi	2.164 ± 0.003
BAT vs. R	1.0922 ± 0.0009

Table 5.1: Linear fit slope values for the complete run of the leptohadronic energy injection rate variability of Fig. 5.9.

and Discrete Correlation Function (DCF) diagrams.

In Fig. 5.9 we present the flux-flux diagrams comparing the Fermi flux to the flux in the VHE range (a), the harder X-ray range probed by BAT (b), and the softer X-ray range probed by XRT (c). Furthermore, we compare the BAT flux to the R-band flux (d), comparing hard X-ray to low-energy photons. We present the variability for the complete leptohadronic run (blue circles) and the results for flare α (yellow stars) and flare β (purple squares). We see the steady flux increase of both flares during the increasing phase and decline during the decaying phase. For flare α we see a "stalling" in the diagram for the period between 10 and 30 days of Fig. 5.2. We note how the flares (yellow star and purple square symbols) track the shape of the complete numerical run (blue circle symbols). Therefore, we conclude that flaring states in this scenario can be studied accurately separately or as part of a longer time variable numerical run. Lastly, we calculate the slopes of the complete run via a linear fit (Table. 5.1). We recover the quadratic scaling between synchrotron and SSC fluxes. Moreover, we calculate a linear scaling between different regions within the SSC component (Fermi vs. VHE) and between X-rays and optical.

The CV is defined through the mean μ and the standard deviation σ of a TS as CV$=\frac{\sigma}{\mu}$. In Fig. 5.10 we present the results for the discussed energy ranges. We conclude that the high energy ranges exhibit increased variability compared to the X-rays and IR. This is expected as the quadratic scaling between the synchrotron and SSC component leads to higher standard deviations in the TS. Comparing our results to observational CVs we conclude that we approximate the variation in the Fermi Band. However, we have not recovered the observational values in the X-ray and R-band ranges: our model underestimates by a lot the variability in X-rays, and in particular in the BAT range, while it overpredicts the CV found in the R-band (keeping in mind that for the latter the duration of the model light curve is longer than the observed R-band). This result is expected from our discussion on the flux histograms and LCs and is another indication of the need for a more complex model.

Lastly, we will discuss the DCF of the flux variability for the complete TS run. In a DCF diagram, we compare the similarity between two TS by shifting the temporal domain of one relative to the other. We define a positive lag in TS "A" vs. TS "B" as a leading TS "A". Through this tool, we can investigate time lags and correlations between TS in different energy bands. The DCF of a TS with itself is called the Auto-Correlation Function (ACF), a sharply peaked curve at a time lag of 1 and close to zero everywhere else for non-periodic TS. In

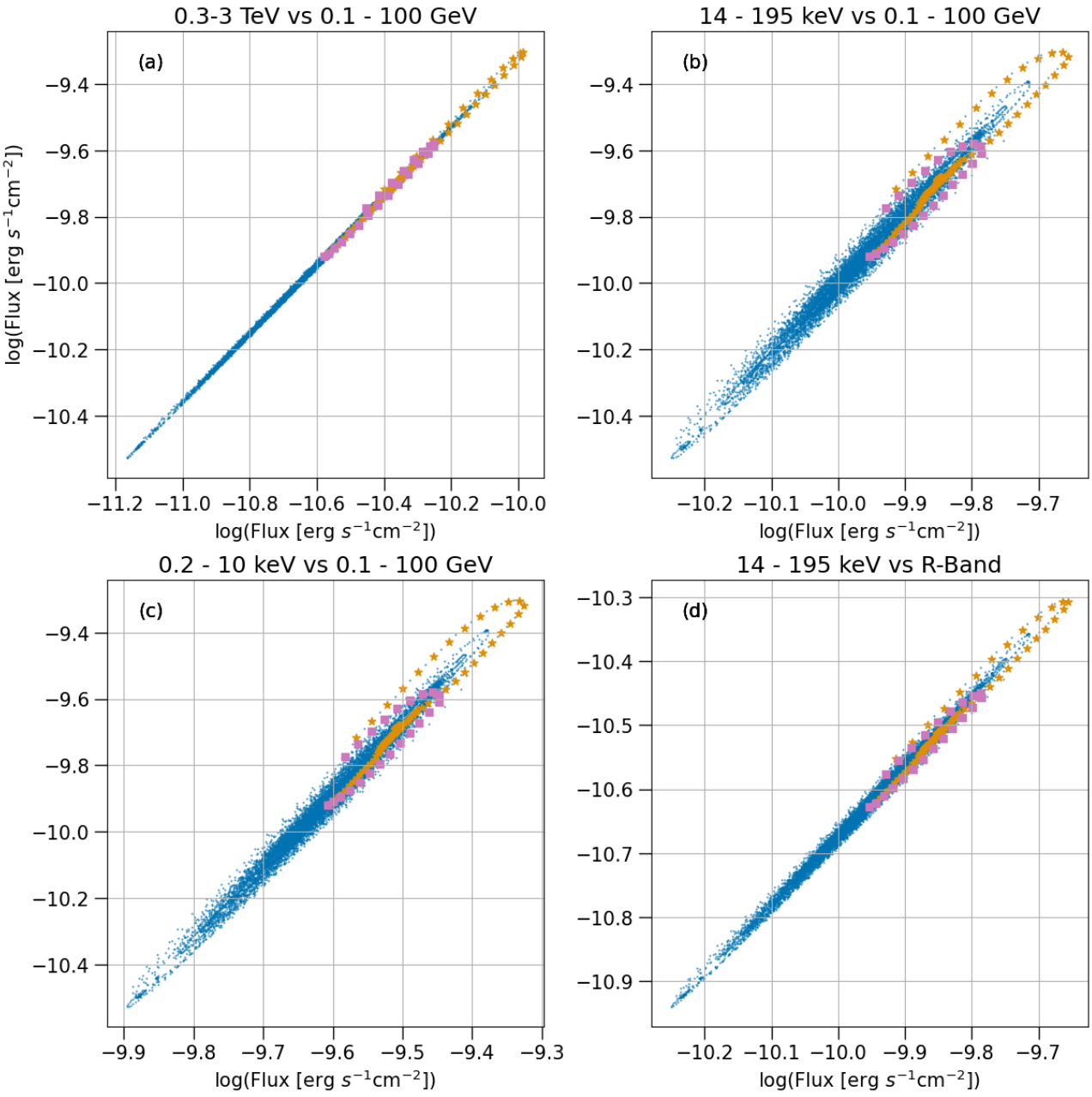

Figure 5.9: Flux-flux diagrams for leptohadronic energy injection rate variability, comparing the flux variabilities between Fermi vs. VHE (a), Fermi vs. BAT (b), Fermi vs. XRT (c), BAT vs. R-Band (d). The cases for the complete TS (blue circles), as well as the results for flare α (yellow stars) and flare β (purple squares) are indicated.

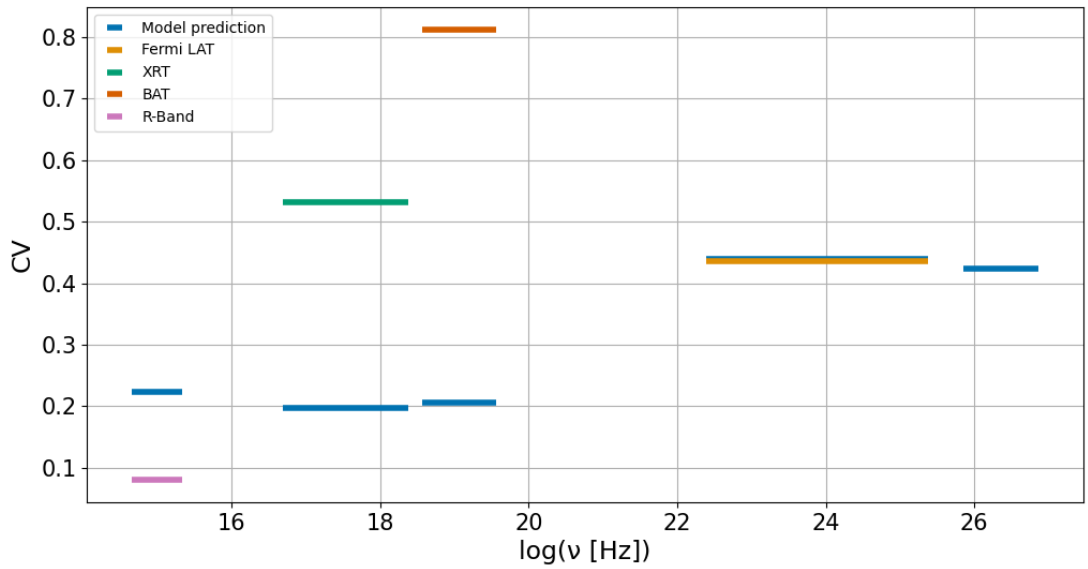

Figure 5.10: Coefficient of variation (CV) for the Fermi, BAT, XRT, and R-band energy ranges in the complete leptohadronic particle energy rate variability run.

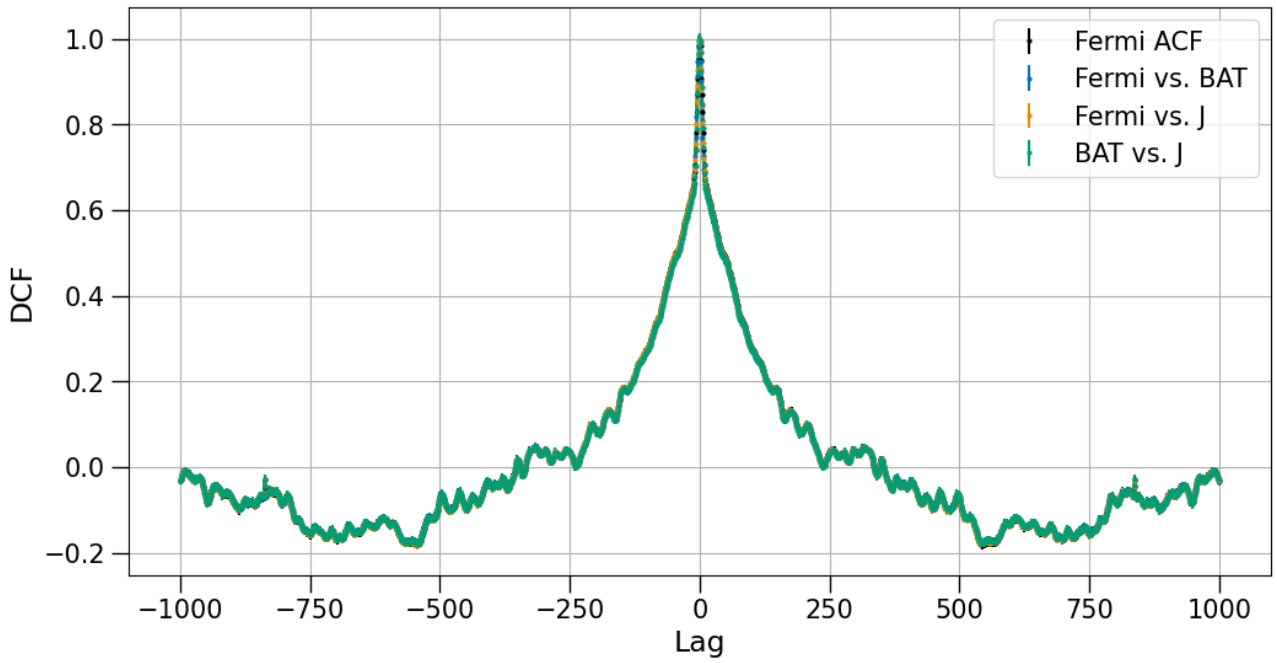

Figure 5.11: Discrete Correlation Function (DCF) for time lags up to 1000 days. Comparisons between Fermi vs. BAT, Fermi vs. R-band, and BAT vs. R-band. The Auto-Correlation function (ACF) for Fermi is noted.

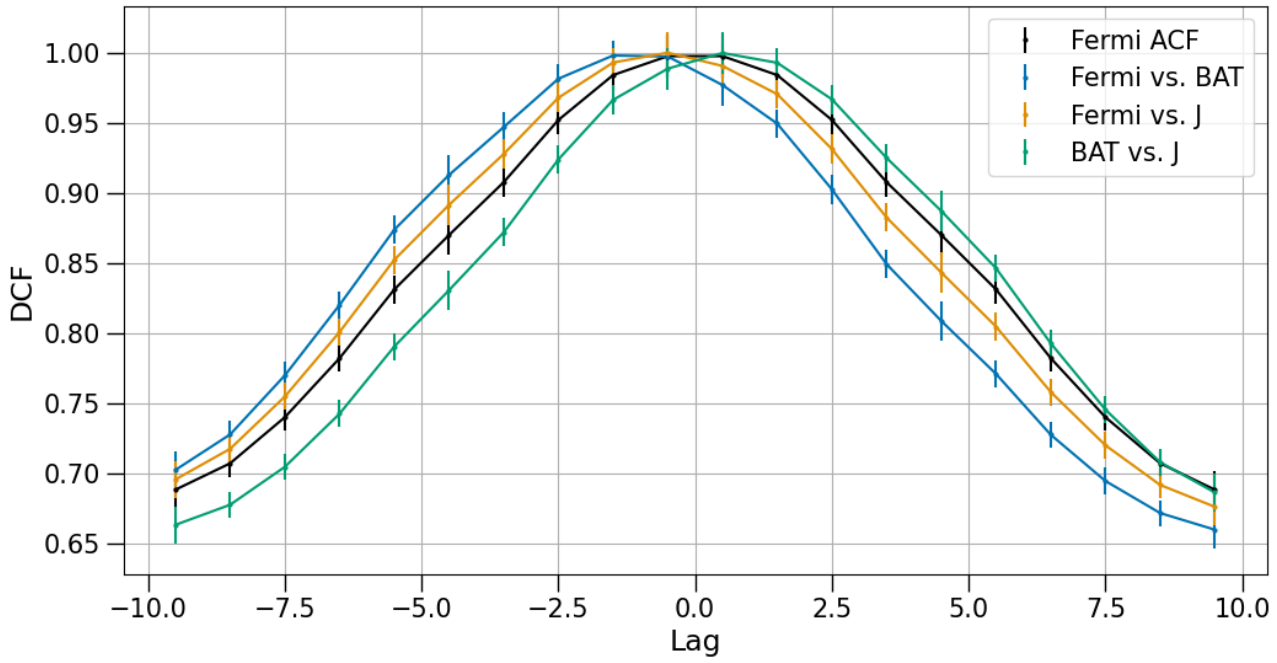

Figure 5.12: Zoomed in version of Fig. 5.11 focusing on timelags -+10 days.

Fig. 5.11 we present, for a total time lag of 1000 days, the DCF between Fermi vs. BAT, Fermi vs. R-band, BAT vs. R-band, and the ACF of the Fermi band. Through this selection, we investigate possible lags between representative high-energy, X-ray, and low-energy regions on large timescales. In all cases, we derive results similar to the Fermi ACF. Although the morphology of the DCF at $t \neq 0$ is not a flat line, the existing structures are sufficiently close to zero, indicating the absence of any significant time lags. In Fig. 5.12 we repeat the above DCF calculations for a total time lag of 10 days to investigate changes on small timescales. For all three cases, we see a peak shift for about less than a day in either direction and a skewness of the DCF. These findings are similar to the delay/skewness of Fig. 5.8. One proposed theoretical explanation is a delayed response between synchrotron emission/cooling and SSC upscattering of synchrotron emission. However, we were unable to explain those features of the DCF or the LCs through any theoretical calculations. Therefore, this constitutes another open question of this thesis work. *"How can we predict the time lag and skewness of the DCFs/LCs? Do these features stem from underlying physical processes or are they results of numerical approximations?"* are questions that must be explored and answered in future works.

5.3 Variability in the magnetic field strength

We will repeat the methodology outlined in Section 5.2 for time variability in the magnetic field strength. To relate the LC in the Fermi energy band to the strength of the magnetic field, we note from Eq.(2.12):

$$f_{\epsilon}^{syn} \propto U_B \Rightarrow f_{\epsilon}^{syn} \propto B^2, \tag{5.5}$$

and thus from Eq.(2.24):

$$f^{Fermi} \propto f_{\epsilon_s}^{SSC} \propto (f_e^{syn})^2 B^{-2} \Rightarrow f^{Fermi} \propto B^2 \tag{5.6}$$

or

$$log(f^{Fermi}) \propto 2log(B). \tag{5.7}$$

Therefore, similar to the previous section, the time evolution of B is:

$$log(B(t_i)) = log(\langle B \rangle) + \frac{1}{2} y(t_i). \tag{5.8}$$

In Fig. 5.13 and Fig. 5.14 we present, the results for the full leptohadronic/leptonic and the leptohadronic runs for flares α/β respectively.

We draw several conclusions from these runs:

- We accurately predict the synchrotron and SSC scaling. The high-energy portion of the SED produced by SSC exhibits approximately equal amounts of variability compared to the synchrotron component. This is expected from Eq.(5.5) and Eq.(5.6). The scaling is illustrated in the flux-flux diagram of Fig. 5.15 comparing the peak fluxes of the synchrotron and the SSC component for the full leptohadronic run.

- The cooled part of the synchrotron spectrum increases as the synchrotron peak shifts to the left. This is expected as the peak frequency is approximately at the critical frequency defined in Eq.(2.9). Therefore, $\nu_c \propto b\gamma_c^2 \propto BU_B^{-2} \propto B^{-3} \Rightarrow \nu_{pk}^{syn} \propto B^{-3}$ or $\log\left(\nu_{pk}^{syn}\right) \propto -3\log(B)$. As the SSC flux is dependent on the synchrotron component, a displacement of ν_{pk}^{syn} results in a displacement of ν_{pk}^{SSC}. The exact scaling cannot accurately be described in the delta approximation and thus won't be discussed.

- The flux of the pion bump around $\nu = 10^{30}$Hz decreases. This is expected as the optical depth for $\gamma\gamma$ interactions increases slightly. This change is caused by the increase of low-energy photon targets. A detailed discussion on the impact of $\gamma\gamma$ absorption is found in Section 5.4.2 when a significant pion bump contribution is expected.

- The model cannot account for the observed range of fluxes. In particular, it fails to explain the highest fluxes observed in X-rays and VHE gamma-rays. The flux variations do not follow the observational trends in any energy band. The discrepancies will be highlighted below through flux histograms, LCs, and coefficients of variation.

- The inclusion of a hadronic population does not impact the above results.

- Focusing on small timescales of high variability does not change the above results. Isolated flaring states follow the above trends.

We repeat the comparisons outlined in the previous section. In Fig. 5.17 and Fig. 5.16 we present the result for the LCs and the flux histograms for the full leptohadronic run while in Fig. 5.18 we present the LCs for the flares. From this run, we report greater discrepancies

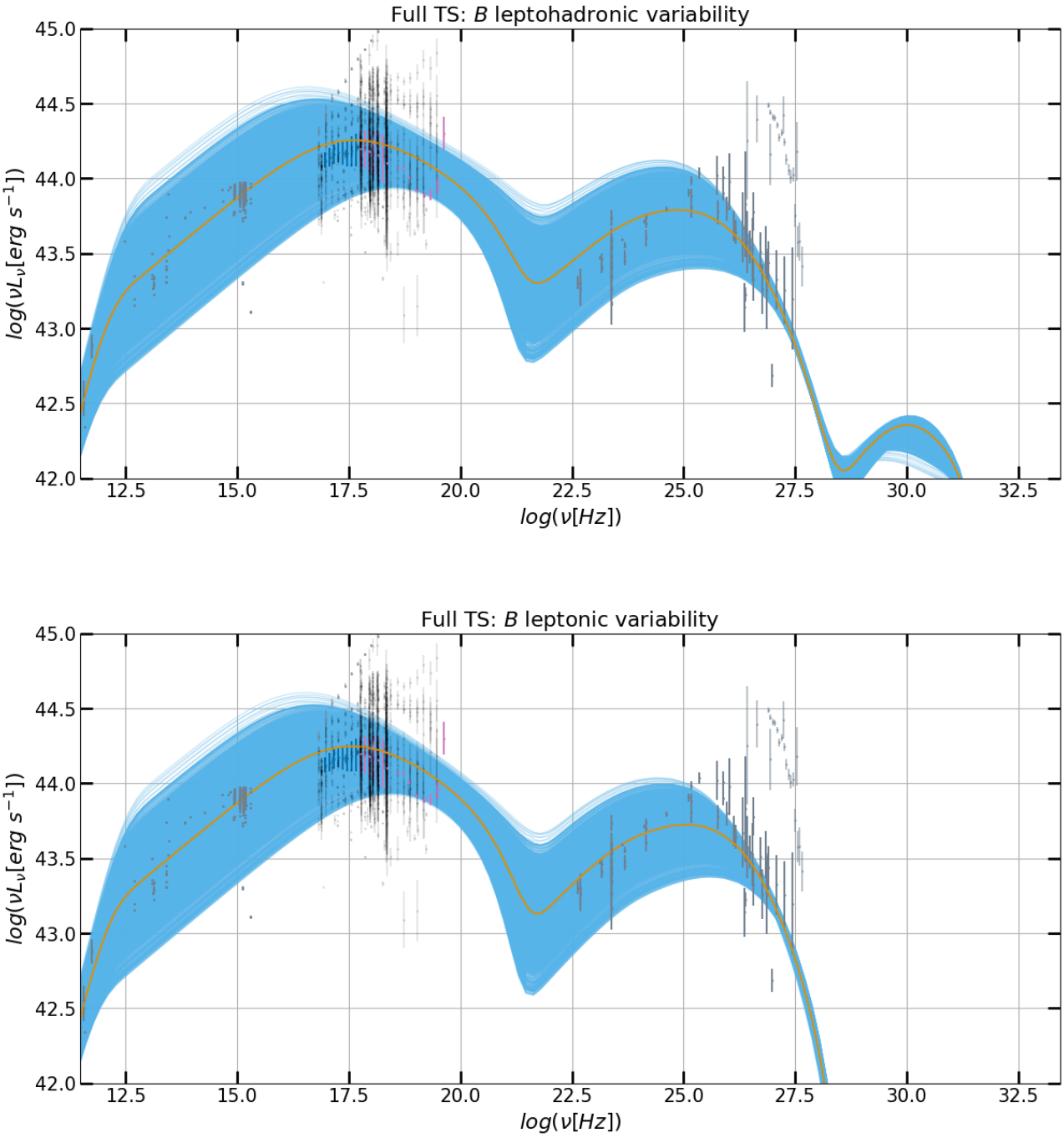

Figure 5.13: Time evolution SED plots for magnetic field strength variability with the full TS. Leptohadronic (upper panel) and leptonic (lower panel) cases are shown, both with the average state of Mrk 501 indicated in mustard color. An animated version of the leptohadronic time evolution is found Here.

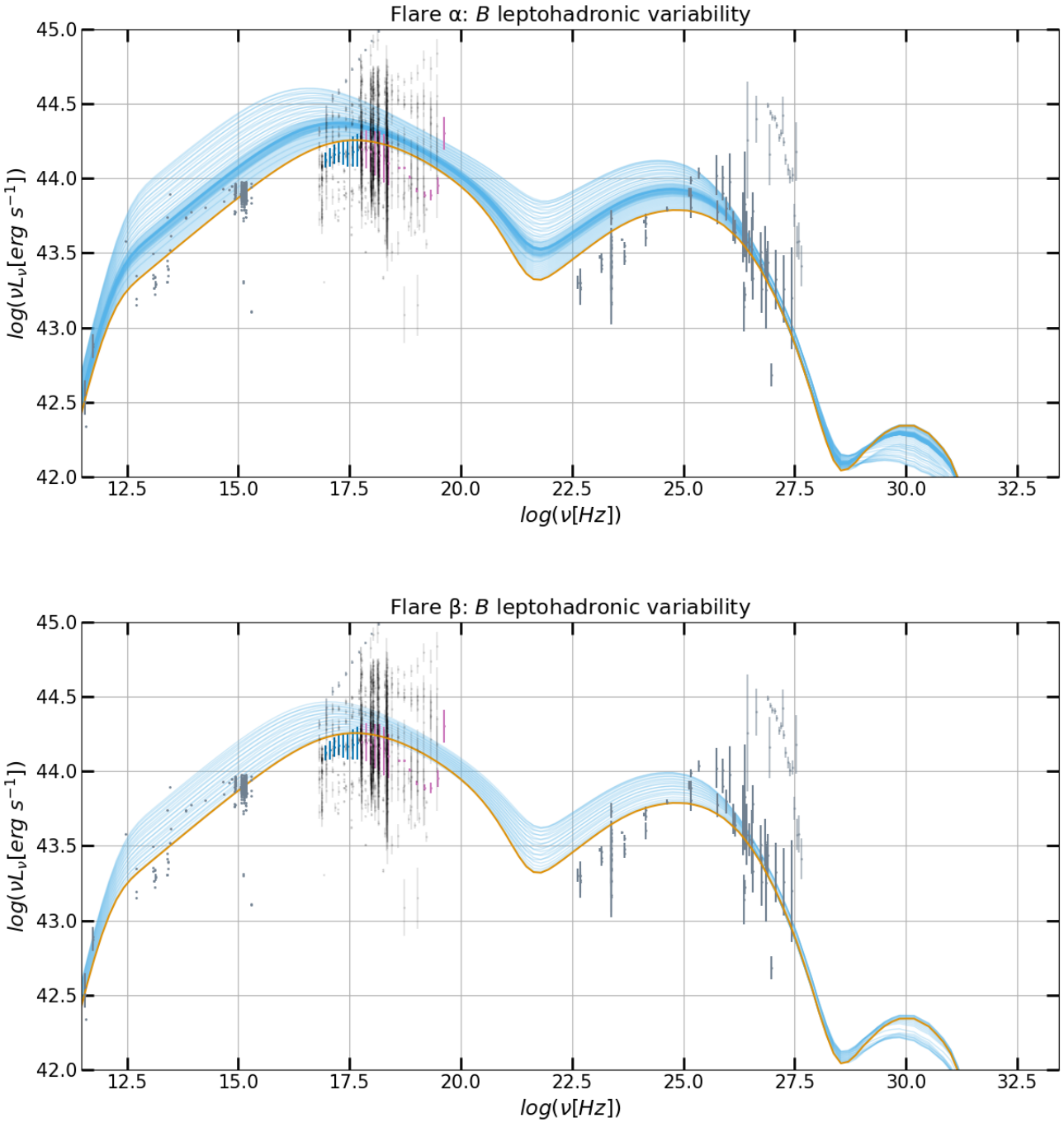

Figure 5.14: Time evolution SED plots for leptohadronic magnetic field strength variability. Flare α (upper panel) and Flare β (lower panel) are shown, both with the average state of Mrk 501 indicated in mustard color.

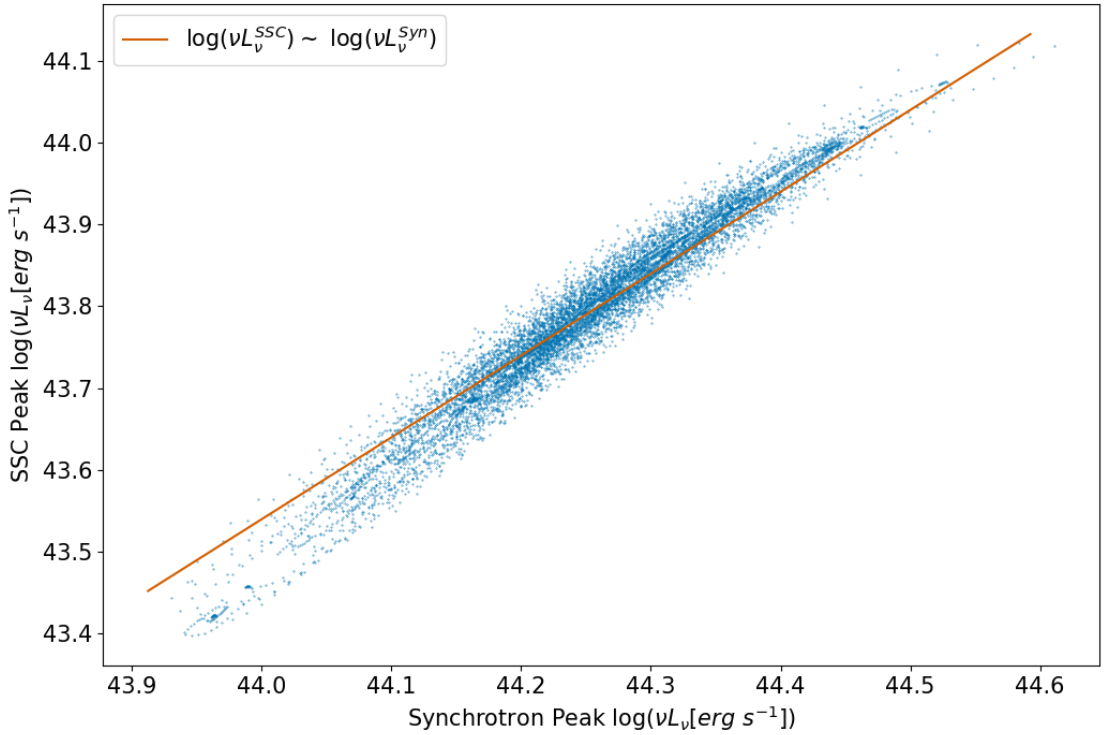

Figure 5.15: Flux-flux diagram of the synchrotron and SSC component peak in the leptohadronic time-variable magnetic field strength run. Noted with an orange line is the expected scaling of 1 between SSC and synchrotron peak luminosity.

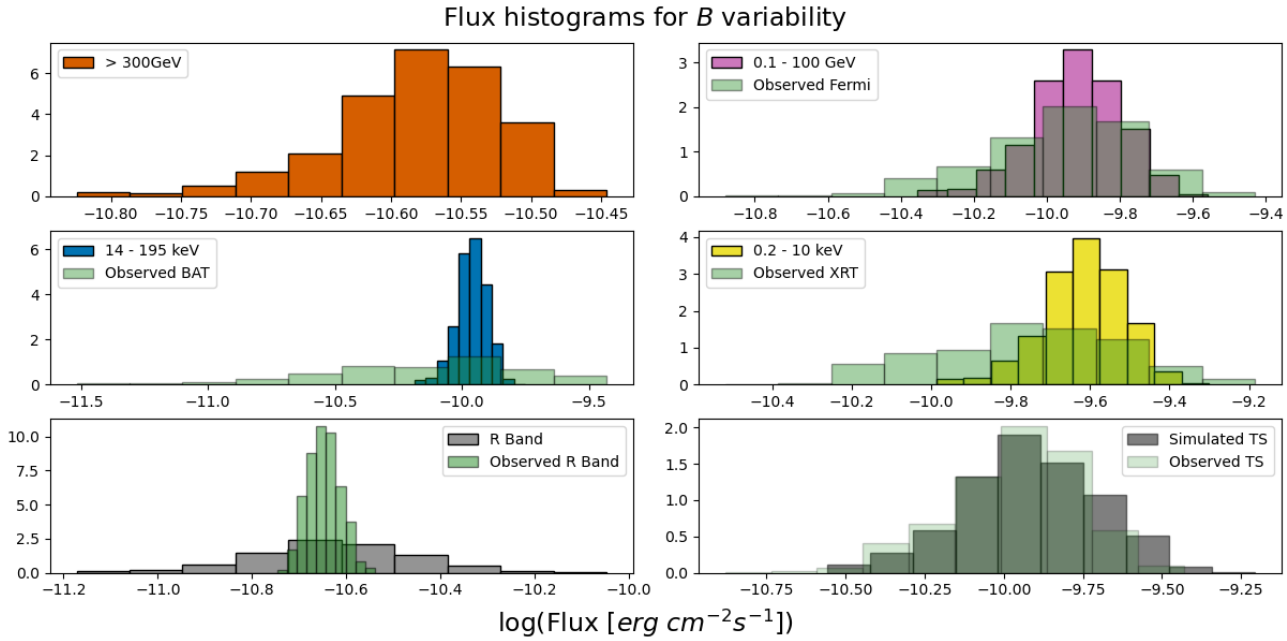

Figure 5.16: Same as Fig. 5.6 for the complete leptohadronic run for magnetic field variability.

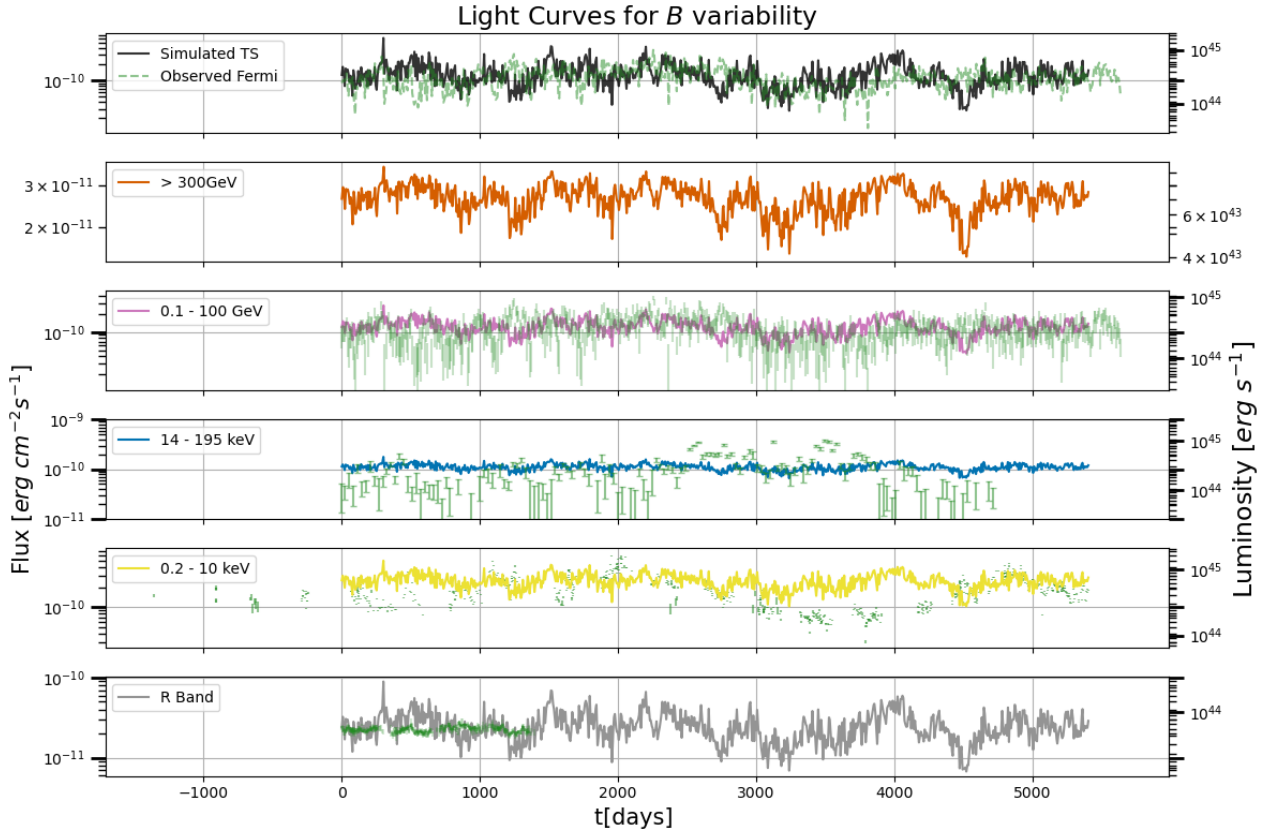

Figure 5.17: Same as Fig. 5.7 for the complete leptohadronic run for magnetic field variability.

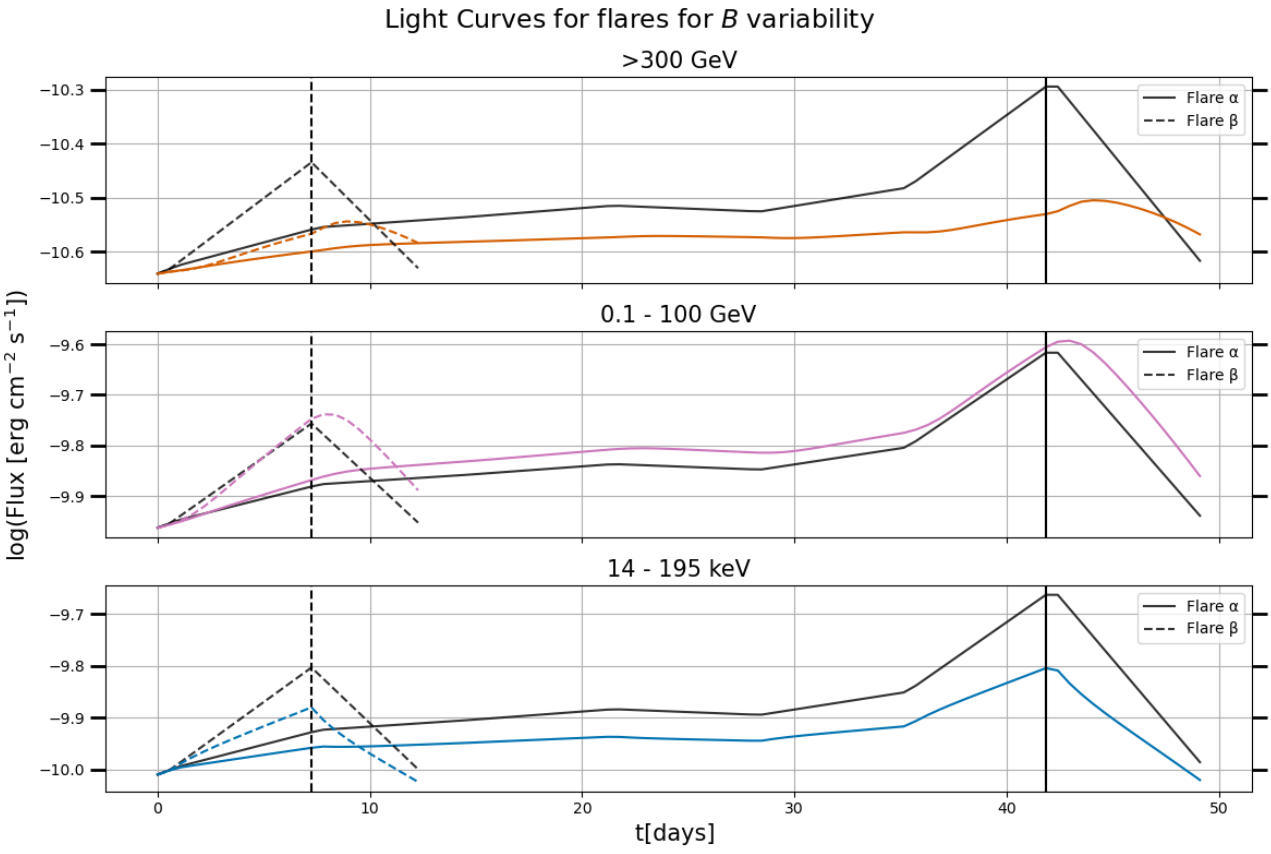

Figure 5.18: Same as Fig. 5.8 for flares α (solid line) and β (dashed line) for magnetic field variability.

between our model and observations than in the energy injection rate numerical run. In particular, we predict a smaller spread in the Fermi band. Similar to before, we underpredict the variability in the X-ray range and overpredict it in the R-band. For the flare analysis, we report the same conclusions for discrepancies on the horizontal axis. On the vertical axis, we do not recover the previously expected trends. This deviation is a result of the peak shifts of the synchrotron and SSC components. The proposed linear and quadratic scaling is only correct for the peak values of each component.

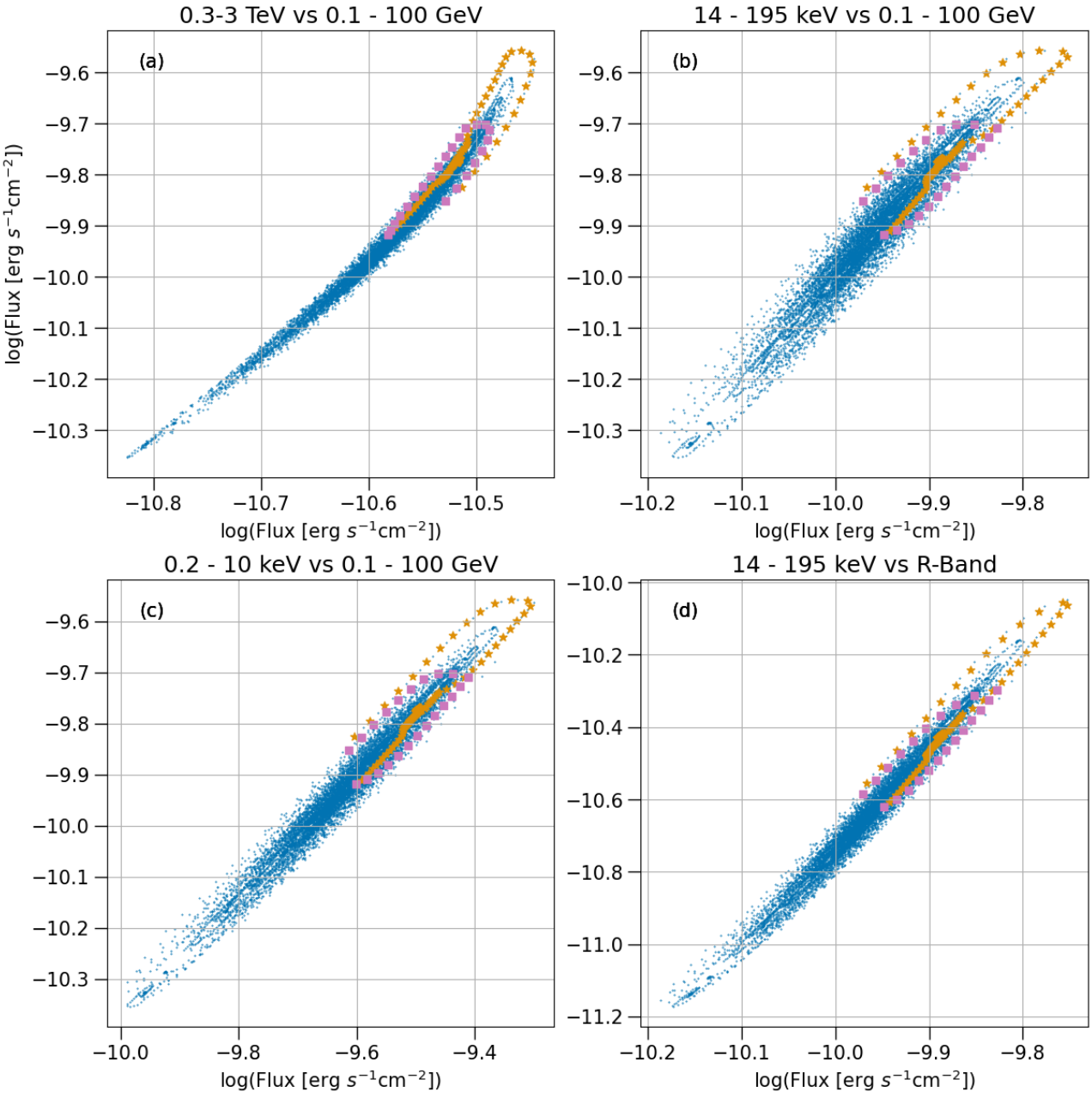

Figure 5.19: Flux-flux diagrams for leptohadronic magnetic field strength variability, comparing the flux variabilities between Fermi vs. VHE (a), Fermi vs. BAT (b), Fermi vs. XRT (c), BAT vs. R-Band (d). The cases for the complete TS (blue circles), as well as the results for flare α (yellow stars) and flare β (purple squares) are indicated.

In Fig. 5.19 we present the flux-flux diagrams for the leptohadronic magnetic field strength

Energy bands	Slope value
VHE vs. Fermi	2.075 ± 0.003
BAT vs Fermi	1.980 ± 0.005
XRT vs Fermi	1.182 ± 0.002
BAT vs. R	2.751 ± 0.005

Table 5.2: Linear fit slope values for the complete run of the leptohadronic magnetic field variability of Fig. 5.19.

variability. The conclusions and open questions of the previous section apply to this scenario. Furthermore, we attribute the slight curvature at the ends of the flux-flux diagrams (see for example upper right of panel a) to the previously discussed shift of the peak frequency of the synchrotron and SSC component

In Table 5.2 we present the slopes of the complete run via a linear fit. We recover the linear scaling between XRT and Fermi. The deviation from this value in the BAT vs. Fermi comparison is a result of the peak shift of the synchrotron and SSC component. The BAT vs R comparison yields the greatest deviation from the expected value. We attribute this discrepancy in parts to the aforementioned peak shift resulting in a smaller BAT variability. Simultaneously, we note how the quadratic scaling is correct only for the peak frequency in the delta approximation. For increasing values of B, the effects of electron cooling increase resulting in an increase of low energy electrons. Thus, in the optical, we expect a higher scaling on the magnetic field than previously predicted.

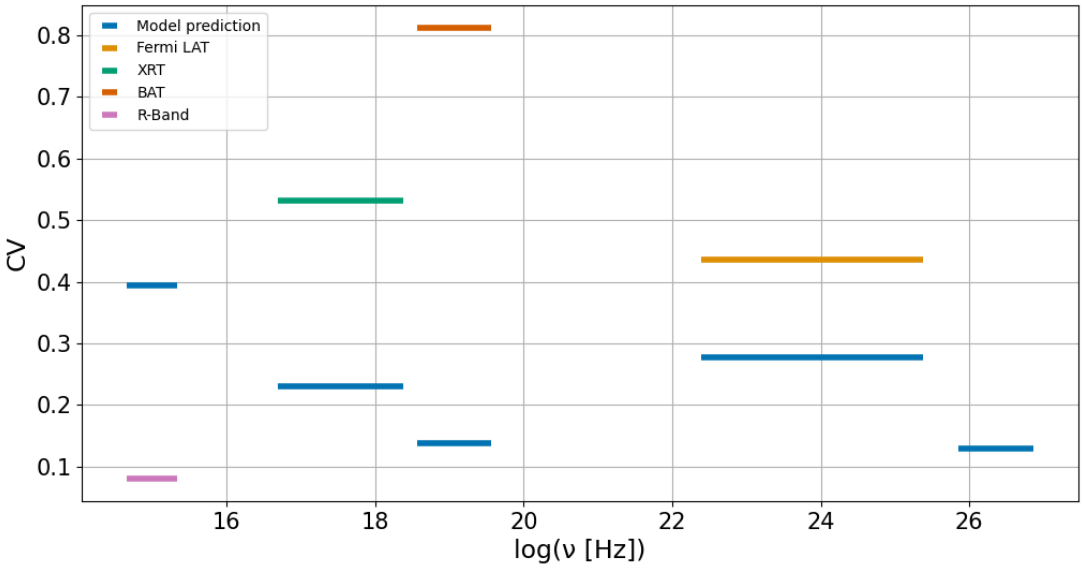

Figure 5.20: Coefficient of variation (CV) for the Fermi, BAT, XRT, and R-band energy ranges in the complete leptohadronic magnetic field variability run.

In Fig. 5.20 we present the CV plot for the time variability of the magnetic field strength. The lower energy regions exhibit greater variability, in both synchrotron and SSC components.

This is expected as the peaks shift to the upper left. Previous peak frequencies are past the current peak leading to lower flux values comparable to the maximum flux. Therefore, this displacement creates a greater CV value for the XRT and Fermi regions compared to the BAT and VHE regions. The R-band variability is a result of the quadratic scaling between synchrotron flux and magnetic field. Unaffected by the peak shifts, it exhibits the greatest amount of variability. Comparing the model predictions to the observational data we arrive at the same results as in our discussion of the histograms and LCs.

Lastly, the DCF diagrams for long and short timescales are presented in Fig. 5.22 and Fig. 5.12 respectively. The conclusions and open questions of the previous section apply to this scenario.

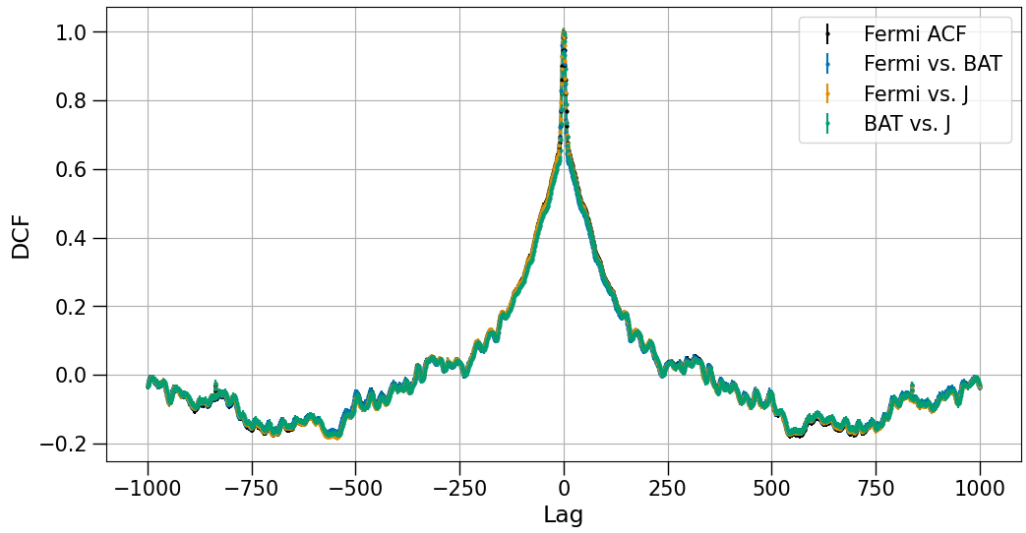

Figure 5.21: Discrete Correlation Function (DCF) for time lags up to 1000 days. Comparisons between Fermi vs. BAT, Fermi vs. R-band, and BAT vs. R-band. The Auto-Correlation function (ACF) for Fermi is noted.

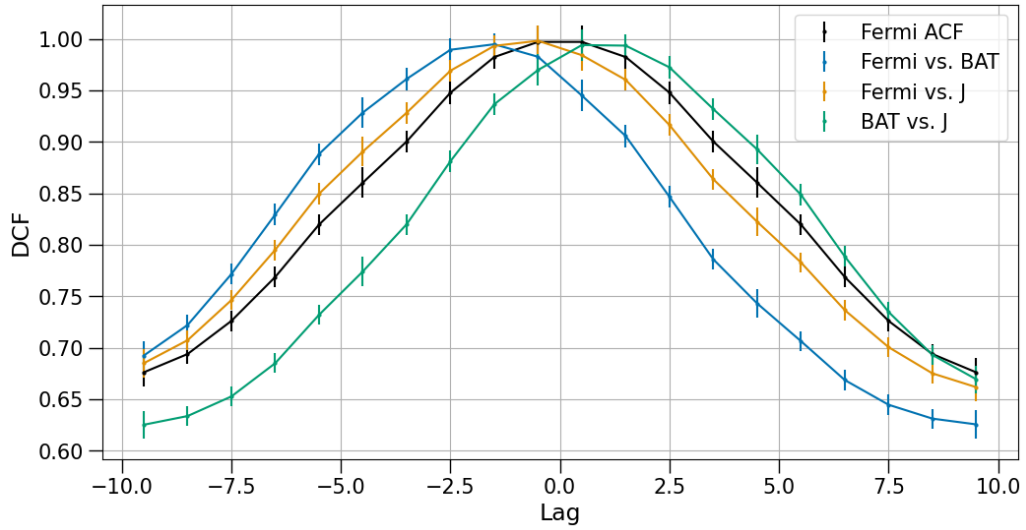

Figure 5.22: Same as Fig. 5.22 for time lags up to 10 days.

5.4 Variability in the power law slope of particle distribution

In this section, we will investigate changes in the power law index of the particle populations. In Section 5.4.1 we will provide physical motivations for power law slope changes in a leptonic population and investigate various scenarios. Moreover, we will briefly discuss simultaneous changes in the escape timescale. In Section 5.4.1 we will extend our analysis to a complete treatment for a leptonic and hadronic population and provide a qualitative example for long-term variability.

5.4.1 One species changes

We note the relation for the power law index in terms of the escape and acceleration timescale in the acceleration region [57]:

$$p_{el} = 1 + \frac{t_{acc}}{t_{esc}}.$$

Expressions for t_{acc} depend on the assumed acceleration mechanism. In a Fermi acceleration scenario, we predict a dependence on the magnetic field either implicitly or explicitly through the gyroradius ($r_g \propto B^{-1}$). In particular, for first and second-order Fermi acceleration we have the dependences of $t_{FI} \propto r_g$ and $t_{FII} \propto r_g/B^2$ respectively [58]. Therefore, assuming the ratio t_{acc}/t_{esc} to be a function of the above Fermi timescales we parameterize our problem as:

$$p_{el}(t) = 1 + p_{el,0}\left(\frac{B(t)}{B_0}\right)^{-m}, \tag{5.9}$$

where $B_0 = B(t_0)$ and $p_{el,0} = p_{el}(t_0)$ are the values of the magnetic field and the power law index at the start of the time variation, i.e. in the average state of the source. In this investigation, we leave m as a free parameter. Therefore, utilizing Eq. (5.8) (with the substitution $\langle B\rangle \to B_0$) and choosing a value of m we transform the TS of Fig. 5.1 into variability for the power law index for the electron particle distribution.

To illustrate the impact of m, we present Eq.(5.9) for the full TS for different values of it. In Fig. 5.23 - Fig. 5.27 we showcase the values of $m = 0.5, 1, 2, 3, 4$. In each figure, we highlight the minimum and average value of p_{el}, $p_{el} = 1$ and $p_{el} = 2.5$ respectively. As expected, increasing the value of m leads to increased spectral hardening ($p_{el} \to 1$) during periods of high activity and to monoenergetic distributions ($p_{el} \gg 1$) during periods of low activity.

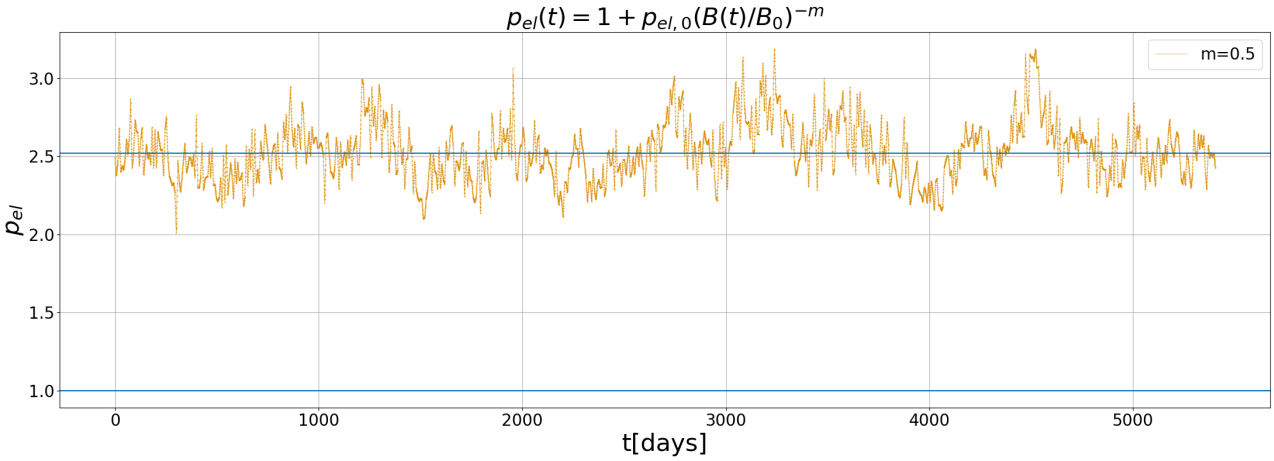

Figure 5.23: Complete TS for $p_{el}(t) = 1 + p_{el,0}\left(\frac{B(t)}{B_0}\right)^{-m}$ for $m = 0.5$. Indicated are the average and minimum values of p_{el}, $p_{el} = 1$ and $p_{el} = 2.5$ respectively.

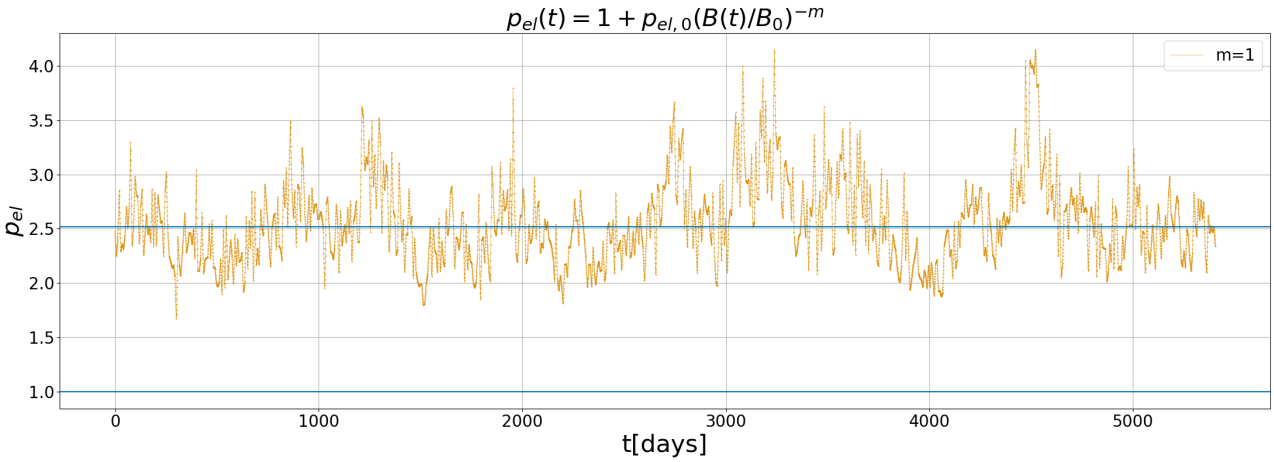

Figure 5.24: Same as Fig. 5.23 for $m = 1$.

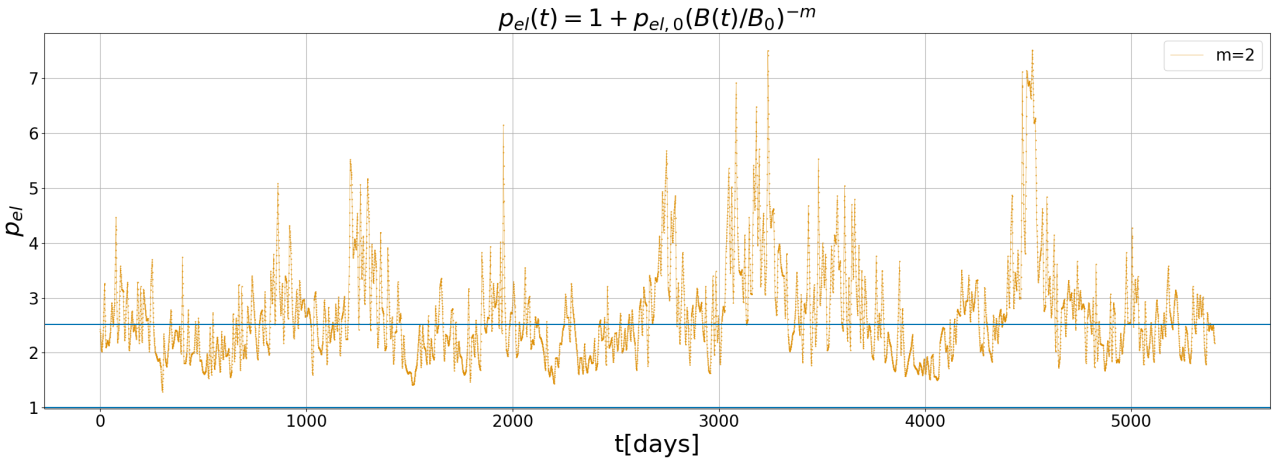

Figure 5.25: Same as Fig. 5.23 for $m = 2$.

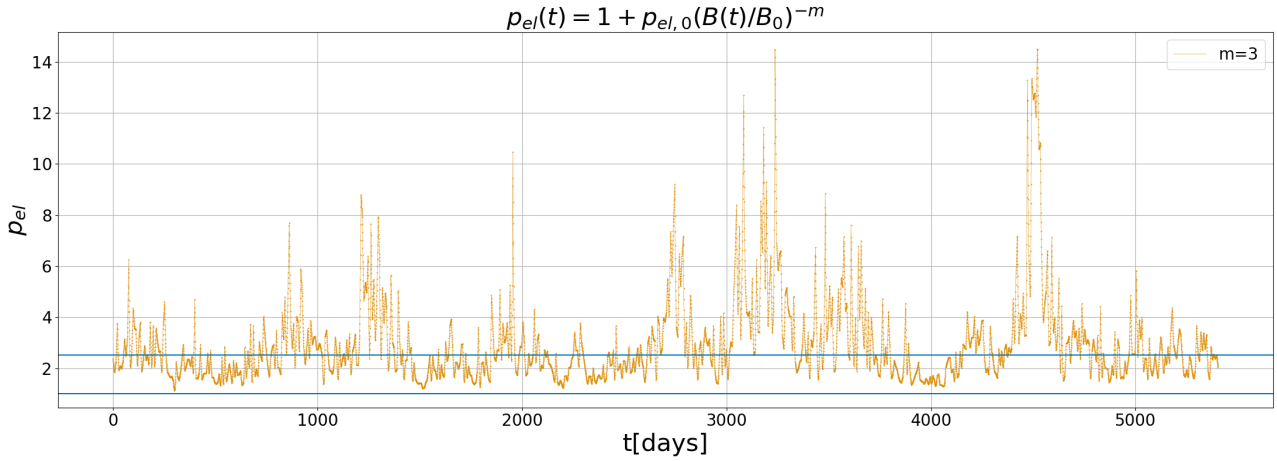

Figure 5.26: Same as Fig. 5.23 for $m = 3$.

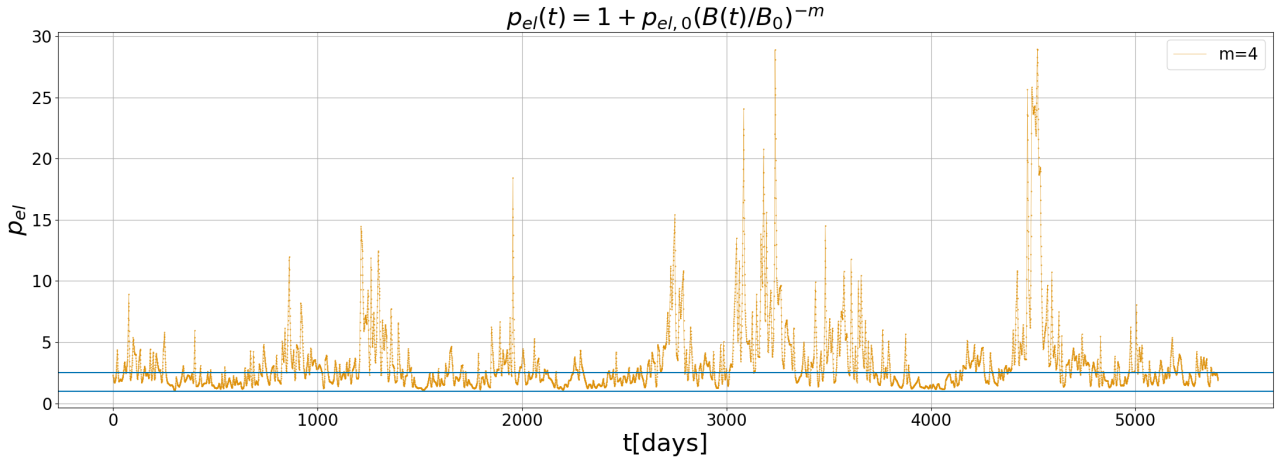

Figure 5.27: Same as Fig. 5.23 for $m = 4$.

We are not interested in investigations of monoenergetic distributions created by periods of low activity in cases similar to Fig. 5.27 and thus focus on flares α and β for the time variability of p_{el}. This is shown in Fig. 5.28 and Fig. 5.29. We remind the reader that flare β corresponds to variability in the Fermi band approximately equal to the maximum observed variability. In contrast, flare α exceeds the variability of the observed high activity periods. As previously discussed, p_{el} reaches lower values for greater values of m during flares. The average and minimum p_{el} values of 2.5 and 1 are again noted.

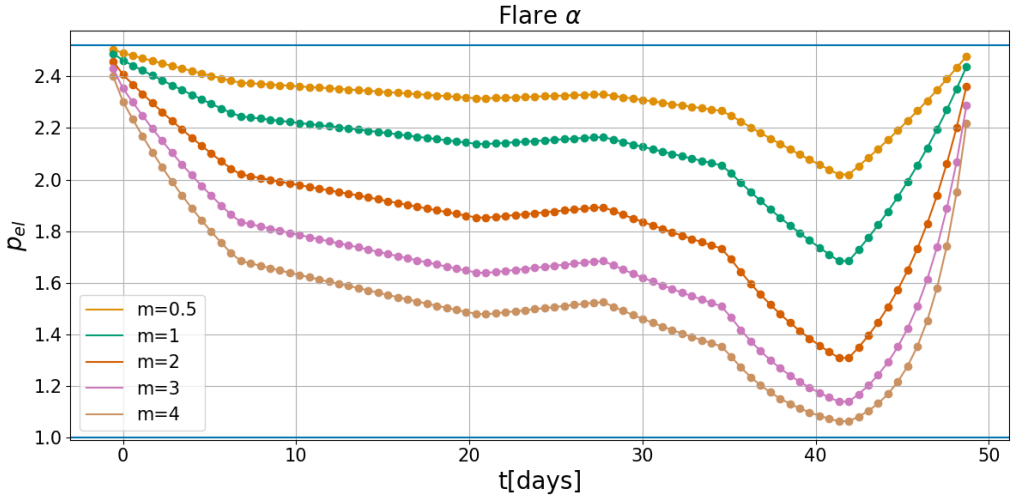

Figure 5.28: $p_{el}(t) = 1 + p_{el,0}\left(\frac{B(t)}{B_0}\right)^{-m}$ variability for flare α. Indicated are the average and minimum values of p_{el}, $p_{el} = 1$ and $p_{el} = 2.5$ respectively.

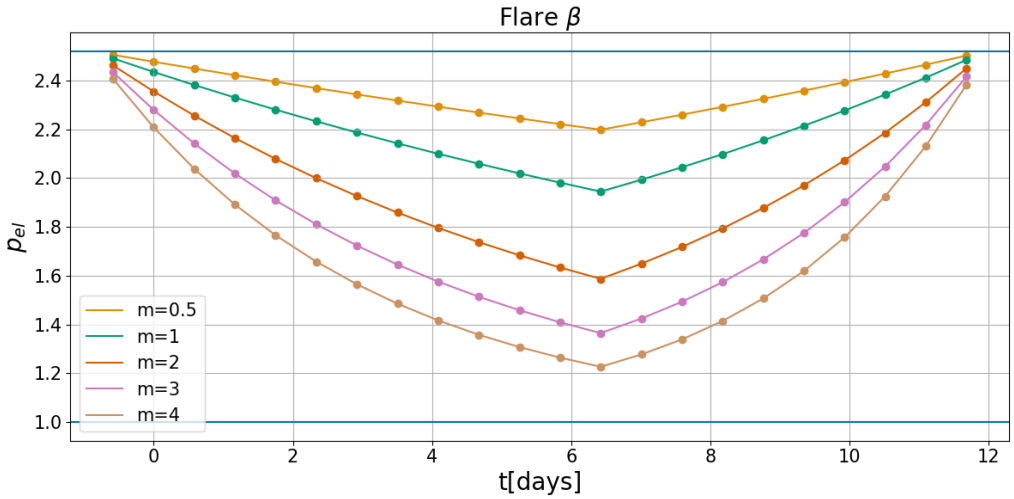

Figure 5.29: Same as Fig. 5.28 for flare β.

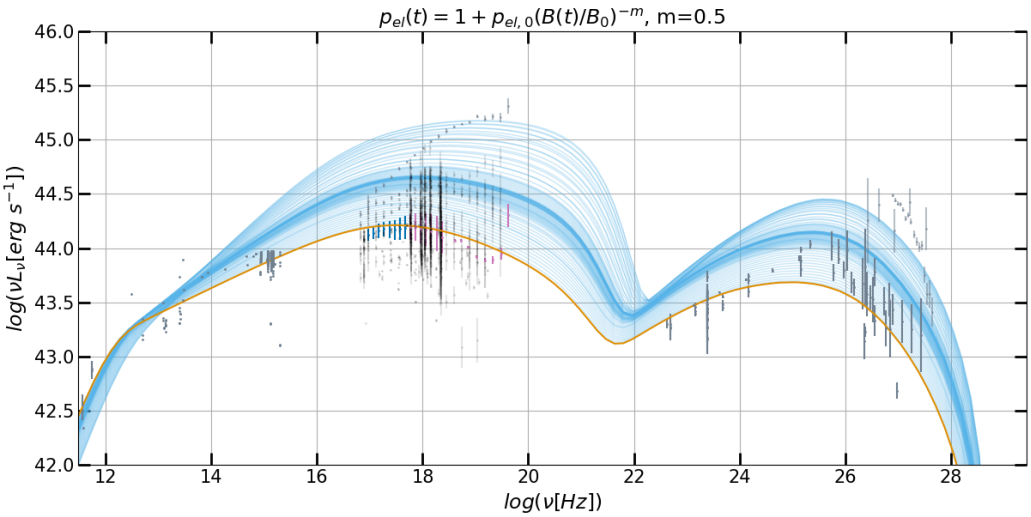

Figure 5.30: Flare α time evolution SED for mild power law index variation with $m = 0.5$.

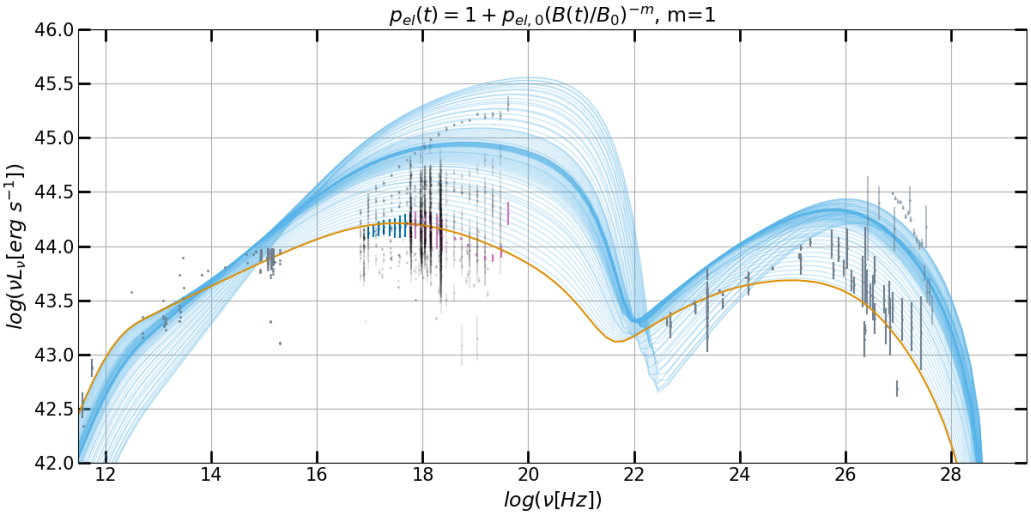

Figure 5.31: Flare α time evolution SED for moderate power law index variation with $m = 1$.

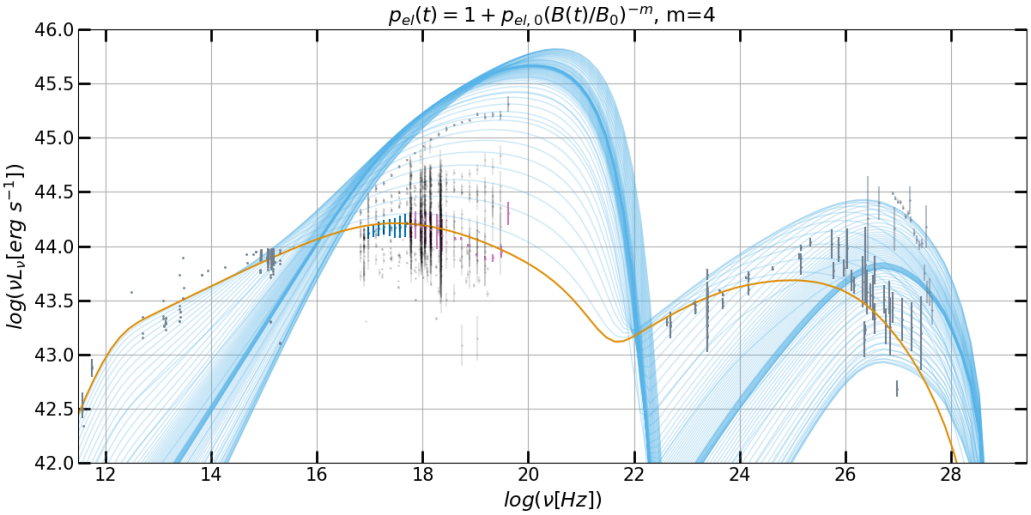

Figure 5.32: Flare α time evolution SED for extreme power law index variation with $m = 4$.

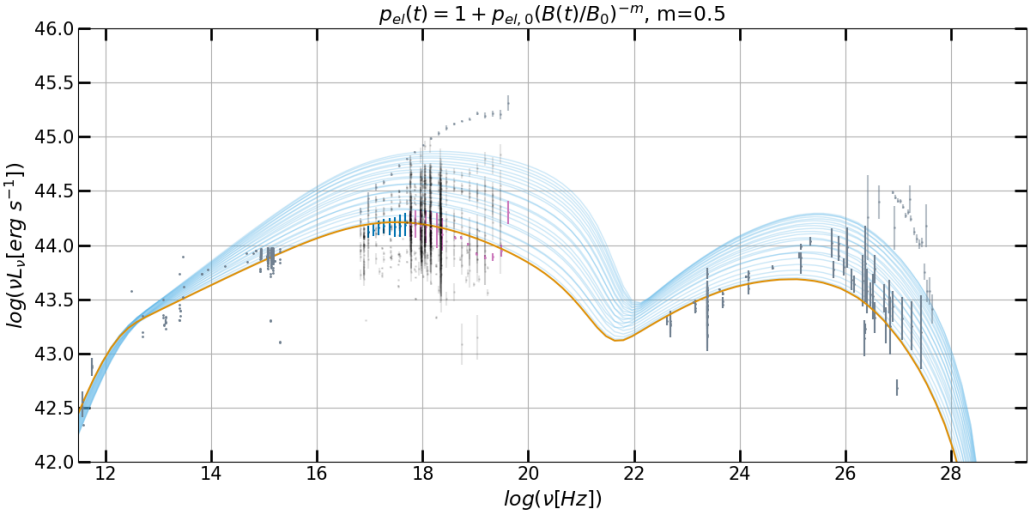

Figure 5.33: Flare β time evolution SED for mild power law index variation with $m = 0.5$.

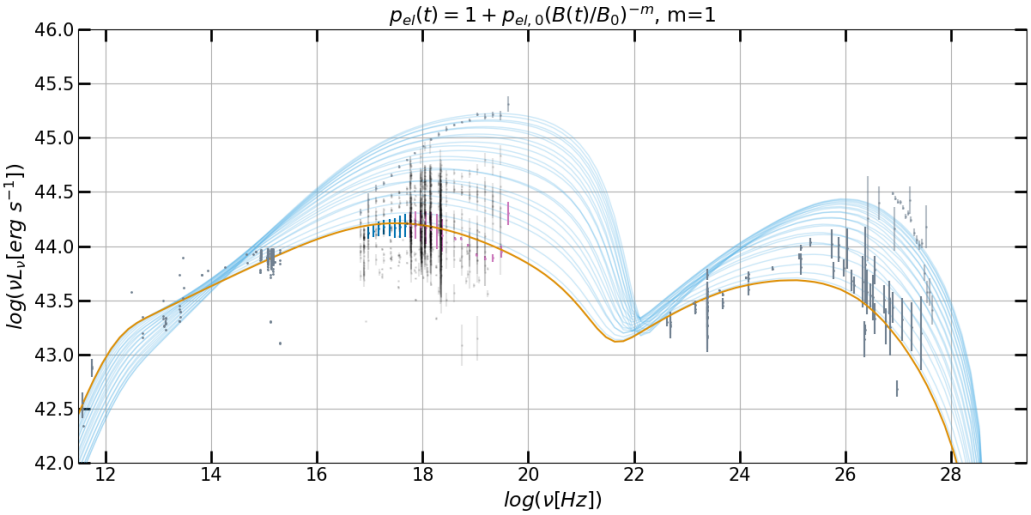

Figure 5.34: Flare β time evolution SED for moderate power law index variation with $m = 1$.

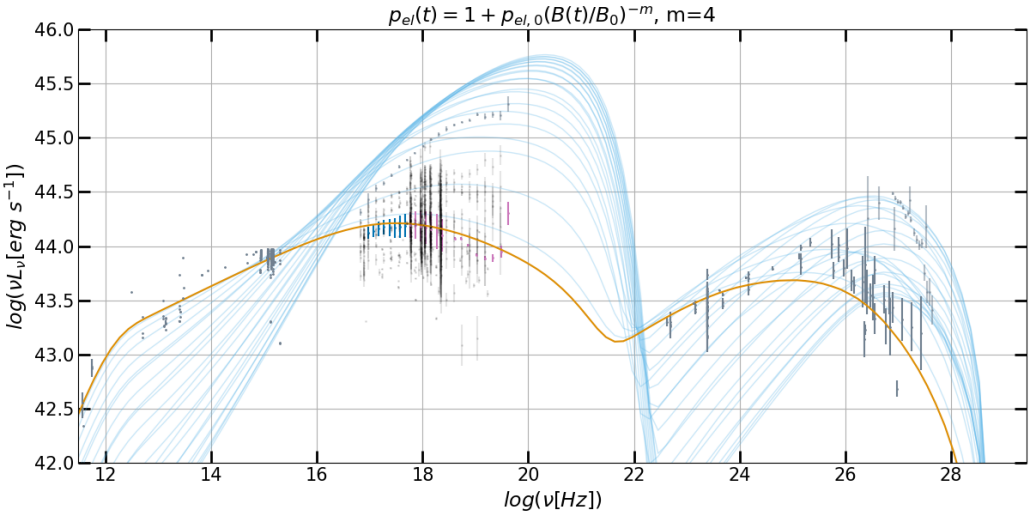

Figure 5.35: Flare β time evolution SED for extreme power law index variation with $m = 4$.

In Fig. 5.30 - Fig. 5.32 and in Fig. 5.33 - Fig. 5.35 we provide the time evolution SEDs for $m = 0.5, 1, 4$ to investigate mild, moderate, and extreme leptonic spectral hardening during flare α and β respectively. Increasing m yields a reduction of the low-energy and (V)HE emission components. The former is expected since a decrease of p results in sharply peaked synchrotron SEDs ($f_{syn} \sim \nu F_\nu \sim \nu^{-\alpha+1}$, $\alpha = (p-1)/2$). A reduction of the SSC flux in the Fermi range causes the latter. To compare the flux variability in those events with the observations we present in Fig. 5.36 the flux histograms of the mild variability ($m = 0.5$) for both flares. We caution the reader to bear in mind that density histograms of short-term events do not capture the true distributions of a source. As such, in the above figures we are interested in the ranges the histograms occupy rather than their densities. In both cases we exceed the observed variability in the X-ray and optical range. Furthermore, we do not recover the expected hardening present in the X-ray flares of 1997. Furthermore, we remind the reader how these X-ray flares are not included in the observational BAT or XRT histograms as they preceded both instruments. Therefore, this caveat needs to be taken into consideration when

comparing model to observational variability.

Therefore, we conclude that in a leptonic Synchrotron+SSC scenario reducing the power law index during flares can lead to spectral hardening and flux increase in the X-ray range but a flux reduction everywhere else. Even small variations in p_{el} create greater than observed flux variabilities. Simultaneously no significant spectral hardening is present in those cases. Therefore, leptonic variations in the power law index through magnetic field variability alone cannot describe the observational features of Mrk 501.

In what follows we conduct a brief investigation of simultaneous changes in the power law index p_{el} and escape timescale τ_{esc}. Motivated by the extreme case of flare α with $m = 4$ (Fig. 5.32) we explore possible scenarios that could lead to spectral hardening in the X-rays without the loss of low- and high-energy emission. In particular, we contrast and compare the following choices in terms of a constant escape timescale of $\tau_{esc,0} = R/c$:

- $\tau_{esc}(B) = \tau_{esc,0} \left(B(t)/B_0\right)^{-m+m_B}$ where m_B is a free parameter. In our testing, we used $m_B = 1.5$.

- $\tau_{esc}(\gamma_{el}) = \tau_{esc,0} \left(\gamma_{el}/\gamma_N\right)^{-m_\gamma}$, where m_γ is a free parameter and γ_N a normalization constant. In our testing, we used $m_\gamma = 1$ for the slope. For a slope of $m_\gamma = 1$, electrons below γ_N remain increasingly unaffected by escape from the source. In other words, for $\gamma \ll \gamma_N$ we do not expect escape from the source. For our testing, we used a value close to γ_c of the average state description, $\gamma_N \sim 10^5$.

- $\tau_{esc}(B, \gamma_{el}) = \tau_{esc,0} \left(B(t)/B_0\right)^{-m+m_B} \left(\gamma_{el}/(\gamma_N)\right)^{-m_\gamma}$. A combination of the two previous scenarios.

In Fig. 5.37 we present the time evolution SEDs for the three cases of τ_{esc}. In no case do we observe an improvement compared to previous results. In particular, a dependence on B reduces the SSC component even further. This is expected as the electron number at each energy shifts downwards. An energy dependence creates a pivot point around γ_N. Increasing γ_N towards γ_{max} would lead to an increasing region of "non-escape" in the low energy part. On the other hand, the opposite would lead to the rapid escape of the majority of electrons. We report the presence of a "bump" at around $\nu = 10^{12.5}$ Hz to be a direct result of the accumulation of non-escaping low energy electrons emitting synchrotron.

Varying the magnetic field B, the power law index p_{el}, and the escape timescale τ_{esc} results in a highly non-linear analysis with a complexity that exceeds the scope of this thesis. Moreover, we did not find any supporting physical evidence explaining deviations from a constant escape time of $\tau_{esc} = R/c$ inside blazar jet radiation zones. Therefore, a complete sampling of the parameter space $(m, m_\gamma, m_B, \gamma_N)$ as well as physical arguments supporting those claims will be left as open questions for future studies.

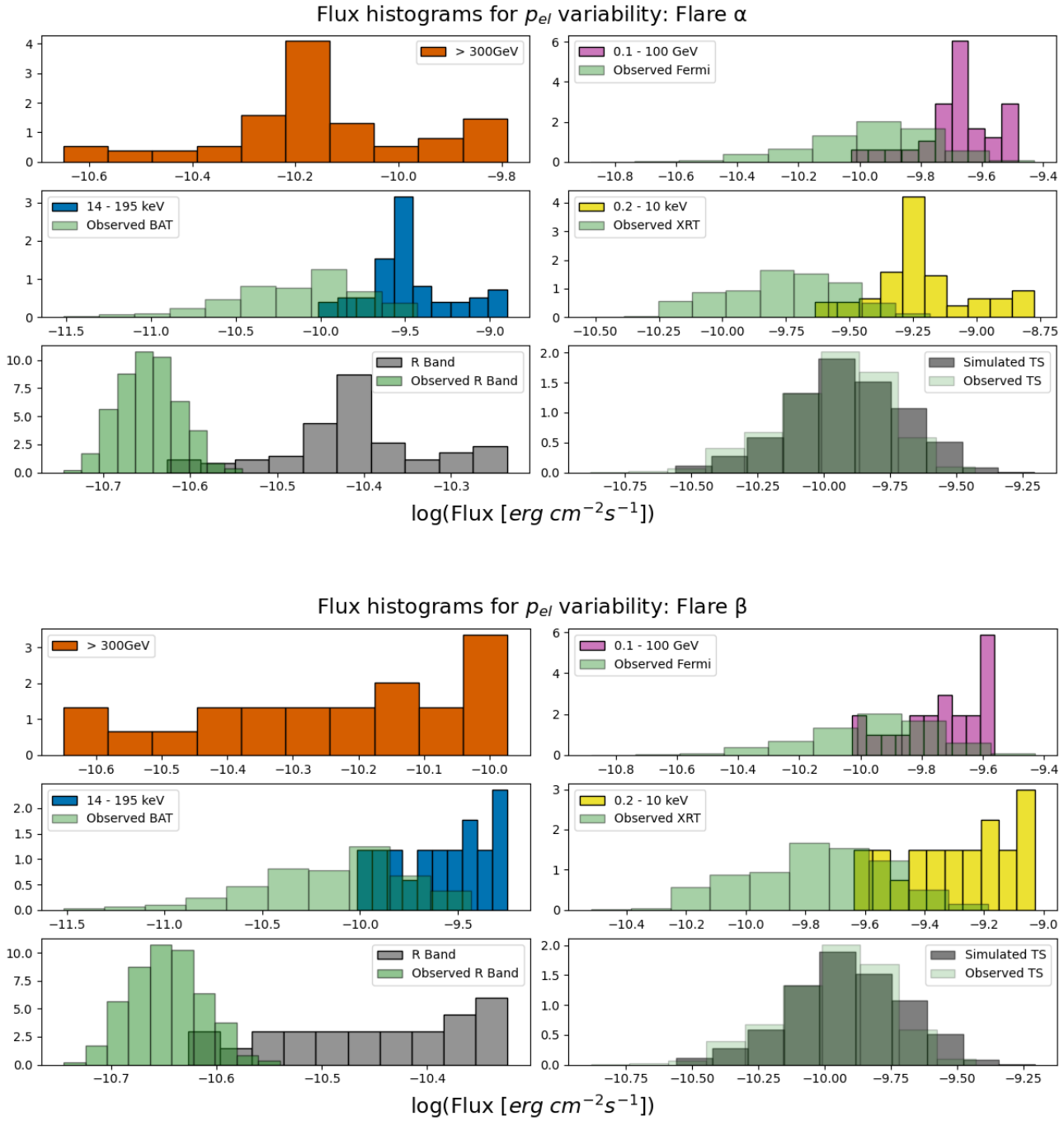

Figure 5.36: Flux histograms for p_{el} variability with $m = 0.5$. The upper panel shows the results for flare α, while the lower panel shows the results for flare β. An analysis of the energy bands is found in Fig. 5.6 and the text discussing it.

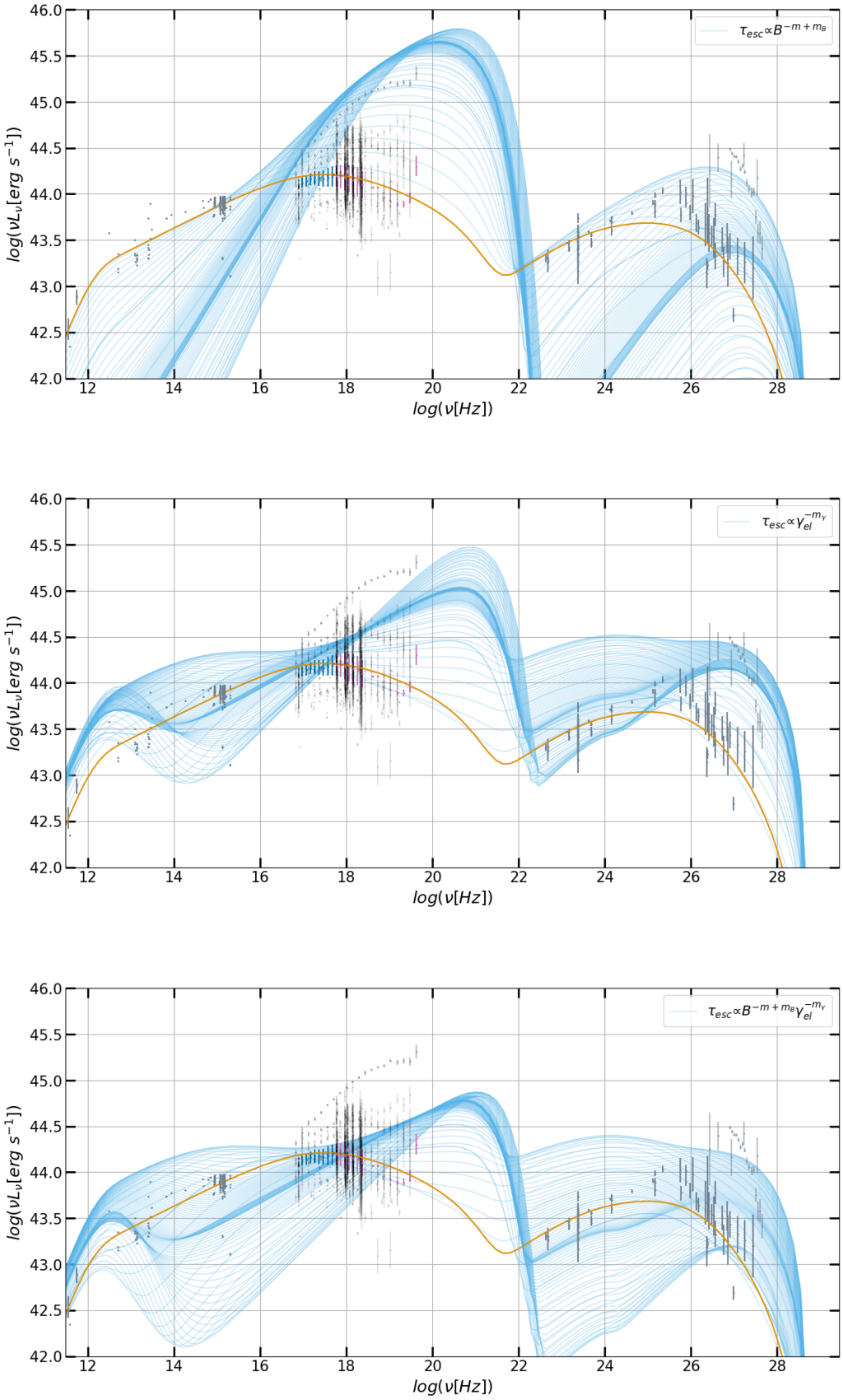

Figure 5.37: Time evolution SED plots for Flare α with $m = 4$ and different τ_{esc} dependencies. Upper panel: $\tau_{esc}(B) = \tau_{esc,0} \left(B(t)/B_0\right)^{-m+m_B}$. Middle panel: $\tau_{esc}(\gamma_{el}) = \tau_{esc,0} \left(\gamma_{el}/\gamma_N\right)^{-m_\gamma}$. Lower panel: $\tau_{esc}(B, \gamma_{el}) = \tau_{esc,0} \left(B(t)/B_0\right)^{-m+m_B} \left(\gamma_{el}/(\gamma_N)\right)^{-m_\gamma}$.

5.4.2 Two-species changes

We remind the reader of our previous estimates (Section 5.2) of the emission frequencies of the injected secondary particles. Assuming our average state values of $B = 0.038$G and $\delta = 20.41$, for photomeson interactions we have from Eq.(2.31):

$$\gamma^{th}_{p,p\gamma} \approx 3.5 \cdot 10^4 (1+z)^{-1} \delta \nu_{18}^{-1} \approx 10^{5.85}.$$

And from Eq.(2.32), Eq.(2.30):

$$\gamma^{th}_{e,p\gamma} \approx K_{p\gamma} \gamma^{th}_p m_p/(4m_e) \approx 10^{7.81} \Rightarrow \nu^{syn}_{e,p\gamma} \approx 3 \cdot 10^6 \delta B \left(\gamma^{th}_{e,p\gamma}\right)^2 \approx 10^{22}\text{Hz}.$$

Similarly, for Bethe-Heitler pair-production we have from Eq.(2.33):

$$\gamma^{th}_{p,pe} \approx 1.2 \cdot 10^2 (1+z)^{-1} \delta \nu_{18}^{-1} \approx 10^{3.38}.$$

And since $\gamma^{th}_{p,pe} \approx \gamma^{th}_{e,pe}$, from Eq.(2.30) it follows:

$$\nu^{syn}_{e,pe} \approx 3 \cdot 10^6 \delta B \gamma^2 \approx 10^{13.12}\text{Hz}.$$

Thus, a harder proton power law increases the available protons for photomeson interactions resulting in a synchrotron emission from secondaries at high energies. While the BH threshold is at low energies, an increase of energetic protons results in a secondary population emitting in the X-ray region (e.g. using the previous equations as a "back-of-the-envelope" approximation: $\gamma_{p,pe} \approx 10^6 \rightarrow \nu^{syn}_{e,pe} \approx 10^{18}$Hz). Therefore, variations in p_{pr} in addition to p_{el} will generally result in a flux increase in the X-ray and high-energy region if the energy injection rate of the proton population is high enough.

In the context of our previous discussion, the above implies possible scenarios of spectral steepening (large values of m) without the large decrease in SSC flux. Adopting the same trend as for p_{el}:

$$p_{pr}(t) = 1 + p_{pr,0} \left(\frac{B(t)}{B_0}\right)^{-m}, \tag{5.10}$$

we present in Fig. 5.38 the time evolution SEDs for joint leptohadronic power law index variations for flare β with $m = 0.5$ and $m = 4$ respectively. Comparing the upper panel of Fig. 5.38 to Fig. 5.33 we see the clear impact of photomeson interactions in the high-energy region. Simultaneously, no dominant BH component is present and the X-ray flux remains unchanged. Contrasting the lower panel of Fig. 5.38 to Fig. 5.35 we now have a dominant hadronic emission component in the (V)HE region, remedying the problems of the low flux values of the previous section. Now, however, the predicted gamma-ray flux vastly exceeds the observations.

The prominent pion bump peaking at $\sim 10^{30}$ Hz of the upper panel of Fig. 5.38 and the flux variability in the low energy component lead us to briefly investigate the optical depth for $\gamma\gamma$, its impact on the predicted VHE flux, and its variation throughout a flare. To conduct this numerical run we use the most extreme of the discussed cases, $m = 4$ and flare α. To calculate $\tau_{\gamma\gamma}$ we use the delta approximation of Eq.(2.28) and the expression for the complete cross-section of [10]:

$$\tau_{\gamma\gamma}(\epsilon'_1) = \frac{R' \pi r_e^2}{\epsilon'^2_1} \int_{1/\epsilon'_1}^{\infty} d\epsilon' n'_{iso}(\epsilon') \bar{\varphi}(s_0) \epsilon'^{-2} \; ; \; \bar{\varphi}(s_0) = 2 \int_1^{s_0} ds \frac{s \sigma_{\gamma\gamma}(s)}{\pi r_e^2}, \tag{5.11}$$

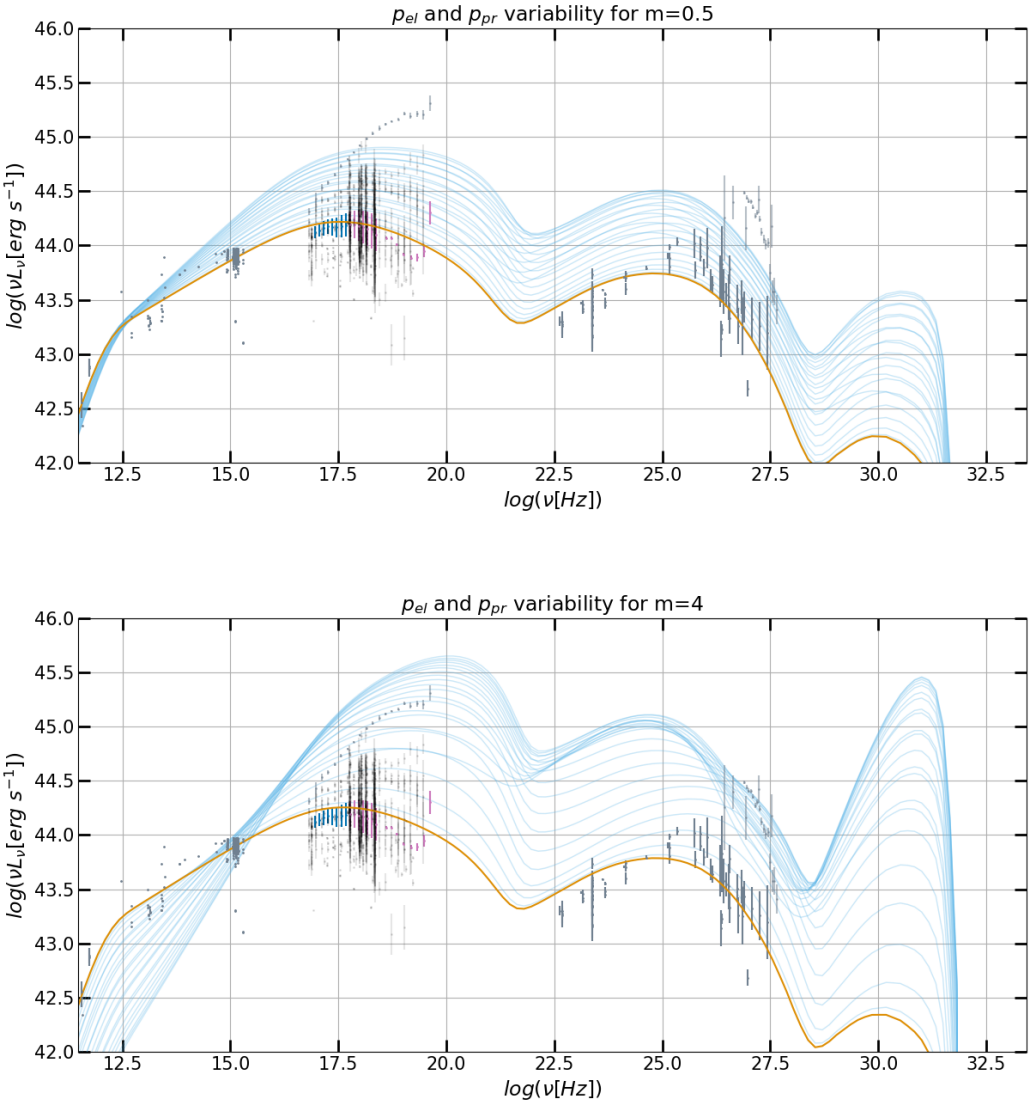

Figure 5.38: Time evolution SED plots of flare β for two-species power-law index variations. The upper panel shows mild variation with $m = 0.5$, while the lower panel shows extreme variation with $m = 4$.

where

$$\sigma_{\gamma\gamma}(s) = \frac{1}{2}\pi r_e^2 \left(1-\beta_{\rm cm}^2\right)\left[\left(3-\beta_{\rm cm}^4\right)\ln\left(\frac{1+\beta_{\rm cm}}{1-\beta_{\rm cm}}\right) - 2\beta_{\rm cm}\left(2-\beta_{\rm cm}^2\right)\right], \tag{5.12}$$

with $\beta_{\rm cm} = (1-\gamma_{\rm cm}^{-2})^{1/2} = \sqrt{1-s^{-1}}$ and $s = \gamma_{\rm cm}^2$. We remind the reader that primed variables indicate parameters in the rest frame of the emission region. Furthermore, R is the radius of the source, r_e is the classical electron radius, and $\gamma_{\rm cm}$ is the Lorentz factor of the 2 photons in their center of momentum frame. In Fig. 5.39 we present the time evolution SEDs for power law index variations with $m = 4$ for flare α with and without $\gamma\gamma$ absorption (top and bottom panels respectively). With a dashed vertical line, we indicate the investigated frequency of $\nu_1 = 10^{31}$Hz or $\varepsilon_1 = 4.14\cdot 10^{16}$eV. With horizontal lines, we indicate at the first time step of the variation the value of the pion bump peak without $\gamma\gamma$ absorption ($\nu L_\nu = 10^{43.15}$ erg s^{-1}) and the respective absorbed luminosity value ($\nu L_\nu = 10^{42.2}$ erg s^{-1}). As seen in the lower panel of Fig. 5.39, we recover the expected value of $(\nu_1 L_\nu)_{absorbed} = \left(\frac{1-e^{-\tau_{\gamma\gamma}}}{\tau_{\gamma\gamma}}\right)\cdot(\nu_1 L_\nu)_{unabsorbed}$ [14]. In Fig. 5.40 we present the time evolution of $\tau_{\gamma\gamma}$ and of the absorbed representative luminosity of $\nu L_\nu = 10^{43.15}$ erg s^{-1} throughout flare α using the analytical expression. From this numerical run, we conclude that we have a significant attenuation due to $\gamma\gamma$ interactions between the pion bump and the low-energy region. Varying the power law index can create spectral hardening leading to a decrease of $\gamma\gamma$ absorption targets increasing the pion bump emission.

Motivated by the results shown in the lower panel of Fig. 5.38 we will finish this chapter by investigating a moderate power law variability with a reduced proton energy injection rate in a long-term scenario. We suggest that such a variation could lead to spectral hardening comparable to the one observed, while a reduced value of L_p^{inj} would ensure a "dampened" high energy component. We try $m = 2$ and $L_p^{inj} = 10^{3.62}L_e^{inj}$, i.e. an injection luminosity 2 orders of magnitude lower than in our average state description. We remind the reader how the average state value of $L_p^{inj} = 10^{5.62}L_e^{inj}$ has been derived as an upper value of our source. As there is no hadronic component in the observational SED of Mrk 501, all values below $L_p^{inj} = 10^{5.62}L_e^{inj}$ should be treated as equally acceptable. This treatment is supported by the available scientific literature [50]. To ensure we don't have monoenergetic distributions, we bound the power law index variation with an (arbitrary) upper value of $p \leq 2.6$. In Fig. 5.41 and Fig. 5.42 we present the time evolution SEDs for the complete run, as well as the two flares.

In Fig. 5.43 - Fig. 5.45 we present the result for the flux histograms and the LCs for the full leptohadronic run as well as the LCs for the flares α/β. We exceed the observed flux variability at all energies except the Fermi band. Furthermore, we report a convoluted LC picture for the flaring states. This is expected as during periods of high activity (as defined by our injected TS) the targets for SSC upscattering are reduced leading to a decrease in the flux contribution of the SSC component. Simultaneously, we see the expected extreme flux increase in the X-ray band as a result of the spectral hardening and the resulting increased synchrotron emission. These two results can also be contrasted by comparing the upper to the lower panel of Fig. 5.45. We see how the VHE flux initially "mimics" the behavior of the X-ray flux corresponding to the initial increase of high-energy electrons. The sudden decrease around the peak of the injected TS corresponds to the spectral hardening in the low-energy synchrotron region and the resulting decrease of available SSC targets.

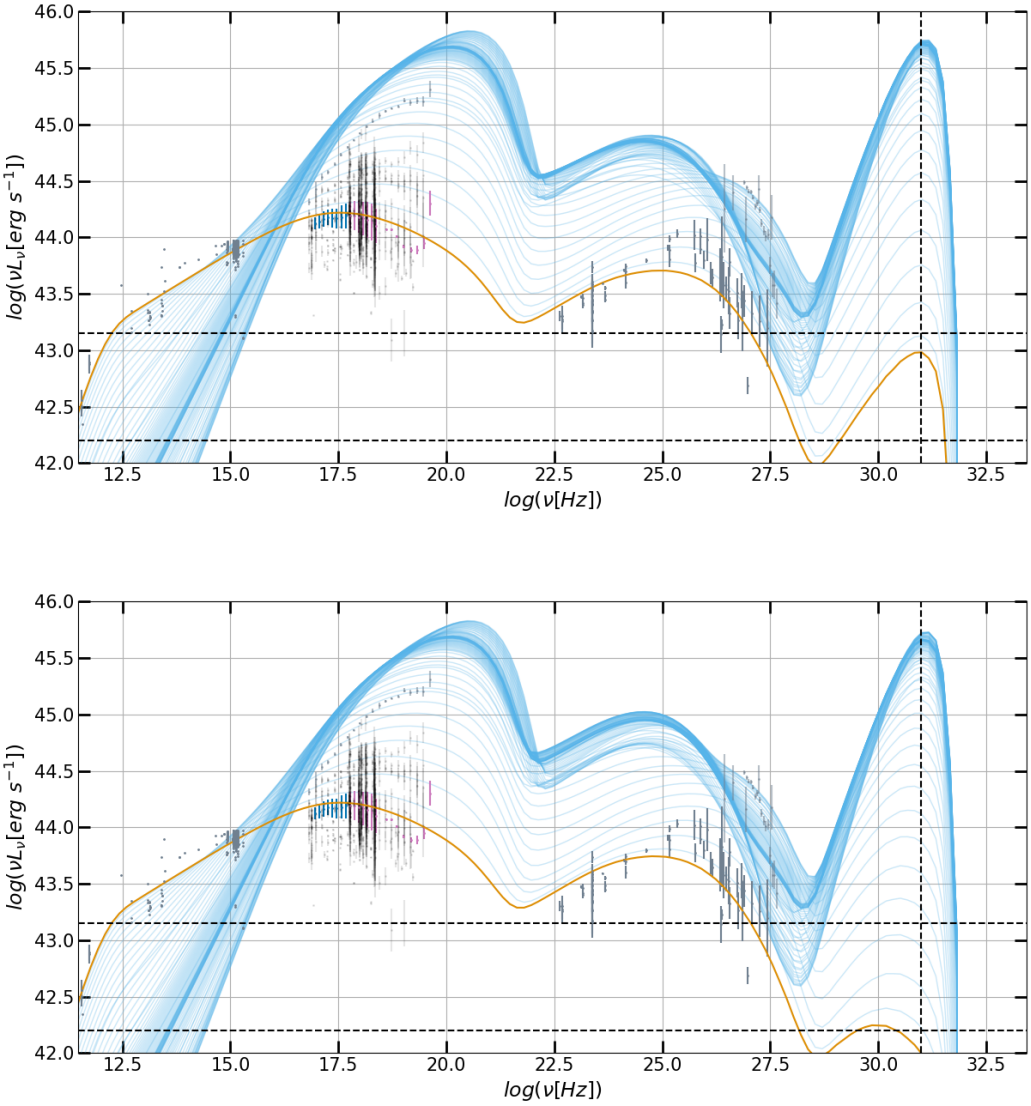

Figure 5.39: Time evolution SED for power law index variations for flare α with $m = 4$ and with $\gamma\gamma$ absorption (upper panel) and without (lower panel). With a dashed vertical line we indicate the investigated frequency of $\nu_1 = 10^{31}$Hz or $\varepsilon_1 = 4.14 \cdot 10^{16}$eV. With vertical lines we indicate at the first time step of the variation the value of the pion bump peak without $\gamma\gamma$ absorption ($\nu L_\nu = 10^{43.15}$ erg s^{-1}) and the respective absorbed luminosity value ($\nu L_\nu = 10^{42.2}$ erg s^{-1}).

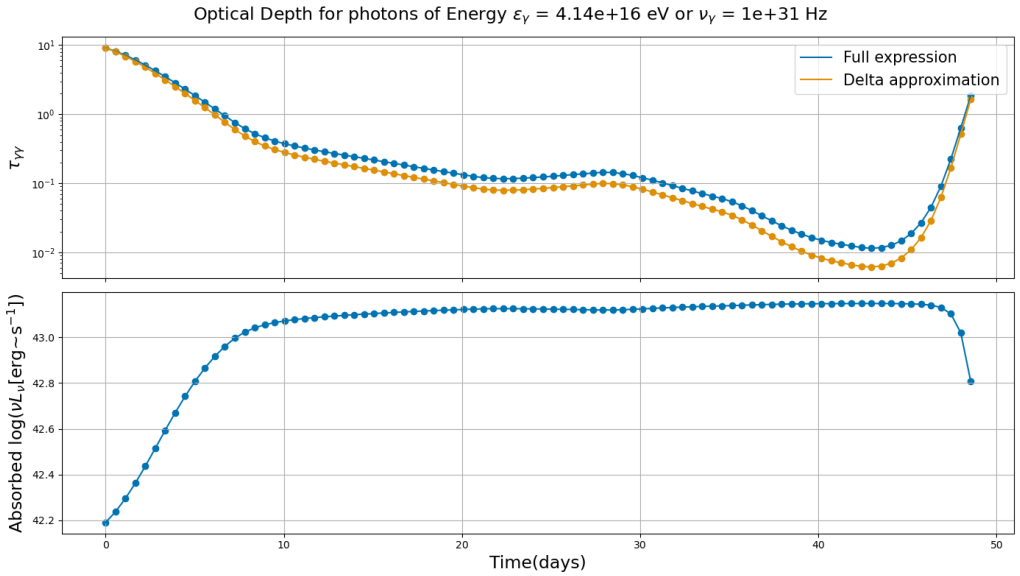

Figure 5.40: *Upper panel:* Optical depth for $\gamma\gamma$ absorption at $\nu_\gamma = 10^{31}$Hz calculated via the full cross section and the delta approximation. *Lower panel:* Attenuation of representative luminosity value of $\nu L_\nu = 10^{43.15}$ erg s^{-1} highlighting the impact of $\tau_{\gamma\gamma}$.

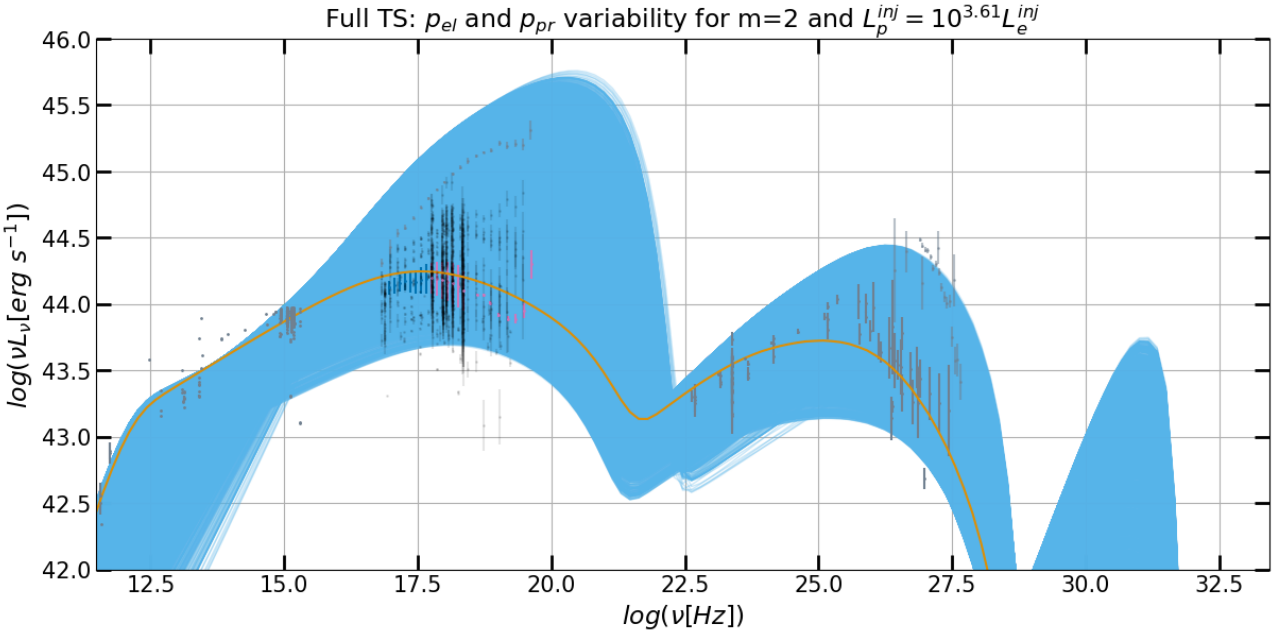

Figure 5.41: Full TS time evolution SED for two-species power law index variation with $m = 2$, $L_p^{inj} = 10^{5.62} L_e^{inj}$, and a hard upper limit on the power law index of $p \leq 2.6$. An animated version of the time evolution is found Here.

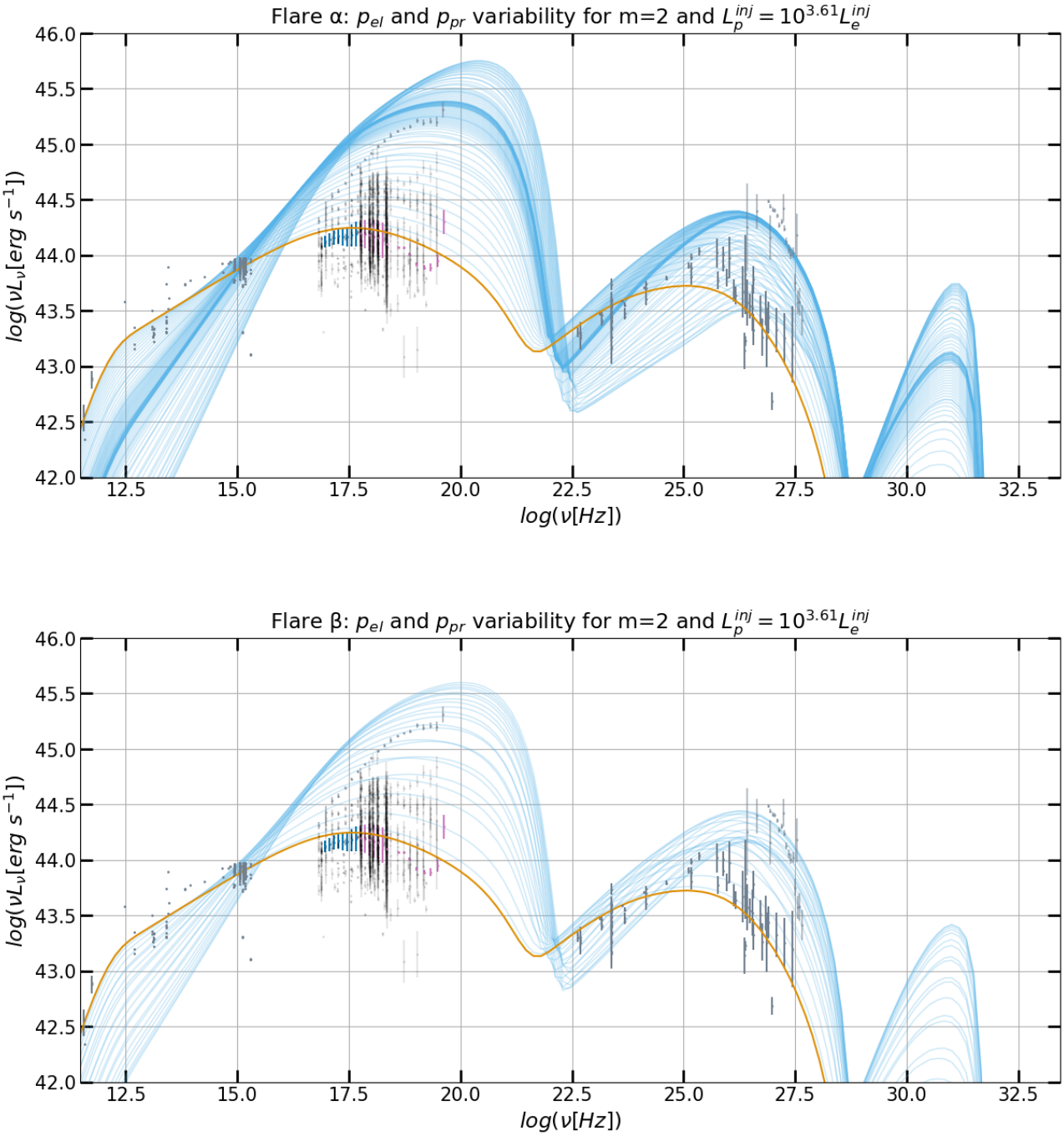

Figure 5.42: Same as Fig. 5.41 for flare α (upper panel) and flare β (lower panel).

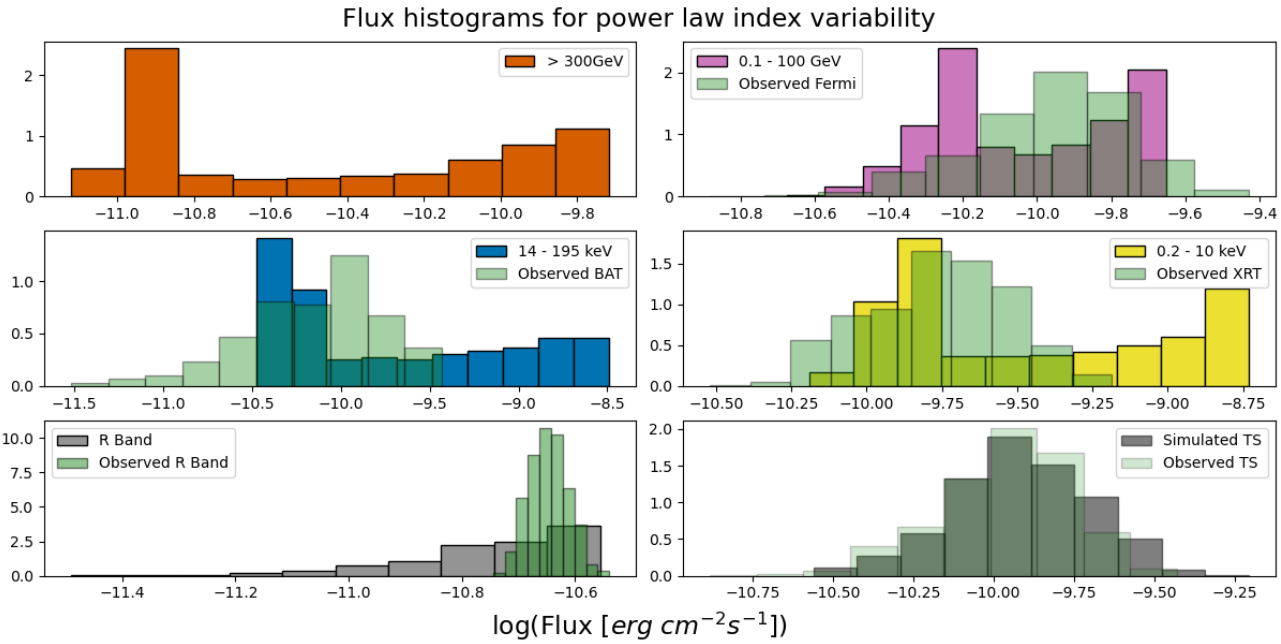

Figure 5.43: Flux histograms for two-species power-law index variation with $m = 2$, $L_p^{inj} = 10^{5.62} L_e^{inj}$, and an upper power law index value of $p \leq 2.6$. An analysis of the energy bands is found in Fig. 5.6 and the text discussing it.

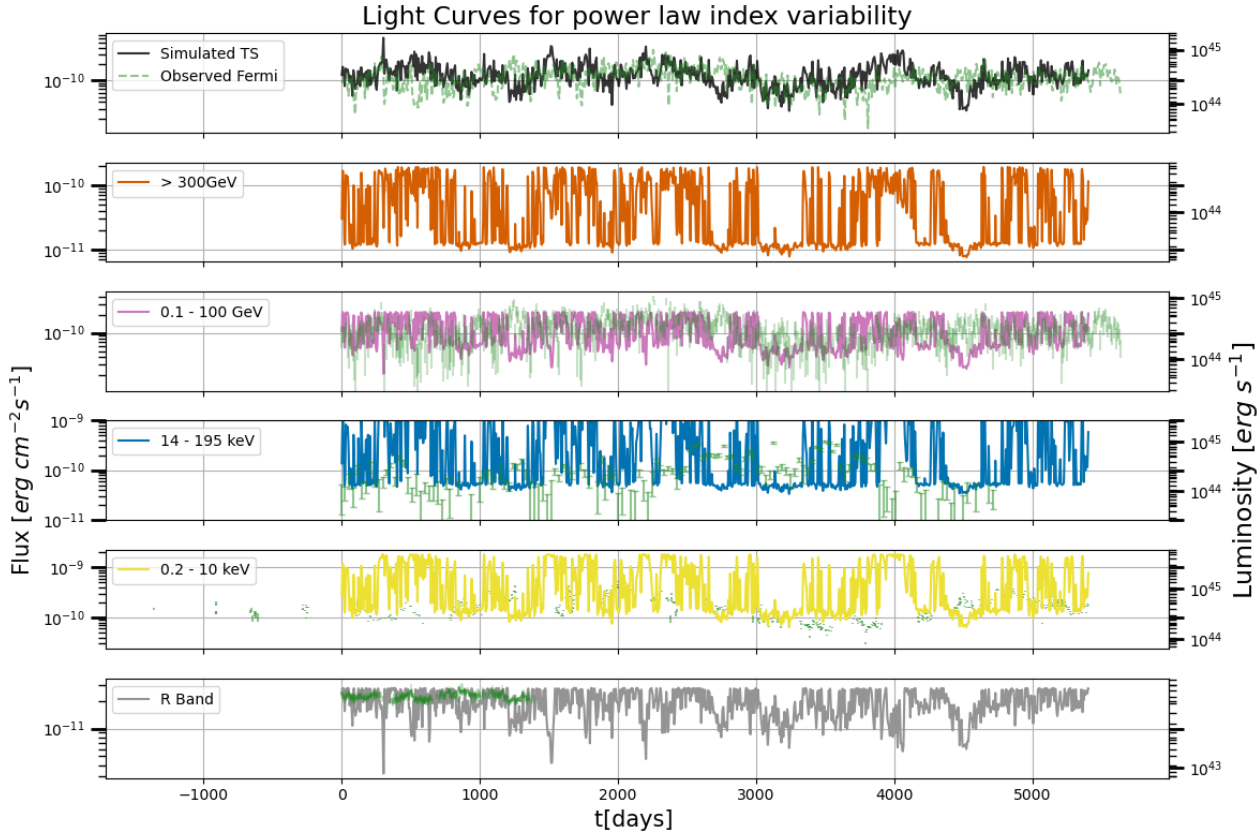

Figure 5.44: LCs for the complete leptohadronic run for power law index variability. Discussion of the superimpositions are found in Fig. 5.7.

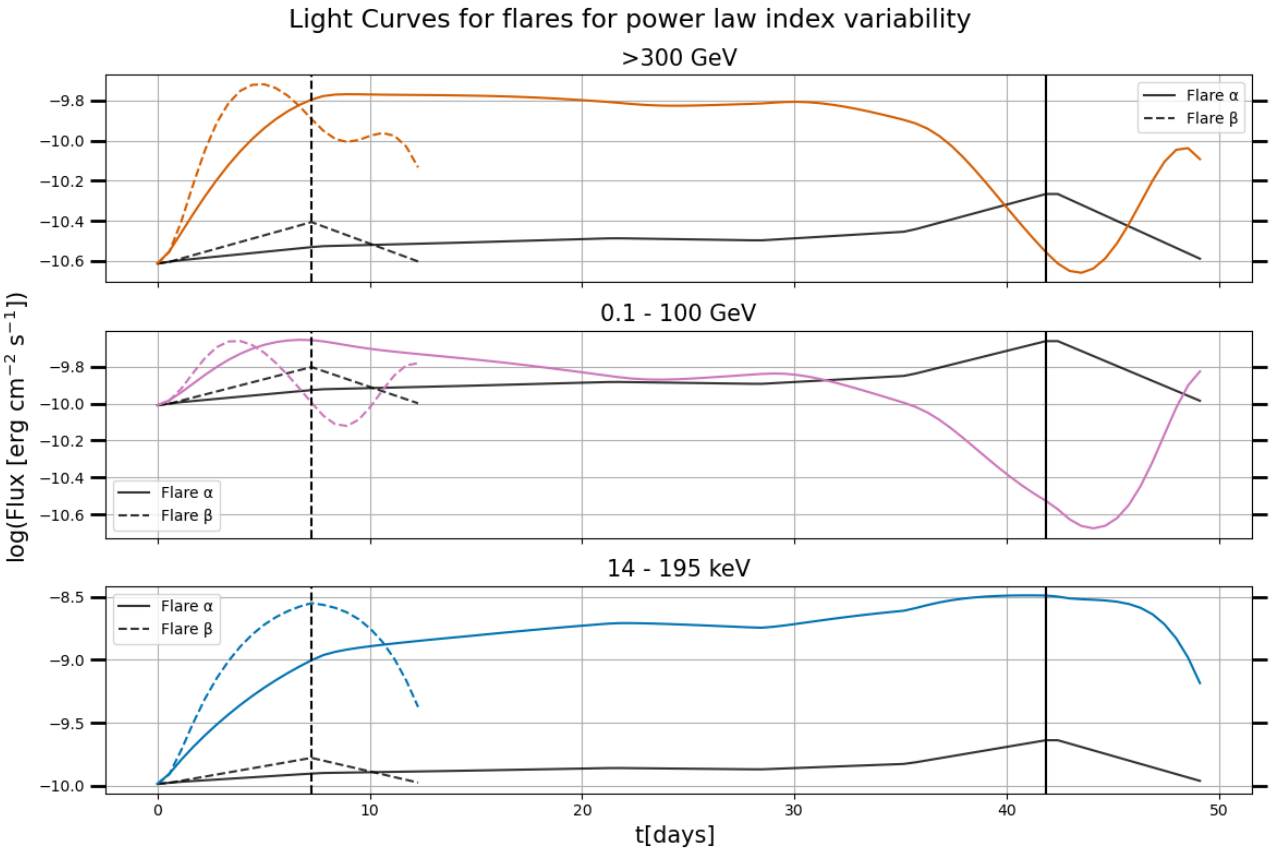

Figure 5.45: LCs for flares α (solid line) and β (dashed line) for power law index variations. With black lines, the renormalized flares TS of Fig.5.2 have been superimposed. The energy ranges of $0.3-3$ TeV (upper panel), $0.1-100$ GeV (middle panel), and $14-195$ keV (lower panel) are shown.

In Fig. 5.46 we present the flux-flux diagrams for the leptohadronic power-law index variability. These diagrams consist of 2 structures. A line segment and a parabola. The decreasing part inside the parabola corresponds to flaring states and is expected as a result of missing SSC targets. Increasing the available L_p^{inj} is a method of counteracting this decrease. Furthermore, we suggest, that the parabola occurs during joint magnetic field + power law index variations while the linear segment corresponds to the magnetic field variations during the upper bound of $p_{el,pr} = 2.6$.

We conclude that leptohadronic variations in the power law index of the 2 injected particle populations lead to greater flux variabilities than purely leptonic variations. Throughout our testing, no significant BH component has been observed. In contrast, synchrotron emission from secondary electrons from photomeson interactions dominates the (V)HE region. The spectral hardening of the particle populations for high m values produces a luminous pion bump as a result of small optical depths $\tau_{\gamma\gamma}$. Choosing an intermediate value of $m = 2$, limiting the slope values to $p_{el,pr} < 2.6$, and reducing L_p^{inj} by two orders of magnitude compared to the upper limit value derived in Section 4.2.2 creates a long-term time variability SED with spectral steepening but flux variability exceeding both observations and previous numerical runs with particle energy injection rate/magnetic field variability. We exceed the observed XRT and BAT variability in all of our tests. However, the data of the 1997 flares that exhibit the drastic spectral hardening are not included in this sample. Therefore, more numerical runs are needed to appropriately sample the parameter space of m and L_p^{inj} to accurately conclude whether power law slope index variations can approximate long-term observational features or short-term periods of high activity.

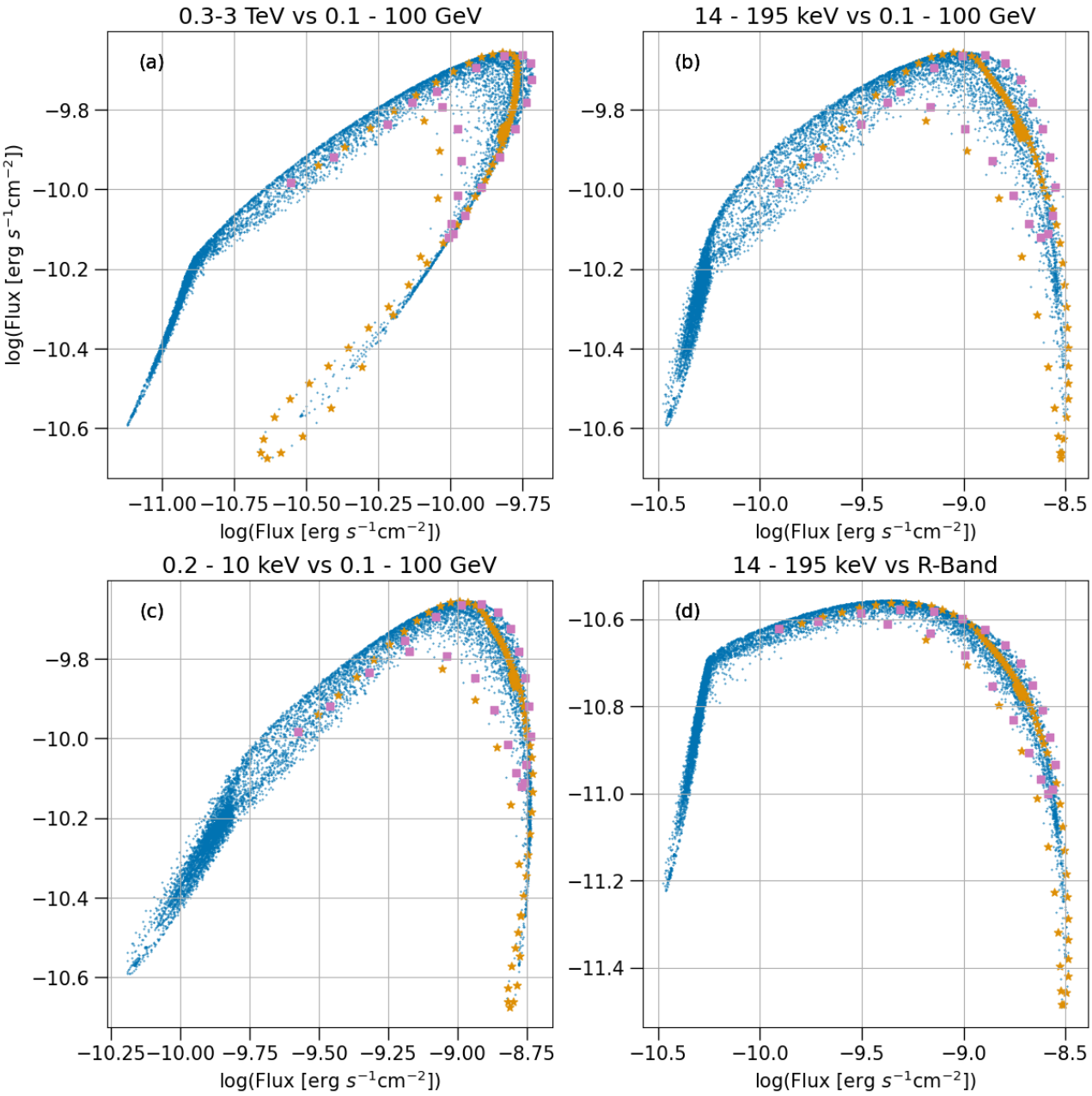

Figure 5.46: Flux-flux diagrams for leptohadronic power law index variability, comparing the flux variabilities between Fermi vs. VHE (a), Fermi vs. BAT (b), Fermi vs. XRT (c), BAT vs. R-Band (d). The cases for the complete TS (blue circles), as well as the results for flare α (yellow stars) and flare β (purple squares) are indicated.

Chapter 6

CTAO Predictions

In this Chapter, we will simulate Light Curves (LCs) and Spectra for the upcoming Cherenkov Array Telescope Observatory (CTAO). In particular, in Section 6.1 we will introduce the concept of Cherenkov radiation and how it can be used to observe γ-rays through ground-based telescopes. Then, in Section 6.2 we will create an EBL-corrected simulated dataset with `Gammapy` for the time-variation models of Chapter 5 and derive predicted LCs and spectra for the simulated long-term time variability as well as flares α/β.

6.1 Cherenkov radiation and the CTAO

The CTAO will consist of ground-based Imaging Air Cherenkov Telescopes (IACTs) utilizing the homonymous Cherenkov radiation. Charged particles moving through a medium can exceed the speed of light in the medium producing Cherenkov radiation. This radiation is emitted at an angle θ to the direction of the particle motion. The angle depends on the particle velocity v, or $\beta = \frac{v}{c}$ normalized at the vacuum light speed, and the refractive index n of the medium [59]:

$$\cos(\theta) = \frac{1}{n\beta}. \tag{6.1}$$

This radiation is caused by the by-products of interactions between Very-High-Energy (VHE) γ-rays or protons with the atmosphere. The resulting cascades are called "Atmospheric Showers". An example for both cases is shown in Fig. 6.1 contrasting lateral extension and elevation between γ-ray and proton secondary particle trajectories. The former consists of $\gamma\gamma/e^-e^+$ pair creations/annihilations. In the latter, proton cascades produce secondary hadronic particles with varying mean free paths resulting in a spatially less confined event.

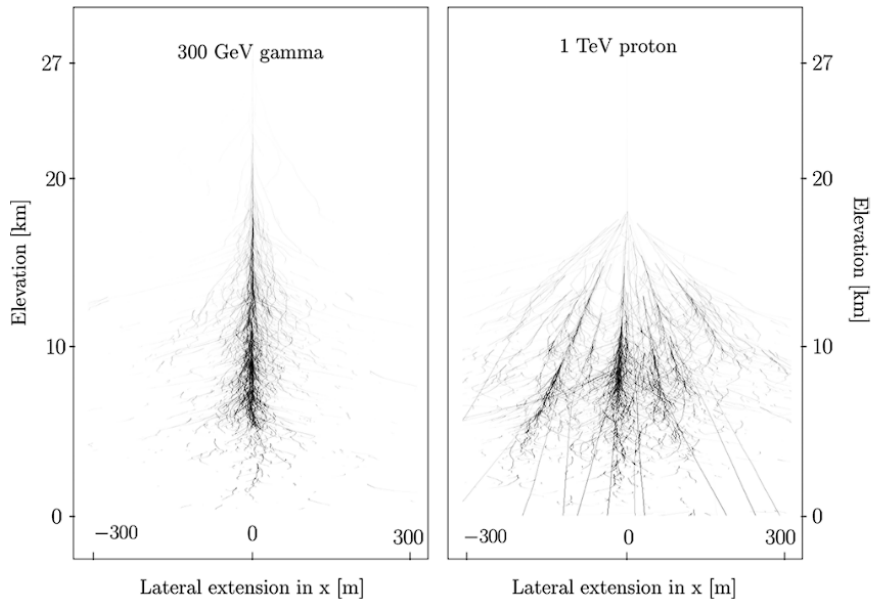

Figure 6.1: Secondary particle trajectories of VHE γ-ray (Left) and proton (Right) air showers [60].

In Fig. 6.2 we showcase how an IACT projects such an event into the camera's focal plane. The extent and intensity of the resulting image depend on the γ-ray's angle and energy. Furthermore, using an array of IACTs, a stereoscopic reconstruction of shower arrival direction and impact position is possible. This is illustrated in Fig. 6.3. Therefore, using the atmosphere as the propagating medium, IACTs observe the Cherenkov radiation of atmospheric showers and reconstruct the energy and position of the VHE γ-ray.

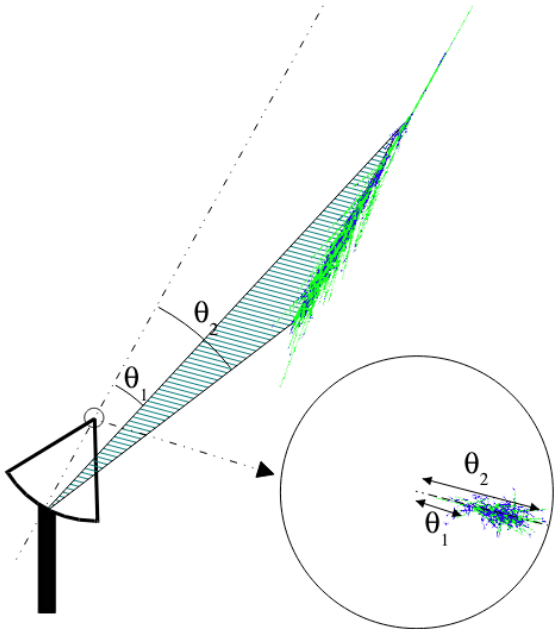

Figure 6.2: Air shower projection into the camera focal plane. Indicated are the angles between the start, θ_1, and end, θ_2, of the shower [61].

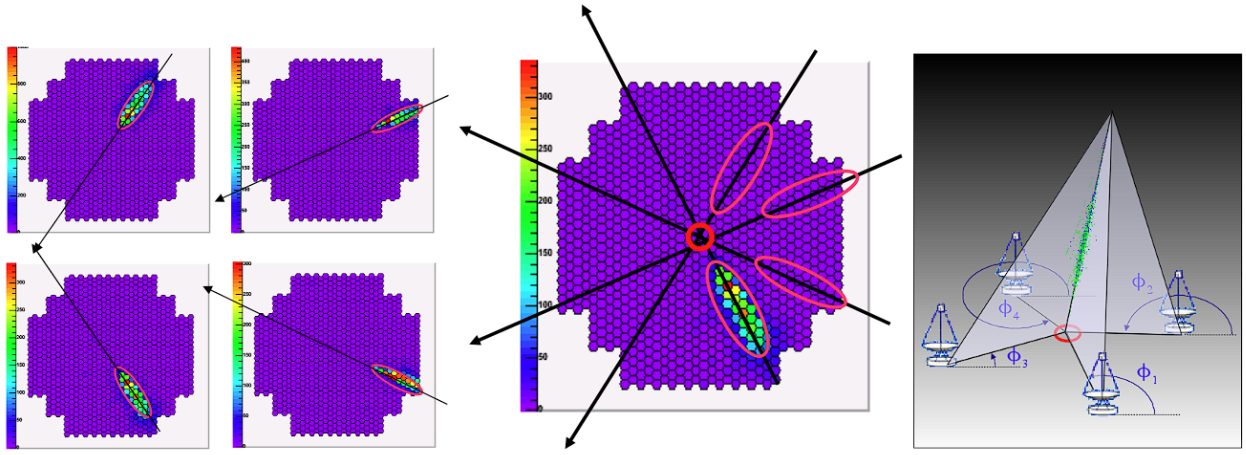

Figure 6.3: Stereoscopic geometric reconstruction. Left: Individual camera image data intensity with arrows directing the main axis of the ellipse. Middle: Superimposed intersection of the individual observations. Right: 3D view of the array. Each telescope's azimuthal angle ϕ to the ellipse's main axis is indicated [61].

The CTAO will be the next-generation observatory of IACTs replacing the current observatories of MAGIC, H.E.S.S., and VERITAS. Its proposed main benefit will be twofold. At the time of the writing of this Thesis, all available VHE Observatories are private collaborations with proprietary rights to the observations. The CTAO will be "the first observatory of its kind to operate as an open, proposal-driven observatory providing public access to its high-level science data and software products"[1]. Furthermore, it will have an unpreceded sensitivity. In Fig. 6.4 we present the flux sensitivity of the CTAO for 3 different livetimes (0.5, 5, 50hrs), and in Fig. 6.5 we show the comparison between the sensitivity of the CTAO North and South array for a livetime of 50 hours and the current observatories. However, a detailed discussion on comparisons between the projected performance of the CTAO and current VHE observatories is beyond the scope of the current discussion, and the interested reader is redirected to the information provided on the performance section of the CTAO website[2].

[1] https://www.ctao.org/for-scientists/
[2] https://www.ctao.org/for-scientists/performance/

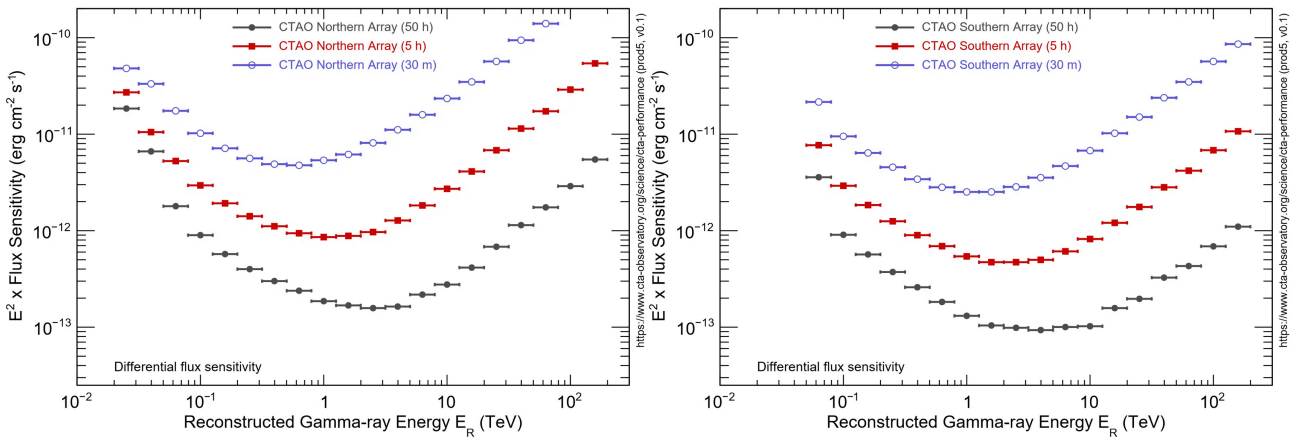

Figure 6.4: Flux sensitivity for the upcoming CTAO North (Left) and South (Right). In each case, 3 representative observation times are provided (black: 50h, red: 5h, and purple: 0.5h)[55].

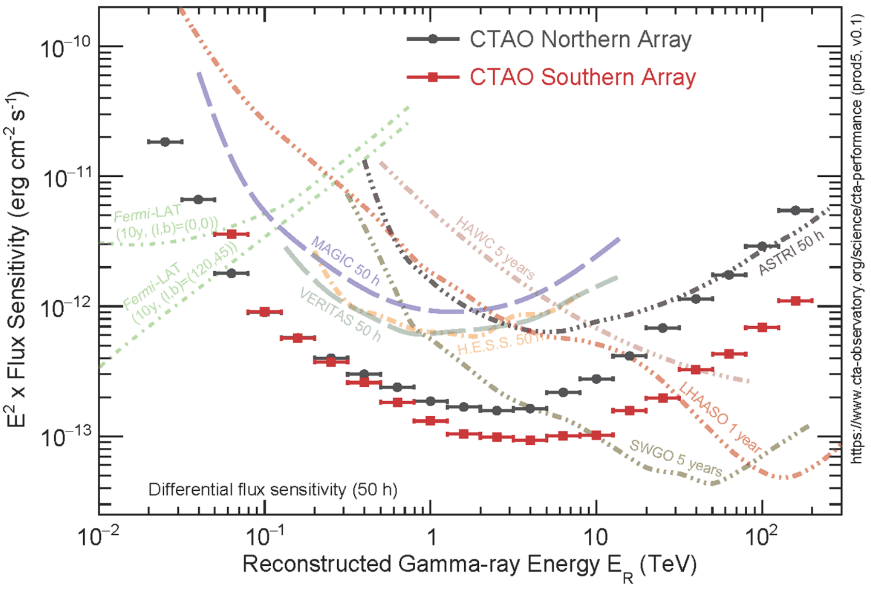

Figure 6.5: CTAO North and South array sensitivity for a 50-hour livetime compared to existing VHE observatories. For a detailed discussion of each observatory see https://www.ctao.org/for-scientists/performance/ and references therein [55].

6.2 CTAO Light Curve predictions with Gammapy

In this section, we will derive predicted LCs for the explored time variable models of the previous Chapter. For this analysis, we use `Gammapy` [62],[63], a community-developed open-source Python library. Built as a core package for CTA, this data analysis tool can be used for current pointing and all-sky γ-ray observatories and neutrino detectors. In conjunction with observations provided by the CTA, the workflow of `Gammapy` can be divided into Data Levels (DLs) from 0-5. CTA carries out the data analysis for the first 3 DLs and provides the user with

γ-like events of DL3. As such, the specifics won't be further discussed. The analysis through `Gammapy` therefore starts at DL3. The description of the workflow is presented in Fig. 6.6. Each section notes its respective core package through a folder icon (denoted by a Python suffix, e.g. `test.data`) while the grey bands indicate the pipeline from one DL to the next. Below each folder, the most prominent objects within the Python sub-package are highlighted. In particular, the provided data from the CTAO at DL3 include a list of γ-like events and the Instrument Response Functions (IRFs). To transform the above into DL4, a data reduction is necessary. The events and IRFs are projected and binned into a shared geometry. Furthermore, the background is estimated, and "safe" energy ranges for the analysis are established. This data reduction results in DL4 object, count data, and reduced IRFs bundled into maps. Lastly, modeling, fitting, and estimating data results in high-level data science products (DL5) such as SED and LC estimations. For further discussion of the `Gammapy` DLs the interested reader is redirected to the `Gammapy` documentation[3] and to [62].

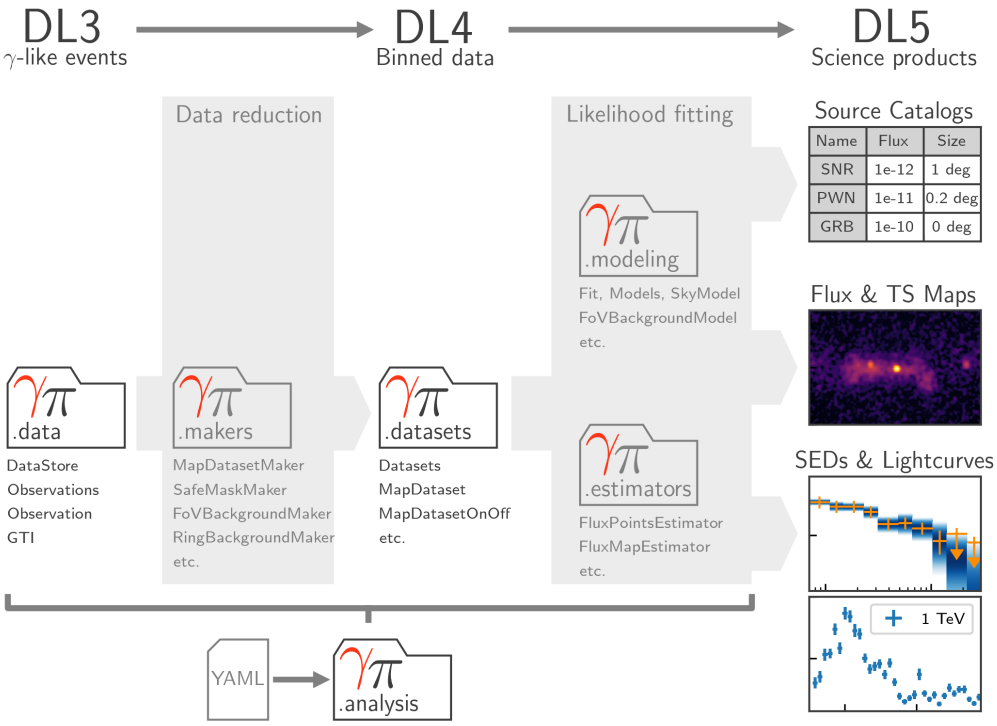

Figure 6.6: `Gammapy` analysis workflow. For each DL defined at the top, the corresponding sub-packages are noted with a folder icon. Below each folder icon, the most prominent objects within the sub-package are highlighted. Grey bands depict transformations to the next DL. Below the DL5 category, example science products are depicted.

For our analysis, we will use the investigated time variable models of Chapter 5. Therefore, we will create predicted CTAO LCs for the energy injection rate variability model of Section 5.2, the magnetic field variability of Section 5.3, and the moderate-to-extreme power law index variability with a reduced proton luminosity component of Section 5.4.2. We aim to model both the long-term variability of the above scenarios as well as flares α/β. In particular, we use

[3] https://docs.gammapy.org/0.20/userguide/package.html

`Gammapy` to create a synthetic dataset (at DL4) based on our SED models for Mrk 501. This is achieved at the previously discussed data reduction step. Instead of using CTA observations, we use our EBL attenuated (Finke model [64]) SED models to create a simulation for each step of the time variation. The resulting count data is shown in Figs. 6.7-6.9. Then, using the `LightCurveEstimator` interface we transform the count data into predicted LCs for each of the 3 scenarios. These results are showcased in Figs. 6.10-6.12. We note, that each input is spaced apart at 1 $t_{cr} = 0.558$days with an observational livetime of 5 hours. Therefore, the cadence of the simulated LCs exceeds the cadence achieved in reality, that is 1 observation per night. This increased prediction cadence is advantageous for our analysis, as it provides more data points than what is available from actual observations. The observational data should fall within the predicted regions if our model is accurate. Having more predictions than observations ensures that our model comprehensively captures the behavior of the data, which would be challenging if the situation were reversed.

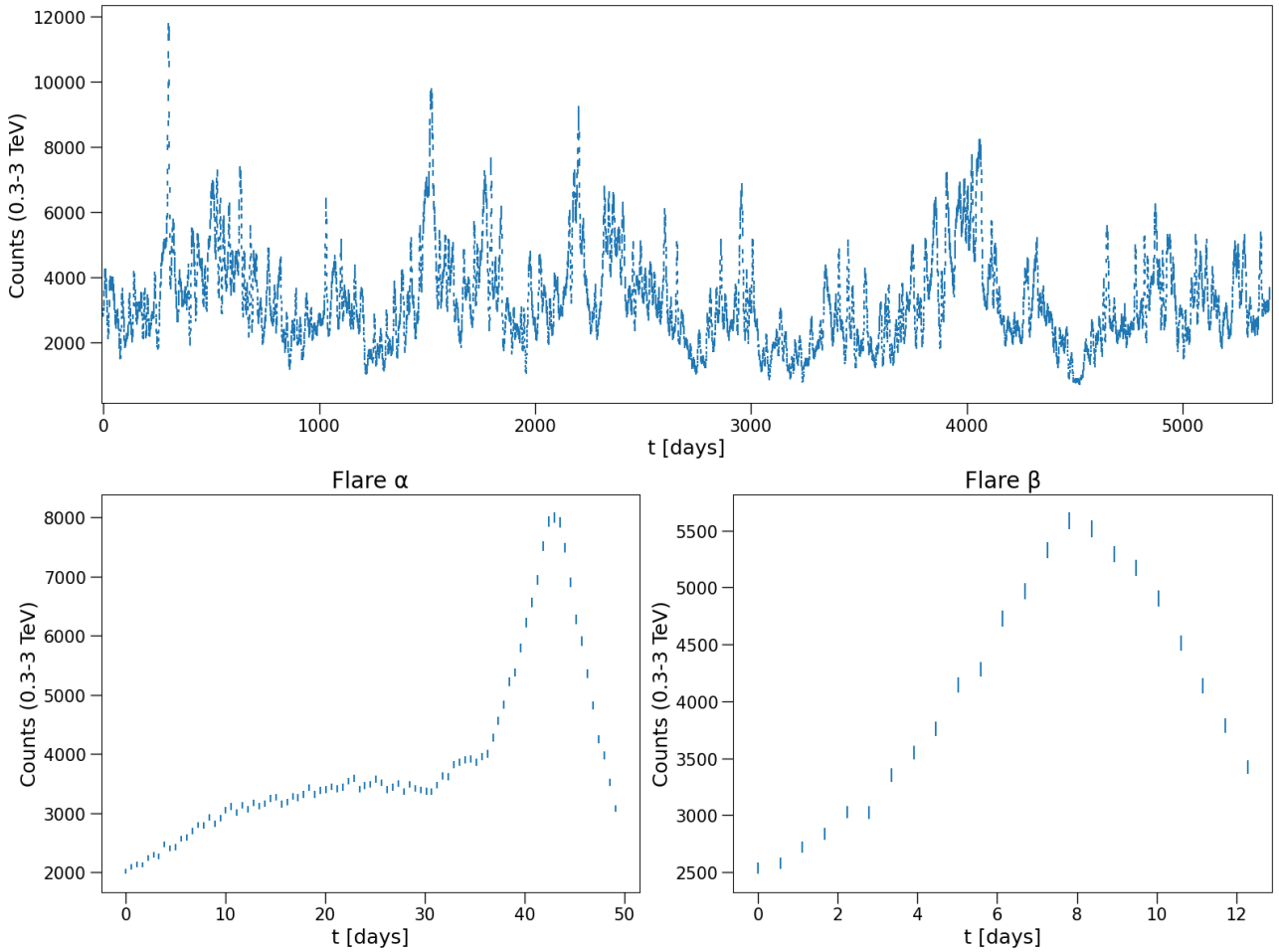

Figure 6.7: Synthetic time series of counts expected in the 0.3-3 TeV energy range for the long-term time variability (upper panel), and flares α/β (lower left/right) for changes in the particle energy injection rate of Section 5.2.

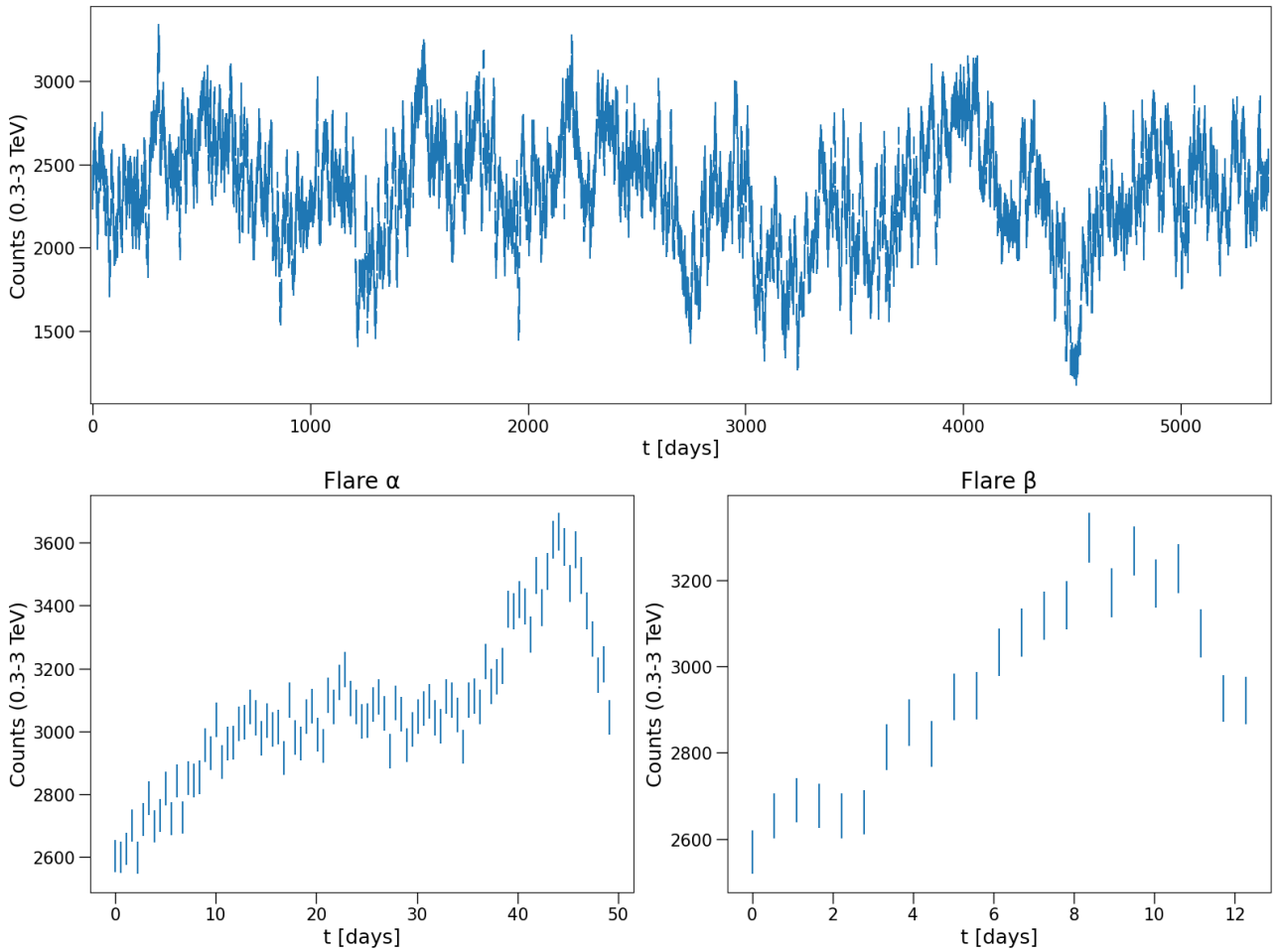

Figure 6.8: Same as Fig. 6.7 for the magnetic field variability of Section 5.3.

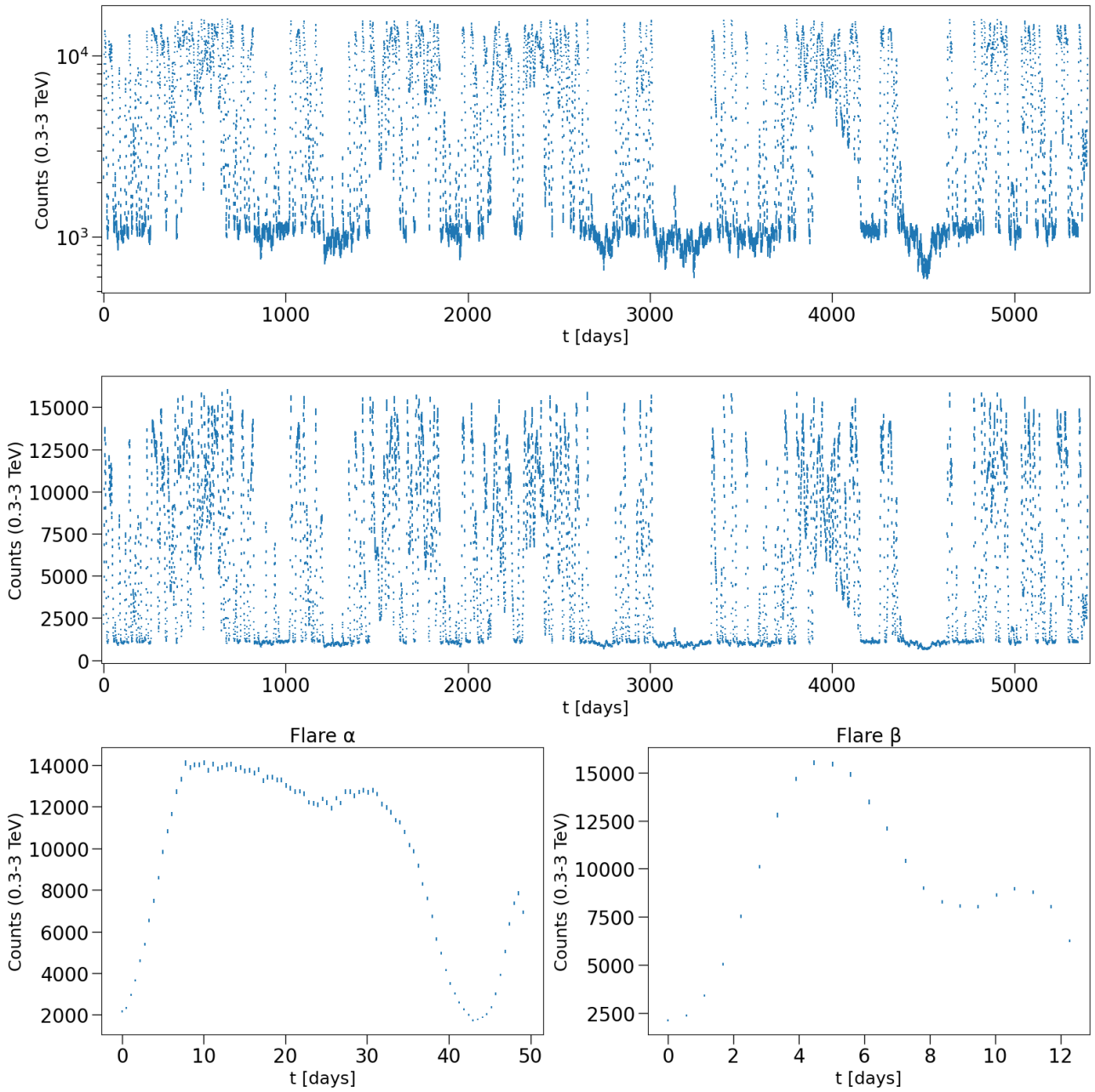

Figure 6.9: Same as Fig. 6.7 for the moderate-to-extreme power law index variability with a reduced proton luminosity component of Section 5.4.2. Upper/middle panel contrasts logarithmic to linear scaling.

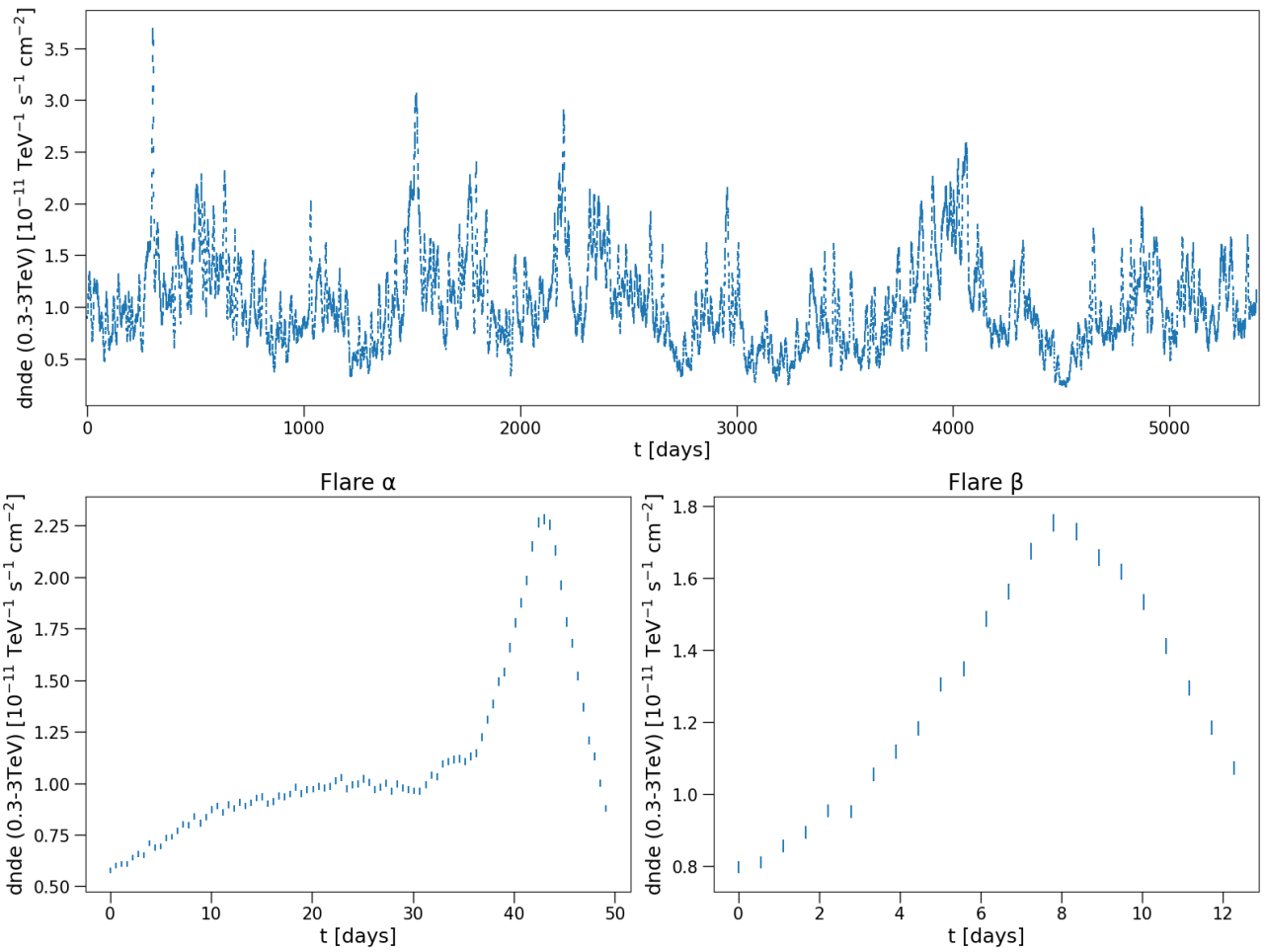

Figure 6.10: Synthetic CTA LCs for the long-term time variability (upper panel), and flares α/β (lower left/right) for changes in the particle energy injection rate of Section 5.2.

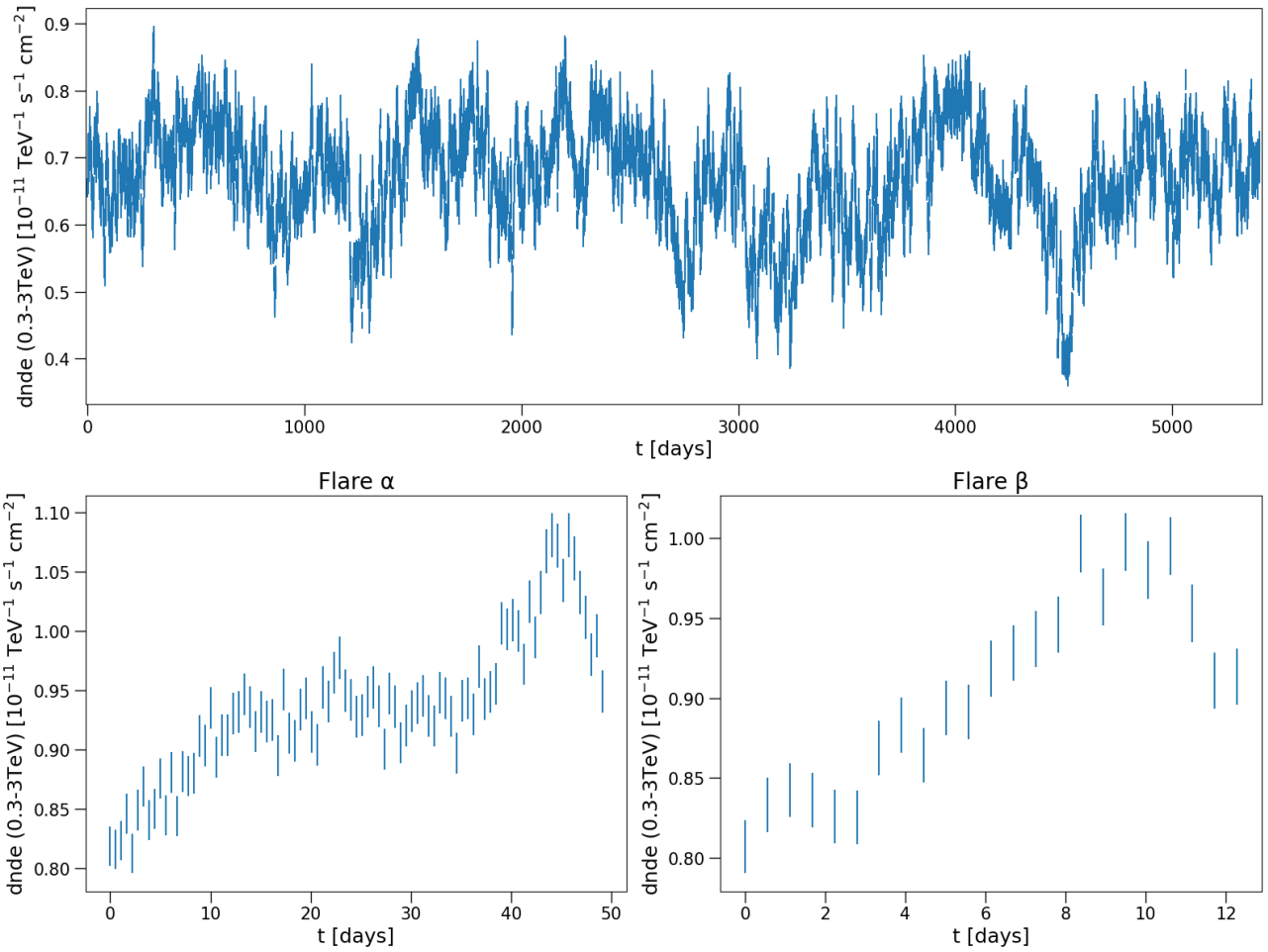

Figure 6.11: Same as Fig. 6.7 for the magnetic field variability of Section 5.3.

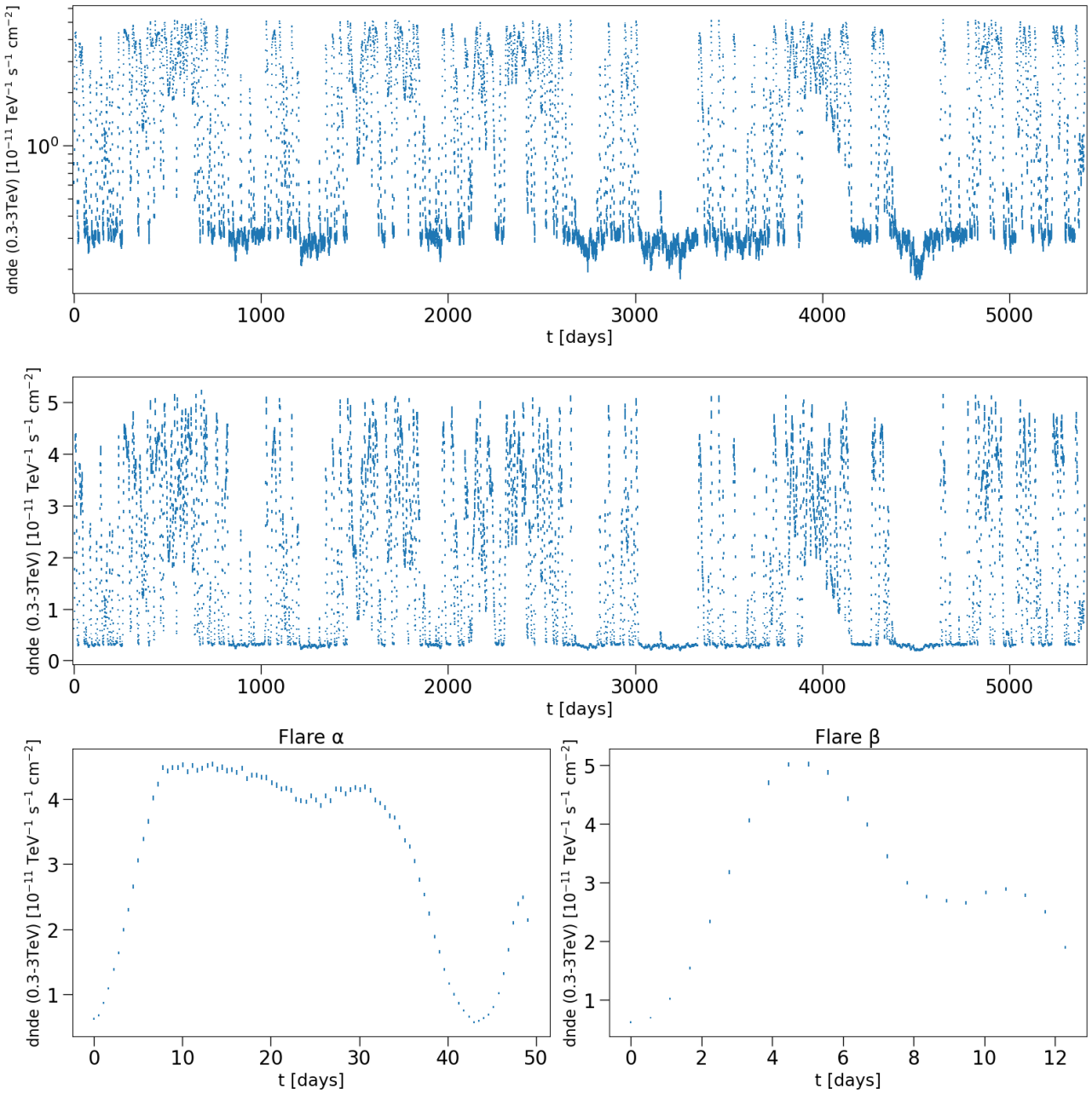

Figure 6.12: Same as Fig. 6.10 for the moderate-to-extreme power law index variability with a reduced proton luminosity component of Section 5.4.2.

Due to the extreme variability presented in Fig. 6.9 and Fig. 6.12 we chose to include a logarithmic scaling in the long-term representation. From the above, we conclude that the long-term variability of each scenario generally follows the trend of the calculated LCs of the SED models in Chapter 5. We note an important outcome of this numerical run for the flare analysis of the injection rate and magnetic field variability (Fig. 6.10 and Fig. 6.11). Specifically, the TS of flare β is a symmetric triangular pulse (as seen in Fig. 5.2). This feature is not recovered in the CTA predictions. Compared to the TS, our CTA prediction reports a skewness. We do not report the same behavior for flare α. The predicted LCs track the shape of the TS in Fig. 5.2. These findings are in line with our results of Chapter 5. Lastly, we report large variability in the predicted long-term LC of the power law index variation of Fig. 6.12.

We suggest that the lower values are more confined and resemble the below-zero section of the TS of Fig. 5.1 as a result of the upper bound on the power law index, $p_{el,pr} \leq 2.6$. Furthermore, in contrast to the two preceding cases, we report a predicted flux reduction at the TS peak of flare α and close to the peak of flare β. Following the discussion of Chapter 5.4 this is to be expected as a result of the reduction of available SSC targets. The LCs of all 3 cases can be used as predictive tools to contrast our investigated models to future long-term observations or observations of flaring events with the CTAO.

Lastly, we will focus on the presented long-term power law index variation model to investigate a scenario with a hadronic signature. First, in Fig. 6.13 we compare the different livetimes of 0.5,1, and 5hrs to investigate the minimum timescale needed to observe Mrk 501. For the discussed variation, we report how detection times of 30min yield high-quality results not obscured by background radiation eliminating the need for longer livetimes.

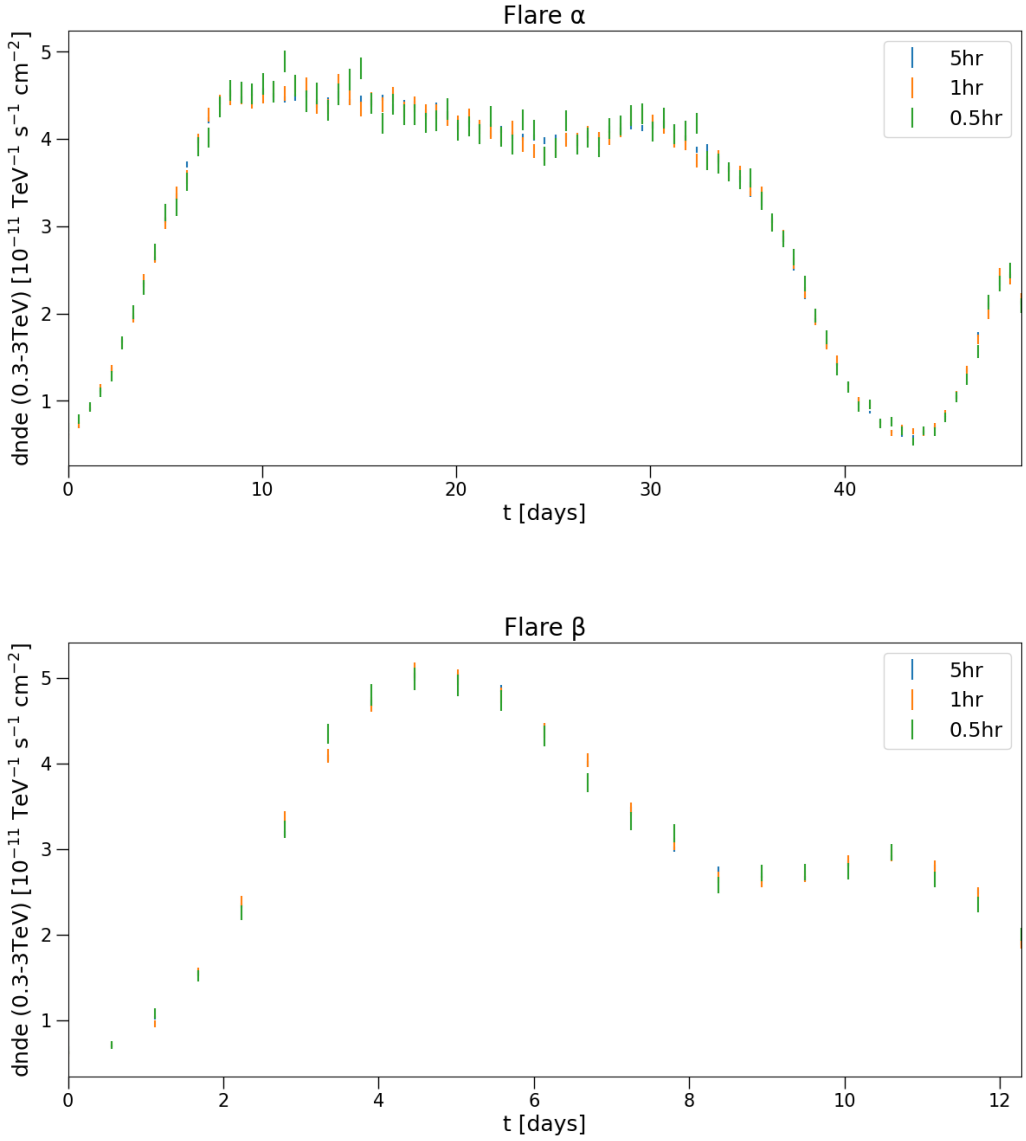

Figure 6.13: Livetime comparison between 0.5,1, and 5hr for flare α (upper panel) and flare β (lower panel) in the power law index variations scenario.

Furthermore, motivated by the 0.3-3 TeV LC of Fig. 6.13 for flare α we extend our region of investigation and present a sample of simulated spectra in the 0.3-10 TeV energy region. To be precise, using our previously generated dataset we present in Fig. 6.14-6.16 the spectra for $t = 0, 11, 43$d. We compare the average state before any time variations ($t = 0$d), to a period of maximum VHE flux before the reduction of the SSC flux ($t = 11$d), and to the anti-correlation peak ($t = 43$d) corresponding to the maximum of the injected TS. In each figure, we present in the upper panel the CTA simulation (blue symbols) alongside our EBL attenuated model (orange line). In the lower panel, we present the residuals between the data and the model. We note how in the low flux states ($t = 0, 11$d) the discrepancies between the model and data increase for higher energy values. This is expected as we are moving away from the region of CTAO's highest sensitivity and are simultaneously lowering the flux to its simulated minimum. Specifically for the anticorrelation peak, we highlight the impact of the hadronic component in Fig. 6.17 contrasting the leptohadronic to a purely leptonic spectrum. We conclude that the hadronic inclusion plays a significant role in the VHE spectrum, especially at the lower energy part, and its significance throughout the VHE can be increased for higher values of L_p^{inj} (see discussion of Section 5.4.2 and the VHE flux of Fig. 5.38).

From this investigation of the power law index variation scenario, we leave as an open question the impact of the upper bound on $p_{el,pr}$ as well as the choices of m and L_p^{inj}. Although, motivated by qualitative arguments, we illustrated the impact of exposure time and hadronic inclusion for specific parameter choices in our parameter space, a thorough investigation of it is missing and should be the focus of future dedicated studies.

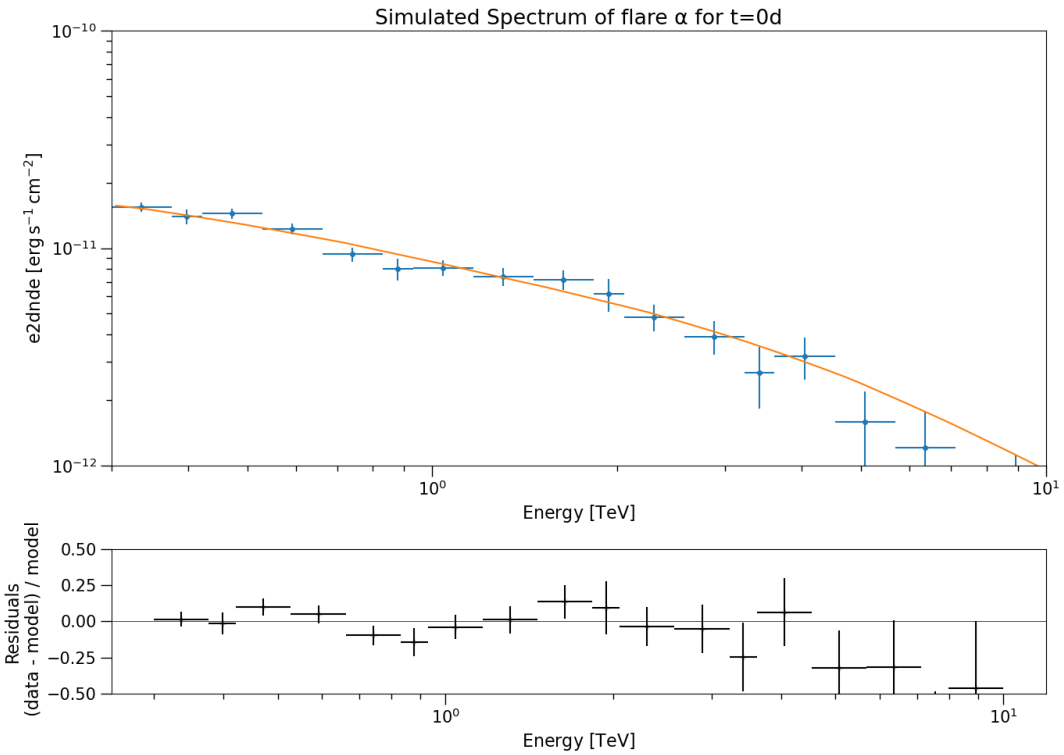

Figure 6.14: Spectrum for flare α at timestep $t = 0$d. Upper panel: Indicated are the simulated data points (blue) and our used SED model (orange). Both have been attenuated by the EBL model of Finke [64]. Lower panel: Residuals between our data and model.

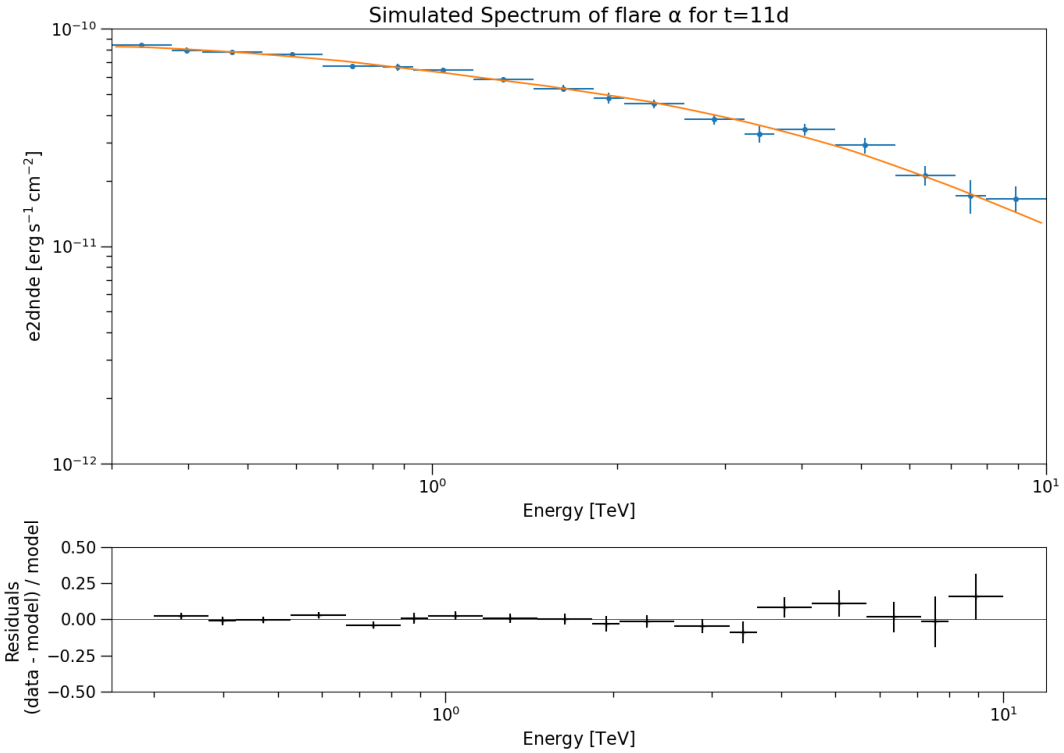

Figure 6.15: Same as Fig. 6.14 for $t = 11$d.

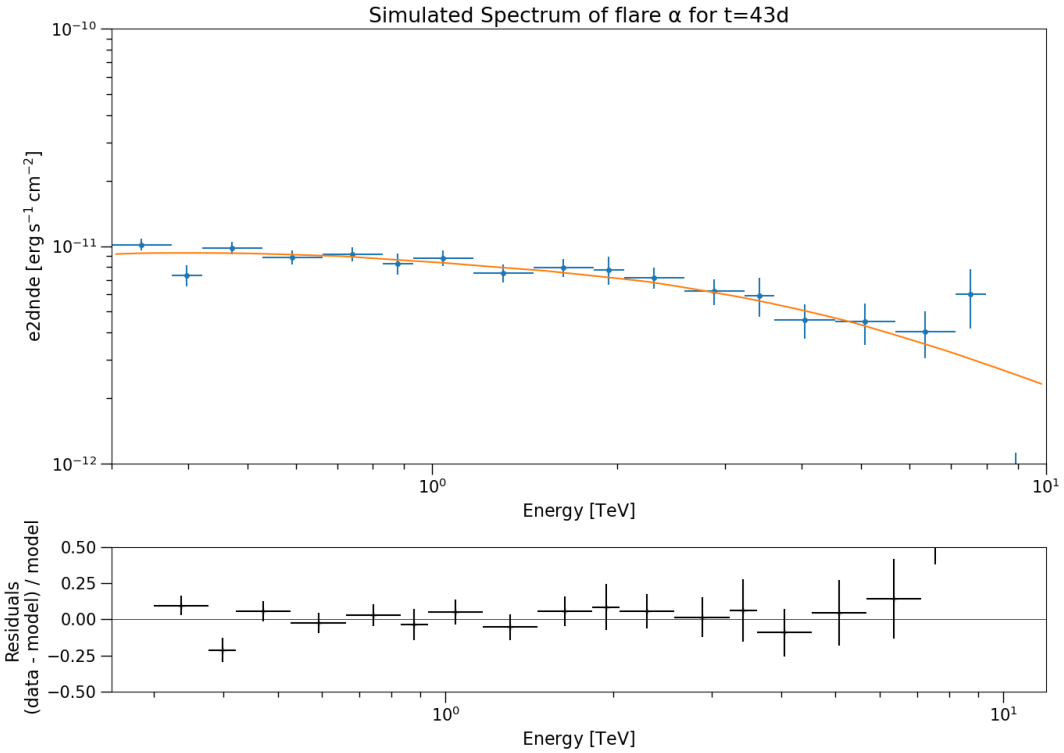

Figure 6.16: Same as Fig. 6.14 for $t = 43$d.

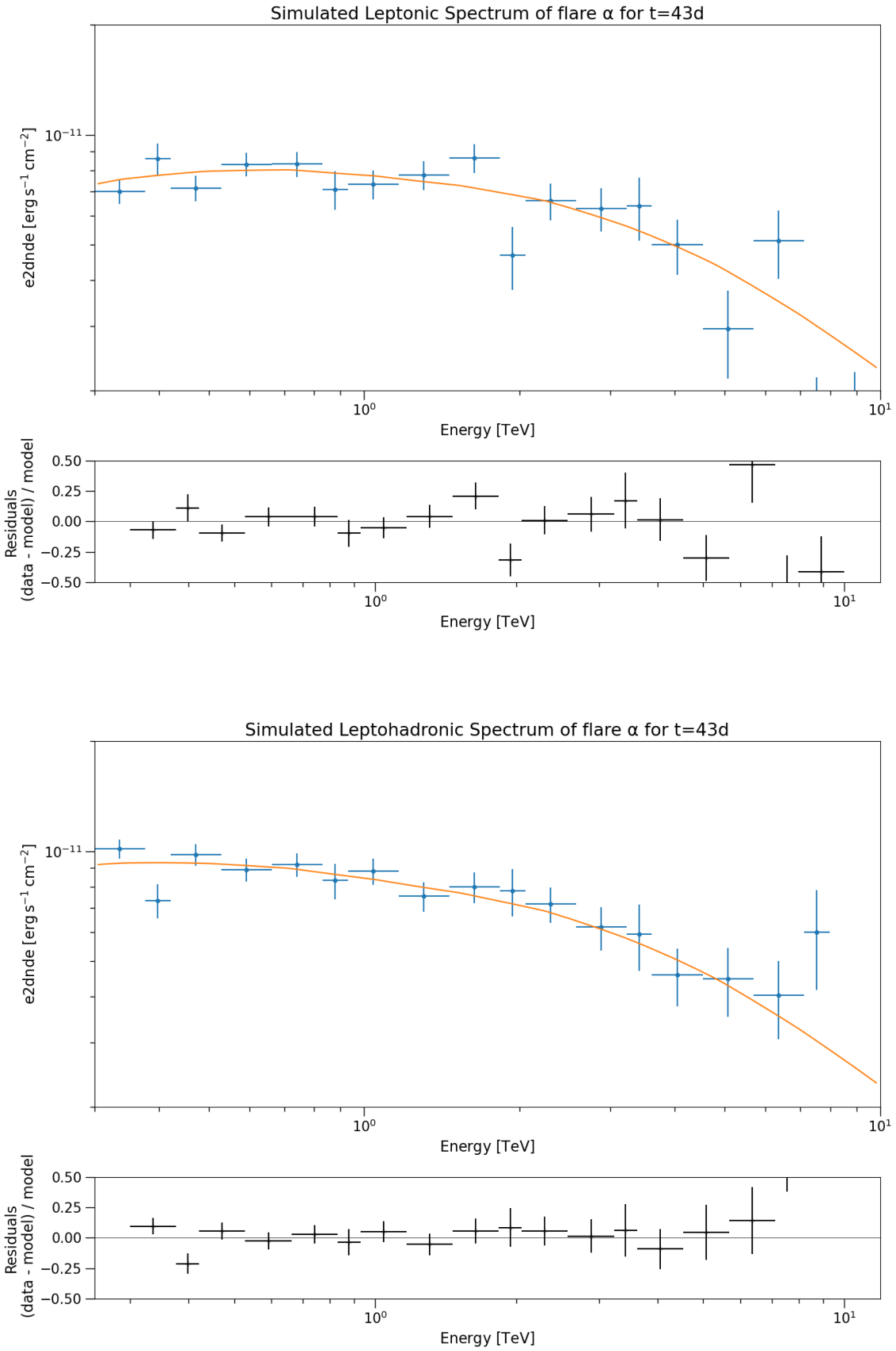

Figure 6.17: Hadronic impact in flare α at $t = 43$d. Each figure presents the simulated spectra (blue) and used SED model (orange) alongside the residuals. Upper figure: Spectrum for a leptonic SED model. Lower figure: Spectrum for a leptohadronic SED model.

Chapter 7

Summary & discussion

In this Chapter, we will summarize our findings and briefly compare them with the currently available literature. We will emphasize our limitations and present suggestions for future bodies of work.

Blazar Time Series Analysis

We analyzed a broad sample of TeV-detected blazars (Fig. 3.3) to derive their statistical properties in the high-energy range. Using Gaussian process modeling through the software `celerite2` we employed the celerite method to fit stochastically-driven damped simple harmonic oscillators (SHOs) to observational Fermi Light Curves (LCs). For each source, we fitted a singular SHO and derived their celerite parameters, which are summarized in Table 3.1. These create SHO models that accurately describe the statistical behavior of each source in the Fermi energy band enabling us to create synthetic LCs for it. Furthermore, we investigated the values of our PSD slopes and breaks. We have found how the latter are in the hundreds of days. As the values are not multiples of 365 days we can exclude artificial origins caused by the earth's rotation around the sun. A prevalent suggestion is to connect this relaxation time of the γ-ray variability to processes responsible for X-ray and optical variability (e.g., thermal timescales of the innermost parts of the disks [31], perturbations originating at the outer radii of an accretion disk propagating inward and creating a dependence on diffusion timescale and the viscosity of the flow [32]). However, to the best of the author's knowledge, no conclusive theory has been proposed to explain these findings.

To prove the goodness of our celerite fits, we performed a number of statistical tests, with summarized results in Table 3.2. This approach aligns with the current literature [28],[27],[24]. Through our tests, we report in some cases better statistical fits than those available in the literature. Additionally, we examined the slopes of the resulting blazar Power Spectrum Densities (PSDs) to determine deviations from the expected value of two (See discussion in Section 3.1). We found tighter constraints (i.e., smaller errors) compared to earlier works. We attribute this primarily to differences in data treatment. We conducted our analysis in logarithmic space with data provided by the Fermi Light Curve Repository (LCR) with a mean cadence of 7 days.

Previous authors conducted their own γ-ray event data reduction, resulting in observations of varying mean cadence. Furthermore, they fitted their models on linearly scaled data. We suggest the parameter investigation to be sensitive to these steps. There is also a discrepancy between the model usage. We chose a singular SHO, while previous contributions investigated combinations of SHOs and the additions of damped random walks to the models. Moreover, other authors considered different models altogether (e.g. CARMA).

We also acknowledged the limitations of our method. A time series analysis cannot describe extreme variability on timescales comparable to the mean cadence. To address this, we recommend supplementing the investigation with time-series models focusing on short flaring timescales. Moreover, our approach did not reveal the periodicity of PG 1553+113 hidden by the statistical noise (Section 3.3). This limitation can be addressed by increasing the model complexity (e.g. combining SHOs) to describe the main component while identifying secondary features. This aspect is worth investigating in the future.

In summary, we have derived the celerite parameters for the sources of our blazar sample, which can be used in future studies to create synthetic LCs in the Fermi band. We highlighted the fit quality and PSD slopes as comparison tools and discussed the limitations of our contribution.

Mrk 501: A Time Variability Study

Using Mrk 501 as our test case we investigated the behavior of time variations in hybrid leptohadronic SSC scenarios. After discussing and selecting the appropriate data bounds and initial parameters we argued and derived its average state description using the numerical code `LeHaMoC`. Our approach is consistent with the available literature [50], in treating the hadronic component. More specifically, we attribute the time-average SED to processes associated with primary leptons, and set an upper limit on the hadronic/proton population in the jet. There are no visible hadronic components in the observational SED of Mrk 501 such as in 3C 371 and PKS 0735+17 [50]. In those BL Lacs, a hadronic population is necessary to explain the observations between the broad-band features of the leptonic synchrotron+SSC scenario. As we are unable to constrain the hadronic contribution we take the derived upper limit as our representative value.

Using the time-average SED model as a starting point, we argue in favor of key parameter variations motivated by the synthetic LCs of the Fermi band calculated in `celerite2`. For each time step of 1 light-crossing time t_{cr} we vary 1 or more parameters in the calculations of `LeHaMoC`. This results in time-variable SED models which we present and discuss. Specifically, we model variations in the particle energy injection rate, the magnetic field strength, and changes in the power law index of the (joint) particle population.

For the first two variations, we connect the synthetic LC to the parameters directly via theoretical arguments. We calculate the long-term time evolution of the SED and supplement our analysis with short-term periods of high activity to simulate flaring events. For specific representative energy bands, we present the flux variability through flux histograms, calculate

the coefficients of variations, and investigate time lags with Discrete Correlation Functions (DCFs). We have found our model results to underestimate the observed flux variability in most energy bands. We present the flux-flux diagrams of the discussed energy bands and derive their scaling. This constitutes a predictive tool for future observations, enabling us to compare our models to any observed variability.

For the power law index variations we first investigate changes in a purely leptonic population and later expand our analysis to include a hadronic component. We analyzed and discussed leptonic variabilities of various degrees and discussed their benefits and shortcomings in approximating the observed behavior of Mrk 501. We have found that greater variations lead to spectral hardening and a flux increase in the X-ray range but a drastic flux reduction at energies below optical and in the SSC component above 10^{22}GHz. Mild power law index variations are not accompanied by significant spectral hardening in the power-law synchrotron component, extending from optical to X-ray energies, but do not predict the aforementioned flux reduction in the other two energy bands. This could suggest that such a leptonic model could describe a period of moderate activity of Mrk 501. We expand our analysis on two-species changes in the power law index. Our previous results for X-ray and optical flux variability do not change but we report extreme flux values at high energies caused by the presence of a significant photo-meson contribution. Lastly, we investigate an alternative scenario with a reduced proton energy injection rate compared to the derived upper limit value and an upper limit to the power law index to model the long-term scenario of moderate-to-extreme variability in the power law index. We present our findings through flux histograms and flux-flux diagrams and discuss their implications. We conclude, that to accurately describe simultaneous extreme flares in the X-ray and (V)HE region both a leptonic and hadronic component are necessary, whereas modeling moderate X-ray activity could be achieved by leptonic means.

Following recent studies, [51] investigates a rare spectral feature of Mrk 501 that a purely leptonic model cannot explain. They suggest a π^0-decay scenario to model a "bump" at 3 TeV during an extreme X-ray flaring event in 2014. This indicates the presence of an underlying hadronic component within the source dominating the emission at a narrow γ-ray region during a period of high X-ray activity. This result should be taken into consideration when trying to model moderate leptonic power law variations to explain periods of increased X-ray activity. Furthermore, features like these could be used in future studies to decouple the power law index variations between electron and proton populations. Another important aspect of this thesis is the derived flaring LC behavior of the energy injection rate/magnetic field strength and the time lag/skewness compared to the injected TS when investigating flare α and β. These features are also present in the derived DCFs. In Ref. [65] the authors recover similar results within their model description. Specifically for the magnetic field, they assume an inverse relationship between the magnetic field and the expanding emission region size, $B \propto 1/r$. They find flares peaking earlier than for a constant magnetic field and attribute this feature to the shift of the synchrotron critical frequency ($\nu_{syn} \propto B$) to lower values. Moreover, they argue how this creates a scenario where it takes more time to accumulate the required number of electrons to generate a peak at higher frequencies, attributing the time lags to it. In our analysis, we

notice the opposite, a delayed peak. One could investigate whether the reverse is true, that since the magnetic field strength is rising one should expect a delayed peak. Similarly, by changing the injection profile, Ref. [65] predict varying degrees of lags in the flare profiles compared to the profile. A detailed comparison of our results in light of those findings and the assumptions therein will be left for future endeavors. Lastly, we report how a similar study has been conducted in the past for blazar sources PKS 2155-304 and 3C 273 [66]. Although the method behind our works is similar, we report 3 key differences in our approaches besides the different investigated sources. The first difference is found in the time series analysis. While we have used the Gaussian process celerite (Section 3), in Ref. [66] the authors use the Emmanoulopoulos method [67]. This method takes as input parameters an evenly spaced TS, and thus the authors were forced to join the "gaps" of an unevenly spaced TS. On the contrary, the celerite approach is unaffected by unevenly spaced data. The effect of this as well as a detailed investigation of the differences between the two time series methods as well as their impact on the resulting blazar time variability should be the focus of future studies in the field. The second and most major difference is our leptohadronic model description. Ref. [66] focuses on describing the average leptonic state of their test cases and consequently model variations of their leptonic model. On the contrary, in our investigation, we consider a hybrid leptohadronic model and search for hadronic signatures such as those present during power law index variations. This constitutes also the third key difference, an investigation of different parameter variabilities. While we do not investigate changes in the Doppler factor or in external photon fields we investigate 3-parameter (magnetic field and power law index of both populations) variability and discuss the importance of the resulting hadronic signatures. Thus, our methodology significantly enhances the flexibility in studying the time variability of blazars by expanding the parameter space and establishing a coupling between the variable source parameters.

To summarize, we derived the average state description of Mrk 501 and discussed various scenarios of key parameter variability. This contribution has led to a qualitative description of the impact of each variation and its comparison to the observational behavior. We proposed statistical tools, such as flux-flux diagrams, CVs, and DCFs, for the comparison between our model and observations while posing key questions for further research in this field. Therefore, we suggest future studies to focus on the minutiae of the DCFs at small time values and a detailed investigation of the power law index variability parameter space, constraining and explaining the morphology behind the flux-flux diagram structure of the long-term variability. Lastly, using this contribution as a groundwork we suggest future studies to focus on more complex parameter combinations, such as a detailed exploration of varying escape times. Furthermore, varying Lorentz factor limits, or even a multi-zone model description could jointly be investigated by considering a two-zone model of an emission and acceleration region and connecting the maximum Lorentz factor to the efficiency of the acceleration mechanism.

Mrk 501: CTAO predictions

Using `Gammapy` we attenuated our SED models with the EBL model of Finke [64] and simulated results for the investigated variations of the energy injection rate, the magnetic field, and the power law index for both populations. Specifically, we simulated for all 3 cases the predicted count rate time series and the LCs of each scenario in the 0.3-3 TeV energy band. In this energy band, CTAO is expected to be the most sensitive, thus our results can be used as predictive tools for future observations. We note how all the simulated results follow our discussion when investigating our theoretical findings. As the power-law index variability exhibits a prominent hadronic signature we investigate various detector livetimes for this scenario. We have found that a livetime as low as 30min is capable of observing our proposed time variations in Mrk 501. Furthermore, motivated by the simulated LC of flare α, we calculated simulated spectra in the 0.3-10 TeV range for the average state of Mrk 501, its flux maximum during the flare, as well as the anti-correlation peak corresponding to the maximum of the injected TS. Lastly, we repeated our simulation for a purely leptonic scenario and contrasted our spectral results for the anti-correlation peak showcasing the clear hadronic impact on our model.

Conclusions

Throughout this thesis, we investigated a sample of blazars, conducted a time series analysis in the Fermi energy band with celerite, and derived their celerite parameters capable of creating synthetic Fermi LCs. Creating such a LC for the BL Lac Mrk 501 we investigated time variability utilizing a 12-year-long LC, in which week-long flares could be isolated. We examined variations in the particle energy injection rate, the magnetic field strength, and the power law index. For the first two, we have found that we are underpredicting the observational variability in the X-ray ranges while overpredicting the optical variability. However, the shorter time duration of the used optical data is a caveat that needs to be addressed in future works. For variations in the power law index, we investigated both leptonic and leptohadronic scenarios. We have found that to explain simultaneous flares in the X-ray range and the (V)HE range a dominant hadronic component is necessary. Furthermore, we found that by modifying the injected proton luminosity and putting an upper bound on the power law index we can find a parameter space capable of producing various strengths of flux and spectral variability. However, in the cases we tested, we exceeded the observational variability in the X-ray and optical region. We suggest the exploration of this parameter space as a topic for future studies. Lastly, we created CTAO simulations, showed the clear hadronic impact of power-law index variations, and illustrated how small livetimes can observe the proposed variability.

Appendix A

Posterior distributions without parameter bounds in the average state `emcee` investigation

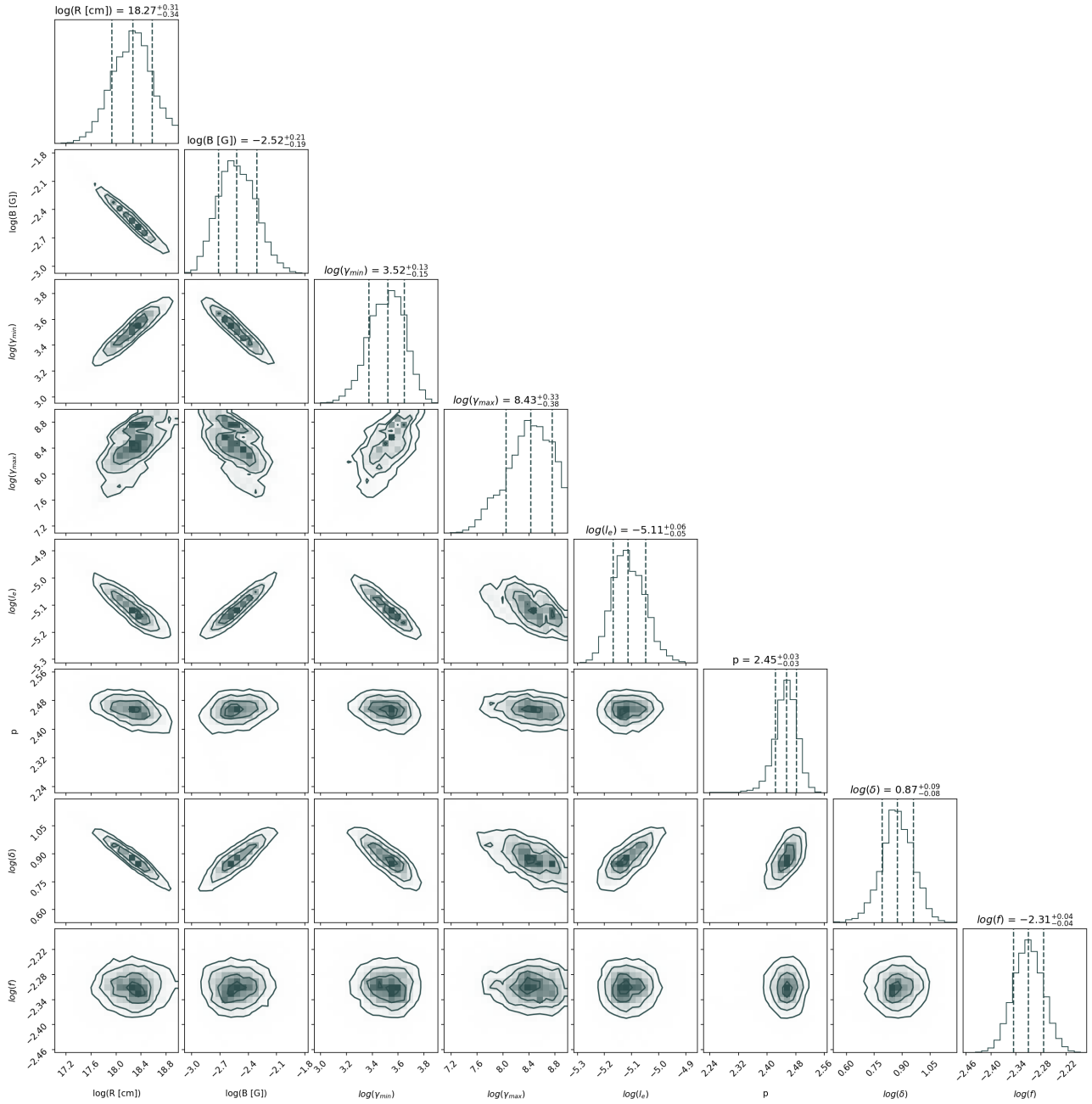

Figure A.1: Posterior distributions for the fitting process with `emcee` and `LeHaMoC` for Mrk 501 for an unbounded parameter space.

Appendix B

Posterior distributions with(out) X-ray observations in the average state `emcee` investigation

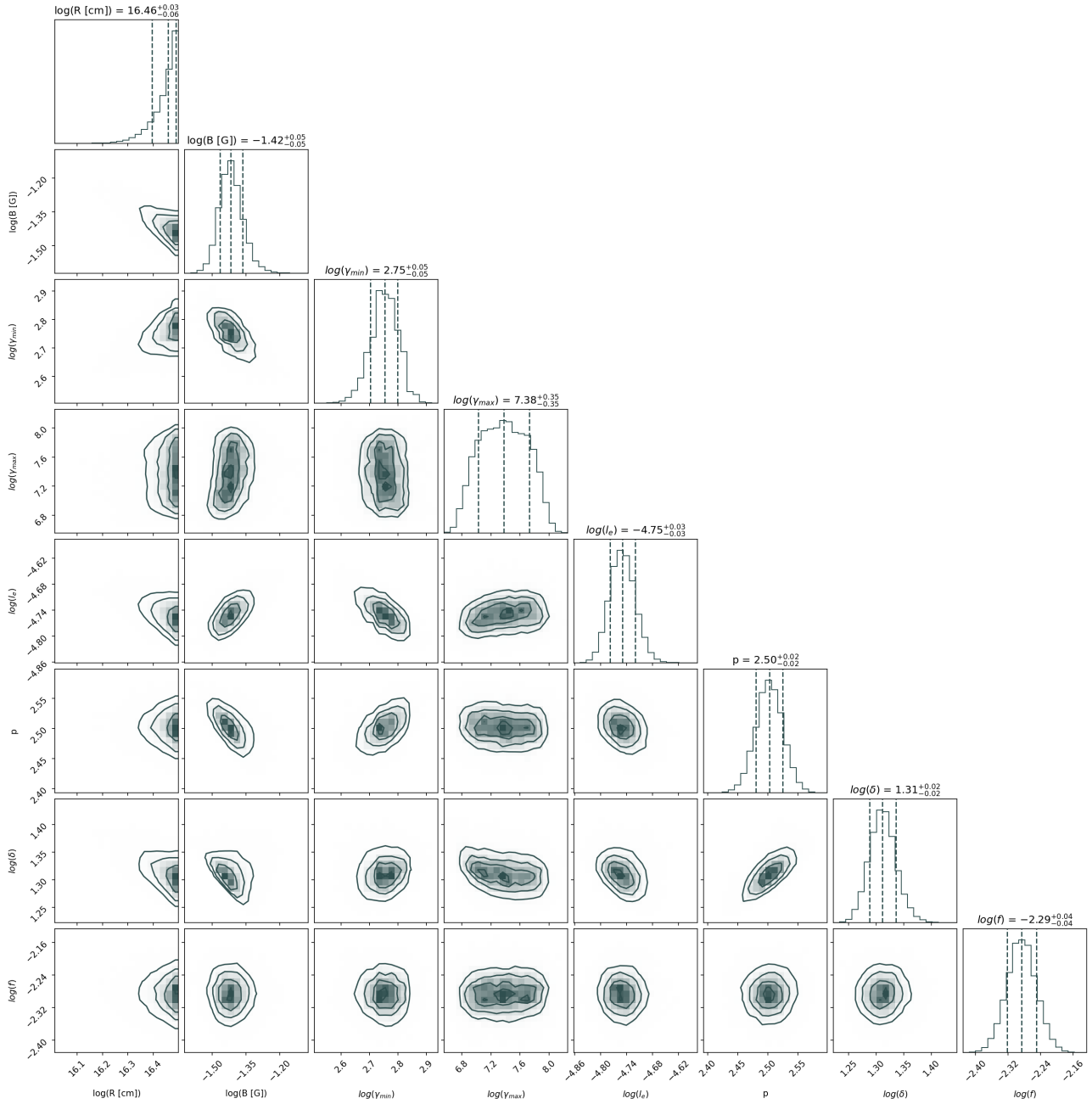

Figure B.1: Posterior distributions for the fitting process with `emcee` and `LeHaMoC` for Mrk 501 with X-ray data.

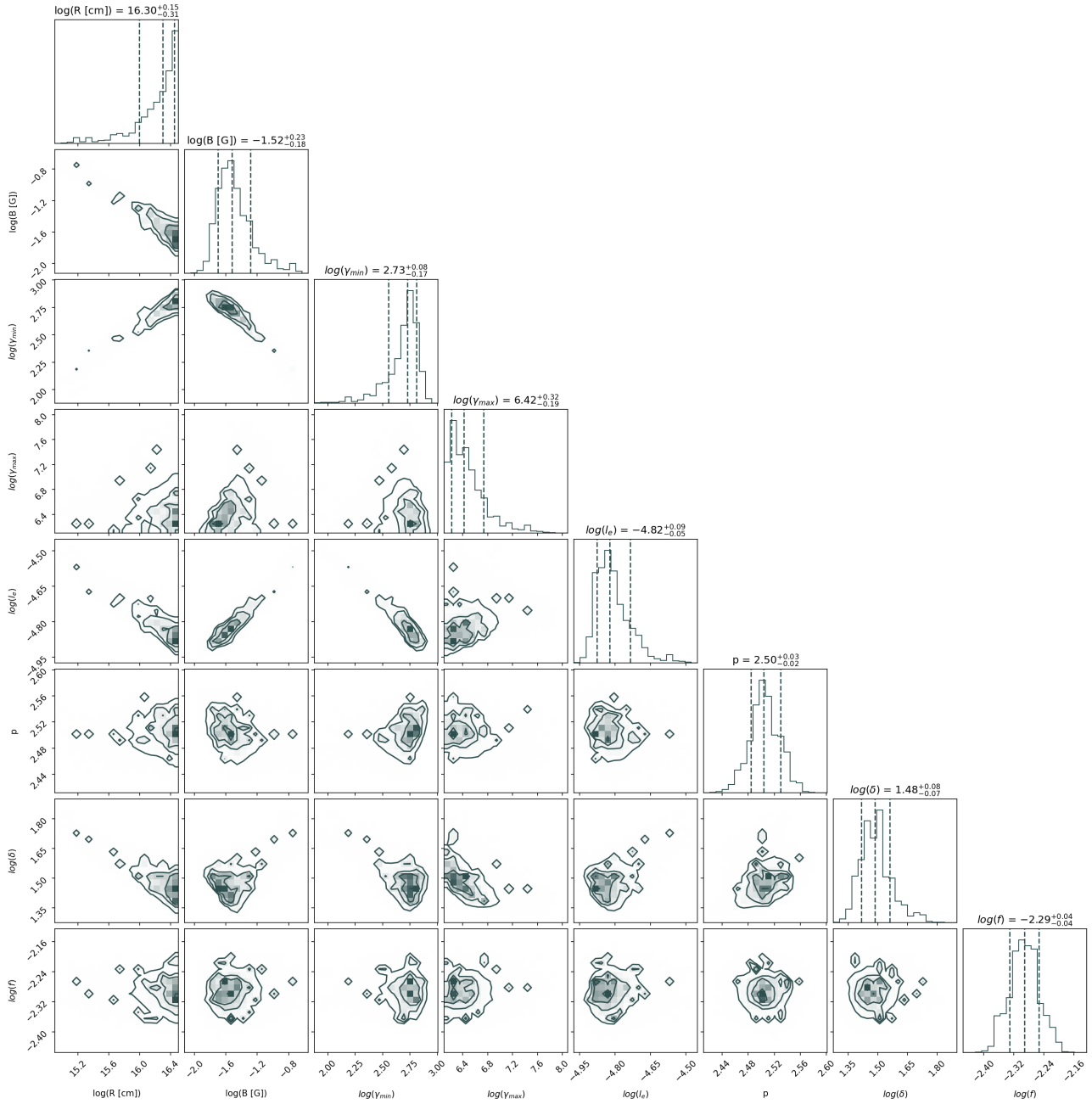

Figure B.2: Posterior distributions for the fitting process with `emcee` and `LeHaMoC` for Mrk 501 without X-ray data.

Bibliography

[1] Volker Beckmann and Chris R. Shrader. *Active Galactic Nuclei*. 2012.

[2] C. Urry. AGN Unification: An Update. In Gordon T. Richards and Patrick B. Hall, editors, *AGN Physics with the Sloan Digital Sky Survey*, volume 311 of *Astronomical Society of the Pacific Conference Series*, page 49, June 2004.

[3] Bhoomika Rajput, C. S. Stalin, and Suvendu Rakshit. Long term γ-ray variability of blazars. , 634:A80, February 2020.

[4] A. A. Abdo, M. Ackermann, I. Agudo, M. Ajello, H. D. Aller, M. F. Aller, E. Angelakis, A. A. Arkharov, M. Axelsson, U. Bach, L. Baldini, J. Ballet, G. Barbiellini, D. Bastieri, B. M. Baughman, K. Bechtol, R. Bellazzini, E. Benitez, A. Berdyugin, B. Berenji, R. D. Blandford, E. D. Bloom, M. Boettcher, E. Bonamente, A. W. Borgland, J. Bregeon, A. Brez, M. Brigida, P. Bruel, T. H. Burnett, D. Burrows, S. Buson, G. A. Caliandro, L. Calzoletti, R. A. Cameron, M. Capalbi, P. A. Caraveo, D. Carosati, J. M. Casandjian, E. Cavazzuti, C. Cecchi, Ö. Çelik, E. Charles, S. Chaty, A. Chekhtman, W. P. Chen, J. Chiang, G. Chincarini, S. Ciprini, R. Claus, J. Cohen-Tanugi, S. Colafrancesco, L. R. Cominsky, J. Conrad, L. Costamante, S. Cutini, F. D'ammando, R. Deitrick, V. D'Elia, C. D. Dermer, A. de Angelis, F. de Palma, S. W. Digel, I. Donnarumma, E. do Couto e. Silva, P. S. Drell, R. Dubois, D. Dultzin, D. Dumora, A. Falcone, C. Farnier, C. Favuzzi, S. J. Fegan, W. B. Focke, E. Forné, P. Fortin, M. Frailis, L. Fuhrmann, Y. Fukazawa, S. Funk, P. Fusco, J. L. Gómez, F. Gargano, D. Gasparrini, N. Gehrels, S. Germani, B. Giebels, N. Giglietto, P. Giommi, F. Giordano, A. Giuliani, T. Glanzman, G. Godfrey, I. A. Grenier, C. Gronwall, J. E. Grove, L. Guillemot, S. Guiriec, M. A. Gurwell, D. Hadasch, Y. Hanabata, A. K. Harding, M. Hayashida, E. Hays, S. E. Healey, J. Heidt, D. Hiriart, D. Horan, E. A. Hoversten, R. E. Hughes, R. Itoh, M. S. Jackson, G. Jóhannesson, A. S. Johnson, W. N. Johnson, S. G. Jorstad, M. Kadler, T. Kamae, H. Katagiri, J. Kataoka, N. Kawai, J. Kennea, M. Kerr, G. Kimeridze, J. Knödlseder, M. L. Kocian, E. N. Kopatskaya, E. Koptelova, T. S. Konstantinova, Y. Y. Kovalev, Yu. A. Kovalev, O. M. Kurtanidze, M. Kuss, J. Lande, V. M. Larionov, L. Latronico, P. Leto, E. Lindfors, F. Longo, F. Loparco, B. Lott, M. N. Lovellette, P. Lubrano, G. M. Madejski, A. Makeev, P. Marchegiani, A. P. Marscher, F. Marshall, W. Max-Moerbeck, M. N. Mazziotta, W. McConville, J. E. McEnery, C. Meurer, P. F. Michelson, W. Mitthumsiri, T. Mizuno, A. A. Moiseev, C. Monte, M. E. Monzani, A. Morselli, I. V. Moskalenko, S. Murgia, I. Nestoras, K. Nilsson, N. A. Nizhelsky, P. L. Nolan, J. P. Norris, E. Nuss,

T. Ohsugi, R. Ojha, N. Omodei, E. Orlando, J. F. Ormes, J. Osborne, M. Ozaki, L. Pacciani, P. Padovani, C. Pagani, K. Page, D. Paneque, J. H. Panetta, D. Parent, M. Pasanen, V. Pavlidou, V. Pelassa, M. Pepe, M. Perri, M. Pesce-Rollins, S. Piranomonte, F. Piron, C. Pittori, T. A. Porter, S. Puccetti, F. Rahoui, S. Rainò, C. Raiteri, R. Rando, M. Razzano, A. Reimer, O. Reimer, T. Reposeur, J. L. Richards, S. Ritz, L. S. Rochester, A. Y. Rodriguez, R. W. Romani, J. A. Ros, M. Roth, P. Roustazadeh, F. Ryde, H. F. W. Sadrozinski, A. Sadun, D. Sanchez, A. Sander, P. M. Saz Parkinson, J. D. Scargle, A. Sellerholm, C. Sgrò, M. S. Shaw, L. A. Sigua, E. J. Siskind, D. A. Smith, P. D. Smith, G. Spandre, P. Spinelli, J. L. Starck, M. Stevenson, G. Stratta, M. S. Strickman, D. J. Suson, H. Tajima, H. Takahashi, T. Takahashi, L. O. Takalo, T. Tanaka, J. B. Thayer, J. G. Thayer, D. J. Thompson, L. Tibaldo, D. F. Torres, G. Tosti, A. Tramacere, Y. Uchiyama, T. L. Usher, V. Vasileiou, F. Verrecchia, N. Vilchez, M. Villata, V. Vitale, A. P. Waite, P. Wang, B. L. Winer, K. S. Wood, T. Ylinen, J. A. Zensus, G. V. Zhekanis, and M. Ziegler. The Spectral Energy Distribution of Fermi Bright Blazars. , 716(1):30–70, June 2010.

[5] Donald E. Osterbrock. *Astrophysics of gaseous nebulae and active galactic nuclei*. 1989.

[6] Julian H. Krolik. *Active galactic nuclei : from the central black hole to the galactic environment*. 1999.

[7] D. J. Saikia. Jets in radio galaxies and quasars: an observational perspective. *Journal of Astrophysics and Astronomy*, 43(2):97, December 2022.

[8] Talvikki Hovatta and Elina Lindfors. Relativistic Jets of Blazars. , 87:101541, December 2019.

[9] George B. Rybicki and Alan P. Lightman. *Radiative Processes in Astrophysics*. 1986.

[10] Charles D. Dermer and Govind Menon. *High Energy Radiation from Black Holes. Gamma Rays, Cosmic Rays, and Neutrinos*. 2010.

[11] Malcolm S. Longair. *High Energy Astrophysics*. 2011.

[12] A. Mastichiadis, Mastichiadis and N Vlachakis, Vlachakis. *Αστροφυσική υψηλών ενεργειών[Undergraduate textbook]*. 2015.

[13] George R. Blumenthal and Robert J. Gould. Bremsstrahlung, Synchrotron Radiation, and Compton Scattering of High-Energy Electrons Traversing Dilute Gases. *Reviews of Modern Physics*, 42(2):237–271, January 1970.

[14] Justin D. Finke, Charles D. Dermer, and Markus Böttcher. Synchrotron Self-Compton Analysis of TeV X-Ray-Selected BL Lacertae Objects. , 686(1):181–194, October 2008.

[15] M. Petropoulou and A. Mastichiadis. Bethe-Heitler emission in BL Lacs: filling the gap between X-rays and γ-rays. , 447(1):36–48, February 2015.

[16] Robert J. Gould and Gérard P. Schréder. Pair Production in Photon-Photon Collisions. *Physical Review*, 155(5):1404–1407, March 1967.

[17] R. W. Brown, K. O. Mikaelian, and R. J. Gould. Absorption of High-Energy Cosmic Photons through Double-Pair Production in Photon-Photon Collisions. , 14:203, January 1973.

[18] A. A. Zdziarski and A. P. Lightman. Nonthermal electron-positron pair production and the 'universal' X-ray spectrum of active galactic nuclei. , 294:L79–L83, July 1985.

[19] Laura Dondi and Gabriele Ghisellini. Gamma-ray-loud blazars and beaming. , 273(3):583–595, April 1995.

[20] A. Mastichiadis, R. J. Protheroe, and J. G. Kirk. Spectral and temporal signatures of ultrarelativistic protons in compact sources. I. Effects of Bethe-Heitler pair production. , 433(3):765–776, April 2005.

[21] D. Foreman-Mackey, E. Agol, S. Ambikasaran, and R. Angus. Fast and Scalable Gaussian Process Modeling with Applications to Astronomical Time Series. , 154:220, December 2017.

[22] D. Foreman-Mackey. Scalable Backpropagation for Gaussian Processes using Celerite. *Research Notes of the American Astronomical Society*, 2(1):31, February 2018.

[23] S. Abdollahi, M. Ajello, L. Baldini, J. Ballet, D. Bastieri, J. Becerra Gonzalez, R. Bellazzini, A. Berretta, E. Bissaldi, R. Bonino, A. Brill, P. Bruel, E. Burns, S. Buson, R. A. Cameron, R. Caputo, P. A. Caraveo, N. Cibrario, S. Ciprini, P. Cristarella Orestano, M. Crnogorcevic, S. Cutini, F. D'Ammando, S. De Gaetano, S. W. Digel, N. Di Lalla, L. Di Venere, A. Domínguez, V. Fallah Ramazani, S. J. Fegan, E. C. Ferrara, A. Fiori, H. Fleischhack, A. Franckowiak, Y. Fukazawa, P. Fusco, V. Gammaldi, F. Gargano, S. Garrappa, C. Gasbarra, D. Gasparrini, N. Giglietto, F. Giordano, M. Giroletti, D. Green, I. A. Grenier, S. Guiriec, M. Gustafsson, E. Hays, D. Horan, X. Hou, G. Jóhannesson, M. Kerr, D. Kocevski, M. Kuss, L. Latronico, J. Li, I. Liodakis, F. Longo, F. Loparco, L. Lorusso, B. Lott, M. N. Lovellette, P. Lubrano, S. Maldera, A. Manfreda, G. Martí-Devesa, M. N. Mazziotta, I. Mereu, M. Meyer, P. F. Michelson, T. Mizuno, M. E. Monzani, A. Morselli, I. V. Moskalenko, M. Negro, N. Omodei, E. Orlando, J. F. Ormes, D. Paneque, G. Panzarini, J. S. Perkins, M. Persic, M. Pesce-Rollins, R. Pillera, T. A. Porter, G. Principe, J. L. Racusin, S. Rainò, R. Rando, B. Rani, M. Razzano, S. Razzaque, A. Reimer, O. Reimer, M. Sánchez-Conde, P. M. Saz Parkinson, Jeff Scargle, L. Scotton, D. Serini, C. Sgrò, E. J. Siskind, G. Spandre, P. Spinelli, D. J. Suson, H. Tajima, D. J. Thompson, D. F. Torres, J. Valverde, T. Venters, Z. Wadiasingh, S. Wagner, and K. Wood. The Fermi-LAT Lightcurve Repository. , 265(2):31, April 2023.

[24] Shenbang Yang, Dahai Yan, Pengfei Zhang, Benzhong Dai, and Li Zhang. Gaussian Process Modeling Fermi-LAT γ-Ray Blazar Variability: A Sample of Blazars with γ-Ray Quasi-periodicities. , 907(2):105, February 2021.

[25] Stefano Covino, Marco Landoni, Angela Sandrinelli, and Aldo Treves. Looking at Blazar Light-curve Periodicities with Gaussian Processes. , 895(2):122, June 2020.

[26] Colin J. Burke, Yue Shen, Yu-Ching Chen, Simone Scaringi, Claude-Andre Faucher-Giguere, Xin Liu, and Qian Yang. Optical Variability of the Dwarf AGN NGC 4395 from the Transiting Exoplanet Survey Satellite. , 899(2):136, August 2020.

[27] Haiyun Zhang, Dahai Yan, and Li Zhang. Gaussian Process Modeling Blazar Multiwavelength Variability: Indirectly Resolving Jet Structure. , 944(1):103, February 2023.

[28] Haiyun Zhang, Dahai Yan, and Li Zhang. Characterizing the γ-Ray Variability of Active Galactic Nuclei with the Stochastic Process Method. , 930(2):157, May 2022.

[29] Kip S. Thorne and Roger D. Blandford. *Modern Classical Physics Optics, Fluids, Plasmas, Elasticity, Relativity, and Statistical Physics*. 2017.

[30] T O'Haver. A pragmatic* introduction to signal processing with applications in scientific measurement; an illustrated essay with free software and spreadsheet templates to download. *terpc onnec t. umd. edu/˜ toh/spect rum/. Accessed*, 14, 2018.

[31] A. Goyal, Ł. Stawarz, S. Zola, V. Marchenko, M. Soida, K. Nilsson, S. Ciprini, A. Baran, M. Ostrowski, P. J. Wiita, Gopal-Krishna, A. Siemiginowska, M. Sobolewska, S. Jorstad, A. Marscher, M. F. Aller, H. D. Aller, T. Hovatta, D. B. Caton, D. Reichart, K. Matsumoto, K. Sadakane, K. Gazeas, M. Kidger, V. Piirola, H. Jermak, F. Alicavus, K. S. Baliyan, A. Baransky, A. Berdyugin, P. Blay, P. Boumis, D. Boyd, Y. Bufan, M. Campas Torrent, F. Campos, J. Carrillo Gómez, J. Dalessio, B. Debski, D. Dimitrov, M. Drozdz, H. Er, A. Erdem, A. Escartin Pérez, V. Fallah Ramazani, A. V. Filippenko, E. Gafton, F. Garcia, V. Godunova, F. Gómez Pinilla, M. Gopinathan, J. B. Haislip, S. Haque, J. Harmanen, R. Hudec, G. Hurst, K. M. Ivarsen, A. Joshi, M. Kagitani, N. Karaman, R. Karjalainen, N. Kaur, D. Kozieł-Wierzbowska, E. Kuligowska, T. Kundera, S. Kurowski, A. Kvammen, A. P. LaCluyze, B. C. Lee, A. Liakos, J. Lozano de Haro, J. P. Moore, M. Mugrauer, R. Naves Nogues, A. W. Neely, W. Ogloza, S. Okano, U. Pajdosz, J. C. Pandey, M. Perri, G. Poyner, J. Provencal, T. Pursimo, A. Raj, B. Rajkumar, R. Reinthal, T. Reynolds, J. Saario, S. Sadegi, T. Sakanoi, J. L. Salto González, Sameer, A. O. Simon, M. Siwak, T. Schweyer, F. C. Soldán Alfaro, E. Sonbas, J. Strobl, L. O. Takalo, L. Tremosa Espasa, J. R. Valdes, V. V. Vasylenko, F. Verrecchia, J. R. Webb, M. Yoneda, M. Zejmo, W. Zheng, P. Zielinski, J. Janik, V. Chavushyan, I. Mohammed, C. C. Cheung, and M. Giroletti. Stochastic Modeling of Multiwavelength Variability of the Classical BL Lac Object OJ 287 on Timescales Ranging from Decades to Hours. , 863(2):175, August 2018.

[32] M. A. Sobolewska, A. Siemiginowska, B. C. Kelly, and K. Nalewajko. Stochastic Modeling of the Fermi/LAT γ-Ray Blazar Variability. , 786(2):143, May 2014.

[33] H. E. S. S. Collaboration, A. Abramowski, F. Acero, F. Aharonian, A. G. Akhperjanian, G. Anton, U. Barres de Almeida, A. R. Bazer-Bachi, B. Becherini, Y. Behera, W. Benbow, K. Bernlöhr, A. Bochow, C. Boisson, J. Bolmont, V. Borrel, J. Brucker, F. Brun, P. Brun, R. Bühler, T. Bulik, I. Büsching, T. Boutelier, P. M. Chadwick, A. Charbonnier, R. C. G. Chaves, A. Cheesebrough, L. M. Chounet, A. C. Clapson, G. Coignet,

J. Conrad, L. Costamante, M. Dalton, M. K. Daniel, I. D. Davids, B. Degrange, C. Deil, H. J. Dickinson, A. Djannati-Ataï, W. Domainko, L. O'C. Drury, F. Dubois, G. Dubus, J. Dyks, M. Dyrda, K. Egberts, P. Eger, P. Espigat, L. Fallon, C. Farnier, S. Fegan, F. Feinstein, M. V. Fernandes, A. Fiasson, A. Förster, G. Fontaine, M. Füßling, S. Gabici, Y. A. Gallant, L. Gérard, D. Gerbig, B. Giebels, J. F. Glicenstein, B. Glück, P. Goret, D. Göring, D. Hampf, M. Hauser, S. Heinz, G. Heinzelmann, G. Henri, G. Hermann, J. A. Hinton, A. Hoffmann, W. Hofmann, P. Hofverberg, M. Holleran, S. Hoppe, D. Horns, A. Jacholkowska, O. C. de Jager, C. Jahn, I. Jung, K. Katarzyński, U. Katz, S. Kaufmann, M. Kerschhaggl, D. Khangulyan, B. Khélifi, D. Keogh, D. Klochkov, W. Kluźniak, T. Kneiske, Nu. Komin, K. Kosack, R. Kossakowski, G. Lamanna, J. P. Lenain, T. Lohse, C. C. Lu, V. Marandon, A. Marcowith, J. Masbou, D. Maurin, T. J. L. McComb, M. C. Medina, J. Méhault, R. Moderski, E. Moulin, M. Naumann-Godo, M. de Naurois, D. Nedbal, D. Nekrassov, N. Nguyen, B. Nicholas, J. Niemiec, S. J. Nolan, S. Ohm, J. F. Olive, E. de Oña Wilhelmi, B. Opitz, K. J. Orford, M. Ostrowski, M. Panter, M. Paz Arribas, G. Pedaletti, G. Pelletier, P. O. Petrucci, S. Pita, G. Pühlhofer, M. Punch, A. Quirrenbach, B. C. Raubenheimer, M. Raue, S. M. Rayner, O. Reimer, M. Renaud, R. de los Reyes, F. Rieger, J. Ripken, L. Rob, S. Rosier-Lees, G. Rowell, B. Rudak, C. B. Rulten, J. Ruppel, F. Ryde, V. Sahakian, A. Santangelo, R. Schlickeiser, F. M. Schöck, A. Schönwald, U. Schwanke, S. Schwarzburg, S. Schwemmer, A. Shalchi, I. Sushch, M. Sikora, J. L. Skilton, H. Sol, Ł. Stawarz, R. Steenkamp, C. Stegmann, F. Stinzing, G. Superina, A. Szostek, P. H. Tam, J. P. Tavernet, R. Terrier, O. Tibolla, M. Tluczykont, K. Valerius, C. van Eldik, G. Vasileiadis, C. Venter, L. Venter, J. P. Vialle, A. Viana, P. Vincent, M. Vivier, H. J. Völk, F. Volpe, S. Vorobiov, S. J. Wagner, M. Ward, A. A. Zdziarski, A. Zech, and H. S. Zechlin. VHE γ-ray emission of PKS 2155-304: spectral and temporal variability. , 520:A83, September 2010.

[34] H. E. S. S. Collaboration, H. Abdalla, A. Abramowski, F. Aharonian, F. Ait Benkhali, A. G. Akhperjanian, T. Andersson, E. O. Angüner, M. Arrieta, P. Aubert, M. Backes, A. Balzer, M. Barnard, Y. Becherini, J. Becker Tjus, D. Berge, S. Bernhard, K. Bernlöhr, R. Blackwell, M. Böttcher, C. Boisson, J. Bolmont, P. Bordas, J. Bregeon, F. Brun, P. Brun, M. Bryan, T. Bulik, M. Capasso, J. Carr, S. Casanova, M. Cerruti, N. Chakraborty, R. Chalme-Calvet, R. C. G. Chaves, A. Chen, J. Chevalier, M. Chrétien, S. Colafrancesco, G. Cologna, B. Condon, J. Conrad, Y. Cui, I. D. Davids, J. Decock, B. Degrange, C. Deil, J. Devin, P. deWilt, L. Dirson, A. Djannati-Ataï, W. Domainko, A. Donath, L. O. 'C. Drury, G. Dubus, K. Dutson, J. Dyks, T. Edwards, K. Egberts, P. Eger, J. P. Ernenwein, S. Eschbach, C. Farnier, S. Fegan, M. V. Fernandes, A. Fiasson, G. Fontaine, A. Förster, S. Funk, M. Füßling, S. Gabici, M. Gajdus, Y. A. Gallant, T. Garrigoux, G. Giavitto, B. Giebels, J. F. Glicenstein, D. Gottschall, A. Goyal, M. H. Grondin, D. Hadasch, J. Hahn, M. Haupt, J. Hawkes, G. Heinzelmann, G. Henri, G. Hermann, O. Hervet, J. A. Hinton, W. Hofmann, C. Hoischen, M. Holler, D. Horns, A. Ivascenko, A. Jacholkowska, M. Jamrozy, M. Janiak, D. Jankowsky, F. Jankowsky, M. Jingo, T. Jogler, L. Jouvin, I. Jung-Richardt, M. A. Kastendieck, K. Katarzyński, U. Katz,

D. Kerszberg, B. Khélifi, M. Kieffer, J. King, S. Klepser, D. Klochkov, W. Kluźniak, D. Kolitzus, Nu. Komin, K. Kosack, S. Krakau, M. Kraus, F. Krayzel, P. P. Krüger, H. Laffon, G. Lamanna, J. Lau, J. P. Lees, J. Lefaucheur, V. Lefranc, A. Lemière, M. Lemoine-Goumard, J. P. Lenain, E. Leser, T. Lohse, M. Lorentz, R. Liu, R. López-Coto, I. Lypova, V. Marandon, A. Marcowith, C. Mariaud, R. Marx, G. Maurin, N. Maxted, M. Mayer, P. J. Meintjes, M. Meyer, A. M. W. Mitchell, R. Moderski, M. Mohamed, L. Mohrmann, K. Morå, E. Moulin, T. Murach, M. de Naurois, F. Niederwanger, J. Niemiec, L. Oakes, P. O'Brien, H. Odaka, S. Öttl, S. Ohm, M. Ostrowski, I. Oya, M. Padovani, M. Panter, R. D. Parsons, N. W. Pekeur, G. Pelletier, C. Perennes, P. O. Petrucci, B. Peyaud, Q. Piel, S. Pita, H. Poon, D. Prokhorov, H. Prokoph, G. Pühlhofer, M. Punch, A. Quirrenbach, S. Raab, A. Reimer, O. Reimer, M. Renaud, R. de los Reyes, F. Rieger, C. Romoli, S. Rosier-Lees, G. Rowell, B. Rudak, C. B. Rulten, V. Sahakian, D. Salek, D. A. Sanchez, A. Santangelo, M. Sasaki, R. Schlickeiser, F. Schüssler, A. Schulz, U. Schwanke, S. Schwemmer, M. Settimo, A. S. Seyffert, N. Shafi, I. Shilon, R. Simoni, H. Sol, F. Spanier, G. Spengler, F. Spies, Ł. Stawarz, R. Steenkamp, C. Stegmann, F. Stinzing, K. Stycz, I. Sushch, J. P. Tavernet, T. Tavernier, A. M. Taylor, R. Terrier, L. Tibaldo, D. Tiziani, M. Tluczykont, C. Trichard, R. Tuffs, Y. Uchiyama, D. J. van der Walt, C. van Eldik, C. van Rensburg, B. van Soelen, G. Vasileiadis, J. Veh, C. Venter, A. Viana, P. Vincent, J. Vink, F. Voisin, H. J. Völk, T. Vuillaume, Z. Wadiasingh, S. J. Wagner, P. Wagner, R. M. Wagner, R. White, A. Wierzcholska, P. Willmann, A. Wörnlein, D. Wouters, R. Yang, V. Zabalza, D. Zaborov, M. Zacharias, A. A. Zdziarski, A. Zech, F. Zefi, A. Ziegler, and N. Żywucka. Characterizing the γ-ray long-term variability of PKS 2155-304 with H.E.S.S. and Fermi-LAT. , 598:A39, February 2017.

[35] Daniel Foreman-Mackey, David W. Hogg, Dustin Lang, and Jonathan Goodman. emcee: The MCMC Hammer. , 125(925):306, March 2013.

[36] H. E. S. S. Collaboration, A. Abramowski, F. Acero, F. Aharonian, A. G. Akhperjanian, G. Anton, A. Balzer, A. Barnacka, U. Barres de Almeida, Y. Becherini, J. Becker, B. Behera, W. Benbow, K. Bernlöhr, A. Bochow, C. Boisson, J. Bolmont, P. Bordas, T. Bouteilier, J. Brucker, F. Brun, P. Brun, T. Bulik, I. Büsching, S. Carrigan, S. Casanova, M. Cerruti, P. M. Chadwick, A. Charbonnier, R. C. G. Chaves, A. Cheesebrough, L. M. Chounet, A. C. Clapson, G. Coignet, G. Cologna, P. Colom, J. Conrad, N. Coudreau, M. Dalton, M. K. Daniel, I. D. Davids, B. Degrange, C. Deil, H. J. Dickinson, A. Djannati-Ataï, W. Domainko, L. O'c. Drury, F. Dubois, G. Dubus, K. Dutson, J. Dyks, M. Dyrda, P. Edwards, K. Egberts, P. Eger, P. Espigat, L. Fallon, C. Farnier, S. Fegan, F. Feinstein, M. V. Fernandes, A. Fiasson, G. Fontaine, A. Förster, M. Füßling, Y. A. Gallant, H. Gast, M. J. Gaylard, L. Gérard, D. Gerbig, B. Giebels, J. F. Glicenstein, B. Glück, P. Goret, D. Göring, S. Häffner, J. D. Hague, D. Hampf, M. Hauser, S. Heinz, G. Heinzelmann, G. Henri, G. Hermann, J. A. Hinton, A. Hoffmann, W. Hofmann, P. Hofvergerg, M. Holler, D. Horns, A. Jacholkowska, O. C. de Jager, C. Jahn, M. Jamrozy, I. Jung, M. A. Kastendieck, K. Katarzyński, U. Katz, S. Kaufmann, D. Keogh, D. Khangulyan, B. Khélifi, M. Klein, D. Klochkov, W. Kluźniak, T. Kneiske, Nu. Komin, K. Kosack,

R. Kossakowski, P. Kubanek, H. Laffon, G. Lamanna, D. Lennarz, J. P. Lenain, T. Lohse, A. Lopatin, C. C. Lu, V. Marandon, A. Marcowith, J. M. Martin, J. Masbou, D. Maurin, N. Maxted, T. J. L. McComb, M. C. Medina, J. Méhault, G. Melady, N. Nguyen, R. Moderski, B. Monard, E. Moulin, C. L. Naumann, M. Naumann-Godo, M. de Naurois, D. Nedbal, D. Nekrassov, B. Nicholas, J. Niemiec, S. J. Nolan, S. Ohm, E. de Oña Wilhelmi, B. Opitz, M. Ostrowski, I. Oya, M. Panter, M. Paz Arribas, G. Pedaletti, G. Pelletier, P. O. Petrucci, S. Pita, G. Pühlhofer, M. Punch, A. Quirrenbach, M. Raue, S. M. Rayner, A. Reimer, O. Reimer, M. Renaud, R. de Los Reyes, F. Rieger, J. Ripken, L. Rob, S. Rosier-Lees, G. Rowell, B. Rudak, C. B. Rulten, J. Ruppel, F. Ryde, V. Sahakian, A. Santangelo, R. Schlickeiser, F. M. Schöck, A. Schulz, U. Schwanke, S. Schwarzburg, S. Schwemmer, M. Sikora, J. L. Skilton, H. Sol, G. Spengler, Ł. Stawarz, R. Steenkamp, C. Stegmann, F. Stinzing, K. Stycz, I. Sushch, A. Szostek, J. P. Tavernet, R. Terrier, M. Tluczykont, A. Tzioumis, K. Valerius, C. van Eldik, G. Vasileiadis, C. Venter, L. Venter, J. P. Vialle, A. Viana, P. Vincent, H. J. Völk, F. Volpe, S. Vorobiov, M. Vorster, S. J. Wagner, M. Ward, R. White, A. Wierzcholska, M. Zacharias, A. Zajczyk, A. A. Zdziarski, A. Zech, and H. S. Zechlin. A multiwavelength view of the flaring state of PKS 2155-304 in 2006. , 539:A149, March 2012.

[37] M. Ackermann, M. Ajello, A. Albert, W. B. Atwood, L. Baldini, J. Ballet, G. Barbiellini, D. Bastieri, J. Becerra Gonzalez, R. Bellazzini, E. Bissaldi, R. D. Blandford, E. D. Bloom, R. Bonino, E. Bottacini, J. Bregeon, P. Bruel, R. Buehler, S. Buson, G. A. Caliandro, R. A. Cameron, R. Caputo, M. Caragiulo, P. A. Caraveo, E. Cavazzuti, C. Cecchi, A. Chekhtman, J. Chiang, G. Chiaro, S. Ciprini, J. Cohen-Tanugi, J. Conrad, S. Cutini, F. D'Ammando, A. de Angelis, F. de Palma, R. Desiante, L. Di Venere, A. Domínguez, P. S. Drell, C. Favuzzi, S. J. Fegan, E. C. Ferrara, W. B. Focke, L. Fuhrmann, Y. Fukazawa, P. Fusco, F. Gargano, D. Gasparrini, N. Giglietto, P. Giommi, F. Giordano, M. Giroletti, G. Godfrey, D. Green, I. A. Grenier, J. E. Grove, S. Guiriec, A. K. Harding, E. Hays, J. W. Hewitt, A. B. Hill, D. Horan, T. Jogler, G. Jóhannesson, A. S. Johnson, T. Kamae, M. Kuss, S. Larsson, L. Latronico, J. Li, L. Li, F. Longo, F. Loparco, B. Lott, M. N. Lovellette, P. Lubrano, J. Magill, S. Maldera, A. Manfreda, W. Max-Moerbeck, M. Mayer, M. N. Mazziotta, J. E. McEnery, P. F. Michelson, T. Mizuno, M. E. Monzani, A. Morselli, I. V. Moskalenko, S. Murgia, E. Nuss, M. Ohno, T. Ohsugi, R. Ojha, N. Omodei, E. Orlando, J. F. Ormes, D. Paneque, T. J. Pearson, J. S. Perkins, M. Perri, M. Pesce-Rollins, V. Petrosian, F. Piron, G. Pivato, T. A. Porter, S. Rainò, R. Rando, M. Razzano, A. Readhead, A. Reimer, O. Reimer, A. Schulz, C. Sgrò, E. J. Siskind, F. Spada, G. Spandre, P. Spinelli, D. J. Suson, H. Takahashi, J. B. Thayer, D. J. Thompson, L. Tibaldo, D. F. Torres, G. Tosti, E. Troja, Y. Uchiyama, G. Vianello, K. S. Wood, M. Wood, S. Zimmer, A. Berdyugin, R. H. D. Corbet, T. Hovatta, E. Lindfors, K. Nilsson, R. Reinthal, A. Sillanpää, A. Stamerra, L. O. Takalo, and M. J. Valtonen. Multiwavelength Evidence for Quasi-periodic Modulation in the Gamma-Ray Blazar PG 1553+113. , 813(2):L41, November 2015.

[38] MAGIC Collaboration, V. A. Acciari, S. Ansoldi, L. A. Antonelli, A. Babić, B. Baner-

jee, U. Barres de Almeida, J. A. Barrio, J. Becerra González, W. Bednarek, E. Bernardini, A. Berti, J. Besenrieder, W. Bhattacharyya, C. Bigongiari, O. Blanch, G. Bonnoli, G. Busetto, R. Carosi, G. Ceribella, S. Cikota, S. M. Colak, P. Colin, E. Colombo, J. L. Contreras, J. Cortina, S. Covino, V. D'Elia, P. da Vela, F. Dazzi, A. de Angelis, B. de Lotto, M. Delfino, J. Delgado, F. di Pierro, E. Do Souto Espiñera, A. Domínguez, D. Dominis Prester, M. Doro, V. Fallah Ramazani, A. Fattorini, A. Fernández-Barral, G. Ferrara, D. Fidalgo, L. Foffano, M. V. Fonseca, L. Font, C. Fruck, D. Galindo, S. Gallozzi, R. J. García López, M. Garczarczyk, S. Gasparyan, M. Gaug, P. Giammaria, N. Godinović, D. Guberman, D. Hadasch, A. Hahn, T. Hassan, J. Herrera, J. Hoang, D. Hrupec, S. Inoue, K. Ishio, Y. Iwamura, H. Kubo, J. Kushida, D. Kuveždić, A. Lamastra, D. Lelas, F. Leone, E. Lindfors, S. Lombardi, F. Longo, M. López, A. López-Oramas, B. Machado de Oliveira Fraga, C. Maggio, P. Majumdar, M. Makariev, M. Mallamaci, G. Maneva, M. Manganaro, L. Maraschi, M. Mariotti, M. Martínez, S. Masuda, D. Mazin, M. Minev, J. M. Miranda, R. Mirzoyan, E. Molina, A. Moralejo, V. Moreno, E. Moretti, P. Munar-Adrover, V. Neustroev, A. Niedzwiecki, M. Nievas Rosillo, C. Nigro, K. Nilsson, D. Ninci, K. Nishijima, K. Noda, L. Nogués, S. Paiano, J. Palacio, D. Paneque, R. Paoletti, J. M. Paredes, G. Pedaletti, P. Peñil, M. Peresano, M. Persic, P. G. Prada Moroni, E. Prandini, I. Puljak, J. R. Garcia, M. Ribó, J. Rico, C. Righi, A. Rugliancich, L. Saha, N. Sahakyan, T. Saito, K. Satalecka, T. Schweizer, J. Sitarek, I. Šnidarić, D. Sobczynska, A. Somero, A. Stamerra, M. Strzys, T. Surić, F. Tavecchio, P. Temnikov, T. Terzić, M. Teshima, N. Torres-Albà, S. Tsujimoto, J. van Scherpenberg, G. Vanzo, M. Vazquez Acosta, I. Vovk, M. Will, D. Zarić, Fact Collaboration, A. Arbet-Engels, D. Baack, M. Balbo, A. Biland, M. Blank, T. Bretz, K. Bruegge, M. Bulinski, J. Buss, M. Doerr, D. Dorner, S. Einecke, D. Elsaesser, D. Hildebrand, L. Linhoff, K. Mannheim, S. Mueller, D. Neise, A. Neronov, M. Noethe, A. Paravac, W. Rhode, B. Schleicher, F. Schulz, K. Sedlaczek, A. Shukla, V. Sliusar, E. von Willert, R. Walter, C. Wendel, A. Tramacere, A. Lien, M. Perri, F. Verrecchia, M. Armas Padilla, C. Leto, A. Lähteenmäki, M. Tornikoski, and J. Tammi. Study of the variable broadband emission of Markarian 501 during the most extreme Swift X-ray activity. , 637:A86, May 2020.

[39] MAGIC Collaboration, V. A. Acciari, S. Ansoldi, L. A. Antonelli, A. Babić, B. Banerjee, U. Barres de Almeida, J. A. Barrio, J. Becerra González, W. Bednarek, E. Bernardini, A. Berti, J. Besenrieder, W. Bhattacharyya, C. Bigongiari, O. Blanch, G. Bonnoli, G. Busetto, R. Carosi, G. Ceribella, S. Cikota, S. M. Colak, P. Colin, E. Colombo, J. L. Contreras, J. Cortina, S. Covino, V. D'Elia, P. da Vela, F. Dazzi, A. de Angelis, B. de Lotto, M. Delfino, J. Delgado, F. di Pierro, E. Do Souto Espiñera, A. Domínguez, D. Dominis Prester, M. Doro, V. Fallah Ramazani, A. Fattorini, A. Fernández-Barral, G. Ferrara, D. Fidalgo, L. Foffano, M. V. Fonseca, L. Font, C. Fruck, D. Galindo, S. Gallozzi, R. J. García López, M. Garczarczyk, S. Gasparyan, M. Gaug, P. Giammaria, N. Godinović, D. Guberman, D. Hadasch, A. Hahn, T. Hassan, J. Herrera, J. Hoang, D. Hrupec, S. Inoue, K. Ishio, Y. Iwamura, H. Kubo, J. Kushida, D. Kuveždić, A. Lamastra, D. Lelas, F. Leone, E. Lindfors, S. Lombardi, F. Longo, M. López, A. López-Oramas, B. Machado

de Oliveira Fraga, C. Maggio, P. Majumdar, M. Makariev, M. Mallamaci, G. Maneva, M. Manganaro, L. Maraschi, M. Mariotti, M. Martínez, S. Masuda, D. Mazin, M. Minev, J. M. Miranda, R. Mirzoyan, E. Molina, A. Moralejo, V. Moreno, E. Moretti, P. Munar-Adrover, V. Neustroev, A. Niedzwiecki, M. Nievas Rosillo, C. Nigro, K. Nilsson, D. Ninci, K. Nishijima, K. Noda, L. Nogués, S. Paiano, J. Palacio, D. Paneque, R. Paoletti, J. M. Paredes, G. Pedaletti, P. Peñil, M. Peresano, M. Persic, P. G. Prada Moroni, E. Prandini, I. Puljak, J. R. Garcia, M. Ribó, J. Rico, C. Righi, A. Rugliancich, L. Saha, N. Sahakyan, T. Saito, K. Satalecka, T. Schweizer, J. Sitarek, I. Šnidarić, D. Sobczynska, A. Somero, A. Stamerra, M. Strzys, T. Surić, F. Tavecchio, P. Temnikov, T. Terzić, M. Teshima, N. Torres-Albà, S. Tsujimoto, J. van Scherpenberg, G. Vanzo, M. Vazquez Acosta, I. Vovk, M. Will, D. Zarić, Fact Collaboration, A. Arbet-Engels, D. Baack, M. Balbo, A. Biland, M. Blank, T. Bretz, K. Bruegge, M. Bulinski, J. Buss, M. Doerr, D. Dorner, S. Einecke, D. Elsaesser, D. Hildebrand, L. Linhoff, K. Mannheim, S. Mueller, D. Neise, A. Neronov, M. Noethe, A. Paravac, W. Rhode, B. Schleicher, F. Schulz, K. Sedlaczek, A. Shukla, V. Sliusar, E. von Willert, R. Walter, C. Wendel, A. Tramacere, A. Lien, M. Perri, F. Verrecchia, M. Armas Padilla, C. Leto, A. Lähteenmäki, M. Tornikoski, and J. Tammi. Study of the variable broadband emission of Markarian 501 during the most extreme Swift X-ray activity. , 637:A86, May 2020.

[40] A. Albert, R. Alfaro, C. Alvarez, J. R. Angeles Camacho, J. C. Arteaga-Velázquez, K. P. Arunbabu, D. Avila Rojas, H. A. Ayala Solares, V. Baghmanyan, E. Belmont-Moreno, K. S. Caballero-Mora, T. Capistrán, A. Carramiñana, S. Casanova, U. Cotti, J. Cotzomi, S. Coutiño de León, E. de La Fuente, R. Diaz Hernandez, M. A. Duvernois, M. Durocher, J. C. Díaz-Vélez, K. Engel, C. Espinoza, K. L. Fan, M. Fernández Alonso, N. Fraija, D. Garcia, J. A. García-González, F. Garfias, M. M. González, J. A. Goodman, J. P. Harding, B. Hona, D. Huang, F. Hueyotl-Zahuantitla, P. Hüntemeyer, A. Iriarte, V. Joshi, A. Lara, W. H. Lee, J. Lee, H. León Vargas, J. T. Linneman, A. L. Longinotti, G. Luis-Raya, K. Malone, O. Martinez, J. Martínez-Castro, J. A. Matthews, P. Miranda-Romagnoli, E. Moreno, M. Mostafá, A. Nayerhoda, L. Nellen, M. Newbold, R. Noriega-Papaqui, A. Peisker, Y. Pérez Araujo, E. G. Pérez-Pérez, C. D. Rho, D. Rosa-González, H. Salazar, F. Salesa Greus, A. Sandoval, M. Schneider, J. Serna-Franco, A. J. Smith, R. W. Springer, K. Tollefson, I. Torres, R. Torres-Escobedo, F. Ureña-Mena, L. Villaseñor, X. Wang, T. Weisgarber, E. Willox, H. Zhou, C. de León, and HAWC Collaboration. Long-term Spectra of the Blazars Mrk 421 and Mrk 501 at TeV Energies Seen by HAWC. , 929(2):125, April 2022.

[41] B. Bartoli, P. Bernardini, X. J. Bi, C. Bleve, I. Bolognino, P. Branchini, A. Budano, A. K. Calabrese Melcarne, P. Camarri, Z. Cao, R. Cardarelli, S. Catalanotti, C. Cattaneo, S. Z. Chen, T. L. Chen, Y. Chen, P. Creti, S. W. Cui, B. Z. Dai, G. D'Alí Staiti, Danzengluobu, M. Dattoli, I. De Mitri, B. D'Ettorre Piazzoli, T. Di Girolamo, X. H. Ding, G. Di Sciascio, C. F. Feng, Zhaoyang Feng, Zhenyong Feng, F. Galeazzi, E. Giroletti, Q. B. Gou, Y. Q. Guo, H. H. He, Haibing Hu, Hongbo Hu, Q. Huang, M. Iacovacci, R. Iuppa, I. James, H. Y. Jia, Labaciren, H. J. Li, J. Y. Li, X. X. Li, G. Liguori, C. Liu, C. Q. Liu, J. Liu, M. Y. Liu, H. Lu, L. L. Ma, X. H. Ma, G. Mancarella, S. M. Mari, G. Marsella,

D. Martello, S. Mastroianni, P. Montini, C. C. Ning, A. Pagliaro, M. Panareo, B. Panico, L. Perrone, P. Pistilli, F. Ruggieri, P. Salvini, R. Santonico, P. R. Shen, X. D. Sheng, F. Shi, C. Stanescu, A. Surdo, Y. H. Tan, P. Vallania, S. Vernetto, C. Vigorito, B. Wang, H. Wang, C. Y. Wu, H. R. Wu, B. Xu, L. Xue, Q. Y. Yang, X. C. Yang, Z. G. Yao, A. F. Yuan, M. Zha, H. M. Zhang, Jilong Zhang, Jianli Zhang, L. Zhang, P. Zhang, X. Y. Zhang, Y. Zhang, J. Zhao, Zhaxiciren, Zhaxisangzhu, X. X. Zhou, F. R. Zhu, Q. Q. Zhu, G. Zizzi, and ARGO-YBJ Collaboration. Long-term Monitoring of Mrk 501 for its Very High Energy γ Emission and a Flare in 2011 October. , 758(1):2, October 2012.

[42] S. V. Godambe, R. C. Rannot, P. Chandra, K. K. Yadav, A. K. Tickoo, K. Venugopal, N. Bhatt, S. Bhattacharyya, K. Chanchalani, V. K. Dhar, H. C. Goyal, R. K. Kaul, M. Kothari, S. Kotwal, M. K. Koul, R. Koul, B. S. Sahaynathan, M. Sharma, and S. Thoudam. Very high energy γ-ray observations of Mrk 501 using the TACTIC imaging γ-ray telescope during 2005 06. *Journal of Physics G Nuclear Physics*, 35(6):065202, June 2008.

[43] F. A. Aharonian, A. G. Akhperjanian, J. A. Barrio, K. Bernlöhr, O. Bolz, H. Börst, H. Bojahr, J. L. Contreras, J. Cortina, S. Denninghoff, V. Fonseca, J. C. Gonzalez, N. Götting, G. Heinzelmann, G. Hermann, A. Heusler, W. Hofmann, D. Horns, A. Ibarra, C. Iserlohe, I. Jung, R. Kankanyan, M. Kestel, J. Kettler, A. Kohnle, A. Konopelko, H. Kornmeyer, D. Kranich, H. Krawczynski, H. Lampeitl, E. Lorenz, F. Lucarelli, N. Magnussen, O. Mang, H. Meyer, R. Mirzoyan, A. Moralejo, L. Padilla, M. Panter, R. Plaga, A. Plyasheshnikov, J. Prahl, G. Pühlhofer, W. Rhode, A. Röhring, G. P. Rowell, V. Sahakian, M. Samorski, M. Schilling, F. Schröder, M. Siems, W. Stamm, M. Tluczykont, H. J. Völk, C. Wiedner, and W. Wittek. Reanalysis of the high energy cutoff of the 1997 Mkn 501 TeV energy spectrum. , 366:62–67, January 2001.

[44] J. Biteau and D. A. Williams. The Extragalactic Background Light, the Hubble Constant, and Anomalies: Conclusions from 20 Years of TeV Gamma-ray Observations. , 812(1):60, October 2015.

[45] P. Giommi, M. Capalbi, M. Fiocchi, E. Memola, M. Perri, S. Piranomonte, S. Rebecchi, and E. Massaro. A Catalog of 157 X-ray Spectra and 84 Spectral Energy Distributions of Blazars Observed with BeppoSAX. In Paolo Giommi, Enrico Massaro, and Giorgio Palumbo, editors, *Blazar Astrophysics with BeppoSAX and Other Observatories*, page 63, January 2002.

[46] A. Acharyya, C. B. Adams, A. Archer, P. Bangale, J. T. Bartkoske, P. Batista, W. Benbow, A. Brill, R. Brose, J. H. Buckley, M. Capasso, J. L. Christiansen, A. J. Chromey, M. K. Daniel, M. Errando, A. Falcone, K. A. Farrell, Q. Feng, J. P. Finley, Juniper Foote, L. Fortson, A. Furniss, G. Gallagher, A. Gent, C. Giuri, O. Gueta, W. F. Hanlon, D. Hanna, T. Hassan, O. Hervet, J. Hoang, J. Holder, G. Hughes, T. B. Humensky, W. Jin, P. Kaaret, M. Kertzman, D. Kieda, T. K. Kleiner, N. Korzoun, F. Krennrich, S. Kumar, M. J. Lang, M. Lundy, G. Maier, C. E. McGrath, M. J. Millard, C. L. Mooney, P. Moriarty,

R. Mukherjee, D. Nieto, M. Nievas-Rosillo, S. O'Brien, R. A. Ong, A. N. Otte, D. Pandel, N. Park, S. R. Patel, S. Patel, K. Pfrang, A. Pichel, M. Pohl, R. R. Prado, E. Pueschel, J. Quinn, K. Ragan, P. T. Reynolds, D. Ribeiro, G. T. Richards, E. Roache, A. C. Rovero, C. Rulten, J. L. Ryan, I. Sadeh, M. Santander, S. Schlenstedt, G. H. Sembroski, R. Shang, M. Splettstoesser, B. Stevenson, D. Tak, V. V. Vassiliev, S. P. Wakely, A. Weinstein, D. A. Williams, T. J. Williamson, L. Angelini, A. Basu-Zych, E. Sabol, and A. Smale. VTSCat: The VERITAS Catalog of Gamma-Ray Observations. *Research Notes of the American Astronomical Society*, 7(1):6, January 2023.

[47] P. W. Guilbert, A. C. Fabian, and M. J. Rees. Spectral and variability constraints on compact sources. , 205:593–603, November 1983.

[48] S. I. Stathopoulos, M. Petropoulou, G. Vasilopoulos, and A. Mastichiadis. LeHaMoC: A versatile time-dependent lepto-hadronic modeling code for high-energy astrophysical sources. *A&A*, 683:A225, March 2024.

[49] J. S. Chang and G. Cooper. A Practical Difference Scheme for Fokker-Planck Equations. *Journal of Computational Physics*, 6(1):1–16, August 1970.

[50] X. Rodrigues, V. S. Paliya, S. Garrappa, A. Omeliukh, A. Franckowiak, and W. Winter. Leptohadronic multi-messenger modeling of 324 gamma-ray blazars. , 681:A119, January 2024.

[51] M. Petropoulou, A. Mastichiadis, G. Vasilopoulos, D. Paneque, J. Becerra González, and F. Zanias. TeV pion bumps in the gamma-ray spectra of flaring blazars. , 685:A110, May 2024.

[52] Hannes Thiersen, Michael Zacharias, and Markus Böttcher. Characterising the Long-Term Variability of Blazars in Leptonic Models. *Galaxies*, 7(1):35, March 2019.

[53] A. S. Karaferias, G. Vasilopoulos, M. Petropoulou, P. A. Jenke, C. A. Wilson-Hodge, and C. Malacaria. A Bayesian approach for torque modelling of BeXRB pulsars with application to super-Eddington accretors. , 520(1):281–299, March 2023.

[54] Margaritis Chatzis, Maria Petropoulou, and Georgios Vasilopoulos. Radio emission from colliding outflows in high-mass X-ray binaries with strongly magnetized neutron stars. , 509(2):2532–2550, January 2022.

[55] Cherenkov Telescope Array Observatory and Cherenkov Telescope Array Consortium. CTAO Instrument Response Functions - prod5 version v0.1, September 2021.

[56] H. Abe, S. Abe, V. A. Acciari, I. Agudo, T. Aniello, S. Ansoldi, L. A. Antonelli, A. Arbet-Engels, C. Arcaro, M. Artero, K. Asano, D. Baack, A. Babić, A. Baquero, U. Barres de Almeida, J. A. Barrio, I. Batković, J. Baxter, J. Becerra González, W. Bednarek, E. Bernardini, M. Bernardos, A. Berti, J. Besenrieder, W. Bhattacharyya, C. Bigongiari, A. Biland, O. Blanch, G. Bonnoli, Ž. Bošnjak, I. Burelli, G. Busetto, R. Carosi, M. Carretero-Castrillo,

A. J. Castro-Tirado, G. Ceribella, Y. Chai, A. Chilingarian, S. Cikota, E. Colombo, J. L. Contreras, J. Cortina, S. Covino, G. D'Amico, V. D'Elia, P. da Vela, F. Dazzi, A. de Angelis, B. de Lotto, A. Del Popolo, M. Delfino, J. Delgado, C. Delgado Mendez, D. Depaoli, F. di Pierro, L. di Venere, E. Do Souto Espiñeira, D. Dominis Prester, A. Donini, D. Dorner, M. Doro, D. Elsaesser, G. Emery, J. Escudero, V. Fallah Ramazani, L. Fariña, A. Fattorini, L. Foffano, L. Font, C. Fruck, S. Fukami, Y. Fukazawa, R. J. García López, M. Garczarczyk, S. Gasparyan, M. Gaug, J. G. Giesbrecht Paiva, N. Giglietto, F. Giordano, P. Gliwny, N. Godinović, R. Grau, D. Green, J. G. Green, D. Hadasch, A. Hahn, T. Hassan, L. Heckmann, J. Herrera, D. Hrupec, M. Hütten, R. Imazawa, T. Inada, R. Iotov, K. Ishio, I. Jiménez Martínez, J. Jormanainen, D. Kerszberg, Y. Kobayashi, H. Kubo, J. Kushida, A. Lamastra, D. Lelas, F. Leone, E. Lindfors, L. Linhoff, S. Lombardi, F. Longo, R. López-Coto, M. López-Moya, A. López-Oramas, S. Loporchio, A. Lorini, E. Lyard, B. Machado de Oliveira Fraga, P. Majumdar, M. Makariev, G. Maneva, N. Mang, M. Manganaro, S. Mangano, K. Mannheim, M. Mariotti, M. Martínez, A. Mas-Aguilar, D. Mazin, S. Menchiari, S. Mender, S. Mićanović, D. Miceli, T. Miener, J. M. Miranda, R. Mirzoyan, E. Molina, H. A. Mondal, A. Moralejo, D. Morcuende, V. Moreno, T. Nakamori, C. Nanci, L. Nava, V. Neustroev, M. Nievas Rosillo, C. Nigro, K. Nilsson, K. Nishijima, T. Njoh Ekoume, K. Noda, S. Nozaki, Y. Ohtani, T. Oka, A. Okumura, J. Otero-Santos, S. Paiano, M. Palatiello, D. Paneque, R. Paoletti, J. M. Paredes, L. Pavletić, M. Persic, M. Pihet, G. Pirola, F. Podobnik, P. G. Prada Moroni, E. Prandini, G. Principe, C. Priyadarshi, W. Rhode, M. Ribó, J. Rico, C. Righi, A. Rugliancich, N. Sahakyan, T. Saito, S. Sakurai, K. Satalecka, F. G. Saturni, B. Schleicher, K. Schmidt, F. Schmuckermaier, J. L. Schubert, T. Schweizer, J. Sitarek, V. Sliusar, D. Sobczynska, A. Spolon, A. Stamerra, J. Strišković, D. Strom, M. Strzys, Y. Suda, T. Surić, H. Tajima, M. Takahashi, R. Takeishi, F. Tavecchio, P. Temnikov, K. Terauchi, T. Terzić, M. Teshima, L. Tosti, S. Truzzi, A. Tutone, S. Ubach, J. van Scherpenberg, M. Vazquez Acosta, S. Ventura, V. Verguilov, I. Viale, C. F. Vigorito, V. Vitale, I. Vovk, R. Walter, M. Will, C. Wunderlich, T. Yamamoto, D. Zarić, MAGIC Collaboration, M. Cerruti, J. A. Acosta-Pulido, G. Apolonio, R. Bachev, M. Baloković, E. Benítez, I. Björklund, V. Bozhilov, L. F. Brown, A. Bugg, W. Carbonell, M. I. Carnerero, D. Carosati, C. Casadio, W. Chamani, W. P. Chen, R. A. Chigladze, G. Damljanovic, K. Epps, A. Erkenov, M. Feige, J. Finke, A. Fuentes, K. Gazeas, M. Giroletti, T. S. Grishina, A. C. Gupta, M. A. Gurwell, E. Heidemann, D. Hiriart, W. J. Hou, T. Hovatta, S. Ibryamov, M. D. Joner, S. G. Jorstad, J. Kania, S. Kiehlmann, G. N. Kimeridze, E. N. Kopatskaya, M. Kopp, M. Korte, B. Kotas, S. Koyama, J. A. Kramer, L. Kunkel, S. O. Kurtanidze, O. M. Kurtanidze, A. Lähteenmäki, J. M. López, V. M. Larionov, E. G. Larionova, L. V. Larionova, C. Leto, C. Lorey, R. Mújica, G. M. Madejski, N. Marchili, A. P. Marscher, M. Minev, A. Modaressi, D. A. Morozova, T. Mufakharov, I. Myserlis, A. A. Nikiforova, M. G. Nikolashvili, E. Ovcharov, M. Perri, C. M. Raiteri, A. C. S. Readhead, A. Reimer, D. Reinhart, S. Righini, K. Rosenlehner, A. C. Sadun, S. S. Savchenko, A. Scherbantin, L. Schneider, K. Schoch, D. Seifert, E. Semkov, L. A. Sigua, C. Singh, P. Sola, Y. Sotnikova, M. Spencer, R. Steineke, M. Stojanovic, A. Strigachev, M. Tornikoski, E. Traianou, A. Tramacere, Yu. V. Troitskaya, I. S. Troitskiy, J. B. Trump,

A. Tsai, A. Valcheva, A. A. Vasilyev, F. Verrecchia, M. Villata, O. Vince, K. Vrontaki, Z. R. Weaver, E. Zaharieva, and N. Zottmann. Multimessenger Characterization of Markarian 501 during Historically Low X-Ray and γ-Ray Activity. , 266(2):37, June 2023.

[57] J. G. Kirk, F. M. Rieger, and A. Mastichiadis. Particle acceleration and synchrotron emission in blazar jets. , 333:452–458, May 1998.

[58] Joni Tammi and Peter Duffy. Particle-acceleration time-scales in TeV blazar flares. , 393(3):1063–1069, March 2009.

[59] Claus Grupen and Irène Buvat. *Handbook of Particle Detection and Imaging*. 2012.

[60] F. Aharonian, J. Buckley, T. Kifune, and G. Sinnis. High energy astrophysics with ground-based gamma ray detectors. *Reports on Progress in Physics*, 71(9):096901, September 2008.

[61] Mathieu de Naurois and Daniel Mazin. Ground-based detectors in very-high-energy gamma-ray astronomy. *Comptes Rendus Physique*, 16(6-7):610–627, August 2015.

[62] Axel Donath, Régis Terrier, Quentin Remy, Atreyee Sinha, Cosimo Nigro, Fabio Pintore, Bruno Khélifi, Laura Olivera-Nieto, Jose Enrique Ruiz, Kai Brügge, Maximilian Linhoff, Jose Luis Contreras, Fabio Acero, Arnau Aguasca-Cabot, David Berge, Pooja Bhattacharjee, Johannes Buchner, Catherine Boisson, David Carreto Fidalgo, Andrew Chen, Mathieu de Bony de Lavergne, José Vinicius de Miranda Cardoso, Christoph Deil, Matthias Füßling, Stefan Funk, Luca Giunti, Jim Hinton, Léa Jouvin, Johannes King, Julien Lefaucheur, Marianne Lemoine-Goumard, Jean-Philippe Lenain, Rubén López-Coto, Lars Mohrmann, Daniel Morcuende, Sebastian Panny, Maxime Regeard, Lab Saha, Hubert Siejkowski, Aneta Siemiginowska, Brigitta M. Sip"ocz, Tim Unbehaun, Christopher van Eldik, Thomas Vuillaume, and Roberta Zanin. Gammapy: A python package for gamma-ray astronomy. *AA*, 678:A157, 2023.

[63] Fabio Acero, Juan Bernete, Noah Biederbeck, Julia Djuvsland, Axel Donath, Kirsty Feijen, Stefan Frse, Claudio Galelli, Bruno Khlifi, Jana Konrad, Paula Kornecki, Maximilian Linhoff, Kurt McKee, Simone Mender, Daniel Morcuende, Laura Olivera-Nieto, Fabio Pintore, Michael Punch, Maxime Regeard, Quentin Remy, Atreyee Sinha, Hanna Stapel, Katrin Streil, Rgis Terrier, and Tim Unbehaun. Gammapy: Python toolbox for gamma-ray astronomy, 02 2024.

[64] Justin D. Finke, Soebur Razzaque, and Charles D. Dermer. Modeling the Extragalactic Background Light from Stars and Dust. , 712(1):238–249, March 2010.

[65] M. Sikora, M. Błażejowski, Mitchell C. Begelman, and R. Moderski. Erratum: Modeling the Production of Flares in Gamma-Ray Quasars. , 561(2):1154–1154, November 2001.

[66] M. Polkas, M. Petropoulou, G. Vasilopoulos, A. Mastichiadis, C. M. Urry, P. Coppi, and C. Bailyn. A numerical study of long-term multiwavelength blazar variability. , 505(4):6103–6120, August 2021.

[67] D. Emmanoulopoulos, I. M. McHardy, and I. E. Papadakis. Generating artificial light curves: revisited and updated. , 433(2):907–927, August 2013.